The Piezoelectric Effect in II-VI Semiconductors

by

James Milnes B.Sc. Hons.

Submitted for the degree of Doctor of Philosophy at the Department of

Physics, Heriot-Watt University, Edinburgh, UK.

January 1999

TABLE OF CONTENTS

6. CRITICAL THICKNESS OF PIEZOELECTRIC QUANTUM WELLS.

Acknowledgements

I would like to thank my supervisor, Prof. Brian Cavenett for his guidance and support during the period of my research and Dr. Kevin Prior for his useful discussions and his unbeatable publication filing system.

I would also like to thank all the members of the MBE group, past and present, in particular Christian Morhain, Samantha Telfer for growing most of the samples, and Paul Thompson and Shouyin Wang for getting me started. Further thanks must go to Neil Ross for the gold contacts, Donna Bain for the **k·p** calculations and Iain Galbraith for the triangular well solution.

Finally I would like to thank my parents for their constant support, both moral and financial, and Caroline and Jonathan for surviving the three years with me.

Abstract

This thesis explores the nature and application of the piezoelectric effect in ZnSe-based semiconductors, and also includes a chapter on microscope analysis techniques.

Photoelectrochemical etching of ZnSe is shown to reveal defect sites that are related to features observed by a technique of luminescence microscopy. The defect densities are related to the optical quality of the material. Defect annealing under intense optical excitation has been observed.

The piezoelectric effect produces an internal electric field that shifts inter-band transitions to lower energies by the quantum confined Stark effect. Previous experiments of photocurrent on the piezoelectric effect in ZnCdSe / ZnSe quantum wells are expanded and improved on and with similar results obtained by photoluminescence excitation, provide a method of measuring the internal field. Photoluminescence experiments reveal the effect of the internal field on the free and donor bound excitons, as well as the exciton localisation.

Finally the piezoelectric effect is utilised to find the critical thickness of the start of strain relaxation in ZnCdSe / ZnSe quantum wells, as the internal field is directly proportional to the strain in the well layer.

List of Publications

'Compensation in p-type ZnSe based semiconductors' K.A. Prior, W. Meredith, G.D. Brownlie, Z. Zhu, P.J. Thompson, J.S. Milnes, I.S. Hauksson, G. Horsburgh, T.A. Steele, S.Y. Wang and B.C. Cavenett.

MATERIALS SCIENCE AND ENGINEERING B-SOLID STATE MATERIALS FOR ADVANCED TECHNOLOGY, 1997, Vol.43, No.1-3, pp.9-15

'A spectroscopic study of the piezoelectric effect in ZnSe/ZnCdSe single quantum wells grown on (211)B GaAs' J.S. Milnes, C. Morhain, S.A. Telfer, W. Meredith, T.A. Steele, K.A. Prior and B.C. Cavenett.

JOURNAL OF CRYSTAL GROWTH, 1998, Vol.185, pp.714-717

'Growth of ZnSe and ZnCdSe on (211)B GaAs substrates' S.A. Telfer, G. Horsburgh, J.S. Milnes, C. Morhain, P.J. Thompson, K.A. Prior and B.C. Cavenett.

JOURNAL OF CRYSTAL GROWTH, 1998, Vol.185, pp.51-56

'Growth of sulphur-based ternary and quaternary epilayers for use in multilayer devices' G.D. Brownlie, B. Vogele, W. Meredith, J.S. Milnes, K.A. Prior and B.C. Cavenett.

JOURNAL OF CRYSTAL GROWTH, 1998, Vol.185, pp.37-40

'Growth and characterization of ZnSe based blue green VCSELs' K.A. Prior, W. Meredith, G.D. Brownlie, J.S. Milnes, G.S. Buller, B.C. Cavenett, A.J. Dann and M.J. Robertson.

JOURNAL OF MATERIALS SCIENCE-MATERIALS IN ELECTRONICS, 1998, Vol.9, No.3, pp.181-186

'Strain relaxation of ZnCdSe quantum wells grown on (211)B GaAs measured using the piezoelectric effect' J.S. Milnes, S.A. Telfer, C. Morhain, K.A. Prior and B.C. Cavenett.

JOURNAL OF CRYSTAL GROWTH, *in press*

'Measurement of the critical thickness of ZnCdSe quantum wells in ZnSe barrier layers by the piezoelectric effect' J.S. Milnes, C. Morhain, S.A. Telfer, B. Urbaszek, I. Galbraith, K.A. Prior and B.C. Cavenett.

APPLIED PHYSICS LETTERS, 1998 Vol.73, No.21, pp.3141-3143

1. INTRODUCTION

1.1. Introduction.

The interest in the past decade in II-VI semiconductors and ZnSe in particular has been due to the quest to produce a laser diode with a shorter wavelength (in the blue-green region) to extend the established III-V GaAs-based systems. The commercial applications are considerable, from optical storage systems to all-colour image displays. The research into ZnSe-based laser diodes which started with the first structure using current injection at 77K by the 3M company [1] has progressed through to a 100 hour laser at room temperature by Sony [2] who then improved to a device with a commercially acceptable operating voltage with a lifetime of over 300 hours [3], although this has recently been surpassed by lasers based on the GaN compound [4].

The impetus for the work in this thesis was generated by the laser research, although only chapter 2 and, to a lesser extent, chapter 6 have a direct relation to it. However, the majority of the work is based on the core of the laser structure, a quantum well which is constructed of ZnSe and a very thin layer of a ternary alloy $Zn_{1-x}Cd_xSe$. 'x' is the cadmium mole fraction which means the fraction of zinc atoms that are replaced by cadmium atoms. The theory of quantum wells is detailed in chapter 3, which also serves as an introduction to the 'piezoelectric effect' which is

studied in chapters 4, 5 and 6. The drive for the study of piezoelectric semiconductor layers was for the production of modulators and SEEDs, also detailed in chapter 3.

This introductory chapter will briefly explain the growth method (MBE), before describing the zincblende structure of ZnSe and then outlining the aspects of semiconductor theory that are relevant to the thesis.

1.2. Molecular beam epitaxy.

Molecular beam epitaxy (MBE) is a method of producing semiconductor material with very high structural crystal quality. Other methods include metal-organic chemical vapour deposition (MOCVD). MBE operates by placing a substrate crystal in an ultra high vacuum chamber (less than 10^{-11} mbar) which allows thermally effused molecules from selected materials to travel with long mean free paths before reacting at the substrate surface, hence the term 'molecular beam'. 'Epitaxy' refers to the growth of materials one layer at a time. Ideally homoepitaxy using ZnSe substrates would have been preferred but these are not widely available. However the lattice constant of ZnSe is very close to the widely available GaAs (only 0.27% difference) and therefore heteroepitaxy is the most common method. For a detailed description of the growth machine used by the Heriot-Watt MBE group shown on figure 1-1, see reference 5. The first growth of ZnSe on GaAs substrates by MBE was by Yao *et al.* in 1977 [6].

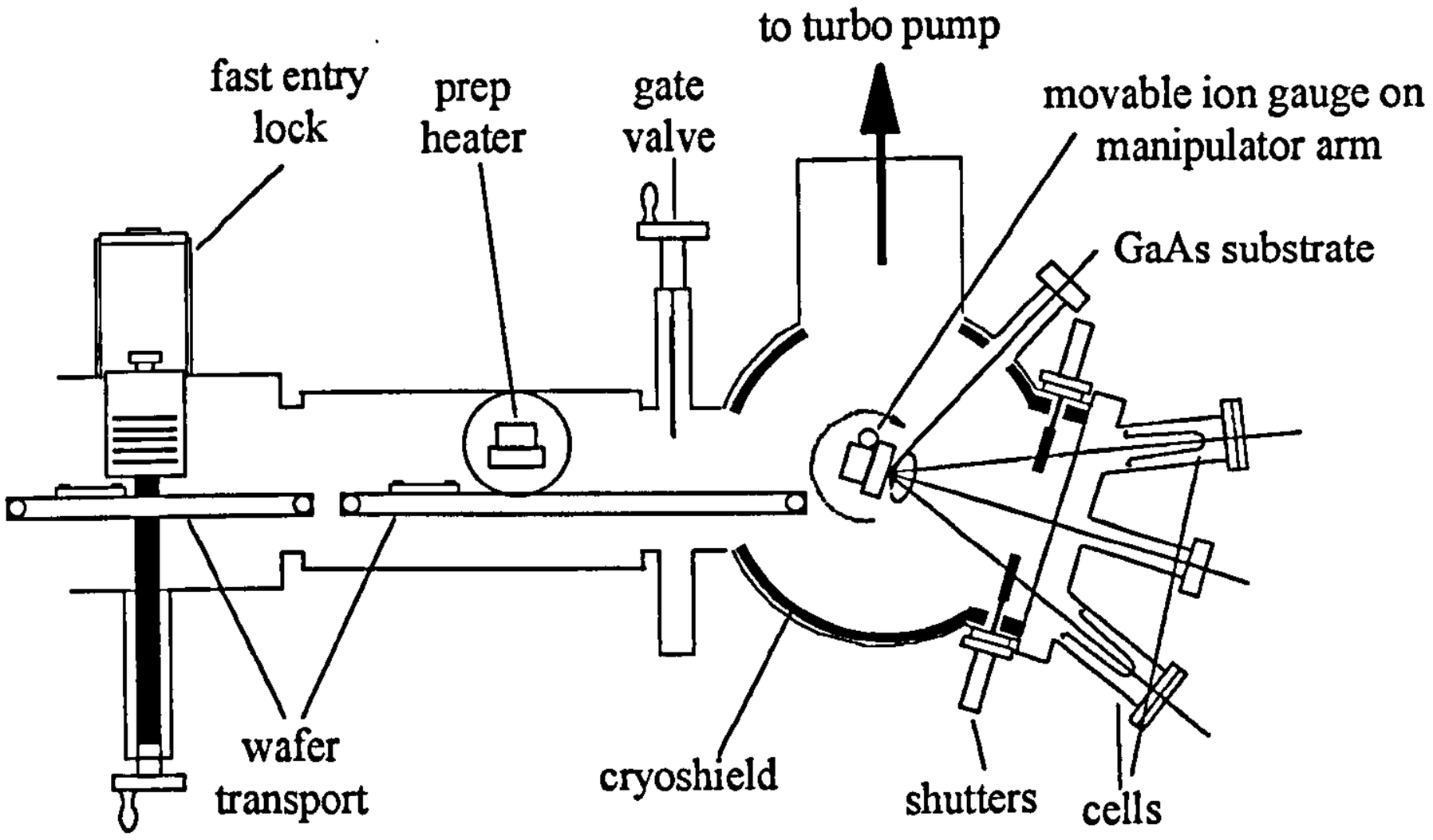

Figure 1-1. *MBE growth machine.*

The GaAs substrate is moved into the vacuum chamber through the entry lock and wafer transport as shown. Once in position the cells containing the source materials (e.g. zinc, cadmium, selenium, *etc.*) are selectively heated so that the material effuses into the chamber and is directed towards the substrate. The actual machine has eight available cells, each with a shutter, to grow a variety of materials. The layer thickness is controlled by limiting the time for the growth. The layer by layer aspect of MBE growth allows very thin layers (of the order of a few nanometers) of a material to be sandwiched between a different material to generate the quantum wells.

1.3. Zincblende crystal structure.

ZnSe-based semiconductor systems, in common with those based on GaAs, have a zincblende structure (*N.B.* while related materials such as CdSe can exist in hexagonal wurtzite form, only zincblende structures are used in this thesis). The zincblende structure can be visualised in two ways. Firstly, it can be seen as two interlaced face-centred-cubic (FCC) lattices, one of zinc atoms and one of selenium atoms.

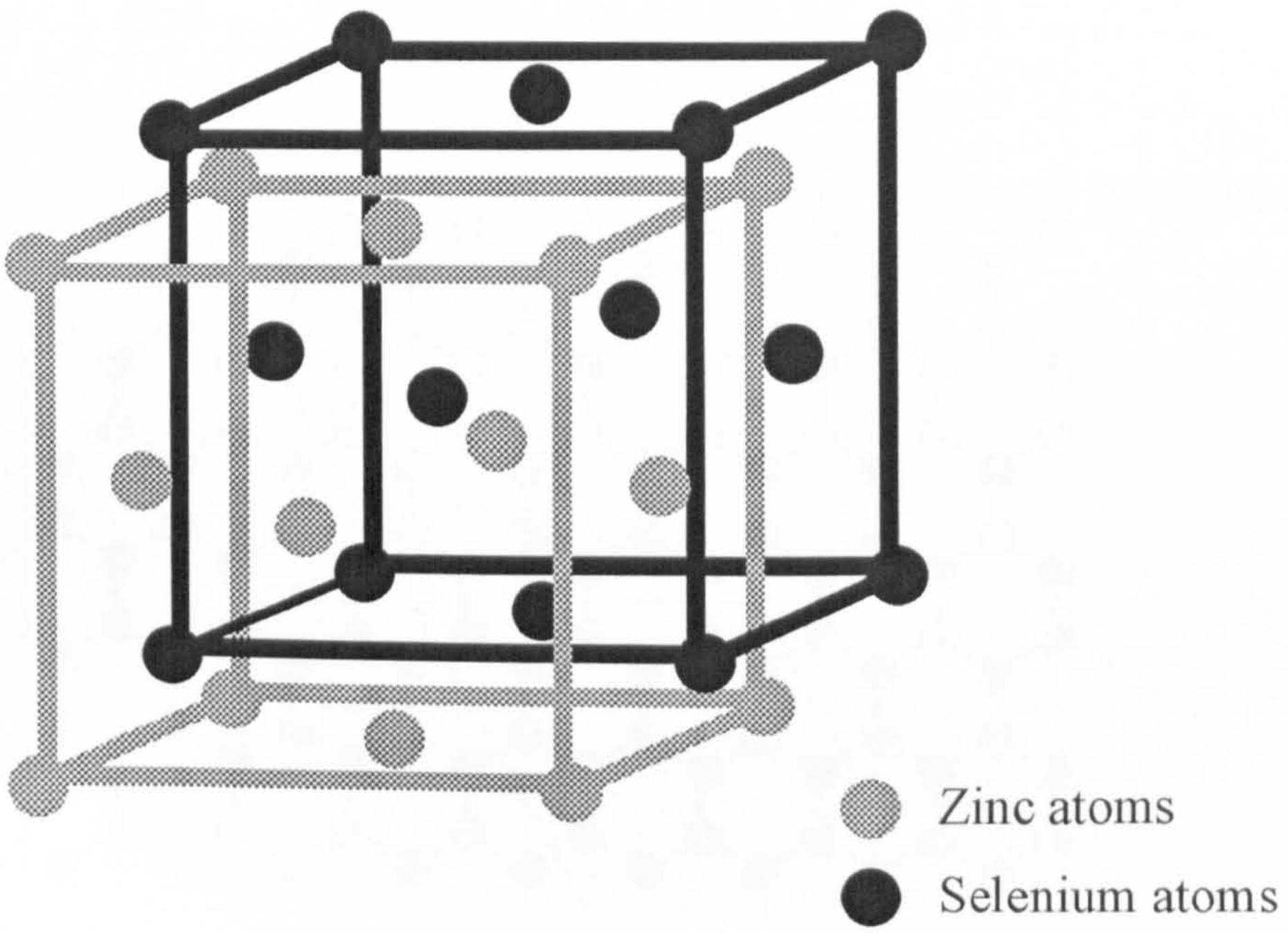

Figure 1-2. *Zincblende structure for ZnSe displayed as two interlaced face-centred-cubic lattices.*

If a zinc atom was placed at the origin of a 3-D Cartesian graph, and the other corners of the cube were at (0,0,1), (0,1,0), (1,0,0), (1,1,0), (1,0,1), (1,1,0) and

(1,1,1), then the corresponding origin for the selenium lattice would be at (¼,¼,¼), as shown on figure 1-2.

Zincblende structures can also be seen as a variation on the diamond structure, with the obvious difference being that each zinc atom is bonded equally to four selenium atoms (and vice versa), instead of all the atoms being the same (*i.e.* carbon). This method makes it easier to visualise the zincblende in a 2-D diagram. Figure 1-3 shows the interbonding between the atoms and the important planes mentioned in this thesis.

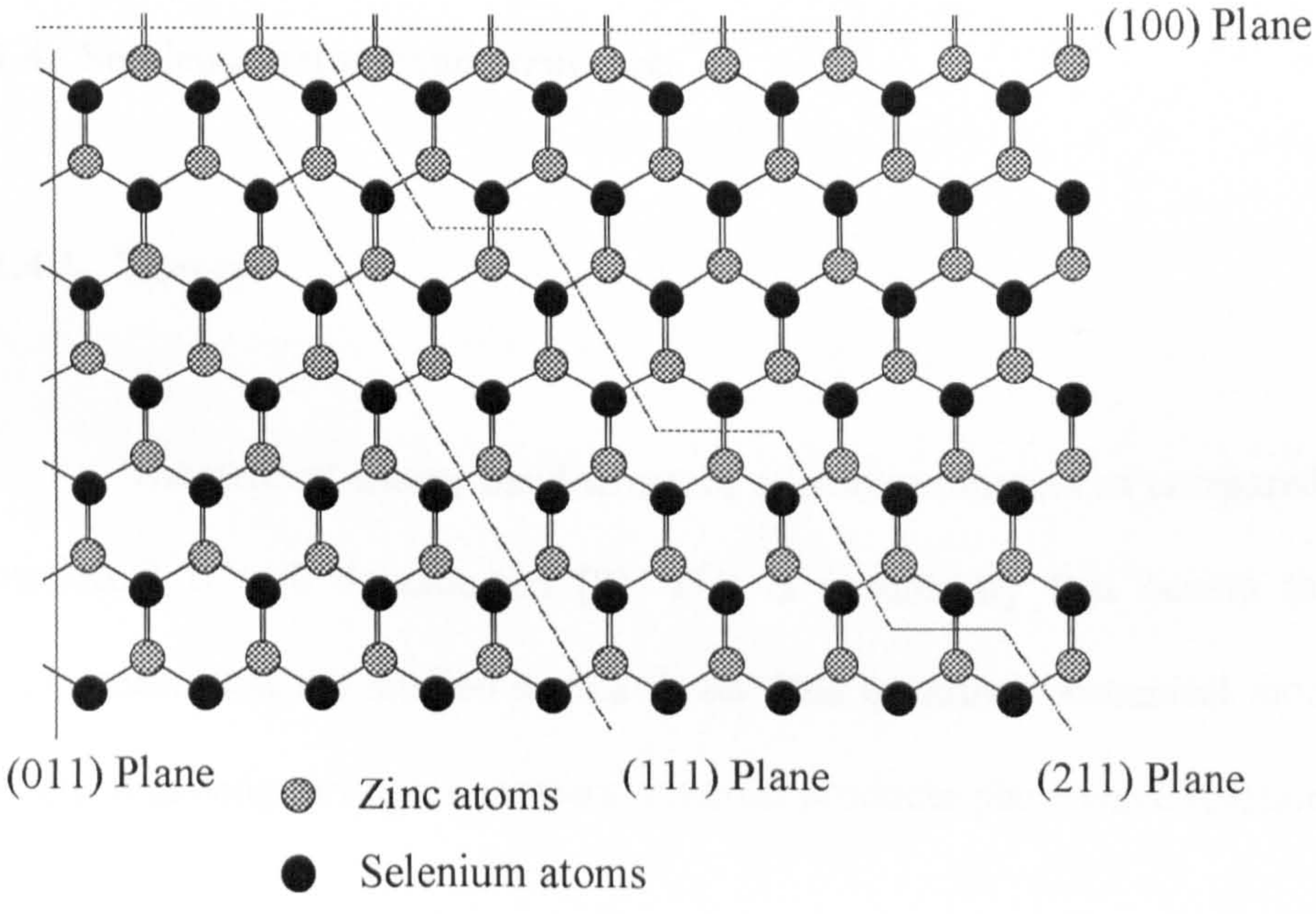

Figure 1-3. *Zincblende structure showing the bonding between the atoms in ZnSe* [7]. *Each single line is a bond on the surface of the page* $(01\bar{1})$. *Each double line represents two bonds, one going diagonally up and one going diagonally down to two different atoms, either of which could be represented by the atom on the figure.*

It can be seen from figure 1-3 that if the zincblende structure is cut along the (111) plane, then one side will terminate in A-atoms triple bonded to the crystal (known as the (111)A surface) and the other will terminate in B-atoms triple bonded to the surface (known as the (111)B surface). A-atoms are defined as the lower valence element (*i.e.* zinc) and B-atoms are defined as the higher valence element (*i.e.* selenium) [8]. Chapters 3 to 6 in this thesis are concerned with structures grown on the (211) plane, and figure 1-3 shows that the (211) surface is not singular, *i.e.* it is made up of steps from the (100) and the (111) planes, however the distinctions for the A and B surfaces still apply.

1.4. Semiconductor band structure.

1.4.1. Theory.

The general energy band structure of semiconductors as compared to metal or insulators is well documented [9]. This is a summary that covers the important phenomena that are studied in this thesis. The quantum mechanical model of a free electron moving through a constant potential produces plane wave solutions given by

$$\varphi = A\exp(ik.r) \tag{1-1}$$

where k is the wavevector which has a magnitude of

$$|k| = \frac{2\pi}{\lambda} \tag{1-2}$$

and points in the direction of the plane electron wave. The allowed values of k decided by boundary conditions (either static or periodic) that demand standing and propagating waves respectively in a reasonably large crystal are so close together that they can be considered as a quasi-continuum of momentum ($\hbar k$) or kinetic energy ($\hbar^2 k^2/2m$) states. Therefore at this basic stage, the relationship between k and the energy of an electron is a simple quadratic one. The potential energy of the electron is independent of k and can be neglected [10].

When this model is combined with the periodic potential created by the nuclei of the crystal lattice, it is found that the electron wave will suffer a Bragg reflection when an integral number of its wavelength matches that of the periodic potential, or more simply, when $|k| = n\pi/a$, $n = \pm1, \pm2, \pm3...$ a is the lattice constant. This means that if k of an electron was increased slowly from zero, when it reached π/a it would be reflected to a value of $-\pi/a$, without being able to reach a value higher than π/a. Furthermore, it was found that when k approaches this condition from higher and lower values, two different figures were obtained for the energy. As shown on figure 1-4, this leads to an energy gap at this value of k. Therefore electrons with certain energy values cannot propagate through the crystal, leading to the idea of gaps separating different energy bands. This is known as the 'nearly free' electron theory.

As mentioned before, there are only a finite number of values for k that are allowed, however it has been shown that the number of allowed values in an energy band is equal to the number of primitive cells in the material [9], and such a large number leads to the idea of a quasi-continuum stated earlier.

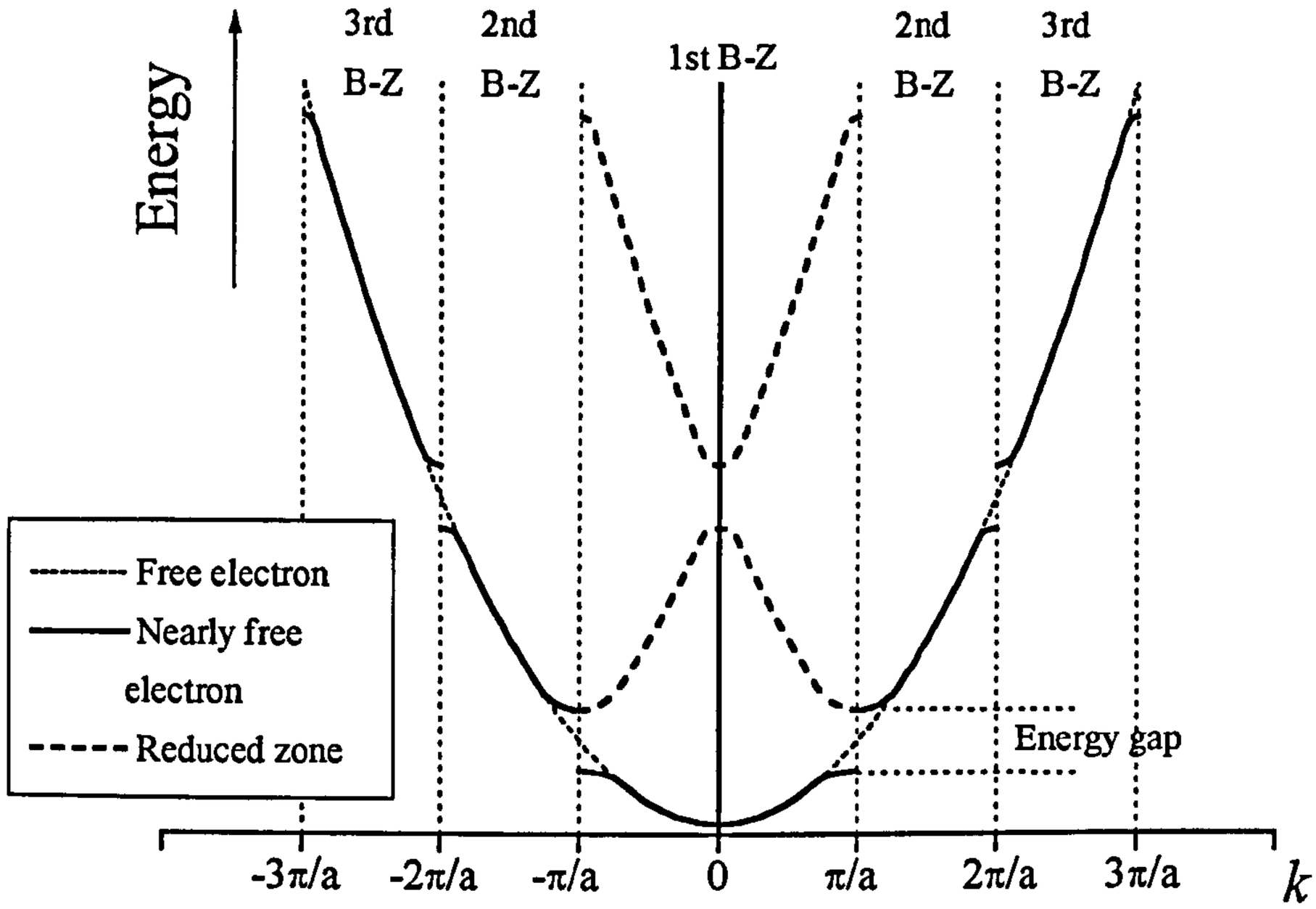

Figure 1-4. *Variation of the energy of an electron with the wavevector for the free electron and nearly free electron theories. Also shown are the Brillouin zones (B-Zs) and the reduced zone scheme.*

The range of values of k between $-\pi/a$ and π/a is known as the first Brillouin zone, the second zone being between π/a and $2\pi/a$, and between $-\pi/a$ and $-2\pi/a$ and so on. However, an application of Bloch's theorem reveals that the values of k are periodic, repeating their nature in units of π/a. It is therefore possible to consider k

only between $-\pi/a$ and π/a, *i.e.* in the first Brillouin zone, which is known as the reduced zone scheme as shown on figure 1-4.

At a theoretical temperature of 0K the electrons will occupy the lowest possible energy bands. If the lowest band is full and the gap between the next is large, then the material is an insulator, and if the lowest band is only partially filled then it is a conductor. However, if the gap to the next band is of the order of a few electron-volts (eV) then it is considered to be a semiconductor.. Electron-volts are the recognised units of energy in semiconductors, $1eV = 1.602 \times 10^{-19}$ joules. The highest full band is known as the valence band, while the lowest empty band is the conduction band. If electrons are removed from a full valence band then they leave behind electron vacancies known as holes which act like positively charged particles. Semiconductors may still be insulating in their pure form, but can be made to conduct by the process of doping where an impurity element is deliberately allowed to occupy sites in the crystal lattice and provide extra electrons or holes, hence the name 'semiconductor'.

The variation from the free electron model occurs at the top and bottom of the energy bands and is therefore crucial when studying semiconductors since they consist of full or nearly full bands. It is also responsible for the phenomena of 'effective mass', where the observed mass of an electron is affected by the crystal lattice [9]. The effective mass is governed by the curvature of the energy / wavevector relationship.

When the influence of the specific atomic nature of the material is considered, the full energy band structure can be obtained for any direction in the first Brillouin

zone in 3 dimensions which for zincblende structures is a truncated octahedron, as shown on figure 1-5. The point labelled Γ is the zone centre at $k = 0$. L is the position on the zone boundary in the [½,½,½] direction from the origin (Γ), X is the corresponding boundary in the [0,1,0] direction, U is the boundary in the [¼,1,¼] direction and K is the boundary in the [¾,¾,0] direction. By symmetry, the points at U and K are the same. The other labels are for the lines separating the specific points ; Λ ($\Gamma \rightarrow$ L), Δ ($\Gamma \rightarrow$ X) and Σ ($\Gamma \rightarrow$ U,K). For a more comprehensive explanation, see reference 9.

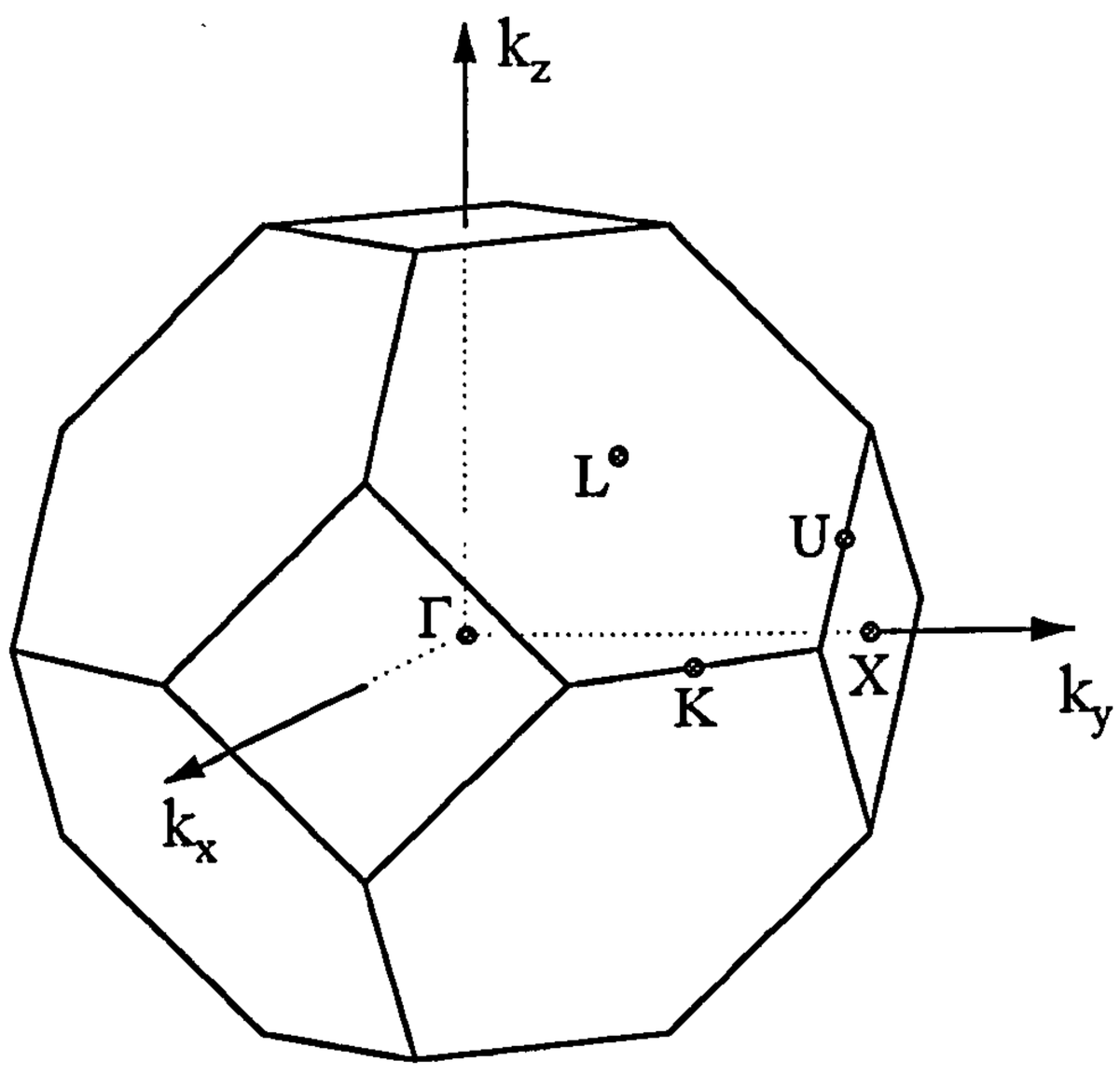

Figure 1-5. *The first Brillouin zone of the zincblende crystal structure with the special points labelled.* k_x, k_y *and* k_z *are in the* [1,0,0], [0,1,0] *and* [0,0,1] *directions respectively.*

This has been calculated for ZnSe by several workers [11,12,13,14] and the band structure shown on figure 1-6 is from reference 12. Clearly the variation of energy with the wavevector throughout the whole of the first 3-D Brillouin zone would be difficult to show on a simple diagram, so figure 1-6 shows the variation along the more important directions.

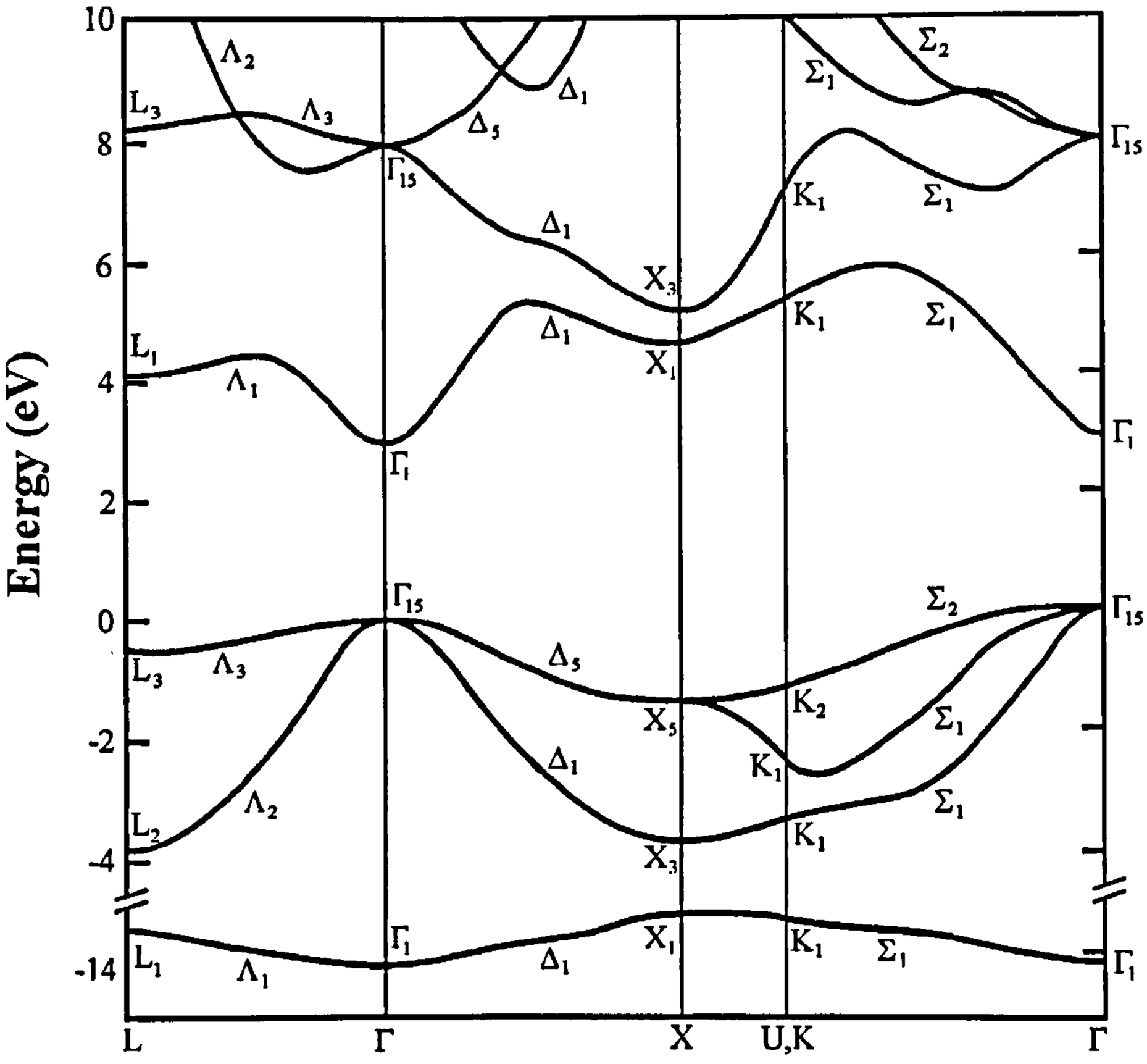

Figure 1-6. *Electronic band structure for ZnSe. The zero energy point is positioned at the top of the valence band* [12].

There are slight variations between references, due to different methods used and different source parameters, but they are not significant. In fact, other materials with the same zincblende crystal structure (GaAs, GaSb, InP, InSb and ZnS) have very similar electronic structure [11], as do germanium and silicon [9], which have the related diamond structure. Ge and Si have a crucial difference, however, in that the lowest point in the conduction band and the highest point in the valence band occur at different values of k and are therefore known as indirect bandgap semiconductors. This has important consequences in the absorption process, but for the purpose of this thesis only direct bandgap structures are of interest, *i.e.* where the minimum conduction band and maximum valence band occur at the same k value. Also given on references 13 and 14 are the calculated density of allowed k values as a function of energy, known as the density of states. This concept will be discussed further in chapter 3 in relation to quantum wells.

The whole band structure is quite complex, however as ZnSe is a direct bandgap semiconductor (at the Γ point) then this is the only point of interest. Furthermore, only the top of the valence band and bottom of the conduction band are of interest, so the band structure can be shown much more simply as in figure 1-7.

The bandgap E_g of ZnSe is 2.70eV at room temperature [15], but its temperature dependence has been extensively studied (see chapter 5). The valence band consists of two energy bands with different curvatures. As mentioned earlier, this curvature is inversely related to the effective mass of the holes that are present, and are therefore labelled the heavy and light hole energy bands as shown. A more detailed

study reveals that the top of the valence band at the Γ point is split into a fourfold state (the heavy and light holes) and a twofold state (a split-off band) when spin-orbit interaction is considered [16], with the split for ZnSe being $\Delta = 0.45eV$ [14]. However, this does not concern this thesis.

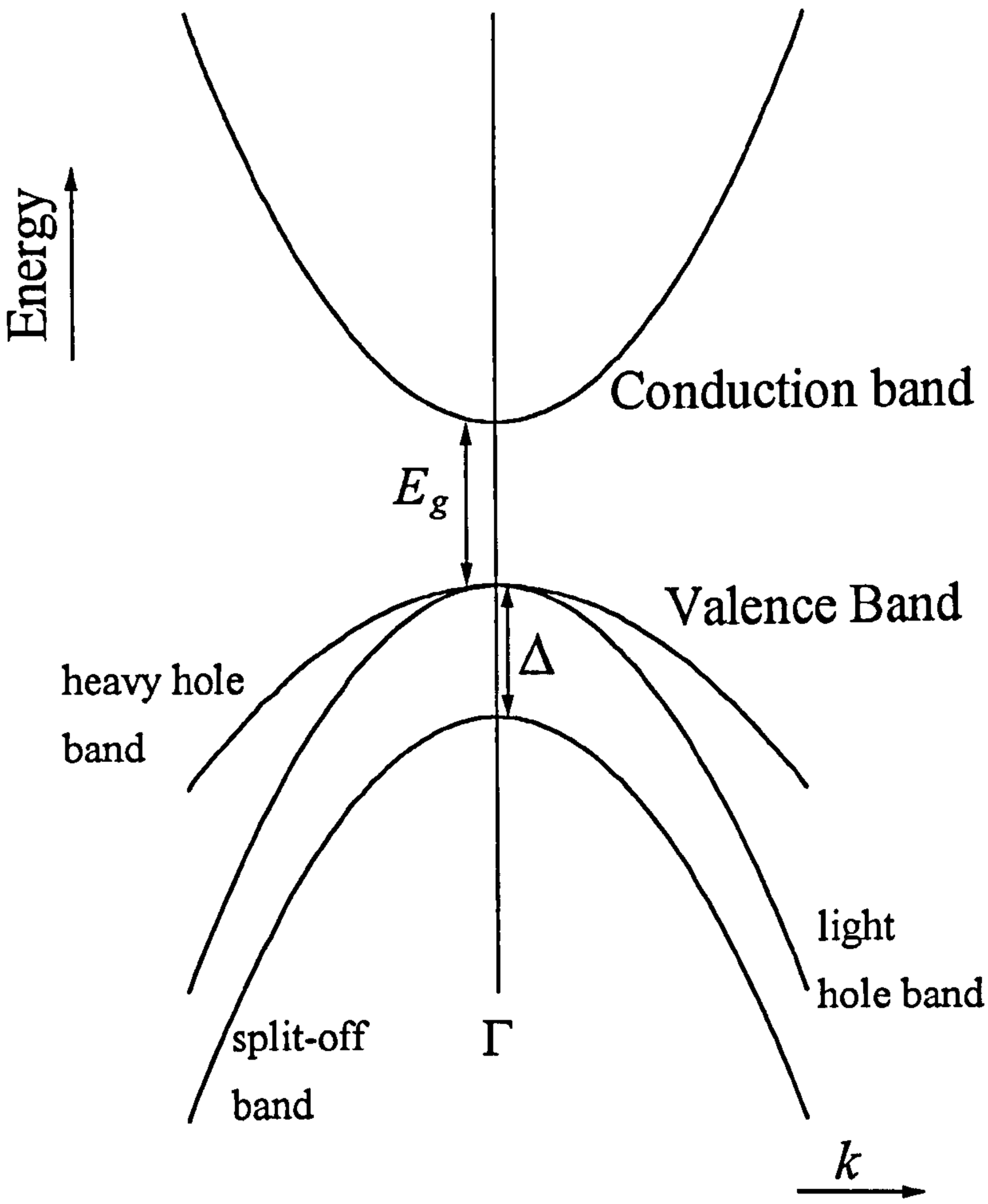

Figure 1-7. *Simplified band structure for ZnSe showing the conduction and valence bands at the zone centre (not to scale), with the split-off band at $\Delta = 0.45eV$.*

1.4.2. Strain effects.

There is one final important issue to be discussed with reference to the ZnSe band structure and this is the effect of strain. The majority of this thesis is concerned with ZnCdSe quantum wells which are very thin (4 ~ 20nm) layers grown between ZnSe barriers. However, there is a difference in the lattice constants of ZnCdSe and ZnSe, and providing that the layers are below a critical thickness then these layers are subject to strain, a subject explored in much more detail in chapter 6.

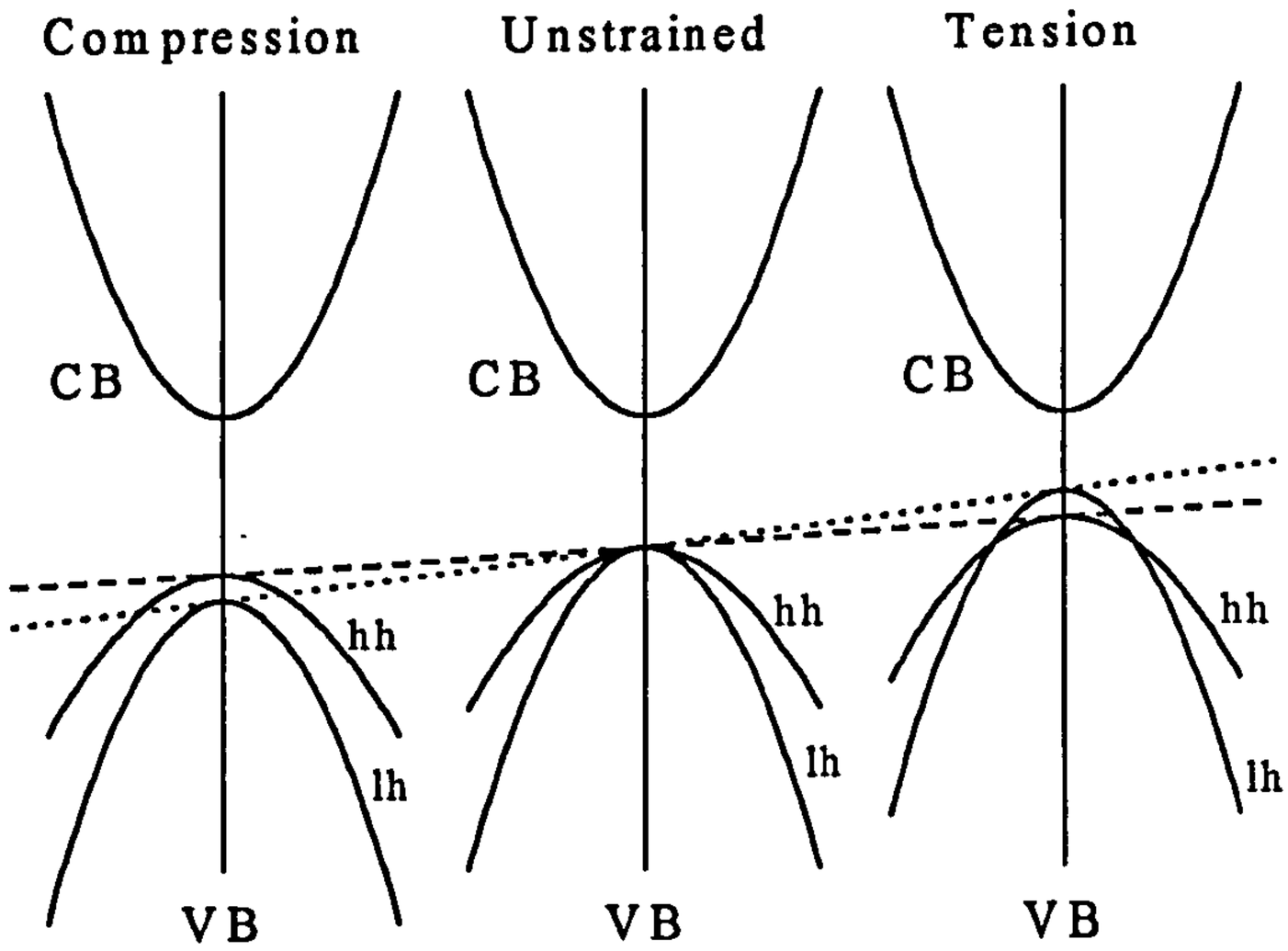

Figure 1-8. *The effect of strain on the heavy hole (hh) and light hole (lh) energy bands in the valence band (VB). The gap to the conduction band (CB) is not to scale.*

The application of compressive or tensile strain (where k is parallel to the strain axis) has the effect of splitting the light and heavy hole energy bands at the Γ point.

This system produces compression strain so the light hole is at a lower energy state than the heavy hole [17], as shown on figure 1-8. This will become evident in chapter 4 when it becomes possible to distinguish between heavy and light hole transitions.

Furthermore the effect of *hydrostatic* strain shifts the whole valence band structure shown in figure 1-7 which has been referred to as shifting its 'centre of gravity' [17]. Tensile or compressive strains refer to distances and are measured in units of $(\Delta L/L)$ while hydrostatic strain refers to the resulting difference in volume and is measured by $(\Delta V/V)$. Strain also has an important role in structures that are grown on certain crystal orientations that produces the piezoelectric effect which is the main area of study for this thesis and is explained in chapter 3.

1.5. References.

[1] M.A. Haase, J. Qiu, J. M. DePuydt and H. Cheng, Appl. Phys. Lett. **59**, 1272 (1991).

[2] S. Taniguchi, T. Hino, S. Itoh, K. Nakano, N. Nakayama, A. Ishibashi and M. Ikeda, Electron. Lett. **32**, 552 (1996).

[3] Y. Sanaka, H. Okuyama, S. Kijima, E. Kato, H. Noguchi and A. Ishibashi, Electron. Lett. **34**, 1891 (1998).

[4] S. Nakamura, M. Senoh, S. Nagahama, N. Iwasa, T. Yamada, T. Matsushita, H. Kiyoku, Y. Sugimoto, T. Kozaki, H. Umemoto, M. Sano and K. Chocho, Appl. Phys. Lett. **72**, 211 (1997).

[5] G. Horsburgh, Thesis of Heriot-Watt University, Edinburgh, 1997.

[6] T. Yao, Y. Miyoshi, Y. Makita and S. Maekawa, Jpn. J. Appl. Phys. **16**, 369 (1977).

[7] M. Henini, III-Vs Review **11**, No.3, 48 (1998).

[8] D.B. Holt, J. Mater. Sci. **19**, 439 (1984).

[9] G. Burns, *Solid State Physics*, Academic Press (1985).

[10] G.F. Imbusch, *Luminescence Spectroscopy*, edited by M.D. Lumb, Academic Press (1978).

[11] M.L. Cohen and T.K. Bergstresser, Phys. Rev. **141**, 789 (1966).

[12] Y. Petroff, M. Balkanski, J.P. Walter and M.L. Cohen, Solid State Commun. 7, 459 (1969).

[13] J.R. Chelikowsky, T.J. Wagener, J.H. Weaver and A. Jin, Phys. Rev. B **40**, 9644 (1989).

[14] R. Markowski, M. Piacentini, D. Debowska, M. Zimnal-Starnawska, F. Lama, N. Zema and A. Kisiel, J. Phys. : Condens. Matter **6**, 3207 (1994).

[15] J.H. Haanstra and J. Dieleman, Ext. Abstr. Electrochem. Soc. **14**, 2 (1965).

[16] B. Sapoval and C. Hermann, *Physics of Semiconductors*, Springer-Verlag (1995).

[17] H. Asai and K. Oe, J. Appl. Phys. **54**, 2052 (1983).

2. ANALYSIS OF ZnSe-BASED EPILAYERS BY OPTICAL MICROSCOPY.

2.1. Introduction.

This chapter will explore microscope analysis techniques. The first section will look at etching processes that reveal defects and are examined by a Nomarski microscope and an atomic force microscope (AFM), while the second section will examine photoluminescence (PL) microscopy where the microscope itself is used to illuminate the sample with UV light and to analyse the results.

2.2. Defect-revealing etching.

2.2.1. Introduction.

During the development of wide band gap II-VI laser diodes a major problem was the device lifetime and the emphasis in the research changed from increasing optical and electrical confinement to the study of failure modes within device structures. The main mode of failure was attributed to the creation of non-radiative recombination centres seen as dark line defects in electroluminescence studies of laser diodes [1] which coincided with dislocations within the crystal structure [2,3].

Methods such as X-ray diffraction (XRD), transmission electron microscopy [4] (TEM), electron beam induced current and cathodoluminescence [5] have all previously been used either individually or in conjunction with chemical etching to estimate dislocation densities, with the aim of using these measured densities to help improve growth procedures or adjust material composition. However, XRD uses a complicated mathematical analysis of peak broadening, the value of which has since been questioned [6]. Furthermore TEM requires extensive sample preparation and can only detect densities greater than $10^5 cm^{-2}$. Other approaches such as CL and X-ray topography, that give direct imaging of defects, require special equipment to observe their densities. In this chapter a simple method using existing apparatus is used to enable routine examination of defect levels in epitaxial layers through the use of photoelectrolytic etching which is used in capacitance-voltage (C-V) profiling.

2.2.2. Method.

Capacitance-voltage measurements have frequently been used to measure carrier concentrations as a function of depth in both III-V [7] and II-VI [8] semiconductors. It is the process of electrochemical etching into the semiconductor layer that allows the depth profile of carrier concentration and as such is an advantage over the alternative Hall effect method. The electrochemical etching requires holes to be transported to a semiconductor electrolyte ($NaOH:Na_2SO_3$) interface by the application of an external bias to the back of the semiconductor sample during the C-V measurements (see figure 2-1) where they are removed to the electrolyte by the

reactions given in equations (2-1) and (2-2) [9]. The electrolyte was developed specifically for the etching of II-VI semiconductors from a system designed for III-V materials [10].

$$ZnSe(s) + 2h \rightarrow Zn^{2+}(aq) + Se(s) \qquad (2\text{-}1)$$

$$Se(s) + SO_3^{2-}(aq) \rightarrow SeSO_3^{2-}(aq) \qquad (2\text{-}2)$$

In the case of n-type or undoped material the minority carriers (holes) are generated by illumination of the interface with above band gap radiation. The technique should thus be more correctly described as photoelectrolytic etching, and is typically operated under conditions where a flat or featureless etched region is produced. A diagram of the electrochemical cell is shown on figure 2-1, illustrating the position of the semiconductor sample, electrolyte, electrode and the optical illumination. This electrochemical etching is an alternative to the bromine / methanol [11] chemical etching used to define defects in ZnSe and ZnSSe.

Under different etch conditions, photoelectrolytic profiling has been used to reveal the presence of defects within the region and typically exposes these defects as features which can be counted, and their orientation determined, using a Nomarski microscope or a scanning electron microscope (SEM). This type of defect revealing was first reported by Faktor and Stevenson [12] for GaAs, and later by Elliott and Regnault [13] for InP.

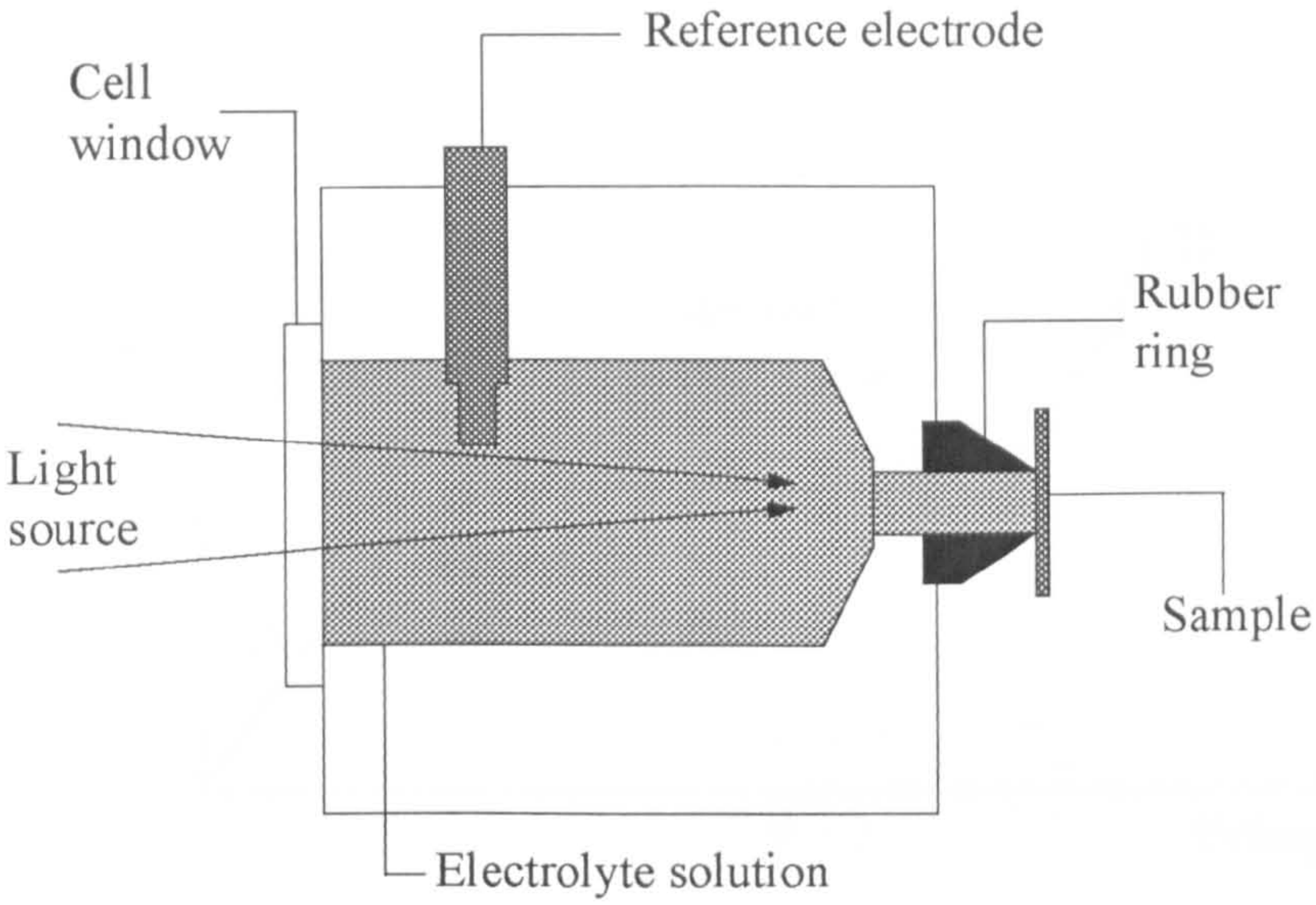

Figure 2-1. *Electrochemical cell used for C-V profiling.*

The typical I-V curve for ZnSe shown on figure 2-2 illustrates the possibility for two kinds of photoelectrolytic etches. In the voltage region between A and B the current density, and hence the etch rate, will vary with any local fluctuations in the voltage. In the voltage region between B and C, however, the current density is constant over a limited voltage range. In the final region between C and D the current density also varies with voltage but etching at these voltage values produces localised pitting that is not associated with defects [14]. Standard etches for doping profiling are performed in the voltage region between B and C and give smooth, featureless surfaces in III-V materials, while etches in the region between A and B are known as defect etches.

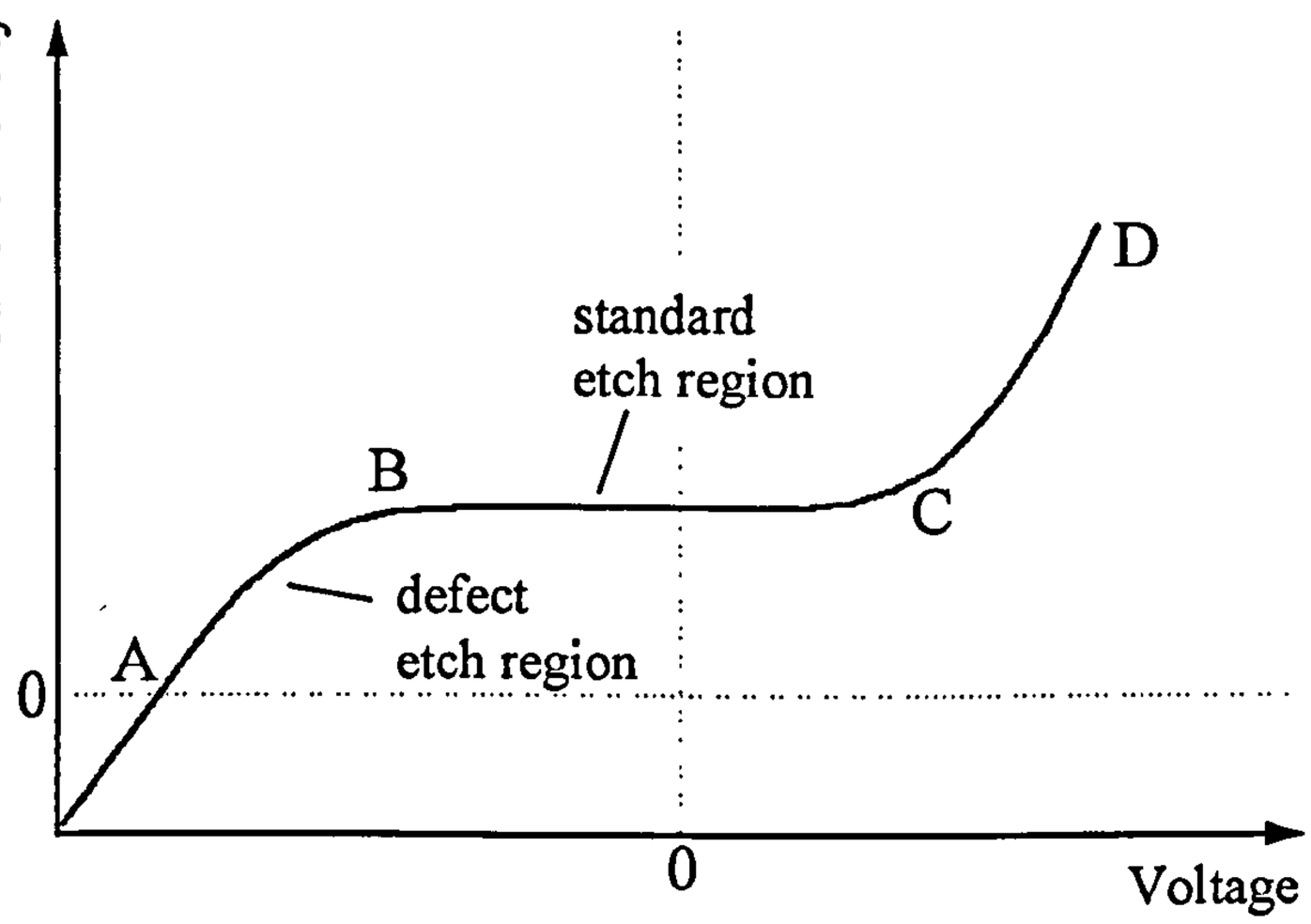

Figure 2-2. *Typical I-V curve indicating voltage regions used in photoelectrolytic etching.*

2.2.3. Experiment.

A variety of doped and undoped layers were studied by the etching process, but this section will focus on seven nominally undoped ZnSe samples grown by molecular beam epitaxy (MBE) on (001) n^+ GaAs substrates. The etch on an n-type sample will be discussed later in section 2.3. The thicknesses of the epilayers were determined by Fabry-Perot reflection methods using bulk refractive indices. The photoluminescence (PL) spectrum (see chapter 5) for each sample was taken at a temperature of 5K using an Ar^+ laser operating at 351nm (3.53eV) (see figure (5-1)). As a rough estimate of the quality of the samples, the ratio of the relative intensity of

the Y_0 line (2.600eV), which is related to structural defects [15], to the free exciton (FX) line (2.802eV) is considered. The samples used had a broad range of structural quality as shown on figure 2-3 and table 2-1.

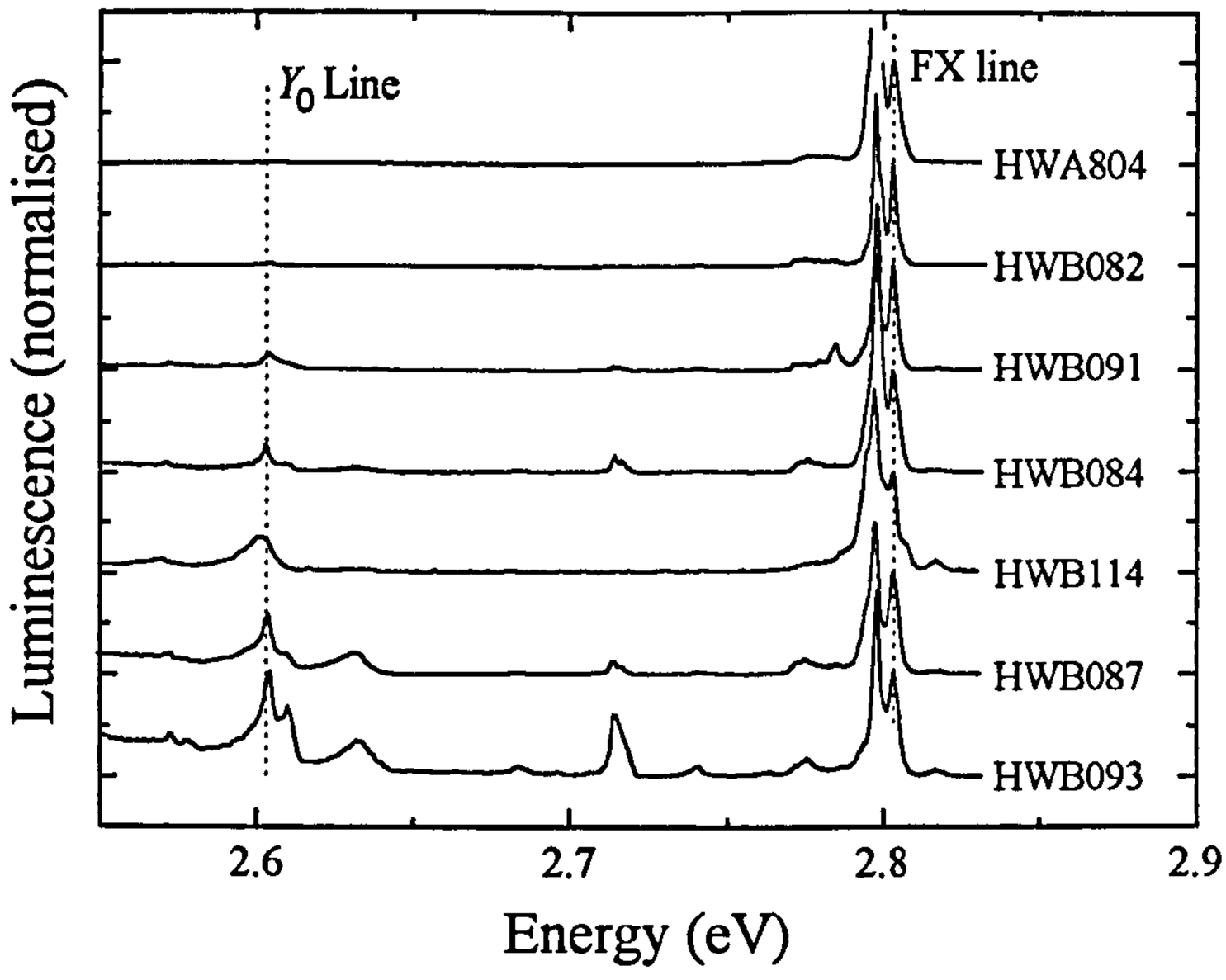

Figure 2-3. *Photoluminescence scans for the seven ZnSe samples used to demonstrate the defect revealing etch, showing the Y_0 line at 2.600eV. The scans have been normalised to the free exciton at 2.802eV.*

The samples were etched using a Bio-Rad PN4300 profiler with a 1M $NaOH:Na_2SO_3$ solution as the electrolyte to a depth of 0.25μm, measured by a Dektak 3030 surface profiler. Standard etches typically required a voltage of about -1V giving a current density of about $0.1mA/cm^2$, while the defect etches used a voltage of -2V giving about $0.05mA/cm^2$ of current density. The voltages were

applied to the back contact of the substrate and are given with respect to the reference electrode. The etched and unetched surfaces were subsequently examined, and compared, using Nomarski microscopy and an atomic force microscope (AFM) to determine densities and orientations of any surface features. Each sample was prepared before etching by cleaning in an acetone bath using ultra-sound.

Table 2-1. *Range of quality of the ZnSe samples.*

Sample Code	I(Y_0) / I(FX)	Thickness (μm)
HWA804	0.019	0.71
HWB082	0.035	0.48
HWB091	0.171	1.01
HWB084	0.274	1.00
HWB114	0.355	0.53
HWB087	0.581	0.85
HWB093	1.034	0.94

Normal etching with electrolytic profiling is entirely dependent upon the photo-generation of minority carriers, in undoped and n-type material. However, to establish the cause of any revealed features, a series of control etches were employed [16]. The control etches were (a) without illumination and without an external bias, (b) with illumination and no bias and (c) with no illumination and an applied bias. Although these control etches resulted in removal of material, with a maximum etch rate of

10nm per hour, no recognisable surface topographical features were revealed apart from a roughening of the surface. When compared with an etch rate of over 500nm per hour for standard etching when using the profiler, the rate of etch of the control tests is negligible. However, when using the profiler for defect revealing, the etch rate is slower and dependent upon material quality.

2.2.4. Results.

Standard etches were performed on each sample to act as a control to the defect etches and were expected to be featureless as in III-V semiconductors. However, SEM and Nomarski microscopy revealed a large number of ridged features aligned in the $[1\bar{1}0]$ direction with a dislocation density ranging between $5\times10^{4}\,cm^{-2}$ and $3.5\times10^{5}\,cm^{-2}$, and an average length of between 30μm and 100μm, see figure 2-4(a). Their relationship with the PL quality on the samples studied is indicated on figures 2-5 and 2-6. These features will henceforth be referred to as type I. The two samples of lowest quality are not included in these graphs because the type I defects were too abundant to resolve. Repeating the process several times on different parts of the same sample, and to different etch depths, produced a density of type I features that varied only by a factor of 2.

A defect etch was then carried out on each sample which produced a similar but slightly reduced abundance of type I features compared to the standard etches on the same samples. However, a comparison of the two samples using a Nomarski

microscope highlighted contrast differences not previously observable with SEM measurements [16]. For the standard etches, the area between the type I features was smooth, see figure 2-4(a). However, for the defect etches, the area between the type I features exhibited a rough disordered formation, see figure 2-4(b). This roughness consists of a series of rounded hillocks and depressions which have been labelled as type II features. The relationship between type II feature density and the PL quality is shown on figure 2-7.

To attempt to define the type I features in more detail, AFM measurements were made on a sample after a defect etch had been performed. These indicated that the revealed type I features were formed from clusters of conical protrusions in groups ranging from 1 to 4 on this sample, see figures 2-8(a) and 2-8(b).

Again, the larger groupings were aligned in the $[1\bar{1}0]$ direction. For one sample, measurement of individual conical protrusions gave dimensions of 1μm by 1μm and heights between 270nm and 300nm, three times as high as the type II defects. The angle of the cone varied little, estimated at between 24° and 27°. While the height of the conical protrusions may appear to be greater than the depth to which the area was etched, it should be noted that the etch depth was an estimate given from *average* etch rates.

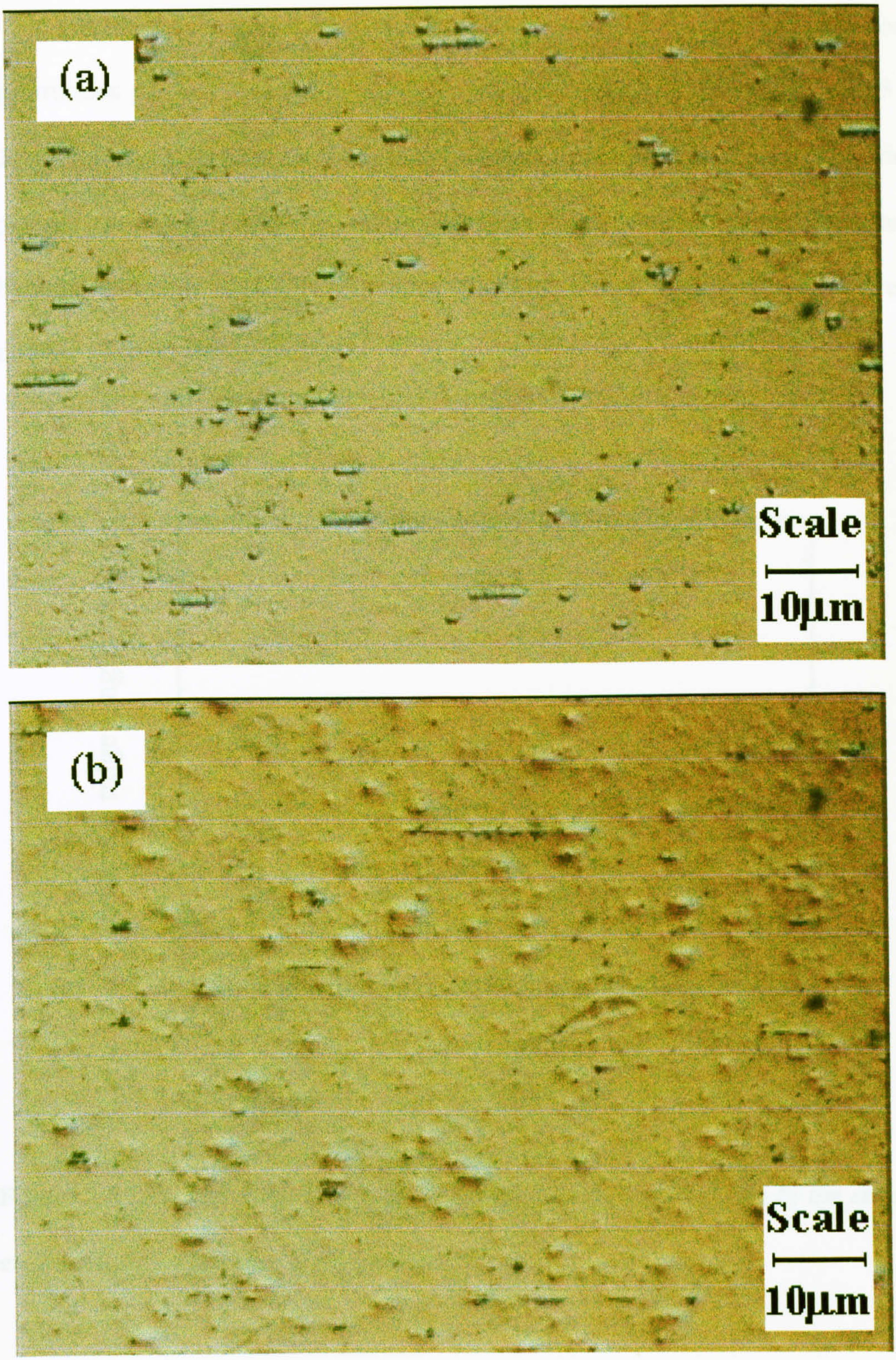

Figure 2-4. *Nomarski images of sample surface after* (a) *standard etch and* (b) *defect etch.*

Given these dimensions, it was possible to estimate the number of the conical protrusions per cm^2 revealed by the standard etches as described by figures 2-5 and 2-6 simply by multiplying the average ridge length (in μm) by the density of the ridges per cm^2. It was found that the number of these cones remained reasonably constant between $6\times10^5 cm^{-2}$ and $7\times10^5 cm^{-2}$ until the final, lowest quality sample where the number of cones nearly doubles.

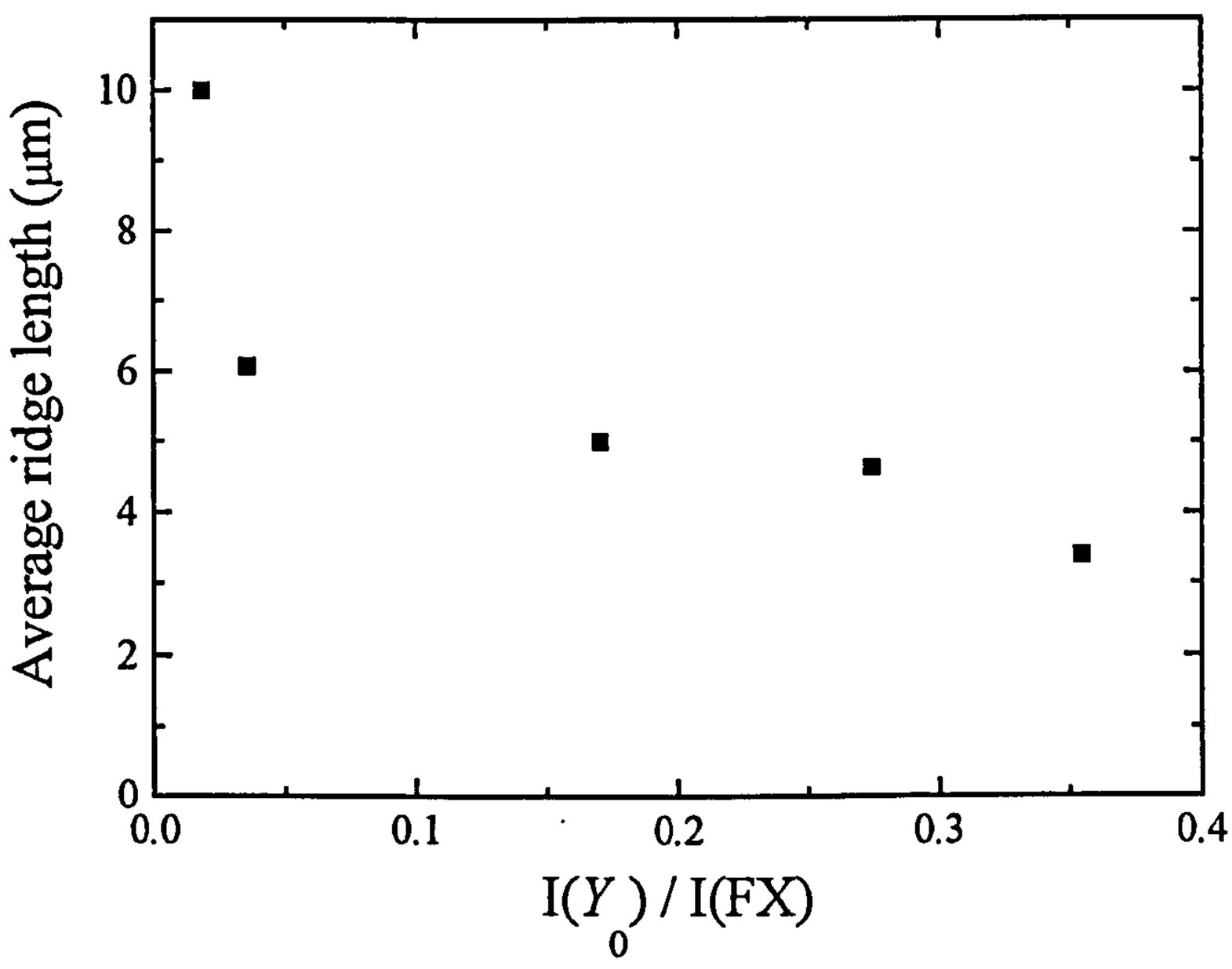

Figure 2-5. *Average ridge length of type I revealed defects as shown by the standard etch plotted as a function of PL quality.*

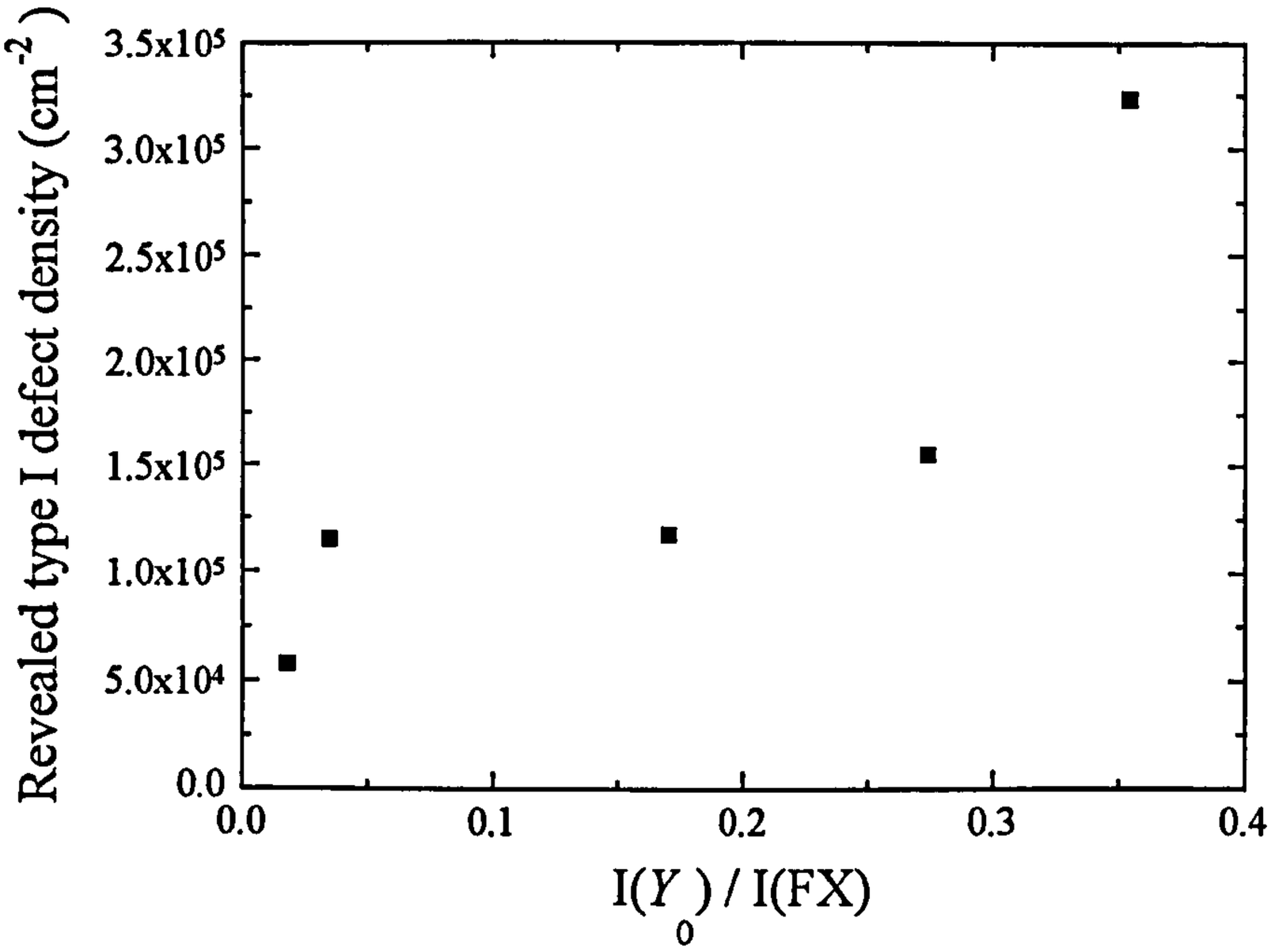

Figure 2-6. *Revealed type I defect density as shown by the standard etch plotted as a function of PL quality.*

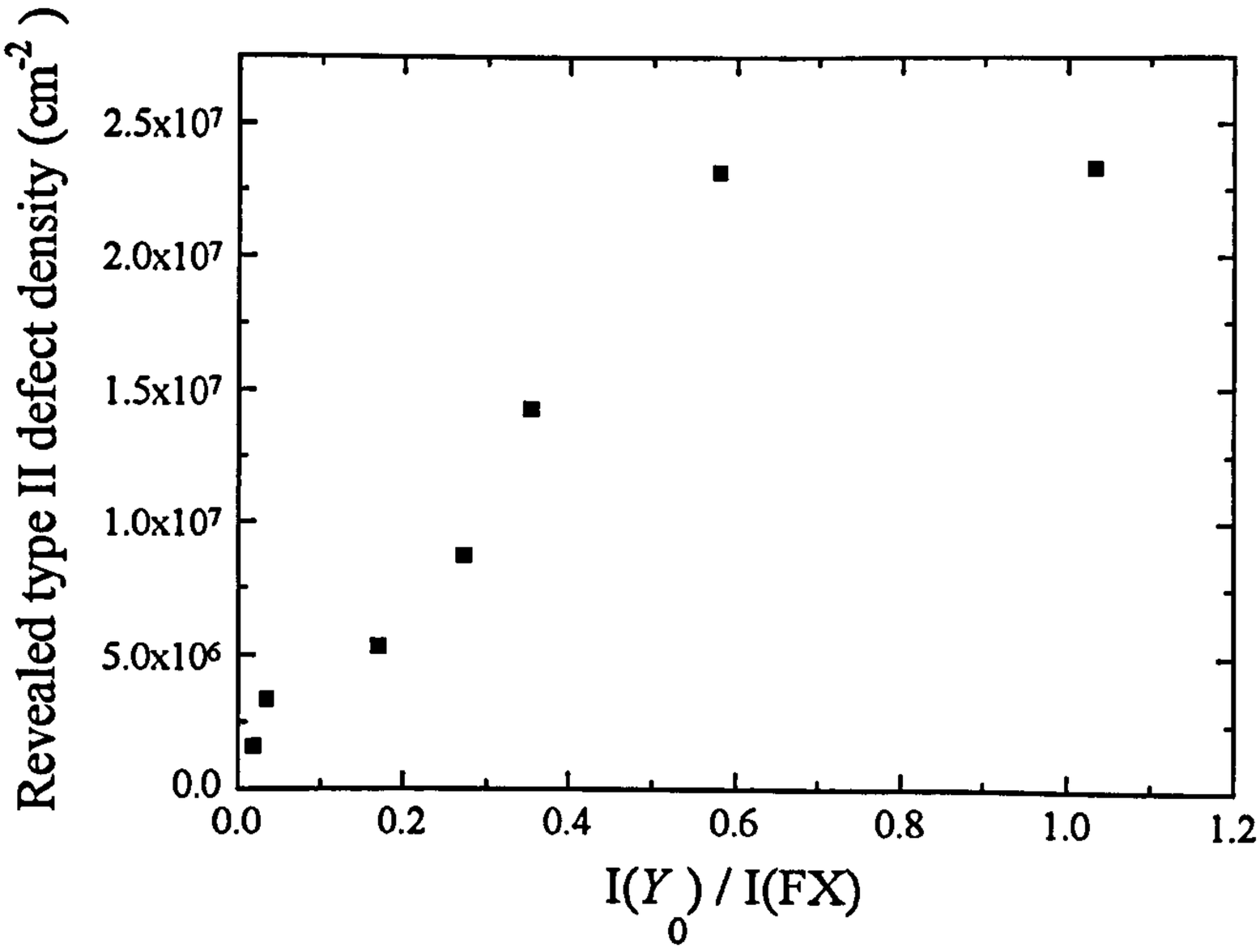

Figure 2-7. *Revealed type II defect density as shown by the defect etch plotted as a function of PL quality.*

(a)

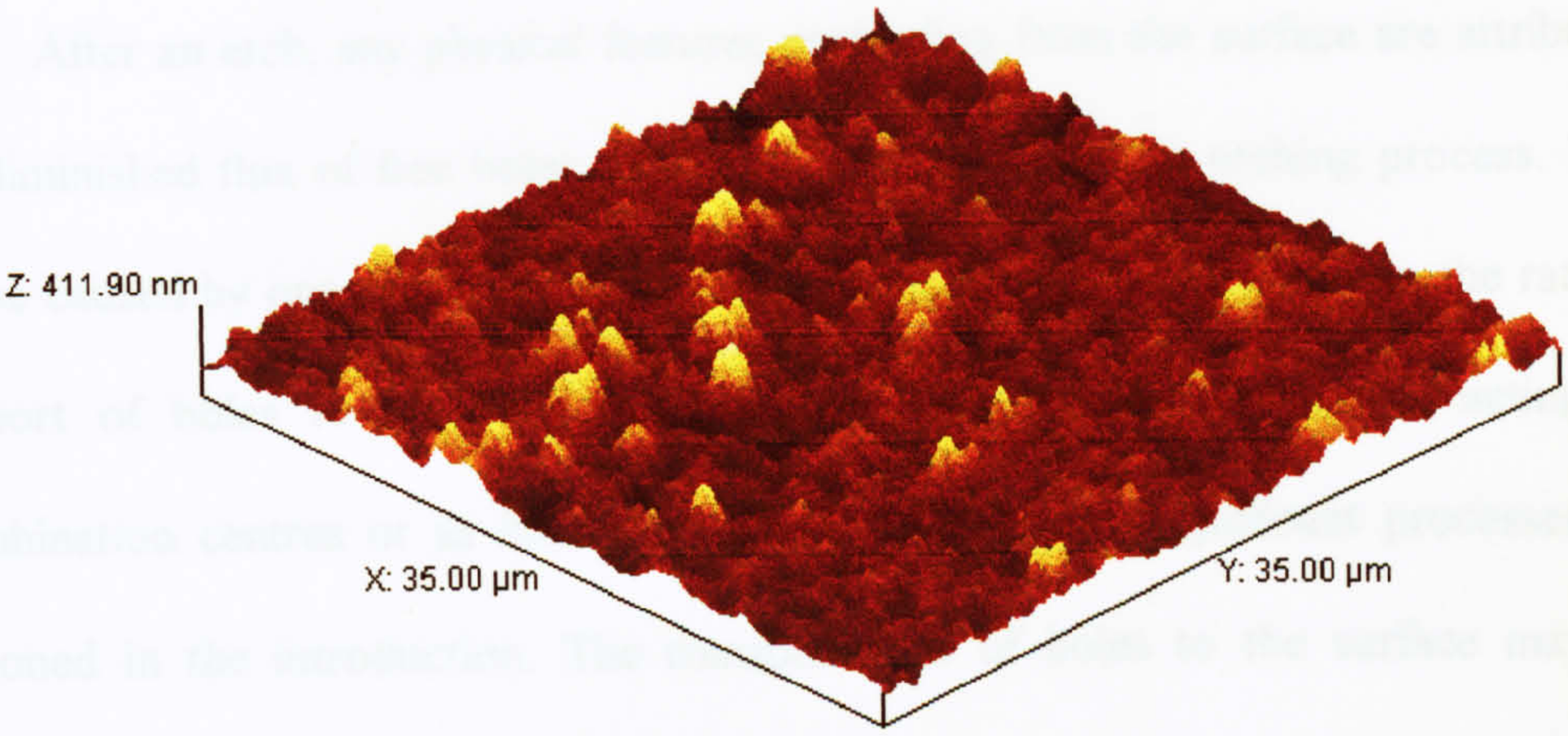

(b)

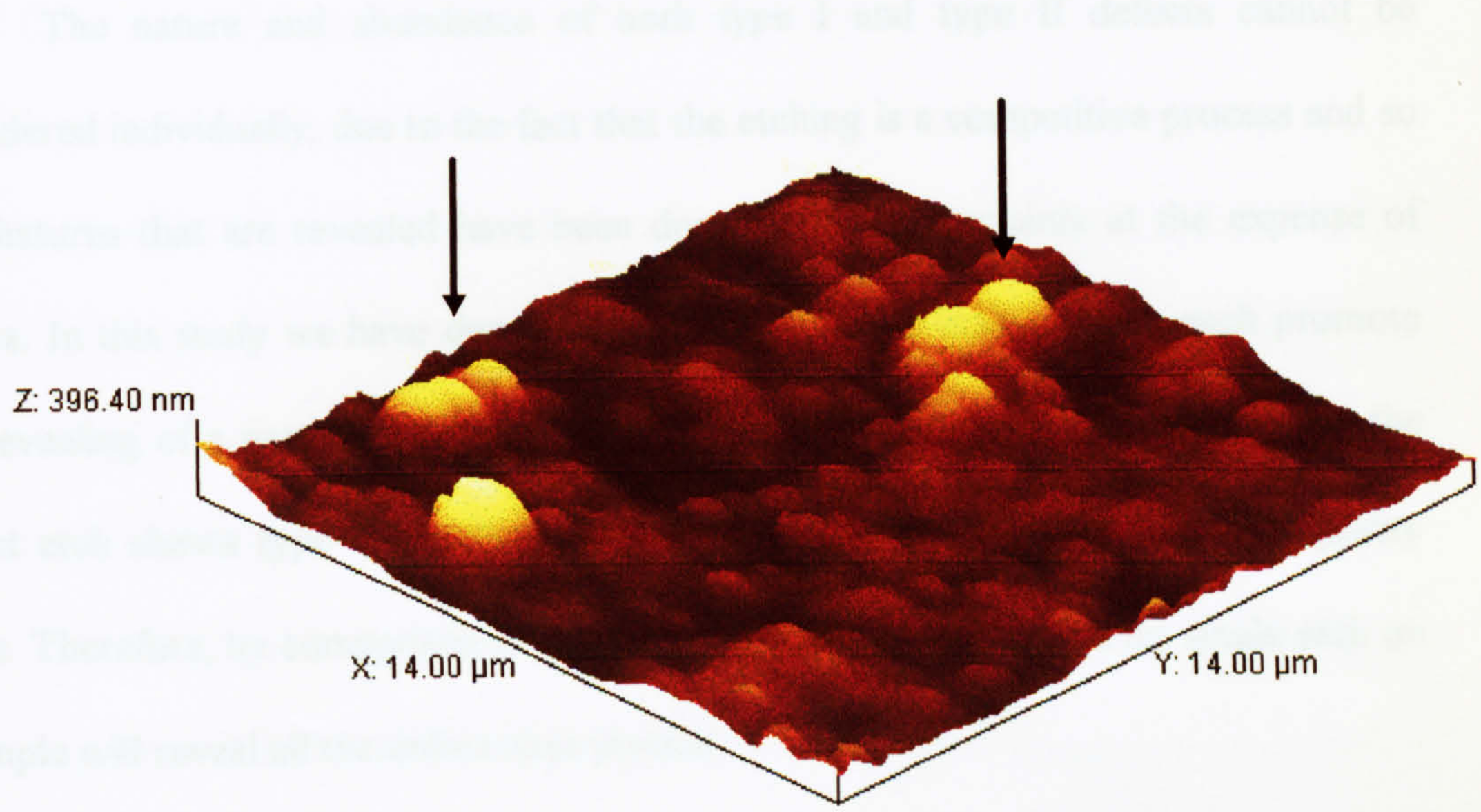

Figure 2-8. *Atomic Force Microscope image of sample surface after defect etch, with* (a) *a broad scan and* (b) *a scan focusing in on some of the type I ridges.*

2.2.5. Discussion.

After an etch, any physical features protruding from the surface are attributed to a diminished flux of free holes, which are necessary for the etching process. This may be caused by one of two processes: hole quenching *or* a reduction in the rate of transport of holes to the surface. Hole quenching is due to defects acting as recombination centres or as hole traps, both of which are significant processes, as mentioned in the introduction. The transport rate of holes to the surface may be lowered by localised reductions in the electric field, caused by electrically polarised defects opposing the applied field. This is the only effect seen in defect etches in III-V semiconductors.

The nature and abundance of both type I and type II defects cannot be considered individually, due to the fact that the etching is a competitive process and so the features that are revealed have been done so almost certainly at the expense of others. In this study we have demonstrated two kinds of etches which each promote the revealing of a particular feature. The standard etch only reveals type I, while the defect etch shows type I but also the emergence of type II defects in poor quality ZnSe. Therefore, by comparison of the two processes, it is clear that no single etch on a sample will reveal all the defect sites present.

Given these restrictions, it is still possible to discuss the significance of figures 2-5, 2-6 and 2-7. The I-V curve on figure 2-1 shows the *average* current density variation over the etched area. Therefore the position chosen for the standard etch may

allow for minor localised variations in the etching rate but should primarily reveal sites of recombination or hole capture, i.e. the type I defects, because any local variation in electric field will not significantly alter the etch rate. While both etching methods reveal type I defects, only defect etching reveals type II, where the only difference between the two methods is the gradient in the I-V curve. Therefore, given that type II defects require an I-V gradient to be revealed, and considering their absence from the standard etches, this would suggest that they are due to the electric field effects mentioned which also occur in III-V semiconductors.

The ridged type I defects are longest in the high quality samples (figure 2-5) but their abundance increases in poor quality material (figure 2-6) coupled with an increase in type II defects (figure 2-7). A possible explanation is that the production of type I features is inherent in ZnSe grown on GaAs due to the lattice mismatch and the fact that all the samples grown were considerably thicker than the critical thickness of 97.5(±2.5)nm [17], see chapter 6. However, as the structural quality decreases, the production of type II features begins to actively compete in the etching process, until it completely dominates in the poorest samples where type I has disappeared completely. Therefore the ridges may still be present in the poor quality samples, but cannot be seen because of the competitive nature of the etching process. Figure 2-6 is therefore misleading, because the increase in the density of type I defect features in poor quality ZnSe is only due to the ridges being separated by the emergence of type II defects, which is supported by the corresponding reduction in the average ridge length (figure 2-5). It should be noted that the plateau reached in figure 2-7 is almost certainly due to the resolution limit of the revealing method rather than a limit in type II defect density.

The effectiveness of etching becomes limited in very poor quality samples because their I-V curves tend to differ wildly from the example shown on figure 2-2, and a certain standard of I-V curve is necessary. Finally, given that the best quality sample used had an excellent PL spectra, this suggests that PL is insensitive to low defect densities.

The fact that any features were revealed in the standard etch illustrates a fundamental difference between II-VI and III-V materials, where standard etches leave smooth, featureless surfaces. From mobility measurements for minority carriers, the chances for hole quenching at defect sites are increased for ZnSe when compared with GaAs. This arises if one considers the drift velocity of both materials :

$$v_d = \mu_p \varepsilon \qquad (2\text{-}3)$$

v_d is the drift velocity, μ_p is the minority carrier mobility and ε is the electric field. In the case of ZnSe the mobility is approximately $30 cm^2 V^{-1} s^{-1}$ [18], whilst for GaAs this is substantially larger and of the order of $300 cm^2 V^{-1} s^{-1}$ [19]. Therefore, for the same electric field, ZnSe minority carriers are slower by an order of magnitude than those of GaAs in moving towards the electrolyte/sample interface, so the holes in GaAs may be too quick to be captured by this kind of defect site. A comparison of the capture cross-section for each material in the literature was not possible due to the conflicting values reached depending on the method used [20].

2.3. PL microscopy.

2.3.1. Introduction.

Photoluminescence (PL) is a common analysis technique in semiconductors and will be explored more fully in later chapters. Briefly, it involves illuminating the sample with above band gap radiation and then analysing the spectral output with a spectrometer, normally performed at cryogenic temperatures. However, with some materials room temperature luminescence is possible and a microscope would allow a study of any surface area variation in the intensity or the wavelength of the output. All that is required for studying II-VI semiconductors is a UV light source. It was found during the course of this study that the intensity of the luminescence from some samples was too low to be properly observed. In order to enhance the image, a frame grabber was connected to the CCD camera used on the microscope which was able to 'layer' images, *i.e.* to add frames on top of each other to increase the definition.

2.3.2. Experiment.

To perform PL using the microscope several modifications had to be made. The white light source was replaced (in fact it was possible to use a spare input port) with a mercury lamp to provide the UV excitation. The focusing optics had to be replaced with a diaphragm module that could transmit UV light. Finally, the filter cube had to be replaced with one that correctly filtered the input and output light from the

sample. The energy of the emission from the sample will be near the energy of the band gap or less, i.e. wavelengths of around 440nm or above. The output filter would also have to remove any of the excitation light reflected of the sample surface. This was achieved by the filter cube shown in figure 2-9.

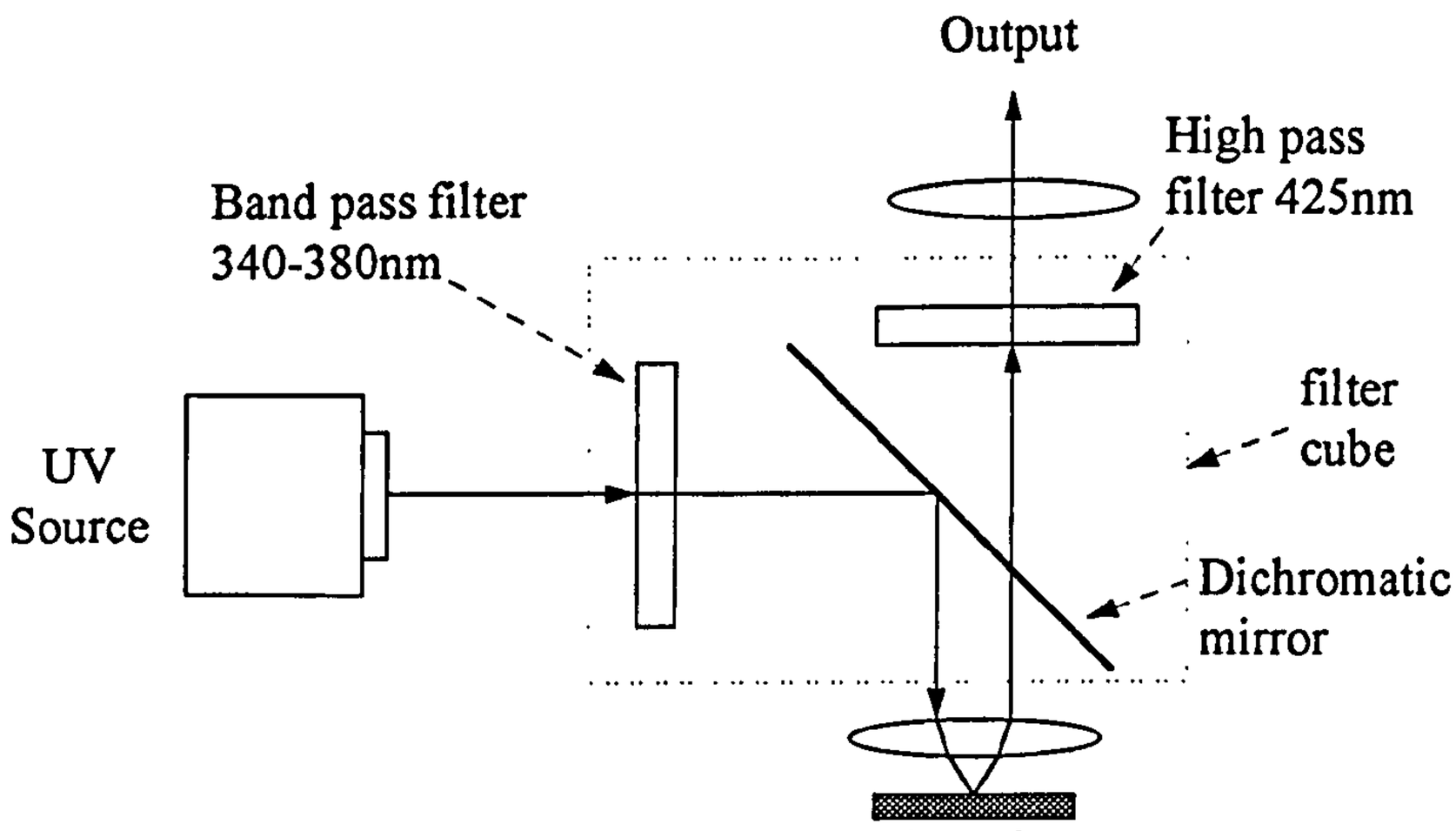

Figure 2-9. *Microscope filter cube for PL microscopy.*

The aim of this section is to test the possible suitability of this PL microscopy system for quick and easy analysis of II-VI semiconductor epilayers. Of course, without the ability to separate the light into a properly resolved spectrum, this method is always going to be limited in its applications. However, through the use of band-pass filters on the output, it should be possible to provide general information on the strength of near band gap energy emissions compared to defect and impurity related emissions at lower energies.

A variety of samples were available to test the system, all grown on GaAs substrates. Most were produced as calibration or test samples for the project to produce blue / green emitting laser diodes, and include undoped, n-type and p-type ZnSe and also several quantum well structures. However it was found that the only samples that produced significantly detectable luminescence at room temperature were n-type ZnSe, those doped by either iodine or chlorine, and some quantum well structures.

The luminescence from the n-type ZnSe is considered, although it was not possible to do a comparison with the structural quality of a range of samples, as described in section 2.2., because the PL of n-type ZnSe gives little indication of the structural quality. For example, a room temperature (RT) photoluminescence spectrum of an n-type ZnSe sample, which had a doping level of $n_d - n_a = 2\times10^{18}$ is shown in figure 2-10 and as a comparison the true colour photoluminescence microscope image from the surface is shown on figure 2-11.

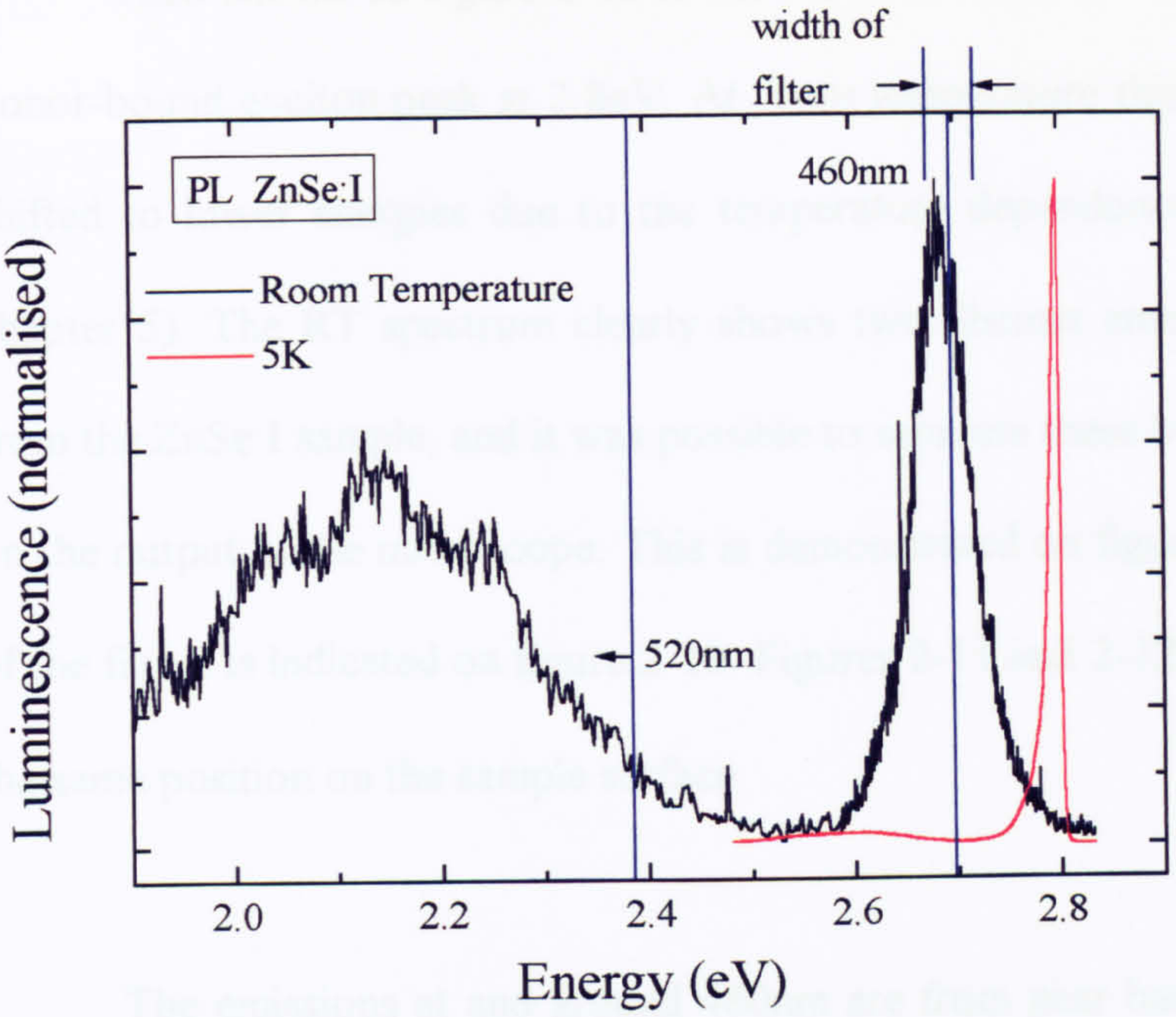

Figure 2-10. *5K and room temperature PL spectrum of n-type ZnSe:I, also showing the position of the output filters used.*

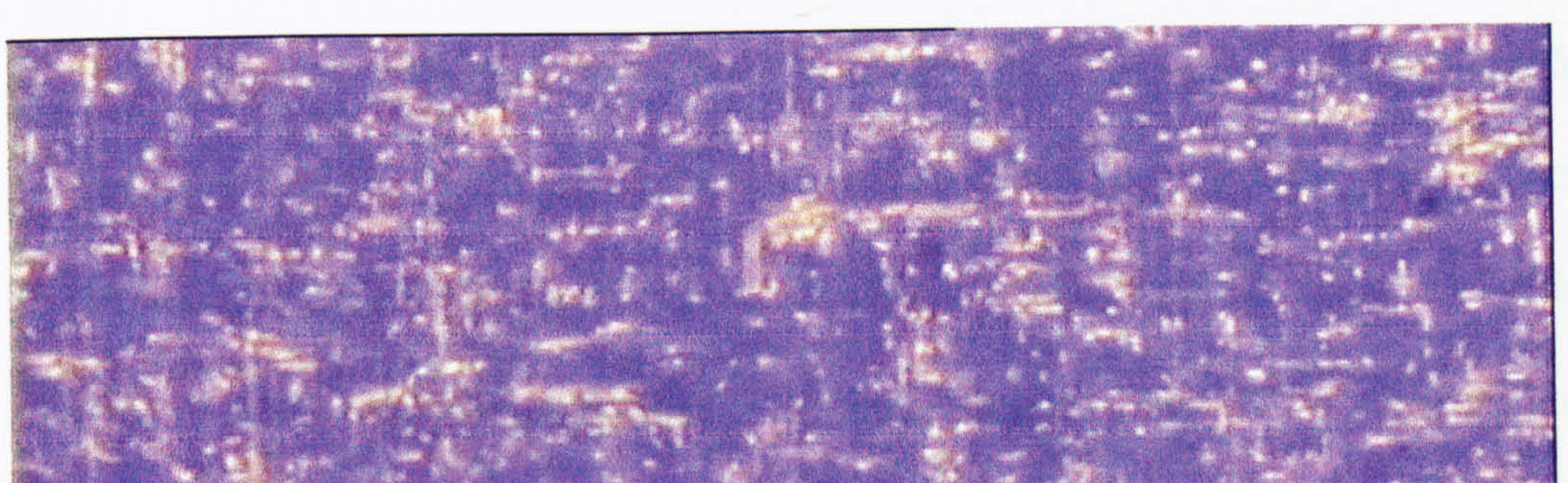

Figure 2-11. *PL microscopy image of ZnSe:I.*

Also shown on figure 2-10 is the PL scan taken at 5K which shows a strong donor-bound exciton peak at 2.8eV. At room temperature this peak is broadened and shifted to lower energies due to the temperature dependence of the band gap (see chapter 5). The RT spectrum clearly shows two distinct emission regions in the PL from the ZnSe:I sample, and it was possible to separate these by using band-pass filters on the output of the microscope. This is demonstrated on figure 2-12 and the position of the filters is indicated on figure 2-10. Figures 2-11 and 2-12 are PL images taken at the same position on the sample surface.

The emissions at and around 460nm are from near band-gap emissions, while those at wavelengths of 520nm or more are from defect-related deep emissions. It was noted that the two images in figure 2-12 had slightly different focus positions, with a difference of approximately 1μm, which is the thickness of the epilayer. After further investigations it was discovered that the defect-related emission was coming from the interface with the GaAs substrate while the near band gap emission was coming from the sample surface. At wavelengths of 520nm or above the absorption coefficient of ZnSe is practically zero, therefore if this light was generated at the substrate interface, then it would easily pass through the epilayer. For light with a wavelength of 460nm, however, ZnSe has a large absorption coefficient of approximately $10^5 cm^{-1}$ [21], therefore this explains why only light emitted from the surface is detectable.

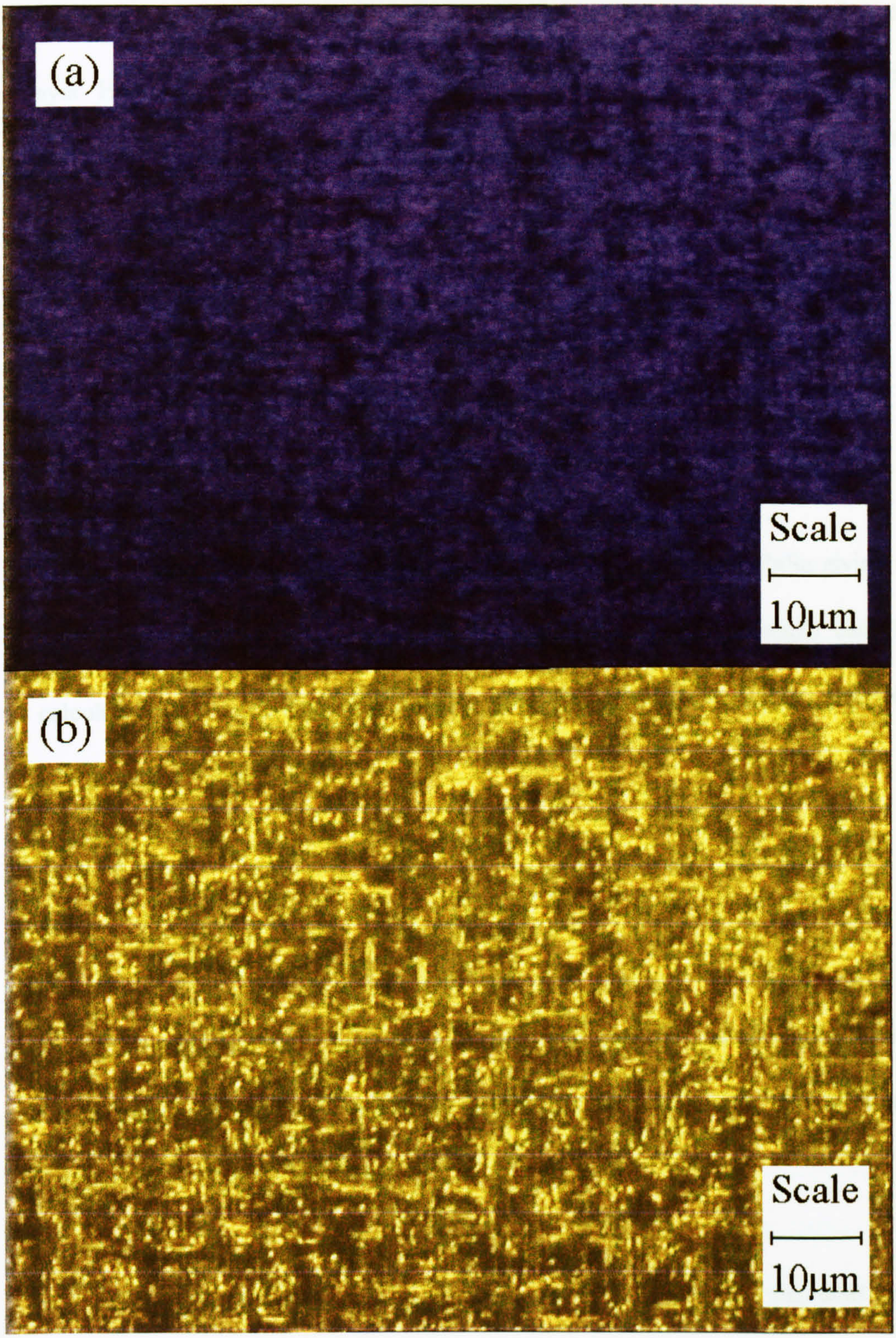

Figure 2-12. *PL microscope images of ZnSe:I with optical filters on the output* : (a) *Band-pass filter centred at 460nm, with a width of 6-8nm.* (b) *High-pass filter with a cut-off at 520nm.*

The excitation wavelengths (340nm - 380nm) have high absorption in the ZnSe layer. However, we can calculate the diffusion length L_h of any minority carriers (*i.e.* holes) generated to see if they would be able to reach the GaAs interface and produce the luminescence. The diffusion coefficient (or constant) D_h can be calculated from the Einstein relation [22] :

$$D_h = \frac{kT}{e}\mu_h \tag{2-4}$$

μ_h is the hole mobility which is about $30 cm^2 V^{-1} s^{-1}$ [18] for ZnSe giving a value of $7.8 \times 10^{-5} m^2 s^{-1}$ for D_h at room temperature. The diffusion length can then be calculated by considering the hole lifetime τ_h, which for ZnSe is approximately 50ns [23], in equation (2-5) [22] :

$$L_h = \left(D_h \tau_h\right)^{1/2} \tag{2-5}$$

This gives a value for L_h of 2μm for ZnSe, twice the thickness of the epilayer. Therefore minority carriers can easily diffuse down to the GaAs interface to generate luminescence around the defects.

Figure 2-12 also shows that there are dark patches in the near band gap emission image (a) that correspond to bright spots from the defect-related emissions (b). This is due to the competitive nature of luminescence, *i.e.* carriers that are trapped by the defects are no longer available for near band gap radiation, which creates the

'dead' areas seen in figure 2-12(a) that clearly extend from the substrate interface up to the epilayer surface. A schematic to explain the images on figure 2-12 is shown in figure 2-13.

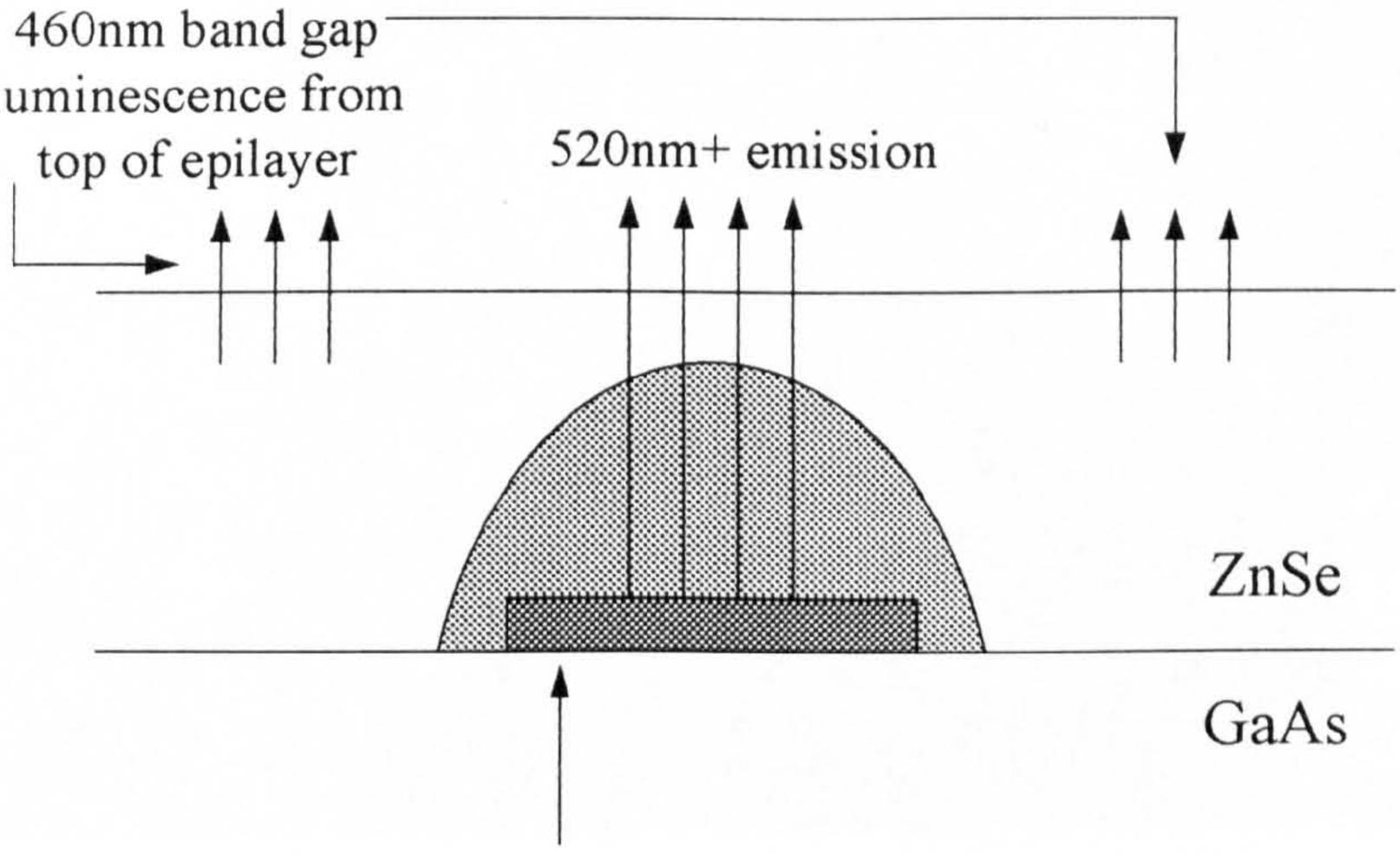

Figure 2-13. *The effect of interface defects on the luminescence from a ZnSe:I sample.*

It was mentioned in the section on defect revealing etches that a variety of samples were studied by that process, which included the n-type ZnSe:I sample examined in this section. Figure 2-14 shows the standard etch for this sample. There is a clear similarity between the cross-hatched features revealed by the etching process and those in the PL microscopy. In contrast to the undoped samples which only had ridges in the $[1\,\bar{1}\,0]$ direction, *n*-type ZnSe clearly has features in both [110] and $[1\,\bar{1}\,0]$ directions, the reason for which is unknown at this time.

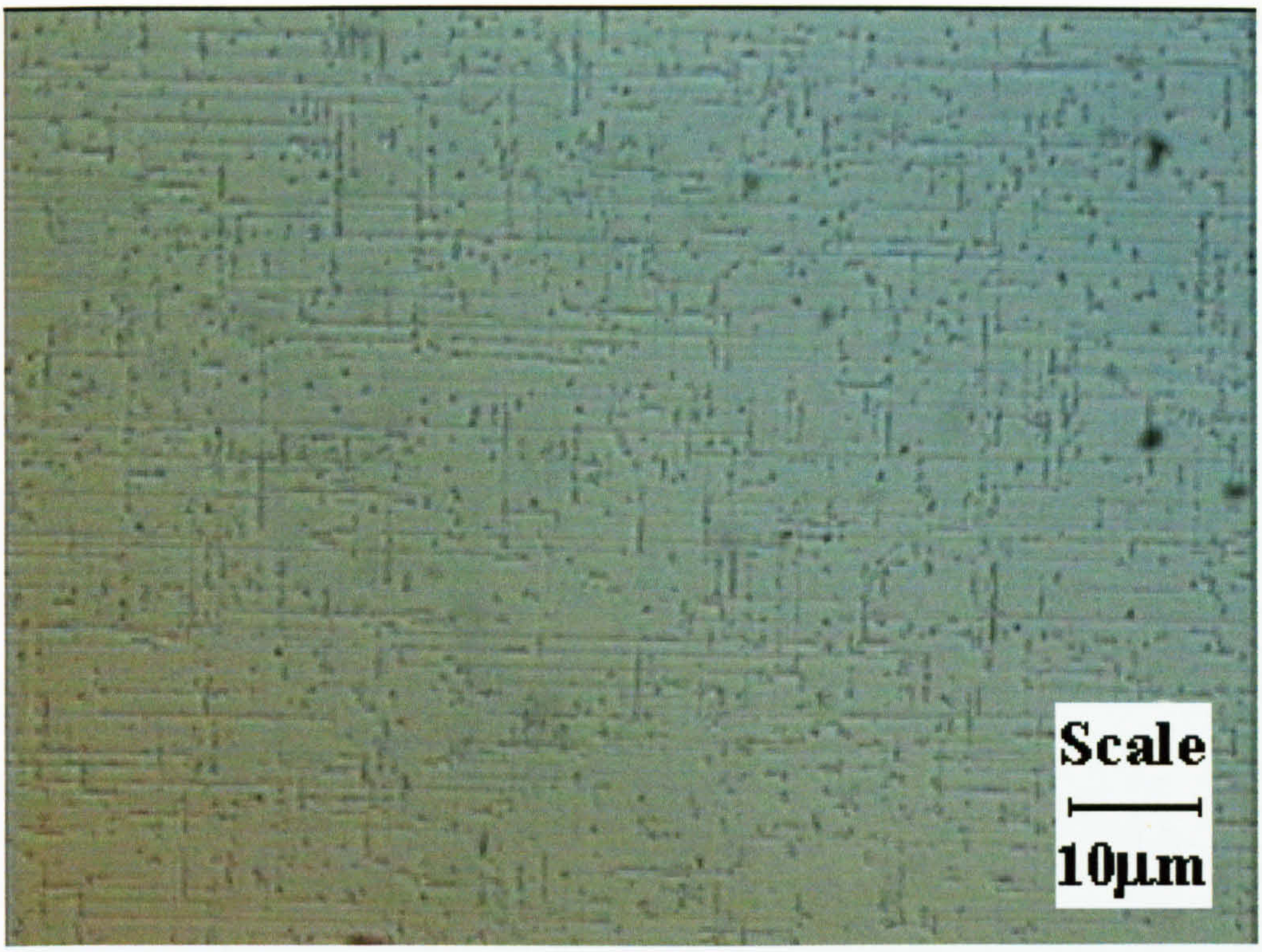

Figure 2-14. *Nomarski image of a standard etch on ZnSe:I.*

Figure 2-15 (a) shows the PL microscopy image at a lower magnification of the edge of the etch ring, while figure 2-15 (b) shows a Normarski image of the same position. Close inspection of these two figures reveals that most of the areas producing the defect related emissions with wavelengths > 520nm on figure 2-15 (a) give a one to one correspondence with the physically revealed defect sites in the Nomarski image on figure 2-15 (b). This offers proof that the features revealed by the etch are not a chemical artefact and are directly related to the deep level luminescence emissions. The defect luminescence on figure 2-15 (a) is brighter on the etched side, as would be expected when the epilayer above the defects has been removed.

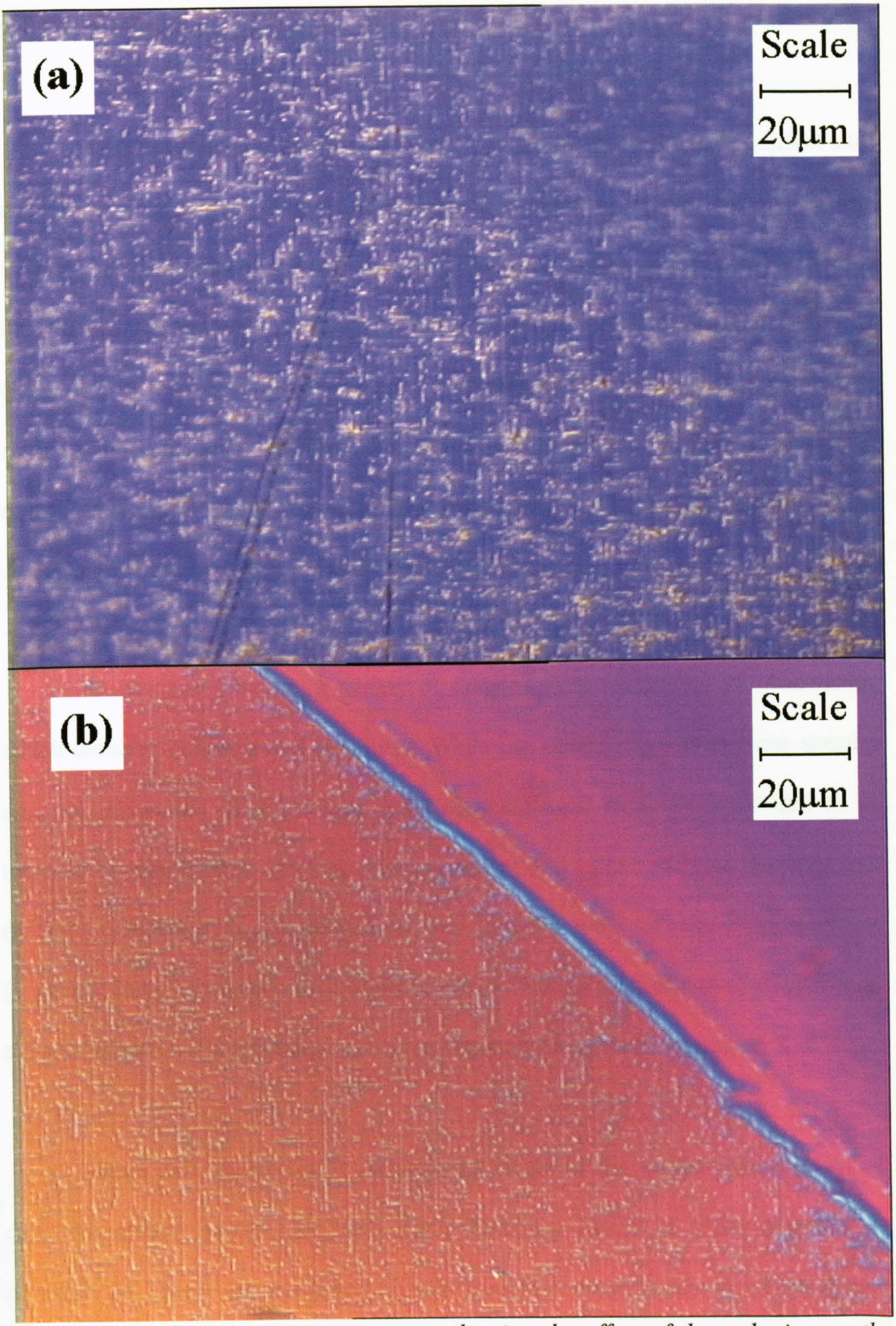

Figure 2-15. (a) *PL microscope image showing the effect of the etch ring on the right-hand side of the figure.* (b) *Normarski image of the same position.*

2.3.3 Defect annealing.

It has recently been shown that intense optical excitation can anneal defect sites and produce an increase in photoluminescence intensity by Jordan *et al.* [24] who studied a single quantum well structure modelled on a II-VI laser diode and attributed this to recombination-enhanced defect annealing which has been observed before in GaAs [25]. A theory proposed by Weeks *et al.* [26] suggests that when an electron or a hole is non-radiatively captured at a defect site then large amounts of vibrational energy is released which can promote defect motion and reaction, leading to the defects either multiplying or reducing (annealing).

As mentioned before, a variety of samples were studied by PL microscopy which included quantum well structures. While the luminescence from these samples was not particularly bright, it was noted that prolonged exposure could lead to an increase in the intensity. This occurred in one ZnCdSe / ZnSe multiple quantum well (MQW) structure, which consisted of four ZnCdSe wells of increasing thickness (1.2nm, 2.2nm, 5.6nm and 10.4nm) separated by ZnSe barriers of 60nm, all grown on a GaAs substrate. The estimated cadmium percentage in the well layers was 27.5%.

Figure 2-16 shows the PL microscopy image of the MQW sample revealing dark line defects in the [001] and [010] directions similar to those observed in reference 24. This image was taken with the maximum magnification lens (×100), and the power density in this case has been estimated at 4000Wcm^{-2}. Due to the low brightness level, this image was layered 100 times by the multi-image capture option in

the frame grabber software. The power density was maintained for ten minutes, after which the objective lens was replaced with one that had a fifth of the magnification (×20), and a new picture was taken, as shown on figure 2-17.

Figure 2-17 clearly shows the extent of the annealing process over the area of illumination generated by the high magnification (×100) lens (measured as $8.6\times10^{-4}cm^{-2}$). However, the same area on the sample was monitored periodically over the next month and figure 2-18 shows the same area taken thirty-two days after the original illumination clearly indicating a loss of intensity of approximately one order of magnitude.

This drop in intensity indicates that the defects that were annealed have returned in part, an aspect not considered in reference 24. The only mechanism previously observed that is similar to this phenomenon is 'persistent photoconductivity' by Gunshor *et al.* [27] in the ZnSe-based laser diode structure. In this process holes are excited by illumination of sufficient energy from deep to shallow states and are prevented from returning instantly by a capture barrier, and are observed by the persistent photoconductivity mentioned earlier. This process is optically induced and electrically observed, and while the process observed here is optically induced and optically observed, it is suggested that a similar mechanism is taking place, as the sample was held for the thirty-two days at room temperature which could allow thermally active carriers to return slowly to their previous states. Future work on this subject should consider the influence of a longer annealing time and also the loss of intensity over a greater time period.

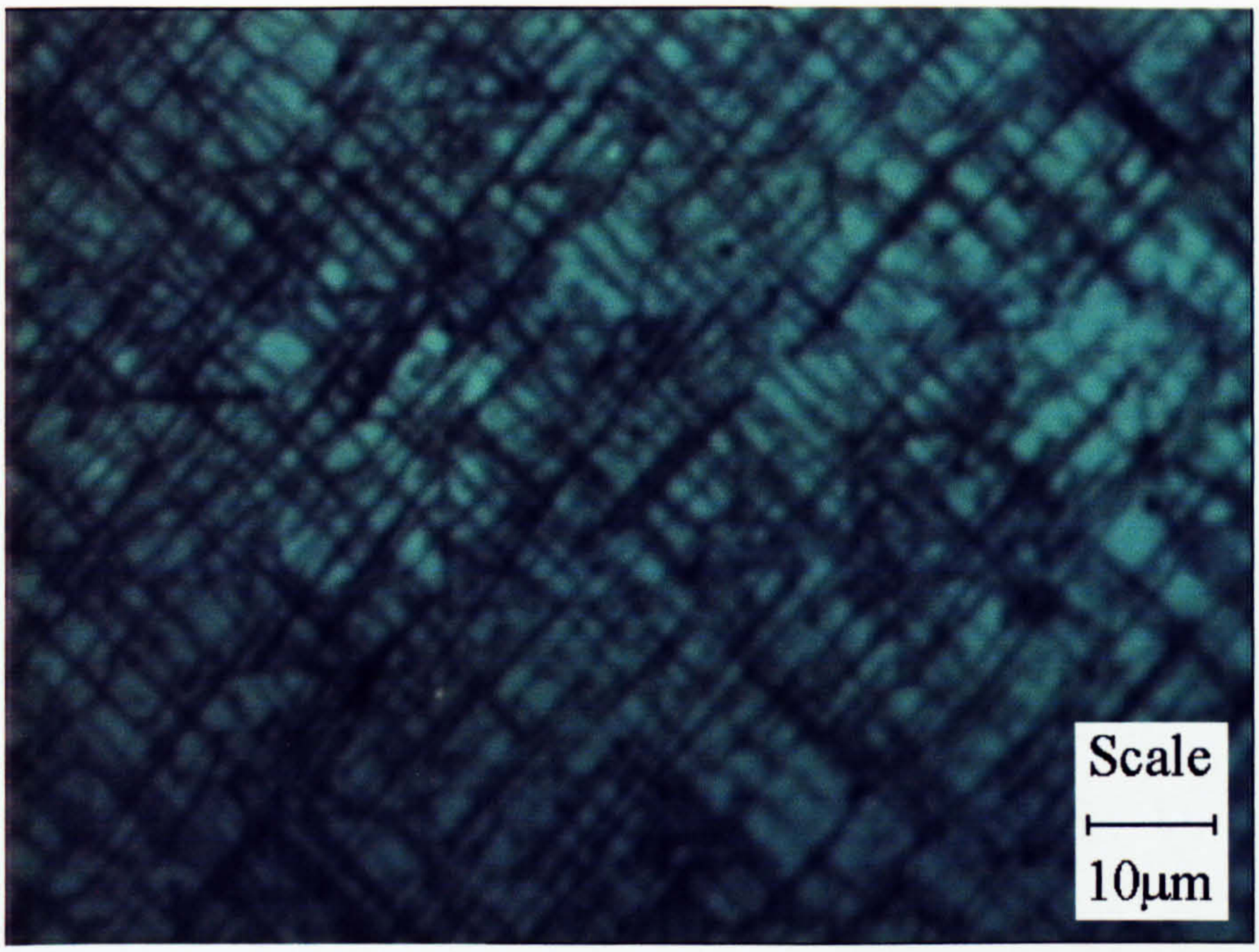

Figure 2-16. *PL microscope image of a ZnCdSe / ZnSe multiple quantum well sample, layered 100 times.*

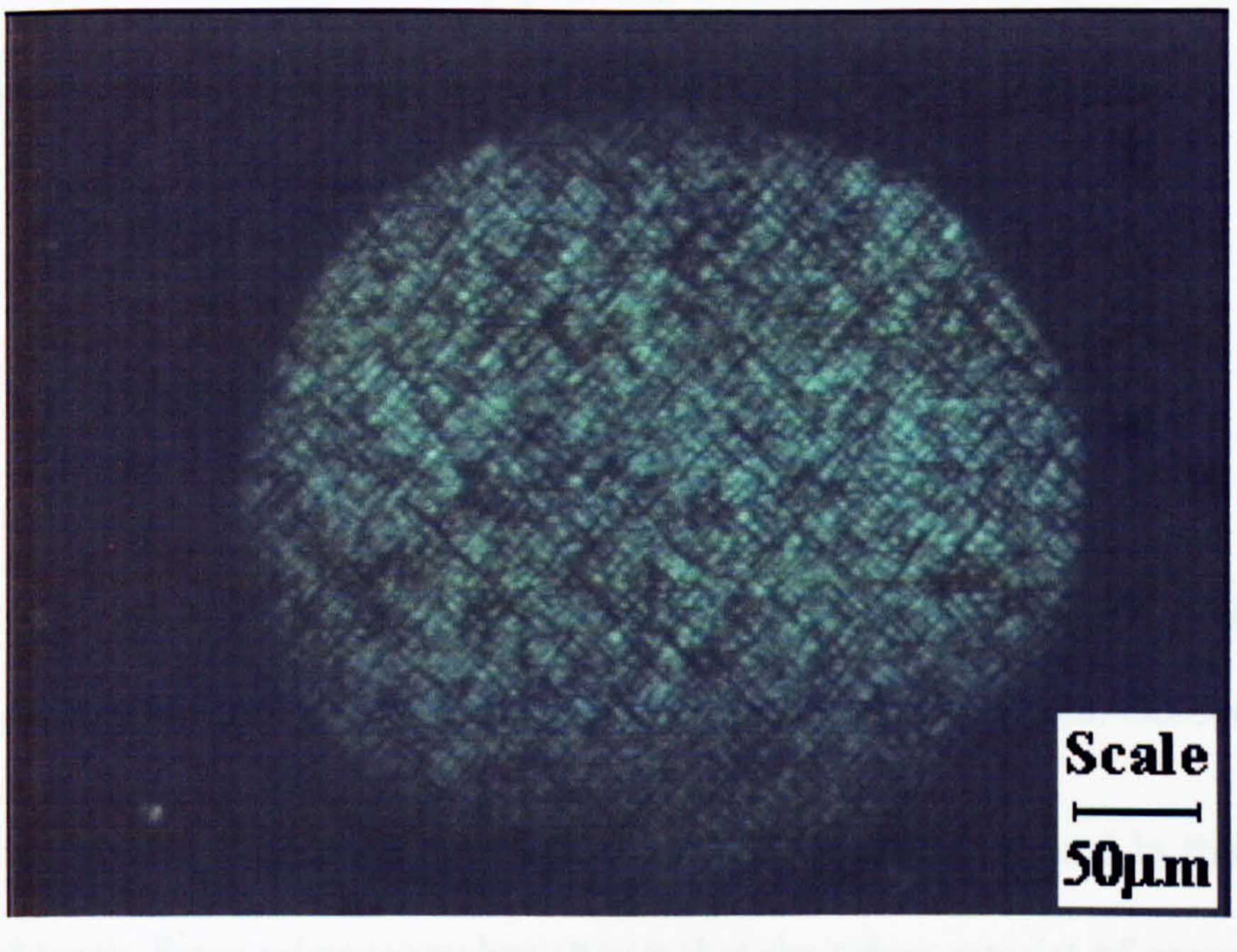

Figure 2-17. *PL microscope image of a ZnCdSe / ZnSe multiple quantum well sample taken at a fifth of the magnification of figure* 2-16 *showing the extent of the defect annealing, layered 100 times.*

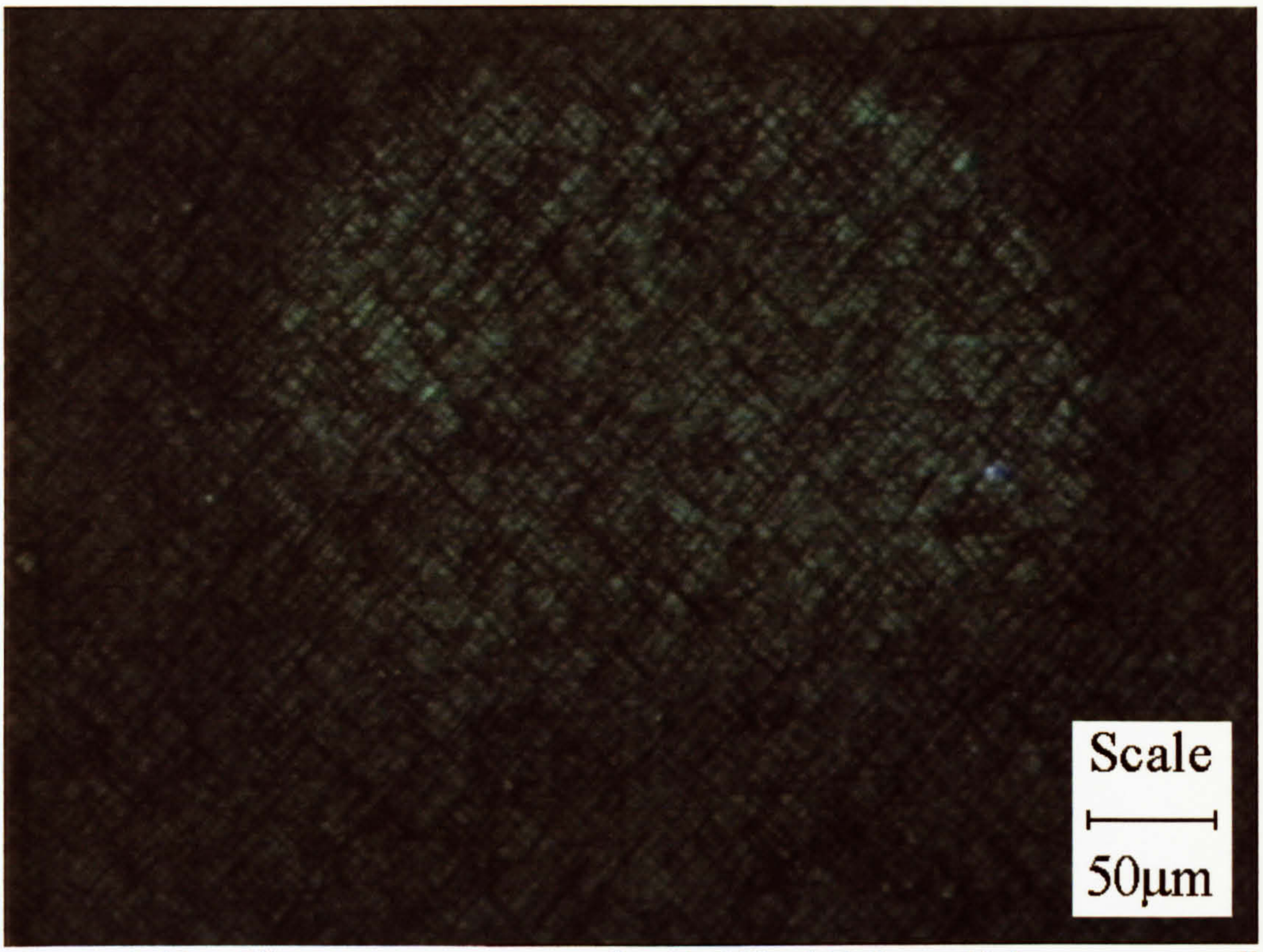

Figure 2-18. *PL microscope image of a ZnCdSe / ZnSe multiple quantum well sample taken thirty-two days after figure* 2-17*, layered 100 times.*

2.4. Conclusion.

Two methods of photoelectrolytic etching have been developed to investigate defects in MBE grown ZnSe epitaxial layers grown on GaAs. Observation of revealed features by Nomarski microscopy has shown ridges aligned in the $[1\bar{1}0]$ direction. Atomic force microscopy has shown that the ridges consist of groups of one or more conical protrusions. Nomarski microscopy also showed a background aspect of rough disordered features. The abundance and nature of both types of feature were shown to

be related to the photoluminescence spectrum of each sample. PL microscopy has been demonstrated on ZnSe:I and ZnCdSe / ZnSe quantum well samples, and has been shown to optically display the same defects revealed by the etching process. Defect annealing has been observed by intense UV illumination in a multiple quantum well sample.

2.5. References.

[1] S. Tomiya, E. Morita, M. Ukita, H. Okuyama, S. Itoh, K. Nakano and A. Ishibashi, Appl. Phys. Lett. **66**, 1208 (1995).

[2] E. D. Bourret-Courchesne, Appl. Phys. Lett. **68**, 1675 (1996).

[3] S. Kalisetty, M. Gokhale, K. Bao, J.E. Ayers and F.C. Jain, Appl. Phys. Lett. **68**, 1693 (1996).

[4] P.D. Brown, Y.Y. Loginov, J.T. Mullins, K. Durose, A.W. Brinkman and C.J. Humphreys, J. Cryst. Growth **138**, 538 (1994).

[5] G.M. Williams, A.G. Cullis, K. Prior, J. Simpson, B.C. Cavenett and S.J.A. Adams, Inst. Phys. Conf. Ser. **134**, 671 (1993).

[6] *personal communication*, M. Halliwell to K.A. Prior, 1998.

[7] T. Ambridge and M.M. Faktor, J. Appl. Electrochem. **5**, 319 (1974).

[8] S.Y. Wang, F. Haran, J. Simpson, H. Stewart, J.M. Wallace, K.A. Prior and B.C. Cavenett, Appl. Phys. Lett. **60**, 344 (1992).

[9] S.Y. Wang, J. Simpson, K.A. Prior and B.C. Cavenett, J. Appl. Phys. **72**, 5311 (1992).

[10] S.Y. Wang, Thesis of Heriot-Watt University, Edinburgh, 1994.

[11] A. Kamata and H. Mitsuhashi, J. Cryst. Growth **142**, 31 (1994).

[12] M.M. Faktor and J.L. Stevenson, J. Electrochem. Soc. : Solid-State Science and Technology **125**, 621 (1978).

[13] C.R. Elliott and J.C. Regnault, J. Electrochem. Soc. : Solid-State Science and Technology **128**, 113 (1981).

[14] T. McHardy and F. Ludwig, *Electrochemistry of Semiconductors and Electronics : Processes and Devices*, Noyes Publications (1992).

[15] Y.G. Shreter, Y.T. Rebane, O.V. Klyavin, P.S. Aplin, C.J. Axon, W.T. Young and J.W.Steeds, J. Cryst. Growth **159**, 883 (1996).

[16] P. Thompson, Thesis of Heriot-Watt University, Edinburgh, 1996.

[17] G. Horsburgh, K.A. Prior, W. Meredith, I. Galbraith, B.C. Cavenett, C.R. Whitehouse, G. Lacey, A.G. Cullis, P.J. Parbrook, P. Möck and K. Mizuno, Appl. Phys. Lett. **72**, 3148 (1998).

[18] J.H. Haanstra and J. Dieleman, Ext. Abstr. Electrochem. Soc. **14**, 2 (1965).

[19] C. Kittel, *Introduction to Solid State Physics*, (7th edition), Wiley (1996).

[20] K. Hellig, G. Prosch, M. Behringer, M. Fehrer, R. Beyer, H. Burghardt, D. Hommel and D.R.T. Zahn, Appl. Phys. Lett. **71**, 2187 (1997).

[21] P.K. Lim and D.E. Brodie, Can. J. Phys. **55**, 1641 (1977).

[22] J.R. Hook and H.E. Hall, *Solid State Physics*, (2nd edition), Wiley (1991).

[23] J.S. Massa, G.S. Buller, A.C. Walker, J. Simpson, K.A. Prior and B.C. Cavenett, Appl. Phys. Lett. **67**, 61 (1995).

[24] C. Jordan, D.T. Fewer, J.F. Donegan, E.M. McCabe, A. Huynh, F.P. Logue, S. Taniguchi, T. Hino, K. Nakano and A. Ishibashi, Appl. Phys. Lett. **72**, 194 (1998).

[25] D.V. Lang and L.C. Kimerling, Phys. Rev. Lett. **33**, 489 (1974).

[26] J.D. Weeks, J.C. Tully and L.C. Kimerling, Phys. Rev. B **12**, 3286 (1975).

[27] R.L. Gunshor, J. Han, G.C. Hua, A.V. Nurmikko and H. Jeon, J. Cryst. Growth, **159**, 1 (1996).

3. THE PIEZOELECTRIC EFFECT IN QUANTUM WELLS : THEORY AND REVIEW

3.1. Quantum well theory.

Quantum wells are at the heart of modern semiconductor technology and form the key component in semiconductor lasers, modulators, SEEDs, etc. As such, they have been extensively studied. This section will briefly describe the energy states in a quantum well and any other aspects of quantum wells that are considered in other chapters. All the structures used in chapters 4, 5 and 6 are single quantum wells. Quantum wells are included in the family of low dimensional systems which have one or more dimensions that is small enough so that the electron and hole wavefunctions are confined. In the case of the quantum well there is an important effect on the density of states in the well layer.

The density of states for bulk semiconductors is well documented and is given by [1] :

$$N_{bulk}(E) = \frac{4\pi}{h^3}(2m_e^*)^{3/2}(E - E_c)^{1/2} \qquad (3\text{-}1)$$

for electrons in the conduction band and

$$N_{bulk}(E) = \frac{4\pi}{h^3}(2m_h^*)^{3/2}(E_v - E)^{1/2} \qquad (3\text{-}2)$$

for holes in the valence band. m^* is the respective effective mass, E_v is the top of the valence band and E_c is the bottom of the conduction band.

3.1.1. Square well model.

In quantum wells, however, the electrons and holes are restricted to two dimensional motion which gives the following expression [2] :

$$N_{QW}(E) = \sum_{n-1}^{\infty} \frac{4\pi}{h^2} m_e^* H(E - E_{nc}) \qquad (3\text{-}3)$$

for electrons and a similar expression for holes. H is the Heaviside function such that $H(x) = 1$ when $x > 0$ and $H(x) = 0$ when $x < 0$. The density of states functions for electrons in the bulk and in a quantum well are shown graphically on figure 3-1.

This equation leads to the idea of a quantum well having discrete energy levels in the conduction and valence bands. It was explained in chapter 1 that electrons in semiconductors existed only in discretely allowed energy levels, but that they were so close together that they formed a quasi-continuum. The action of constraining the electrons to 2-D motion has the effect of stretching out these allowed energy states so

that they can be observed, *i.e.* if the dimensions of a quantum well were slowly increased so that 3-D motion was allowed, then the values E_{1c}, E_{2c} and E_{3c} on figure 3-1 would move closer together and the steps would become shorter until they formed the smooth quasi-continuum shown as N_{bulk}.

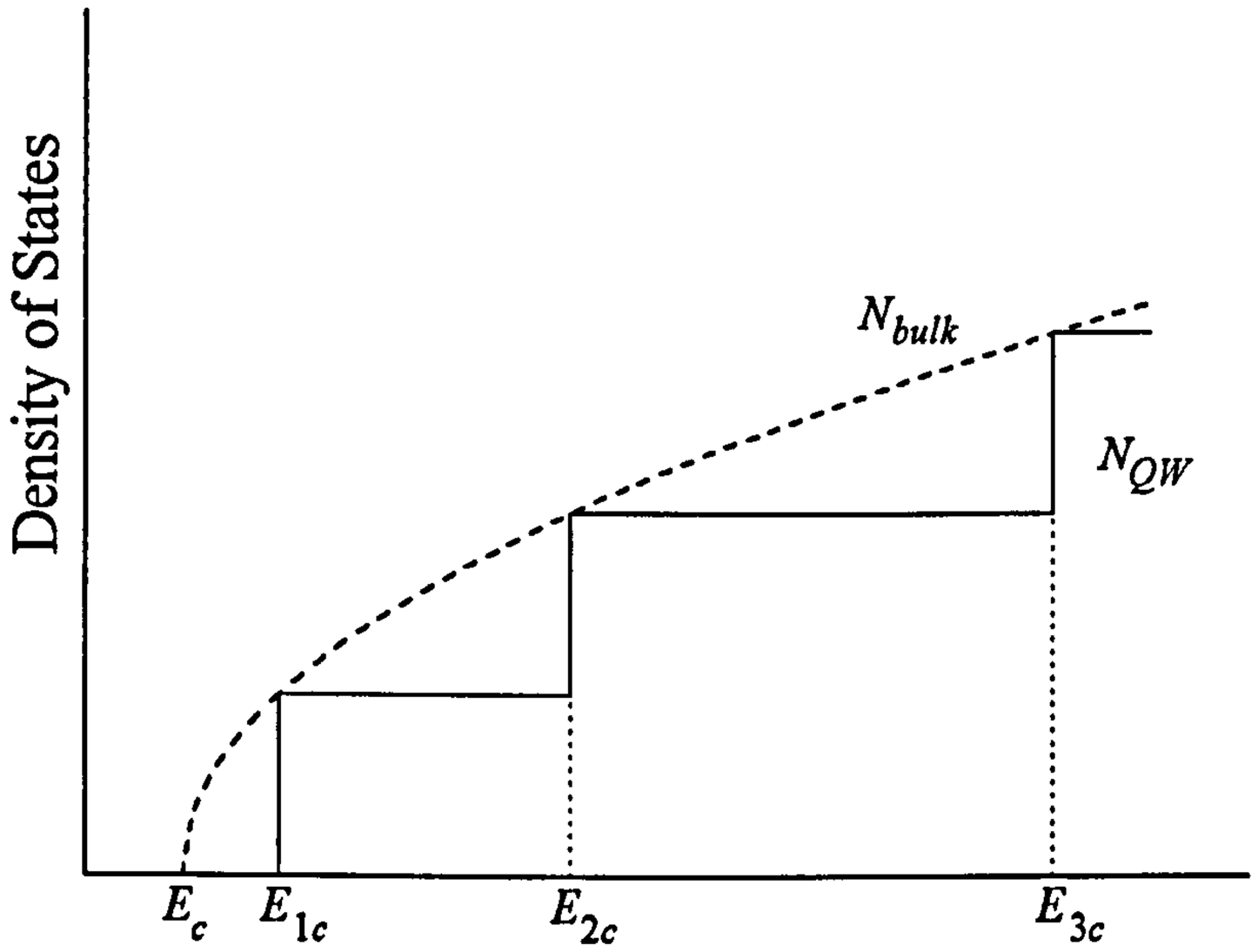

Figure 3-1. *The density of states as a function of energy for bulk semiconductors and for a quantum well.*

The absorption spectra of a quantum well should consist of a similar series of steps to the density of states, along with sharp excitonic peaks just before these steps. Excitons are created by the Coulombic interaction between an electron and a hole in close proximity which reduces their combined energy in the absorption process.

The model of a particle in an infinite 1-D potential well is an elementary and well documented quantum mechanical problem [7]. For a well of length L_z, a particle of mass m^* and infinite potential barriers, the wave equation is given by

$$-\frac{h^2}{8\pi^2 m^*}\frac{d^2\psi}{dz^2} = E\psi \tag{3-4}$$

The eigenvalues of the energy of the particle are given by

$$E_n = \left(\frac{h^2}{8m^* L_z{}^2}\right)n^2 \tag{3-5}$$

The wavefunctions of the particle are given by

$$\psi_n = A\cos\left(\frac{n\pi z}{L_z}\right) \tag{3-6}$$

for odd values of n and

$$\psi_n = A\sin\left(\frac{n\pi z}{L_z}\right) \tag{3-7}$$

for even values of n (n = 1,2,3...). The separation between energy levels given in equation 3-5 will be significant and detectable providing L_z is very small. A finite well has similar solutions, except that instead of vanishing at both ends of the well, the

wavefunctions will have an exponential decay into the well barriers. This only has a significant effect on wavefunctions near the top of the well. When the boundary conditions for an exponential decay on either side of the well are applied the resulting formula, given as equation 3-8, is unable to be solved analytically.

$$-\cot or \tan(\theta) = \frac{m_w^*}{m_b^*}\left[\frac{\theta_0^2}{\theta^2} - \frac{m_b^*}{m_w^*}\right]^{\frac{1}{2}} \tag{3-8}$$

where

$$\theta_0 = \left[\frac{m_b^* V_0 L_w^2}{2\hbar^2}\right]^{\frac{1}{2}} \tag{3-9}$$

and

$$\theta = \left[\frac{m_w^* E L_w^2}{2\hbar^2}\right]^{\frac{1}{2}} \tag{3-10}$$

m_w^* and m_b^* are the effective masses in the well and barrier layers, respectively, V_0 is the finite well height and E is the height of the respective energy level. Equation (3-8) can only be solved by graphing the LHS and RHS and observing where the curves intersect. As an example this has been performed for a 10nm $Zn_{0.85}Cd_{0.15}Se$ /

ZnSe quantum well, and the intersection for the electron and heavy hole solutions are shown on figure 3-2.

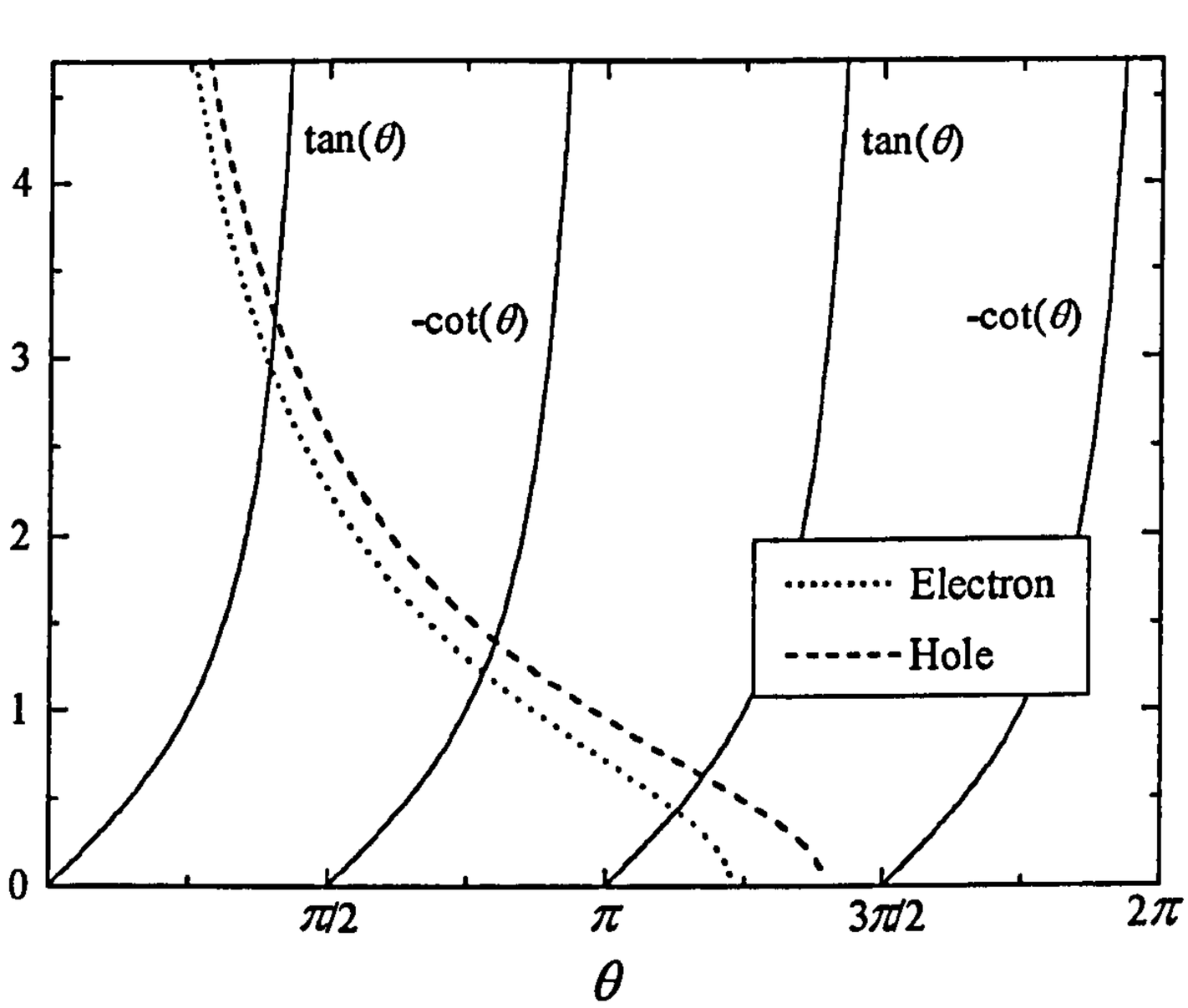

Figure 3-2. *Solutions to the finite well problem for a 10nm $Zn_{0.85}Cd_{0.15}Se$ / ZnSe quantum well, showing the LHS and RHS of equation* (3-8). *The parameters used for the electron are : $V_0 = 142meV$, $m_w^* = 0.16m_0$, $m_b^* = 0.16m_0$; and for the heavy hole : $V_0 = 47meV$, $m_w^* = 0.625m_0$, $m_b^* = 0.656m_0$. m_0 is the free electron mass.*

Figure 3-2 shows that for both the electron and heavy hole there are three possible solutions and therefore three confined energy states in the quantum well. From this it was possible to find the energy levels and to plot their respective wavefunctions, and this is shown for the electron in figure 3-3, while those for the heavy hole look very similar.

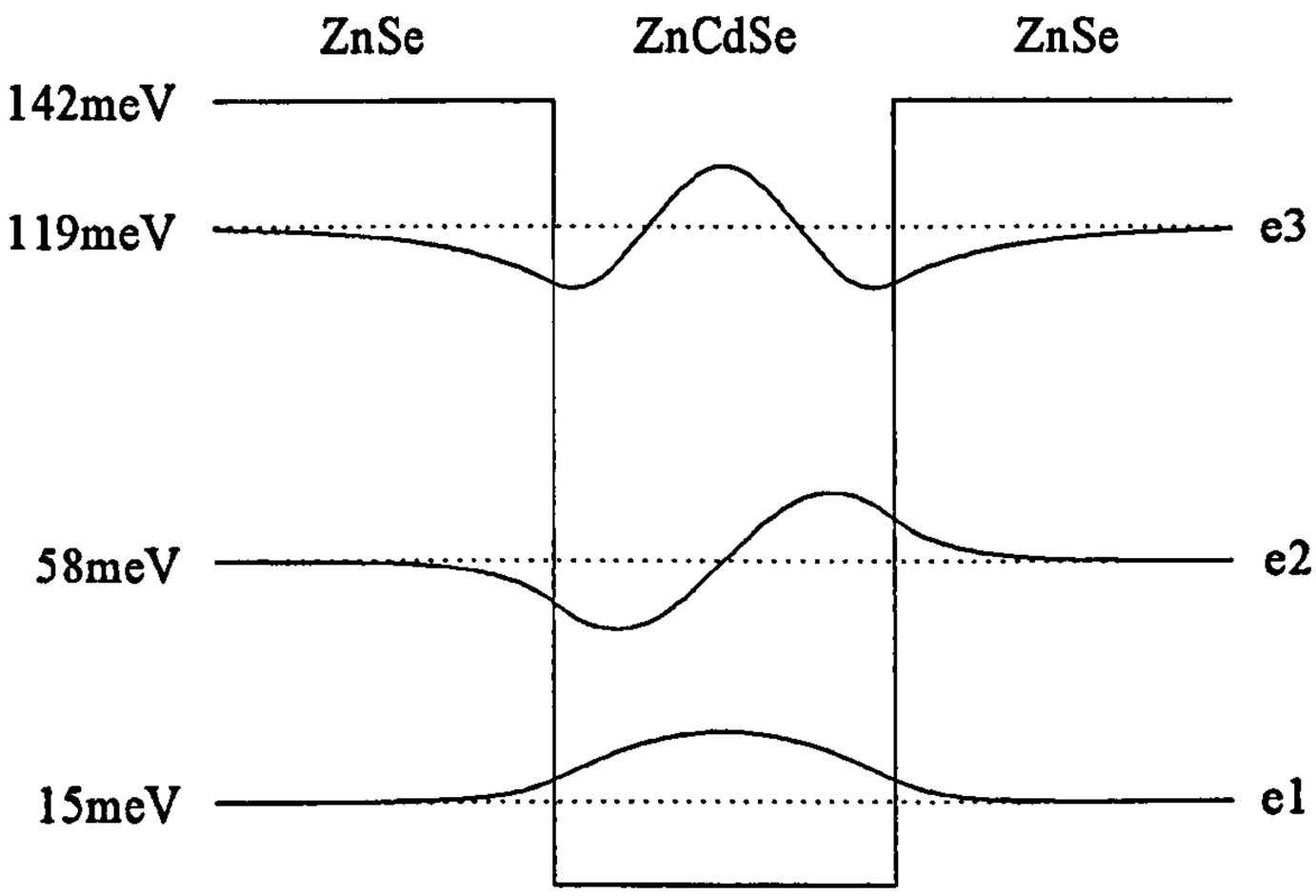

Figure 3-3. *Electron wavefunctions for a 10nm $Zn_{0.85}Cd_{0.15}Se$ / ZnSe quantum well.*

Each wavefunction was normalised such that

$$\int_{-\infty}^{\infty} \varphi^* \varphi \, dz = 1 \tag{3-11}$$

When a photon is absorbed an electron is excited into the conduction band leaving a hole in the valence band. The wavelength of the incident radiation will be very long compared to L_z, therefore transitions only occur between energy levels which have a similar spatial variation in their wavefunctions, leading to the selection rule $\Delta n = 0$ for absorption transitions [1].

3.1.2. Triangular well model.

The quantum wells studied in chapters 4, 5 and 6 all have an internal electric field across their width, the origin of which will be discussed later, which would result in a slope in the band edges inside the well. It is possible to adapt the standard square well model shown above and apply it to a triangular well. To begin with the simplest model will be considered, an infinite triangular well, see figure 3-4.

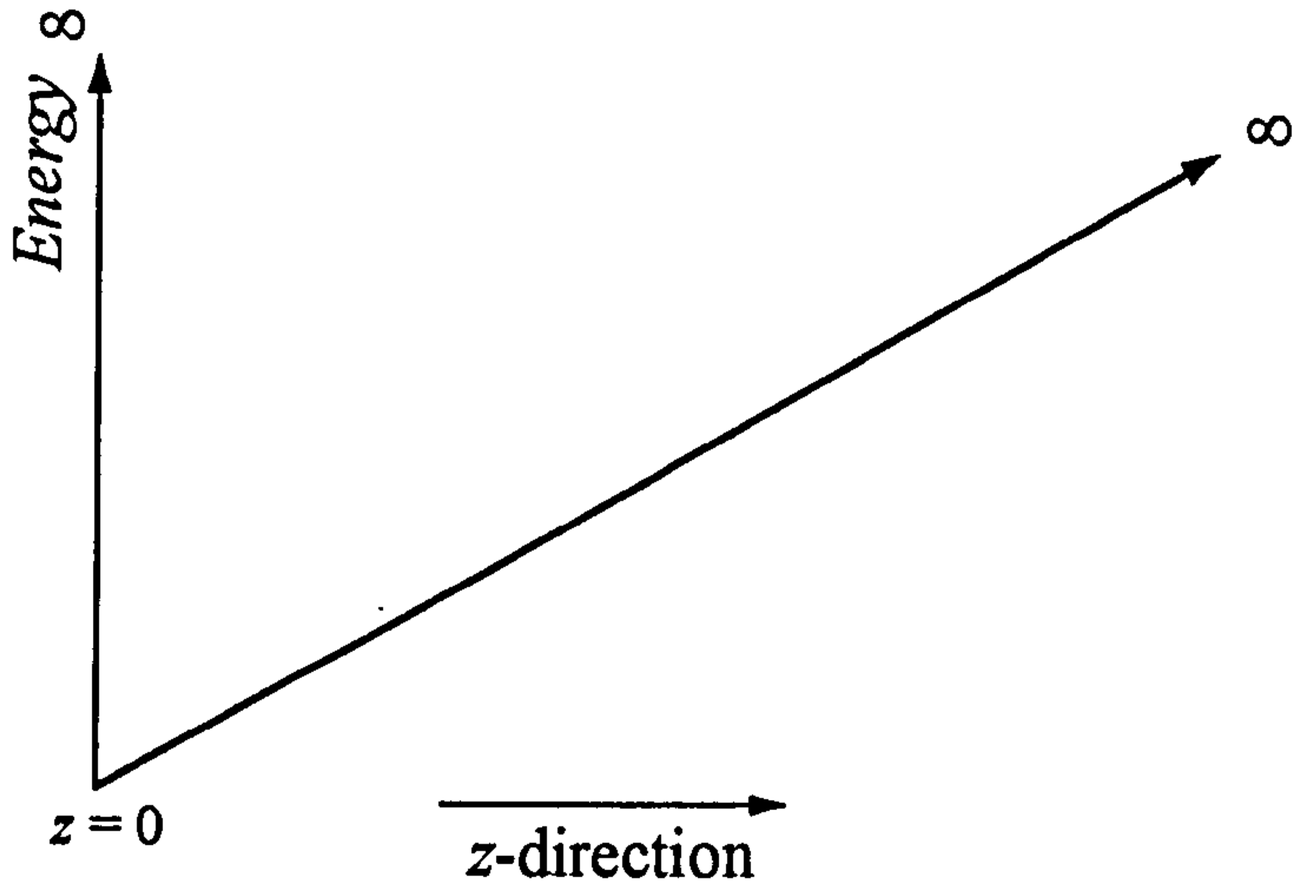

Figure 3-4. *An infinite triangular well.*

The Schrödinger equation for 1 dimension is :

$$\frac{-\hbar^2}{2m^*}\frac{d^2\varphi}{dz^2}+V(z)\varphi = E\varphi \qquad (3\text{-}12)$$

If the bottom of the triangular well is set at $V = 0$ and the slope in the z-direction has a gradient of eF where F is the internal field, then V can be expressed as $V = eFz$. This is substituted into the Schrödinger equation which is rearranged as shown :

$$\frac{\hbar^2}{2m^*}\frac{d^2\varphi}{dz^2} - (eFz - E)\varphi = 0 \qquad (3\text{-}13)$$

To simplify the equation x is substituted for (eFz - E) and to reduce the number of constants in the equation a is defined as :

$$a = \frac{2m^*}{(eF\hbar)^2} \qquad (3\text{-}14)$$

The Schrödinger equation is therefore reduced to :

$$\frac{1}{a}\frac{d^2\varphi}{dx^2} - x\varphi = 0 \qquad (3\text{-}15)$$

To simplify the equation further two more substitutions are made :

$$\phi = a^{2/3}\varphi \qquad (3\text{-}16)$$

and

$$y = a^{1/3}x \qquad (3\text{-}17)$$

which reduce the Schrödinger equation to :

$$\frac{d^2\phi}{dy^2} - y = 0 \tag{3-18}$$

The solution to this differential equation is well documented [3] and is expressed as follows :

$$\phi = C_1 Ai(y) + C_2 Bi(y) \tag{3-19}$$

C_1 and C_2 are constants. $Ai(y)$ and $Bi(y)$ are power series known as Airy functions and they are shown on figure 3-5.

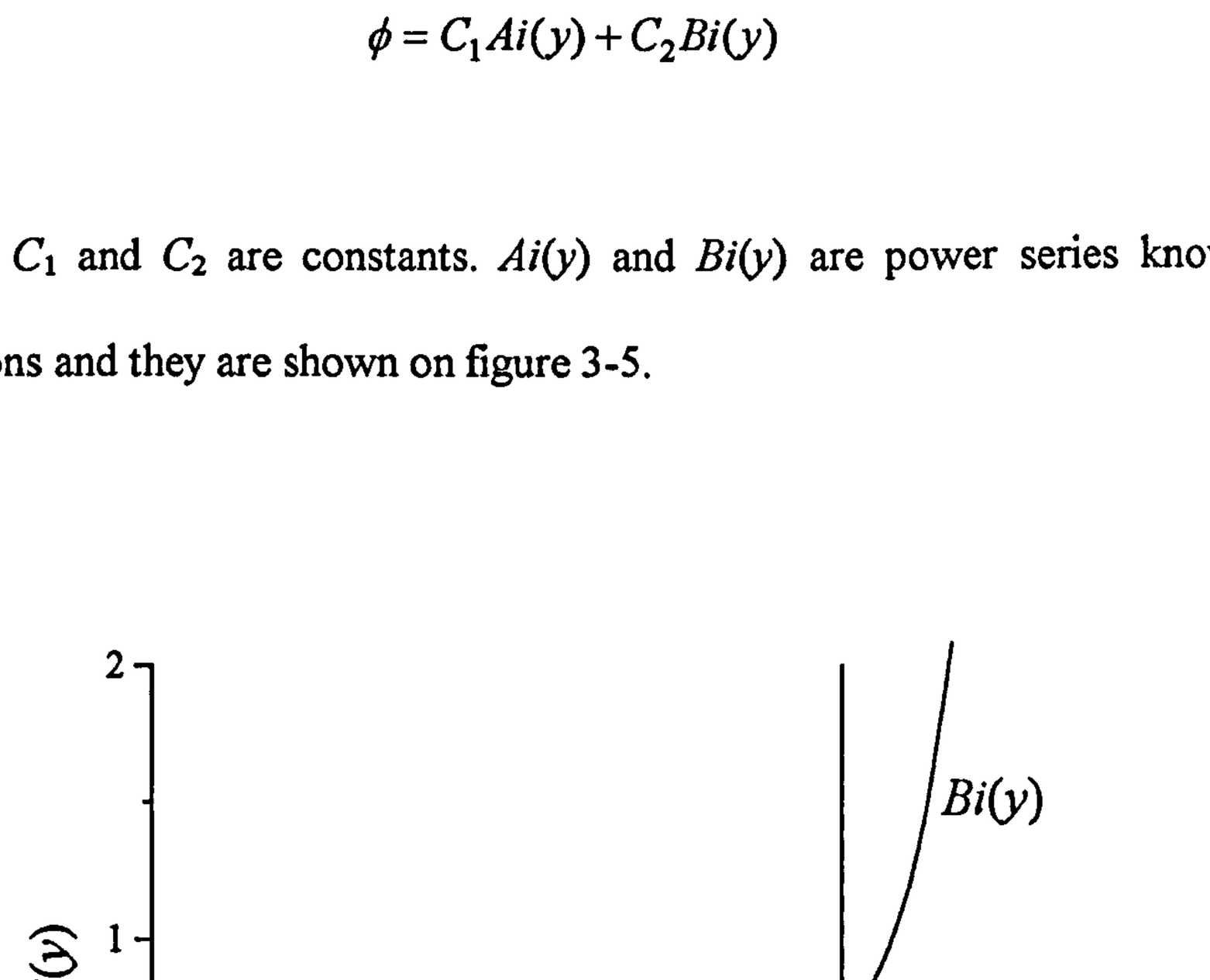

Figure 3-5. *Airy functions.*

It is now possible to re-substitute the formulae for y, φ and x to obtain :

$$\varphi = a^{-2/3}\left[C_1 Ai[a^{1/3}(eFz - E)] + C_2 Bi[a^{1/3}(eFz - E)]\right] \tag{3-20}$$

However, as can be seen from figure 3-5, $Bi(y) \rightarrow \infty$ as $y \rightarrow \infty$ so C_2 is set to zero and therefore the general solution for an infinite triangular well is

$$\varphi = a^{-2/3} C_1 Ai[a^{1/3}(eFz - E)] \tag{3-21}$$

For an infinite well, $\varphi(0) = 0$ (see figure 3-4). Furthermore it is known that $Ai(-2.34) = 0$ (from figure 3-5). Therefore this equation can be easily solved for E by setting $z = 0$ which gives

$$E = 2.34\, a^{-1/3} \tag{3-22}$$

The formula for a can now be re-substituted, giving the final solution for the first energy level in an infinite triangular well :

$$E_1 = 2.34\left[\frac{\hbar^2 e^2}{2}\right]^{1/3} \frac{F^{2/3}}{(m^*)^{1/3}} \tag{3-23}$$

Other energy levels can be found by using the other values where $Ai(y) = 0$. $Ai(y)$ reaches its maximum at $y = -1$, so we can use this and equation (3-21) to find the value of z where the wavefunction has its peak :

$$a^{1/3}\left(eFz_{\max} - E\right) = -1 \tag{3-24}$$

After substituting the value of E from equation (3-23), this gives

$$z_{\max} = 1.34\left[\frac{\hbar^2}{2m^* eF}\right]^{1/3} \tag{3-25}$$

Equations (3-23) and (3-25) are solutions to an infinite triangular well. It is also possible to solve for a triangular well that has a finite offset at $z = 0$ as shown in figure 3-6.

φ_b and φ_w are the wavefunctions in the barrier and well materials respectively. φ_w is equation (3-21) as before, while φ_b is as derived in the standard square well solution :

$$\varphi_b = C_3 \exp\left[z\left(\frac{(V-E)2m_b^*}{\hbar^2}\right)^{1/2}\right] \tag{3-26}$$

It is possible to solve for E by considering the boundary conditions at $z = 0$. These are as follows :

$$\varphi_w = \varphi_b \tag{3-27}$$

and

$$\frac{1}{m_w^*}\frac{d\varphi_w}{dz} = \frac{1}{m_b^*}\frac{d\varphi_b}{dz} \tag{3-28}$$

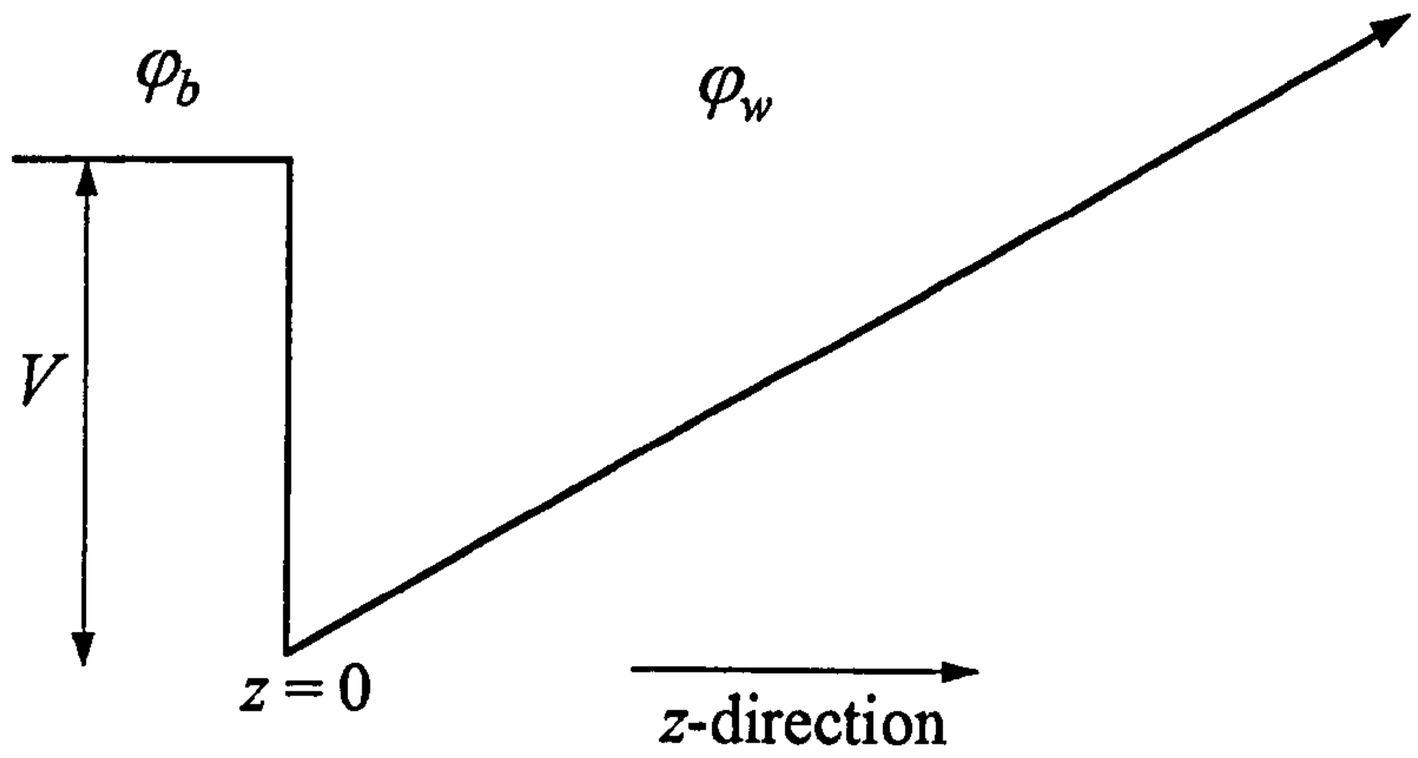

Figure 3-6. *A triangular well with a finite offset on one side and an infinite width.*

Equation (3-28) enables the effective mass theory to work across a boundary change in the crystal [4]. Equations (3-27) and (3-28) are then combined to remove the constants C_1 and C_3 to give

$$\frac{m_w^*}{m_b^*}\sqrt{\frac{(V-E)2m_b^*}{\hbar^2}} = \frac{eFa^{1/3}Ai'(-a^{1/3}E)}{Ai(-a^{1/3}E)} \tag{3-29}$$

which cannot be solved analytically but a value for E can be found numerically. Once this is achieved the wavefunctions can be plotted using equations (3-21) and

(3-26). Figure 3-7 shows an example of such a calculation. Again, each wavefunction was normalised such that

$$\int_{-\infty}^{\infty} \varphi^* \varphi \, dz = 1 \tag{3-30}$$

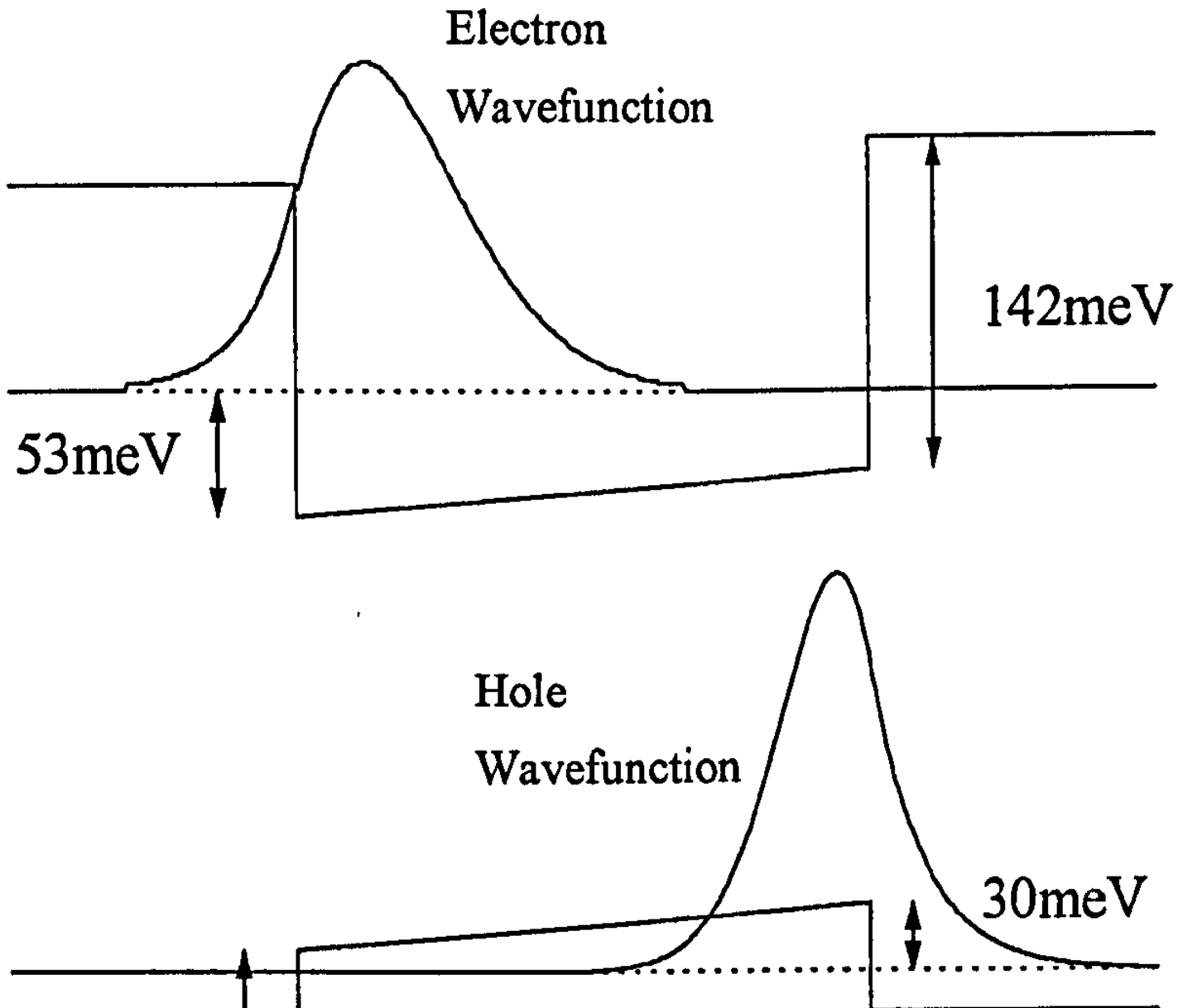

Figure 3-7. *Calculated electron and hole wavefunctions for a 20nm ZnCdSe / ZnSe single quantum well with 15% cadmium.*

The values of 30meV for the hole energy and 53meV for the electron energy were calculated using equation (3-24) and the known values for the band offsets as shown, and a nominal field value of 10^6V/m. The obvious limitation of this model is

that it does not consider the finite band offset at the other end of the well. However, the model is considered to be valid as long as the electron or hole wavefunction is reduced to a negligible amount at the opposing end of the well, as is the case in figure 3-7. Therefore the well width is important in considering electron-hole interactions in piezoelectric quantum wells.

3.2. The piezoelectric effect.

The word "piezo" is derived from a Greek word that means "to press". Piezoelectricity can be defined as "electric polarisation produced by mechanical strain in crystals belonging to certain classes, the polarisation being proportional to the strain and changing sign with it" [5]. For purely historical reasons, the above definition is referred to as 'direct' piezoelectricity, while the 'converse effect' refers to the effect of producing strain in a crystal when applying an electric polarisation. Semiconductor multilayers provide an ideal system to produce crystal structures with a built-in strain, due to the lattice mismatch between layers that have different lattice constants. For sufficiently thin layers, the lattice mismatch is accommodated by internal strains rather than by the formation of dislocations.

The 'certain classes' of crystals mentioned in the above definition refer to crystal structures that are non-centrosymmetrical, i.e. they are not symmetrical with respect to a point. With one exception (irrelevant to this study), all classes devoid of a centre of symmetry are piezoelectric, which includes the zincblende structure of ZnSe.

An example of a piezoelectric material and the effect of external stress is shown on figure 3-8.

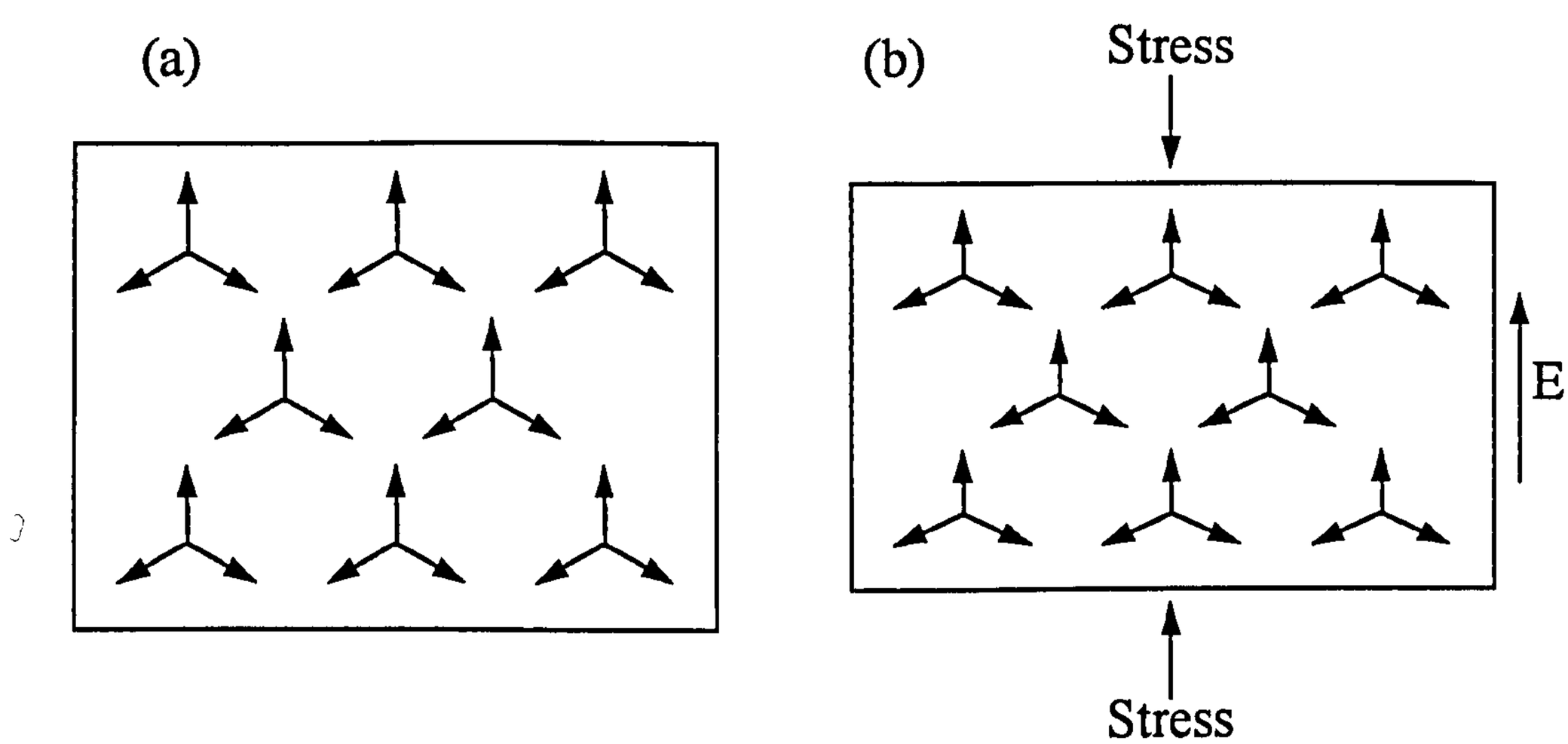

Figure 3-8. (a) *The unstressed crystal has a threefold symmetry axis and the arrows represent dipole moments. The sum of the three dipole moments at each vertex is zero.* (b) *The crystal when stressed produces an electric field in the direction indicated. The sum of the dipole moments about each vertex is no longer zero* [6].

The piezoelectric effect can be described mathematically by the piezoelectric stress coefficient e_{ijk} which is a third-rank tensor that relates the strain in a crystal to an electric polarisation [5]:

$$P_i = e_{ijk}\gamma_{jk} \tag{3-31}$$

i, j and k are all [1..3]. γ is the elastic strain and P is the electric polarisation. Since strain is a symmetric second-rank tensor, i.e. $\gamma_{jk} = \gamma_{kj}$, there are only 18 instead of 27 components of e_{ijk} because $e_{ijk} = e_{ikj}$ [7]. Therefore a contracted notation may be used to allow the tensor to be written more easily by redefining γ_{jk} as γ_k where k ≡ [1..6] ≡ [xx, yy, zz, yz, zx, xy].

The six components of strain comprise of three uniaxial components along each axis (xx, yy, and zz) and three shear strain components in each of the major planes (yz, zx and xy). Zincblende structures have only one independent piezoelectric constant, $e_{14} = e_{25} = e_{36}$, all other values are zero [5], thus

$$\begin{bmatrix} P_x \\ P_y \\ P_z \end{bmatrix} = \begin{bmatrix} 0 & 0 & 0 & e_{14} & 0 & 0 \\ 0 & 0 & 0 & 0 & e_{14} & 0 \\ 0 & 0 & 0 & 0 & 0 & e_{14} \end{bmatrix} \begin{bmatrix} \gamma_{xx} \\ \gamma_{yy} \\ \gamma_{zz} \\ 2\gamma_{yz} \\ 2\gamma_{xz} \\ 2\gamma_{xy} \end{bmatrix} \tag{3-32}$$

Therefore polarisation will only occur along one axis if a strain is present in the plane of the other two axes, i.e. only shear strain will produce an electric field.

It was theoretically proposed by Smith [8] that the strain in layers grown on the (111) plane would be shear and therefore produce an internal electric field, while the strain in layers grown on the (001) plane was purely uniaxial, and therefore had no piezoelectric effect. The field in (111) structures would be purely longitudinal (i.e. parallel to the growth direction) while the field in (110) structures would be purely

transverse. Smith further deduced that any plane other than (001) would have a longitudinal and / or transverse component and that the desired longitudinal field would be maximised on the (111) plane [9]. This study uses strained layers grown on the (211) plane which still have a high longitudinal field (approximately two-thirds that of the (111) plane) while providing easier growth conditions. It was shown in chapter 1 that the (211) surface could either be (211)A or (211)B (see figure 1-3), and it follows that the field generated by strained layer growth on the two surfaces will be equal but opposite.

The magnitude of the longitudinal internal field, F_{piezo}^{st}, in layers grown on substrates other than (001) can be deduced by calculating the off-diagonal strain component to be used in equation (3-31) as a function of the lattice mismatch $\Delta a/a$ and the elastic stiffness tensor elements c_{ij} [10]. The elastic stiffness is a fourth rank tensor relating applied stress to resulting strain that is simplified from 81 to 21 components due to symmetry [7]. The internal field is then given by

$$F_{piezo}^{st} = \frac{P}{\varepsilon \varepsilon_0} \tag{3-33}$$

ε_0 is the permittivity of free space, ε is the dielectric constant. For (111)-oriented structures F_{piezo}^{st} is simply given by [8]

$$F_{piezo}^{st} = \frac{e_{14}}{\varepsilon \varepsilon_0} \times \frac{\Delta a}{a} \tag{3-34}$$

In the case of the (211)-oriented zincblende semiconductors F_{piezo}^{st} has been calculated as [11]

$$F_{piezo}^{st} = \frac{e_{14}}{\varepsilon\varepsilon_0}\frac{8\sqrt{2}}{\sqrt{3}}\frac{(c_{11}+2c_{12})(c_{11}-c_{12})}{D_{211}}\times\frac{\Delta a}{a} \tag{3-35}$$

D_{211} is defined as :

$$D_{211} = \frac{8}{9}\left[13c_{11}c_{44} - 7c_{12}c_{44} + 2c_{44}^2 + 2c_{11}^2 + 2c_{11}c_{12} - 4c_{12}^2\right] \tag{3-36}$$

Examples of the elastic stiffness tensor elements for ZnSe and CdSe are given in table 3-1.

Table 3-1. *Elastic Moduli for ZnSe and CdSe at room temperature. The units are* $10^{11}.dyn.cm^{-2}$.

Material	c_{11}	c_{12}	c_{44}
ZnSe	8.26	4.98	4.20
CdSe	7.49	4.63	8.68

3.3. The quantum confined Stark effect.

It has been established that piezoelectric semiconductor layers that are subject to strain will contain an internal electric field. The effect of electric fields on the properties of semiconductors has been extensively studied. In bulk semiconductors the application of an electric field results in a shift and broadening of the band edge absorption commonly known as the Franz-Keldysh effect [12,13]. At low temperatures the absorption peak will shift by only ~ 10% before the peak becomes unresolvable. This (Stark) broadening is essentially due to the reduction of lifetime of the exciton resulting from field ionisation by the electric field ; with a uniform field there are no longer any bound states of the electron-hole system [14].

In quantum well structures the physics will be significantly different from the bulk material due to the quantum confinement. When an electric field is applied to a quantum well the electrons and holes are pulled towards opposite barriers, decreasing the overlap of the electron and hole wavefunctions which reduces the binding energy of the exciton and the oscillator strength of the transition. Furthermore the subband level energies are decreased as a result of the change in shape of the quantum well. This means that the transition energy is 'red-shifted' (i.e. shifted to lower energies) in the presence of an applied electric field. This is illustrated in figure 3-9. The important aspect of the quantum well is that, as this happens, the electron and hole are prevented from escaping by the walls of the well, this prevents rapid 'field-ionisation' of the exciton. Large shifts of the transition energy can be achieved while still maintaining a sharp exciton peak. The mechanism of the shift in energy and change in oscillator

strength of the transition is the quantum confined Stark effect (QCSE). This was first detected by Wood *et al.* [15] and then studied extensively by Miller *et al.* [14,16].

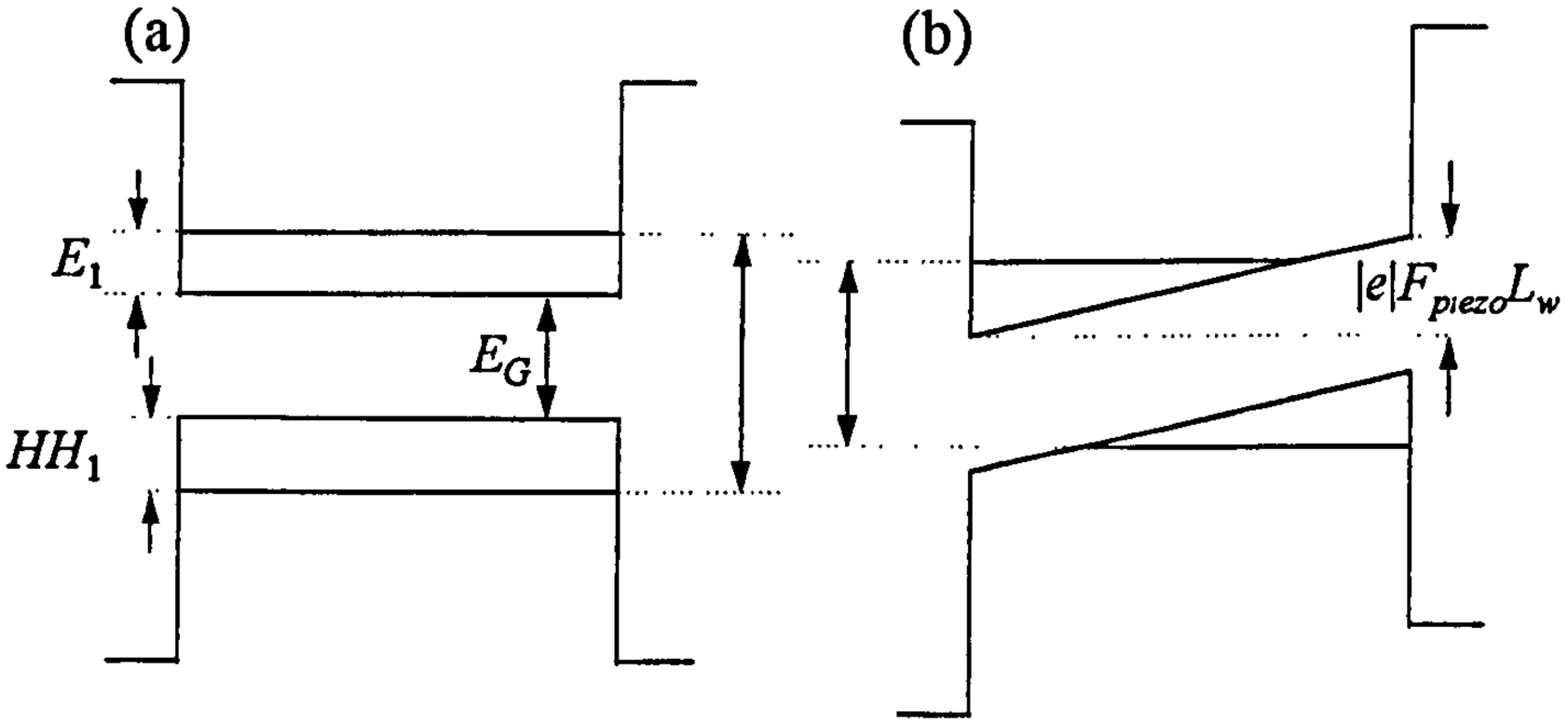

Figure 3-9. *A quantum well band structure* (a) *with no electric field and* (b) *with an electric field. The energy of the transition is reduced.*

The transition energy of a quantum well subjected to an electric field is summarised by equation (3-37).

$$E = E_G + E_1 + HH_1 - |e|F_{piezo}L_w - R_y \qquad (3\text{-}37)$$

E_G is the band gap of the strained layer, E_1 and HH_1 are the first confined energy states in the quantum well and R_y is the exciton binding energy. F_{piezo} is the piezoelectric field, although the equation would be valid with an external field as well.

L_w is the width of the quantum well. The $|e|F_{piezo}L_w$ term demonstrates the reduction in energy by the QCSE due to the internal field.

One can conclude, therefore, that strained zincblende semiconductor layers grown on a piezoelectric growth plane will have their optical transitions shifted to lower energies due to the QCSE.

3.4. Review.

The application of the piezoelectric effect in semiconductor structures was pioneered by the group at the Los Alamos National Laboratory in New Mexico. As mentioned before, it was first theoretically proposed by Smith [8] that internal fields would be present in strained zincblende layers grown on certain substrate orientations. He then went on to collaborate with Mailhiot to produce a **k·p** model for a GaInAs / AlInAs superlattice grown on (001) and (111) growth axis which included piezoelectric effects [17]. Further theoretical exploration by Smith and Mailhiot predicted the screening effect (to be discussed later) and large optical nonlinearities due to the piezoelectric effect [18]. They went on to consider the electrostatic implications and also considered growth on planes other than (111) [9].

The first growth results published by the group was by Beery *et al.* [19] who produced GaInAs / GaAs strained superlattices grown on the (111) plane. Comparison of their initial photoluminescence results with their theoretical calculations gave strong

evidence that internal fields were present. The first real demonstration of the internal field by the group soon followed when they compared identical samples grown on the (001) and (111) growth axis which showed the expected red shift in the absorption and luminescence spectra of the piezoelectric structures [20]. The screening effects and large optical nonlinearities were then demonstrated experimentally by Sela *et al.* [21]. The group then went on to utilise the piezoelectric effect in electro-optic modulation [22] and tunnelling structures [23]. Mailhiot was also involved in an early demonstration of the effect of the internal field on the transitions in an absorption spectra [24]. It was found that the field disrupted the symmetry of the well and therefore allowed previously symmetry-forbidden transitions.

The first direct demonstration of an internal field in piezoelectric structures was by Caridi *et al.* [25] at AT&T Bell labs in New Jersey, the same group responsible for the discovery of the quantum confined Stark effect. They grew a single quantum well of GaInAs in the intrinsic region of a p-i-n diode on (111) GaAs which enabled them to apply an external bias to remove the internal field and this resulted in the now characteristic blue shift of the exciton peaks in photocurrent spectra. They were therefore also able to determine the strength of the internal field. The group immediately followed this by demonstrating optical bistability in a self-electro-optic effect device (SEED) using the piezoelectric effect [26].

Studies in the piezoelectric effect in II-VI semiconductors soon followed the work in III-V. Strained CdS / CdSe wurtzite superlattices were grown [27] and then evidence of piezoelectric fields was first reported by Halsall *et al.* [28,29] which

progressed to studies of the electronic band structure [30] and evidence of screening [31]. This work was then expanded to include CdS / ZnSe superlattices [32] and moved onto the cubic structure of the same material [33,34]. This work has been progressed by several research groups in the UK.

However, the first progress in II-VI zincblende compounds was by a collaboration between the groups at the Université J. Fourier in Saint Martin d'Hères and at Grenoble, both in France, who developed CdTe based structures, either with CdZnTe or CdMnTe alloys. Similarly to the work in III-V compounds, it began by comparing piezoelectric and non-piezoelectric structures [35] and progressed to the screening effect [36,37] and the effects on quantum well transitions [38]. They also demonstrated a novel technique of screening the internal field ; previously the carriers required had been provided by optical pumping, but in this case they were generated by modulation doping of the heterostructures [39]. The group went on to study the exciton effects of localising electrons and holes at opposite ends of a quantum well [40] and nonlinear characteristics of the piezoelectric constant in CdTe [41]. Recently they have used a piezoelectric heterostructure for efficient all-optical light modulation [42].

The group at the University of Sheffield has done extensive work on the piezoelectric effect in InGaAs / GaAs systems, in particular the relevance to devices [43,44,45] along with the usual studies of screening [46] and transition effects [47]. They reported the first optical modulation for piezoelectric devices grown on InP substrates, using InGaAs / InP multiple quantum wells [48]. They went on to observe

Wannier-Stark ladder transitions in piezoelectric superlattices [49], which are transitions between adjacent wells that occur due to the distortion of the band structure by the internal field, and also to consider the implications of the internal field in piezoelectric quantum well lasers [50,51]. They have also detected enhanced mobility in piezoelectric quantum wells due to the positioning of electrons away from ionised impurities [52].

There have been many other groups who have been involved in studying the piezoelectric effect in semiconductor heterostructures to a lesser degree, some looking at subtleties in the screening effect [53], or the effect of the internal field on exciton lifetimes [54,55]. There have been purely electronic studies of the piezoelectric effect on Schottky diode barrier heights [56] and also its application in field effect transistors [57,58]. More recently the piezoelectric aspects of the promising new material, GaN, have been studied [59,60]. Finally, within the Heriot-Watt group the first studies in ZnCdSe / ZnSe piezoelectric structures were by Wang *et al.* [61], and these will be improved and extended in this thesis. Wang had previously developed quantum confined Stark effect modulators using the ZnCdSe / ZnSe system [62] and also went on to produce a bistable SEED device [63], both on (001) GaAs.

3.5. The screening effect.

There are two methods of directly demonstrating the piezoelectric effect by effectively removing the field which would return the transitions to their former

energy, i.e. to produce a blue (higher energy) shift. The first is to simply apply an external bias that opposes the internal field, a method that is used in chapters 4 and 5. Figure 3-10 illustrates that after the initial blue shift the transition will return to lower energies once the external bias has become greater than the internal field. When the external bias exactly matches the internal field (i.e. the maximum blue shift is achieved) it is known as the flat band voltage.

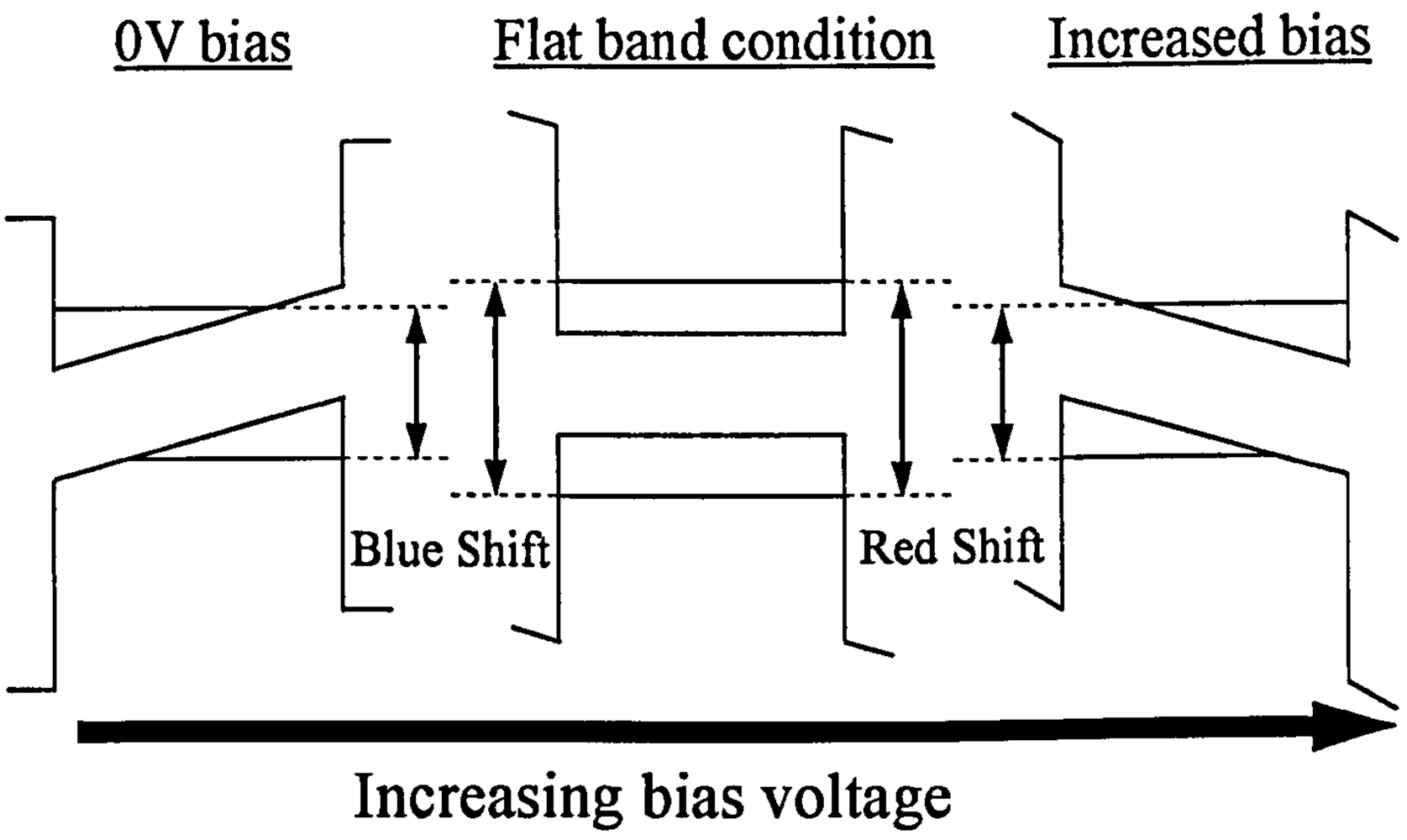

Figure 3-10. *The effect of applying an external bias on the transition energy in a piezoelectric layer quantum well.*

The second method of compensating the internal field is known as 'screening'. It was predicted by Smith *et al.* [18] that large optical nonlinearities would occur when free carriers were created in piezoelectric structures, due to screening of the strain generated internal electric field. This was first demonstrated experimentally by Sela *et*

al. [21] who showed that increasing the excitation intensity in piezoelectric superlattices shifted the transitions to higher energies.

Screening is an unavoidable process when using a technique such as photoluminescence which excites free carriers in the quantum well. When carriers are created in piezoelectric structures, they are subject to the internal electric field. Therefore, electrons and holes will move in opposite directions and populate opposing ends of the quantum well. This physical separation of charge will produce another electric field which will oppose and therefore *screen* the piezoelectric field. If sufficient charge is created in the well, the internal field can be almost completely counteracted, although complete screening of the field is impossible, for there must always be some internal field for the process to occur at all.

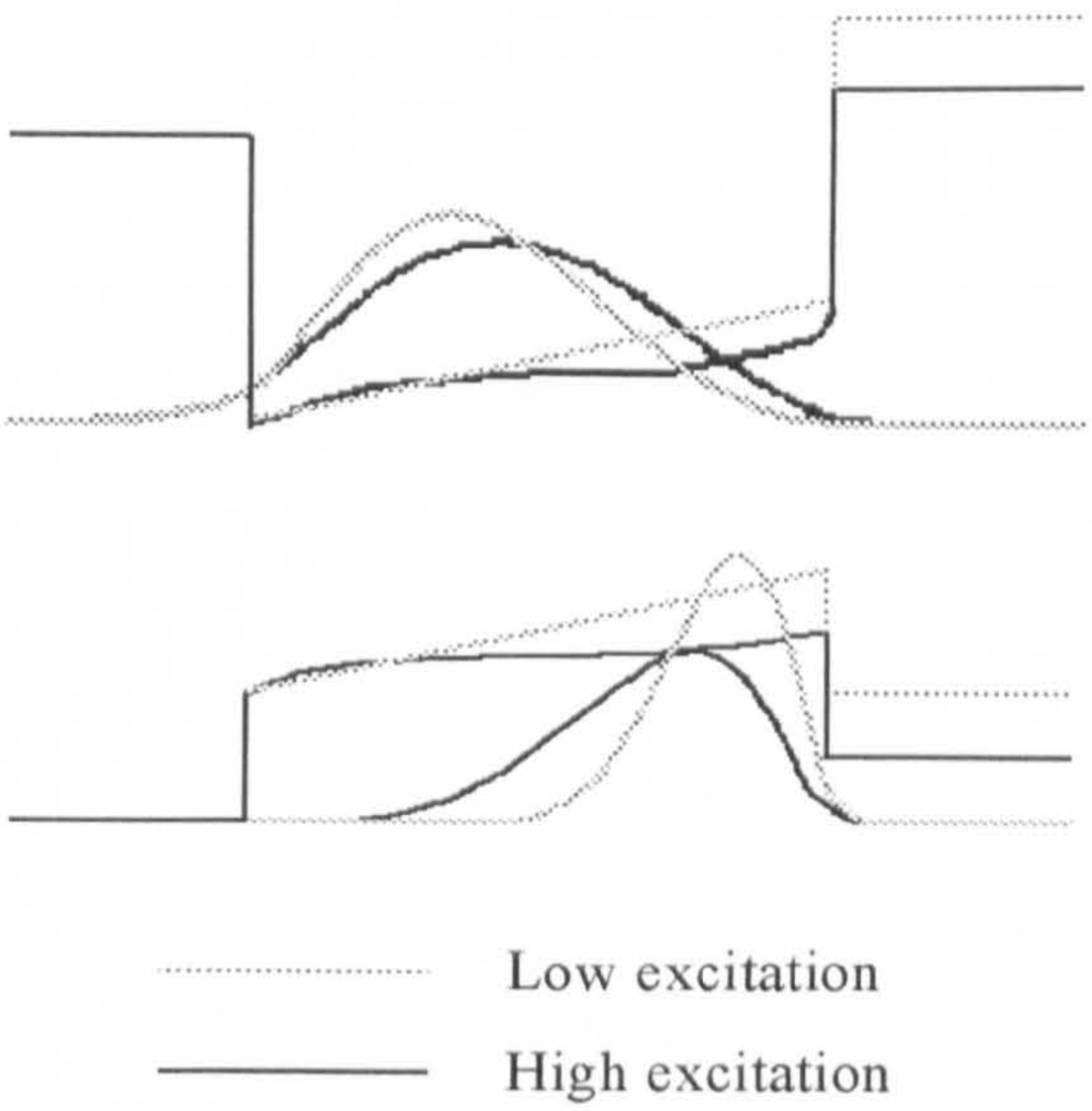

Figure 3-11. *The effect of carrier screening on the band structure and carrier wavefunctions in a piezoelectric quantum well* [64].

The screening effect is shown on figure 3-11. At low excitation the band edge of the quantum well has a strong tilt and the wavefunctions of the electrons and holes are considerably localised at either end of the well. At high excitation the band edge has become flatter and the wavefunctions have moved to a more central position.

3.6. SEEDS.

One of the most common practical uses for the piezoelectric effect in semiconductor structures is the self-electro-optic device (SEED), also known as the optically bistable switch. This was first demonstrated by Miller *et al.* [65] using a non-piezoelectric structure, as a consequence of their groups work discovering the quantum confined Stark effect.

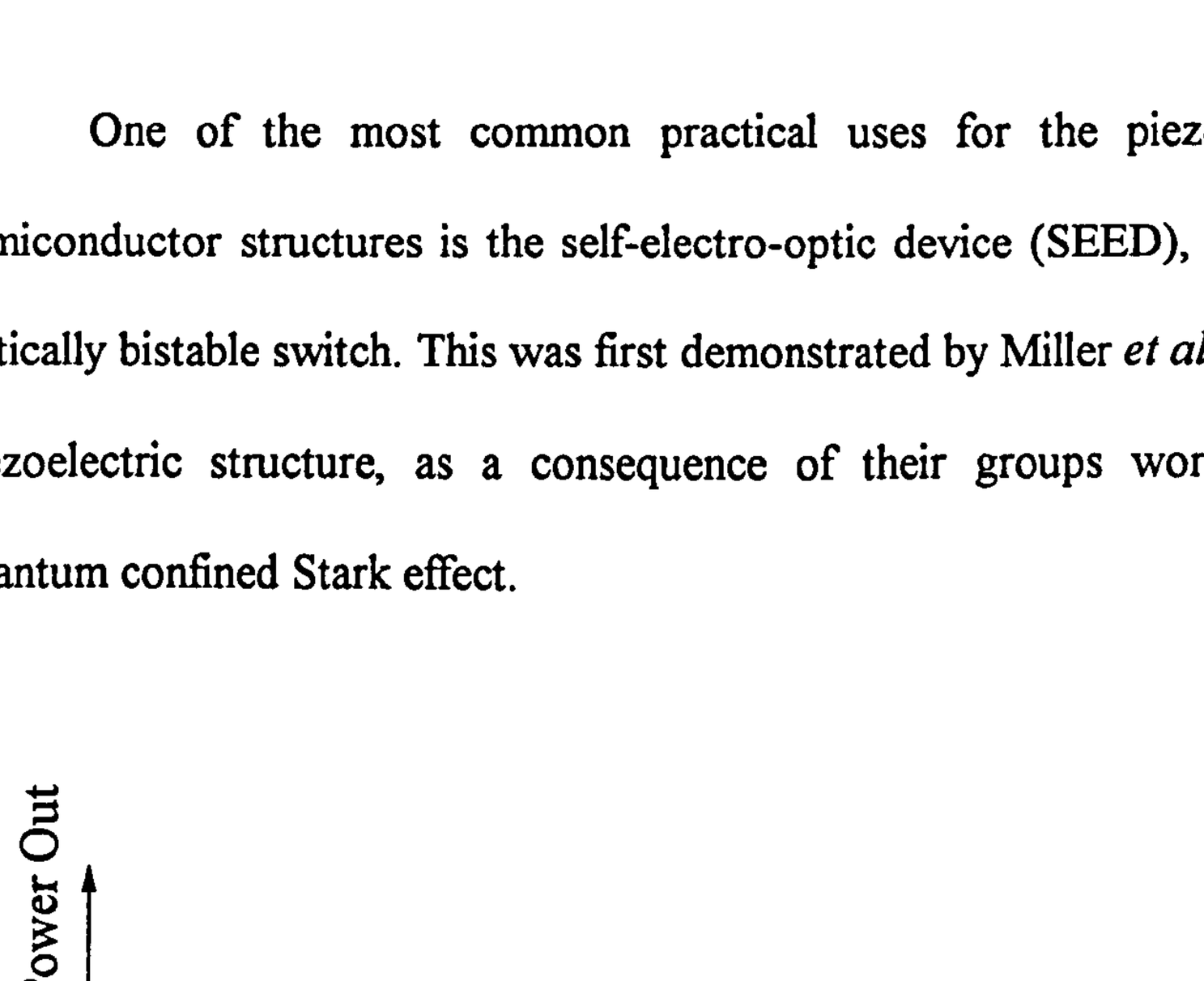

Figure 3-12. *Optical bistability in a SEED.*

Briefly, the SEED requires a nonlinear optical response, in this case a material which has an absorption that increases with input light power, to produce positive feedback. Once the input power has reached the positive feedback point switching occurs, *i.e.* it shifts to a state of higher absorption. Under the correct conditions, this will produce a bistable section in the curve of input power against output power, see figure 3-12.

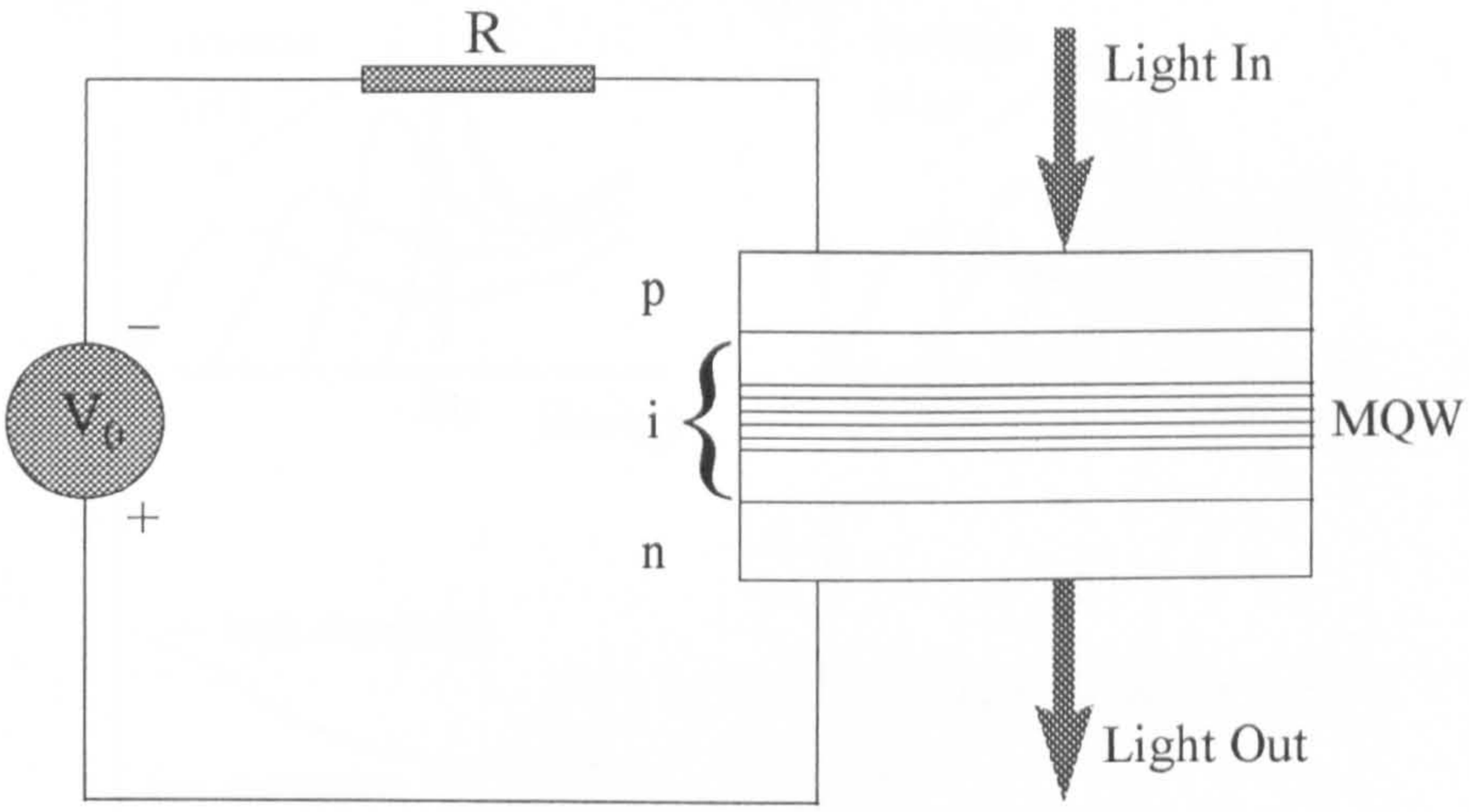

Figure 3-13. *Schematic circuit for a SEED.*

The nonlinear response in this case was generated by the quantum confined Stark effect. In a circuit similar to that shown on figure 3-13, a bias is applied across a multiple quantum well structure in the intrinsic region of p-i-n diode and the wavelength of the input light is chosen to be near the exciton resonance of the quantum wells. However, as nearly all the applied bias will be across the diode, this

shifts the exciton resonance to longer wavelengths by the QCSE and so the structure is in a low absorption state. Furthermore, if the input optical power is increased, it will generate a photocurrent and reduce the voltage across the diode. This in turn will bring the exciton resonance back towards the wavelength of the input light, and having reached that point positive feedback will occur and the diode will be in a high absorption state.

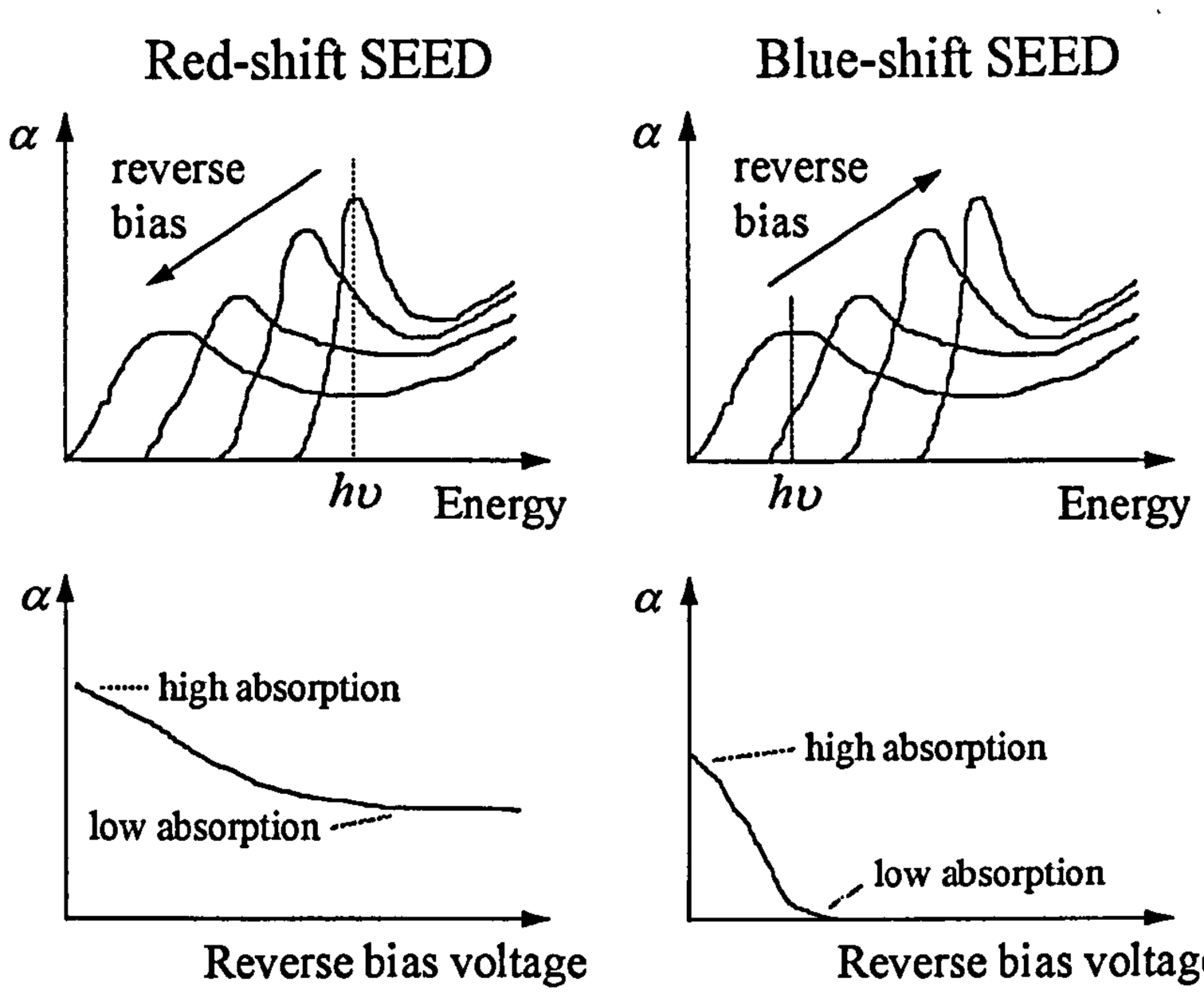

Figure 3-14. *Comparison schematics for a red-shift and a blue-shift SEED clearly show the advantage of using a piezoelectric structure. The contrast between the high absorption and low absorption states for the chosen modulation energy (indicated by hυ) in a blue shift SEED is far greater.*

One short-coming of this system was that because the bias shifted the exciton spectra to lower wavelengths, the wavelength of the incident light would still be above

the band gap and therefore while the absorption may be reduced (with an applied bias), it would still be significant. However, the exciton spectra of a piezoelectric quantum well will shift to higher energies under an applied bias (up to the flat band condition). Therefore the incident light could be chosen to be at the exciton resonance for the high absorption state (with no applied bias) and below band gap for the low absorption state (with applied bias), giving a much higher contrast ratio [66], see figure 3-14, hence the importance of piezoelectric SEEDs. However, current bistable optical switching devices have moved towards hybrid optical / electronic devices using silicon switching circuits [67,68].

3.7. References.

[1] J.R. Hook and H.E. Hall, *Solid State Physics*, (2nd edition), Wiley (1991).

[2] A. Yariv, *Optical Electronics*, (4th edition), Saunders College Publishing (1991).

[3] M. Abramowitz and I.A. Stegun, *Pocketbook of Mathematical Functions*, Verlag Harri Deutsch (1984).

[4] I. Galbraith and G. Duggan, Phys. Rev. B **38**, 10057 (1988).

[5] W.F. Cady, *Piezoelectricity*, McGraw-Hill (1946).

[6] C. Kittel, *Introduction to Solid State Physics*, (7th edition), Wiley (1996).

[7] G. Burns, *Solid State Physics*, Academic Press (1985).

[8] D.L. Smith, Solid State Commun. **57,** 919 (1986).

[9] D.L. Smith and C. Mailhiot, J. Appl. Phys. **63,** 2717 (1988).

[10] D. Sun and E. Towe, Jpn. J. Appl. Phys. **33,** 702 (1994).

[11] R. André, Thesis of the University Joseph Fourier - Grenoble 1, 1994.

[12] W. Franz, Z. Naturforsch. **13a,** 484 (1958).

[13] V. Keldysh, Zh. Eksp. Teor. Fiz. **34,** 1138 (1958) {Sov. Phys. JETP 7, 788 (1958)}

[14] D.A.B. Miller, D.S. Chemla, T.C. Damen, A.C. Gossard, W. Wiegmann, T.H. Wood and C.A. Burrus, Phys. Rev. B **32,** 1043 (1985).

[15] T.H. Wood, C.A. Burrus, D.A.B. Miller, D.S. Chemla, T.C. Damen, A.C. Gossard and W. Wiegmann, Appl. Phys. Lett. **44,** 16 (1984).

[16] D.A.B. Miller, D.S. Chemla, T.C. Damen, A.C. Gossard, W. Wiegmann, T.H. Wood and C.A. Burrus, Phys. Rev. Lett. **53,** 2173 (1984).

[17] C. Mailhiot and D.L. Smith, Phys. Rev. B **35,** 1242 (1987).

[18] D.L. Smith and C. Mailhiot, Phys. Rev. Lett. **58,** 1264 (1987).

[19] J.G. Beery, B.K. Laurich, C.J. Maggiore, D.L. Smith, K. Elcess, C.G. Fonstad and C. Mailhiot, Appl. Phys. Lett. **54,** 233 (1989).

[20] B.K. Laurich, K. Elcess, C.G. Fonstad, J.G. Beery, C. Mailhiot and D.L. Smith, Phys. Rev. Lett. **62**, 649 (1989).

[21] I. Sela, D.E. Watkins, B.K. Laurich, D.L. Smith, S. Subbanna and H. Kroemer, Appl. Phys. Lett. **58**, 684 (1991).

[22] I.H. Campbell, D.E. Watkins, D.L. Smith, S. Subbanna and H. Kroemer, Appl. Phys. Lett. **59**, 1711 (1991).

[23] I.H. Campbell, M.D. Joswick, D.L. Smith and R.H. Miles, Appl. Phys. Lett. **66**, 988 (1995).

[24] H. Qiang, F.H. Pollak, C. Mailhiot, G.D. Pettit and J.M. Woodall, Phys. Rev. B **44**, 9126 (1991).

[25] E.A. Caridi, T.Y. Chang, K.W. Goossen and L.F. Eastman, Appl. Phys. Lett. **56**, 659 (1990).

[26] K.W. Goossen, E.A. Caridi, T.Y. Chang, J.B. Stark, D.A.B. Miller and R.A. Morgan, Appl. Phys. Lett. **56**, 715 (1990).

[27] M.P. Halsall, J.E. Nicholls, J.J. Davies, B. Cockayne, P.J. Wright and A.G. Cullis, Semicond. Sci. Technol. **3**, 1126 (1988).

[28] M.P. Halsall, J.E. Nicholls, J.J. Davies, P.J. Wright and B. Cockayne, Surf. Sci. **228**, 41 (1990).

[29] M.P. Halsall, J.E. Nicholls, J.J. Davies, P.J. Wright and B. Cockayne, J. Cryst. Growth **101**, 616 (1990).

[30] D. Wolverson, M.P. Halsall and J.J. Davies, Semicond. Sci. Technol. **6**, A123 (1991).

[31] M.P. Halsall, J.E. Nicholls, J.J. Davies, B. Cockayne and P.J. Wright, J. Appl. Phys. **71**, 907 (1992).

[32] I.V. Bradley, J.P. Creasley, K.P. O'Donnell, P.J. Wright and B. Cockayne, J. Cryst. Growth **159**, 551 (1996).

[33] I.V. Bradley, J.P. Creasey, K.P. O'Donnell, B. Neubauer and D. Gerthsen, Appl. Phys. Lett. **71**, 671 (1997).

[34] I.V. Bradley, J.P. Creasey, K.P. O'Donnell, B. Neubauer and D. Gerthsen, J. Cryst. Growth **184/185**, 718 (1998).

[35] R André, C. Deshayes, J. Cibert, Le Si Dang, S. Tatarenko and K. Saminadayar, Phys. Rev. B **42**, 11392 (1990).

[36] J. Cibert, R. André, C. Deshayes, Le Si Dang, H. Okumura, S. Tatarenko, G. Feuillet, P.H. Jouneau, R. Mallard and K. Saminadayar, J. Cryst. Growth **117**, 424 (1992).

[37] E. Vanelle, A. Alexandrou, J.-P. Likforman, D. Block, J. Cibert and R. Romestain, Phys. Rev. B **53**, R16172 (1996).

[38] Le Si Dang, R. André, C. Bodin-Deshayes, J. Cibert, H. Okumura, G. Feuillet and P.H. Jouneau, Physica B **185**, 551 (1993).

[39] F. Bassani, S. Tatarenko, K. Kheng, P.H. Jouneau, K. Saminadayar, N. Magnea and R. Cox, Appl. Phys. Lett. **63**, 2106 (1993).

[40] R. André, J. Cibert and Le Si Dang, Phys. Rev. B **52**, 12013 (1995).

[41] R. André, J. Cibert, Le Si Dang, J. Zeman and M. Zigone, Phys. Rev. B **53**, 6951 (1996).

[42] V. Ortiz, N.T. Pelekanos and G. Mula, Appl. Phys. Lett. **72**, 963 (1998).

[43] A.S. Pabla, J.L. Sanchez-Rojas, J. Woodhead, R. Grey, J.P.R. David, G.J. Rees, G. Hill, M.A. Pate, P.N. Robson, R.A. Hogg, T.A. Fisher, A.R.K. Willcox, D.M. Whittaker, M.S. Skolnick and D.J. Mowbray, Appl. Phys. Lett. **63**, 752 (1993).

[44] A.S. Pabla, J. Woodhead, R. Grey, G.J. Rees, J.P.R. David, M.A. Pate and P.N. Robson, Electron. Lett. **62**, 1521 (1994).

[45] L.R. Wilson, D.J. Mowbray, M.S. Skolnick, V.N. Astratov, D.W. Peggs, G.J. Rees, J.P.R. David, R. Grey, G. Hill and M.A. Pate, Phys. Rev. B **55**, R16045 (1997).

[46] T.E. Sale, J. Woodhead, G.J. Rees, R. Grey, J.P.R. David, A.S. Pabla, P.J. Rodriguez-Gírones and P.N. Robson, J. Appl. Phys. **76**, 5447 (1994).

[47] R.A. Hogg, T.A. Fisher, A.R.K. Willcox, D.M. Whittaker, M.S. Skolnick, D.J. Mowbray, J.P.R. David, A.S. Pabla, G.J. Rees, R. Grey, J. Woodhead, J.L. Sanchez-Rojas, G. Hill, M.A. Pate and P.N. Robson, Phys. Rev. B **48**, 8491 (1993).

[48] A.S. Pabla, M. Hopkinson, J.P.R. David, E.A. Khoo and G.J. Rees, Electron. Lett. **30**, 1707 (1994).

[49] D.W. Peggs, M.S. Skolnick, D.M. Whittaker, R.A. Hogg, A.R.K. Willcox, D.J. Mowbray, R. Grey, G.J. Rees, L. Hart, M. Hopkinson, G. Hill and M.A. Pate, Phys. Rev. B **52**, R14340 (1995).

[50] A.S. Pabla, J. Woodhead, E.A. Khoo, R. Grey, J.P.R. David and G.J. Rees, Appl. Phys. Lett. **68**, 1595 (1996).

[51] T.E. Sale, J.S. Roberts, N.D. Whitbread and P.N. Robson, IEEE Phot. Tech. Lett. **8**, 983 (1996).

[52] L.J. Hitchens, P.A. Houston, M. Hopkinson and G.J. Rees, Electron. Lett. **31**, 2215 (1995).

[53] K.J. Moore, P. Boring, B. Gil and K. Woodbridge, Phys. Rev. B **48**, 18010 (1993).

[54] P. Bigenwald, B. Gil and P. Boring, Phys. Rev. B **48**, 9122 (1993).

[55] X. Chen, C.H. Molley, D.A. Woolf, C. Cooper, D.J. Somerford, P. Blood, K.A. Shore and J. Sarma, Appl. Phys. Lett. **67**, 1393 (1995).

[56] K.W. Chung, Z. Wang, J.C. Costa, F. Williamson, P.P. Ruden and M.I. Nathan, Appl. Phys. Lett. **59**, 1191 (1991).

[57] E.T. Yu, G.J. Sullivan, P.M. Asbeck, C.D. Wang, D. Qiao and S.S. Lau, Appl. Phys. Lett. **71**, 2794 (1997).

[58] X. Li, K.F. Longenbach and W.I. Wang, Appl. Phys. Lett. **60**, 1513 (1992).

[59] A.D. Bykhovski, B.L. Gelmont and M.S. Shur, J. Appl. Phys. **81**, 6332 (1997).

[60] Jin Seo Im, H. Kollmer, J. Off, A. Sohmer, F. Scholz and A. Hangleiter, Phys. Rev. B 57, R9435 (1998).

[61] S.Y. Wang, P.J. Thompson, G. Horsburgh, T.A. Steele, G.D. Brownlie, K.A. Prior and B.C. Cavenett, J. Cryst. Growth **159**, 459 (1996).

[62] S.Y. Wang, G. Horsburgh, P. Thompson, I. Hauksson, J.T. Mullins, K.A. Prior and B.C. Cavenett, Appl. Phys. Lett. **62**, 1715 (1993).

[63] S.Y. Wang, G. Horsburgh, P. Thompson, I. Hauksson, J.T. Mullins, K.A. Prior and B.C. Cavenett, Appl. Phys. Lett. **63**, 857 (1993).

[64] E. Vanelle, Thesis of the University of Grenoble, 1995.

[65] D.A.B. Miller, D.S. Chemla, T.C. Damen, A.C. Gossard, W. Wiegmann, T.H. Wood and C.A. Burrus, Appl. Phys. Lett. **45**, 13 (1984).

[66] K.W. Goossen, E.A. Caridi, T.Y. Chang, J.B. Stark, D.A.B. Miller and R.A. Morgan, Appl. Phys. Lett. **56**, 715 (1990).

[67] K.J. Chen, J. Xu, X.F. Huang, D.K. Zhuang, Q. Li, W.Y. Wang, P.H. Qiu and D. Feng, Solid State Commun. **88**, 579 (1993).

[68] Y. Kanemitsu and T. Matsumoto, Superlatt. and Microstruct. **15**, 61 (1994).

4. ABSORPTION SPECTROSCOPY OF PIEZOELECTRIC QUANTUM WELLS.

4.1. Introduction.

In this chapter two absorption techniques, photocurrent spectroscopy and photoluminescence excitation (PLE) spectroscopy, will be used to study the piezoelectric effect in single ZnCdSe / ZnSe quantum wells. Direct linear absorption was not used as it requires removing the GaAs substrate and would alter the strain in the well layer.

4.2. Photocurrent.

4.2.1. Introduction.

Photocurrent is a method of detecting optical radiation that converts the radiant energy into an electrical signal. It is a process that can be observed in semiconductor structures with an internal field (not to be confused with the piezoelectric field). This internal field is often generated by a p-n junction or a metal-semiconductor Schottky contact, and is most commonly combined with an externally applied bias. The electric field is required to generate a depletion region, which is

where the field sweeps out any free charge carriers. Any incident photon that is absorbed in this region will generate an electron-hole pair that, instead of simply recombining, will be separated by the field and transported to opposite ends, creating a detectable current. This process is the basis of semiconductor photodiodes. It has been shown that in this situation the current generated is directly proportional to the absorption coefficient, α, under a small signal condition [1]. Therefore if the wavelength of the input light is scanned then the response of the current will produce a spectrum that closely follows the absorption.

Due to difficulties in growing p-type doped layers, the structures used in this study were undoped (in fact, ZnSe is intrinsically *n*-type, with $n_a \cong 10^{15}\text{cm}^{-3}$) with a gold layer evaporated onto the surface to generate a Schottky contact.

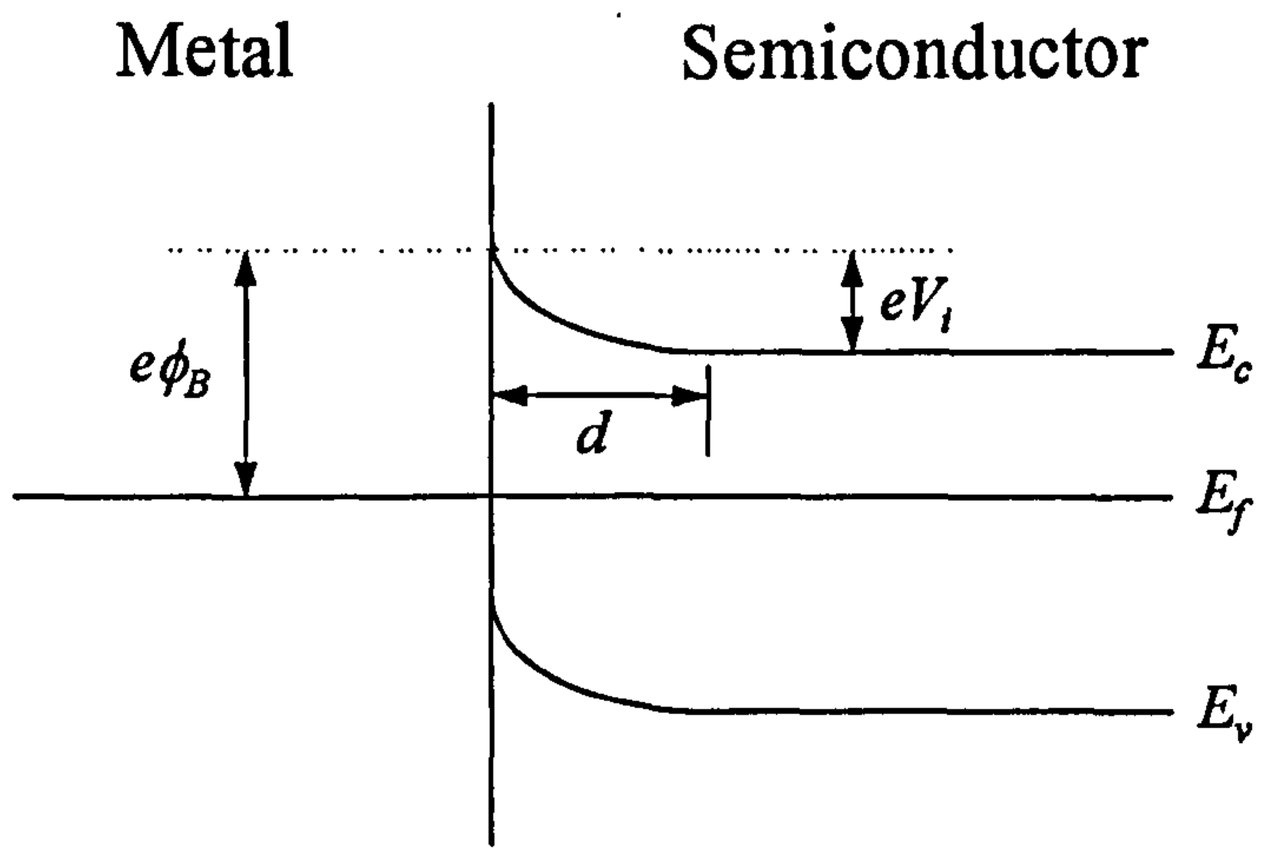

Figure 4-1. *A Schottky junction between a metal and an n-type semiconductor.*

A Schottky contact is a rectifying junction between a metal and a semiconductor. Figure 4-1 shows the energy levels of a metal and *n*-type semiconductor in such an interface.

ϕ_B is the work function of the metal, d is the depletion width, E_f is the Fermi level, E_v is the top of the valence band and E_c is the bottom of the conduction band. V_t is the built-in voltage of the contact. After contact electrons flow from the semiconductor to the metal to line up the Fermi levels, leaving behind positively charged immobile donors over the depletion width d. The Schottky contact makes it possible to apply an external reverse bias without a significant current being drawn.

Gold is widely used to form semi-transparent contacts with *n*-type II-VI semiconductors for its low resistivity and high transmission in the UV-green region of the spectrum, and also for its large work function, essential for a good Schottky contact. Since all the layers in the structures used in this study have low doping, the depletion region covers the whole epilayer.

The experimental set-up for photocurrent is shown in figure 4-2. The PC is used for data acquisition from the lock-in amplifier and also for system control through the stepping motor on the monochromator. This system was also used for direct absorption, transmission and reflection (with a silicon detector). The piezoelectric effect will be investigated by applying an external bias. The voltage is provided by an external power supply with a carefully designed biasing circuit [1], as shown in figure 4-3.

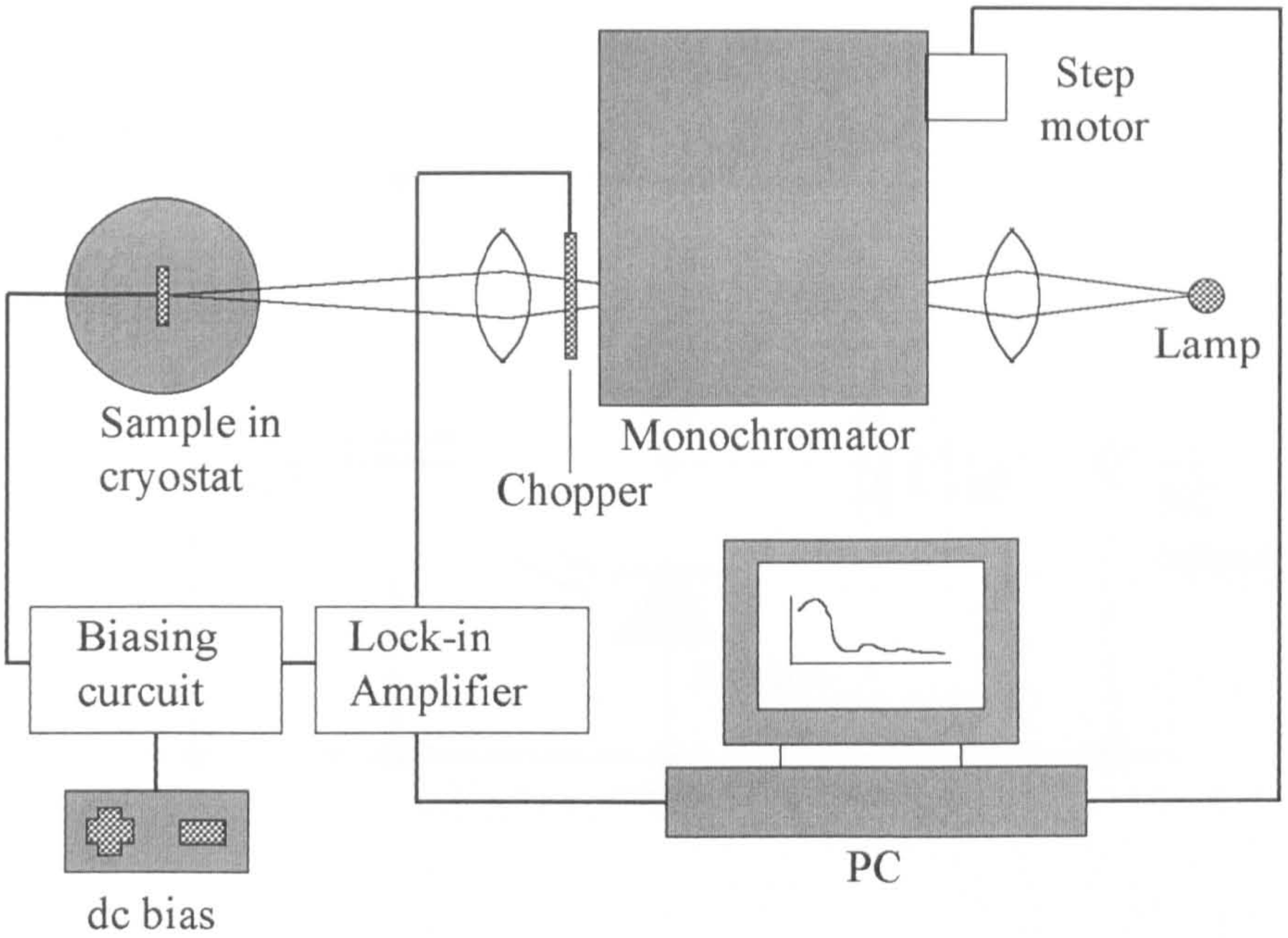

Figure 4-2. *Experimental set-up for photocurrent spectroscopy.*

The sample is biased through the 330kΩ resistor, chosen so that the voltage drop across it is no more than 0.15V, much smaller than the DC bias. The capacitor C_2 blocks the DC bias from the output. C_1 filters noise from the DC supply and external sources. It also provides a short circuit in the equivalent AC circuit so that the AC component at the output (V_{AC}) is equal to the voltage drop across the resistor R, therefore the absolute photocurrent I_p is

$$I_p = \frac{V_{AC}}{R} \tag{4-1}$$

This system was very convenient as all the connections had a common earth and could be connected using normal coaxial cables.

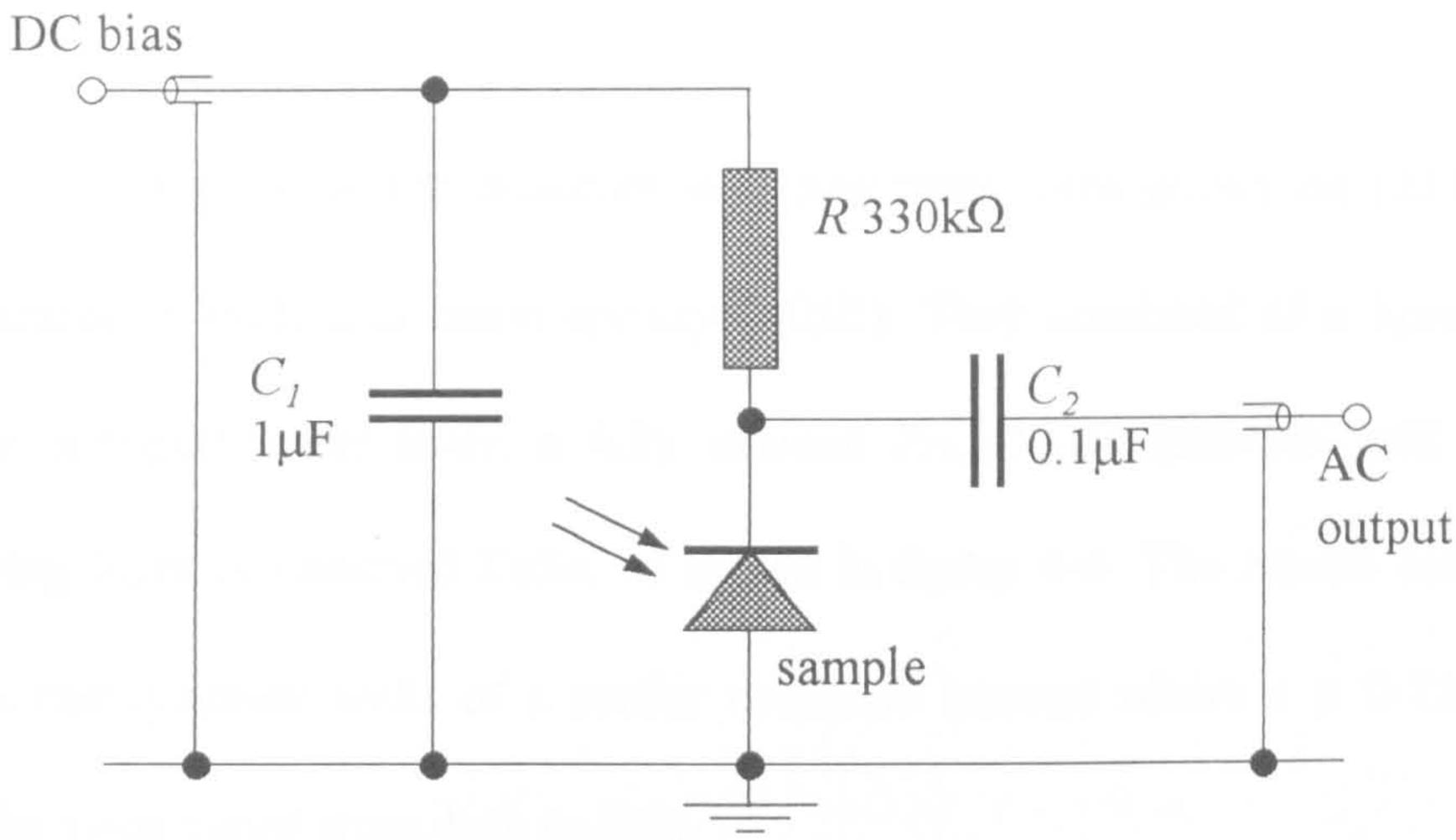

Figure 4-3. *Electrical circuit for providing DC bias and separating the photocurrent signal from the sample.*

Photocurrent is a popular tool to study the piezoelectric effect [2,3,4]. A photocurrent study of a ZnCdSe / ZnSe multiple quantum well structures grown on (211)B GaAs substrates has previously been reported where external electric fields could be applied [5]. However, the results obtained were not completely satisfactory : the two transitions shown give a completely different flat band voltage and the oscillator strengths of the transitions showed an unusual behaviour which was probably due to undesirable contributions from the spatially distributed multiple quantum wells, in which a non-uniform carrier density distribution was likely to exist. Therefore, in this study, a single quantum well (SQW) structure has been adopted.

4.2.2. Experiment.

The piezoelectric quantum well structures were grown on (211)B n^+ GaAs substrates by molecular beam epitaxy (MBE). They consisted of a 1μm fully relaxed ZnSe undoped buffer layer, a fully strained $Zn_{1-x}Cd_xSe$ quantum well and a 0.1μm capping layer of undoped ZnSe, as shown in figure 4-4. The results presented in this work use quantum wells of a similar cadmium content where $x \cong 0.12$ and the well widths were varied from 4nm to 8nm.

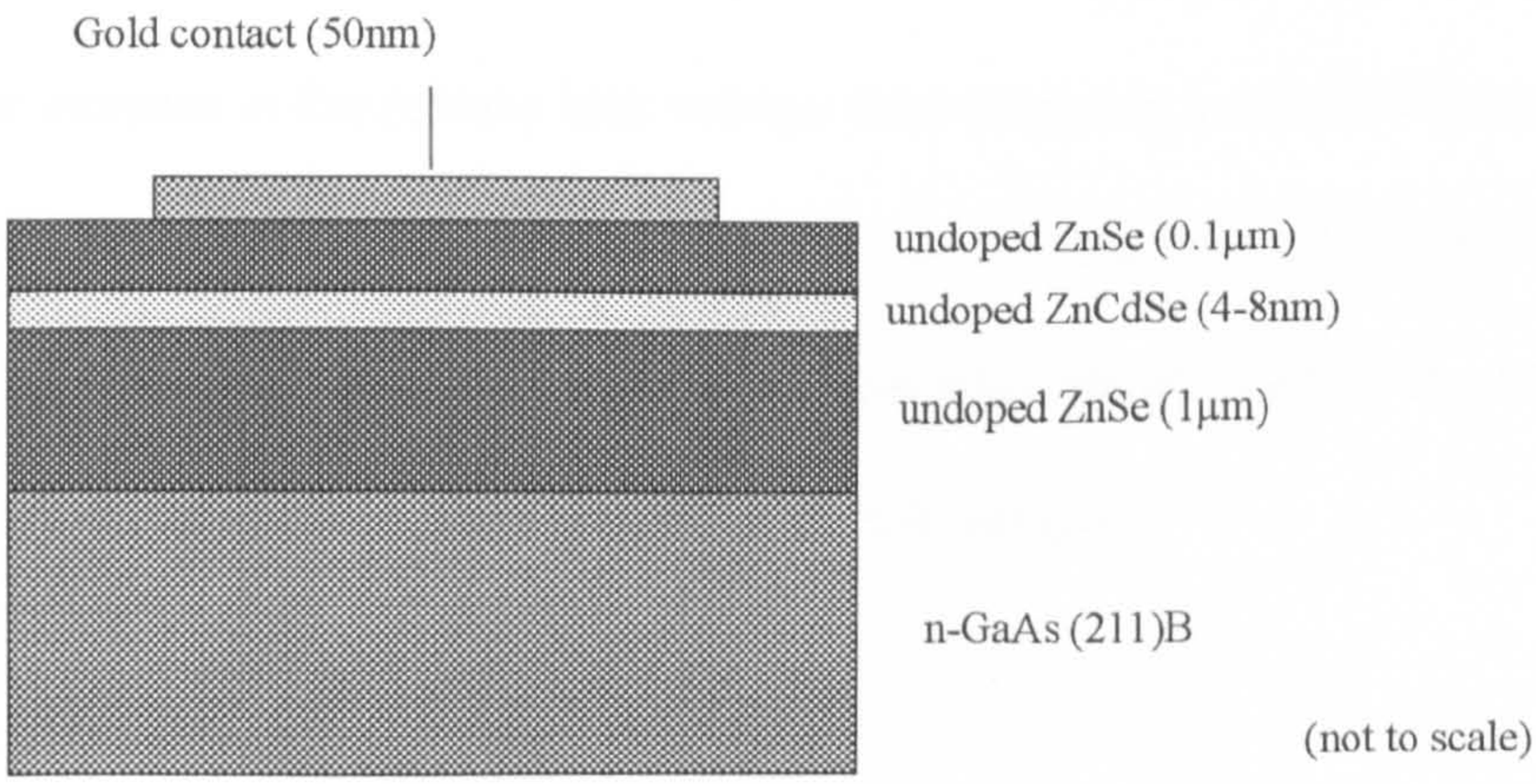

Figure 4-4. *Sample structure for the photocurrent analysis of single quantum wells grown on the (211)B plane.*

A 50nm thick, 1.5mm diameter gold dot was evaporated onto the top surface of each sample to form the Schottky contact. The (211)B face was chosen to ensure

that the internal piezoelectric field could be compensated by a reverse bias on the gold contact. To reduce temperature broadening, the experiment was performed in a nitrogen flow cryostat cooled to 77K.

4.2.3. Results.

Figure 4-5 illustrates the photocurrent spectroscopy results for the 8nm quantum well sample as a function of applied reverse bias. As the voltage is increased a blue shift of the two principal excitonic transitions is observed to occur up to -5V when the internal electric field within the quantum well is balanced by the external field. A further increase in the reverse bias voltage then produces a red shift due to the quantum confined Stark effect. The measurements were repeated with a SQW of 6nm (see figure 4-6) and 4nm (see figure 4-7). Figure 4-8 summarises the shift in the e1hh1 peak as a function of external bias for each quantum well sample.

4.2.4. Discussion.

The magnitude of the electric field generated in the well region is linearly dependent on the strain in the layer [6]. Therefore, the piezoelectric field should be the same for any strained layer of a given cadmium concentration, independent of thickness.

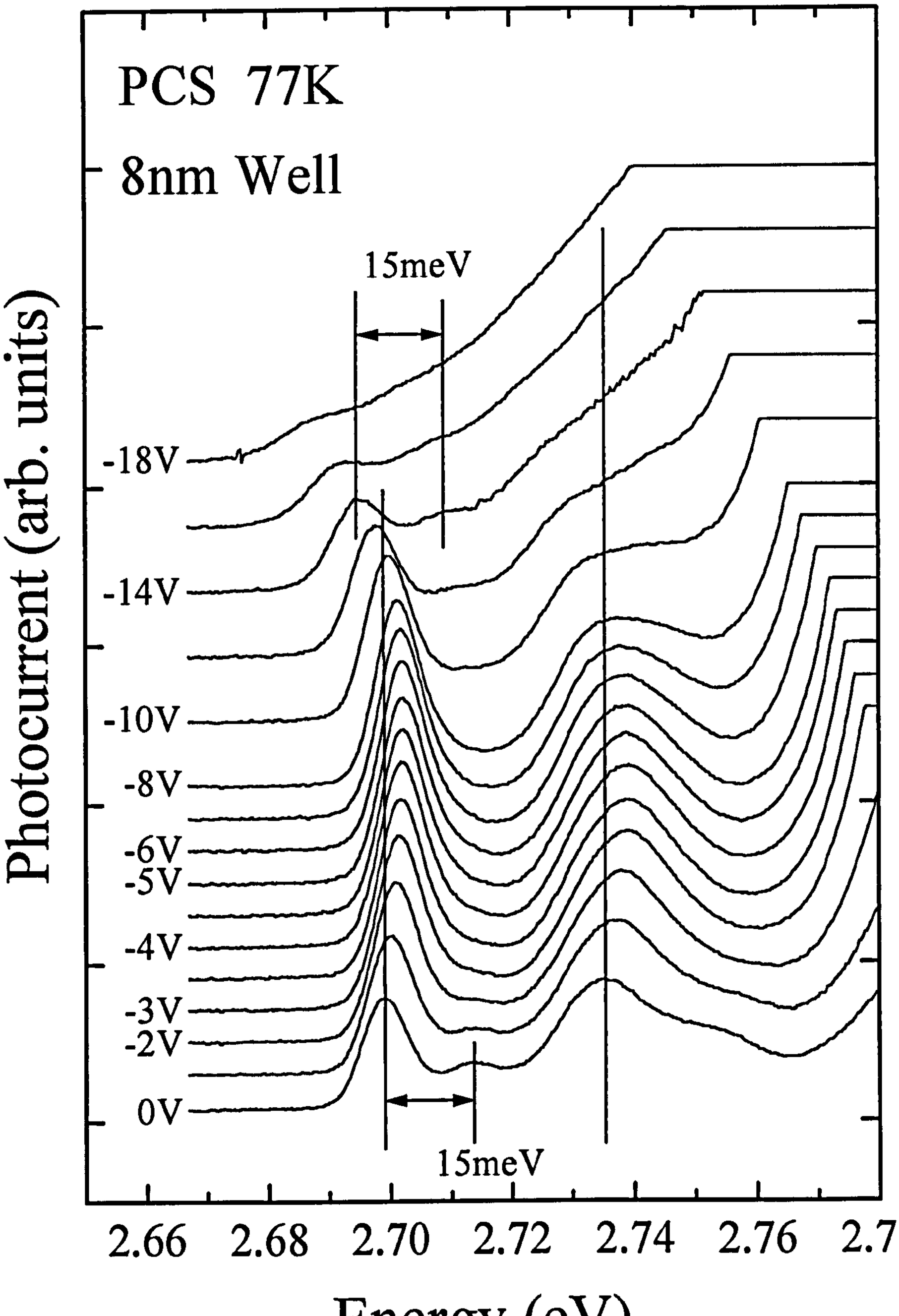

Figure 4-5. *Photocurrent spectra taken at 77K for an 8nm single quantum well piezo structure for a range of external bias values using unpolarised light.*

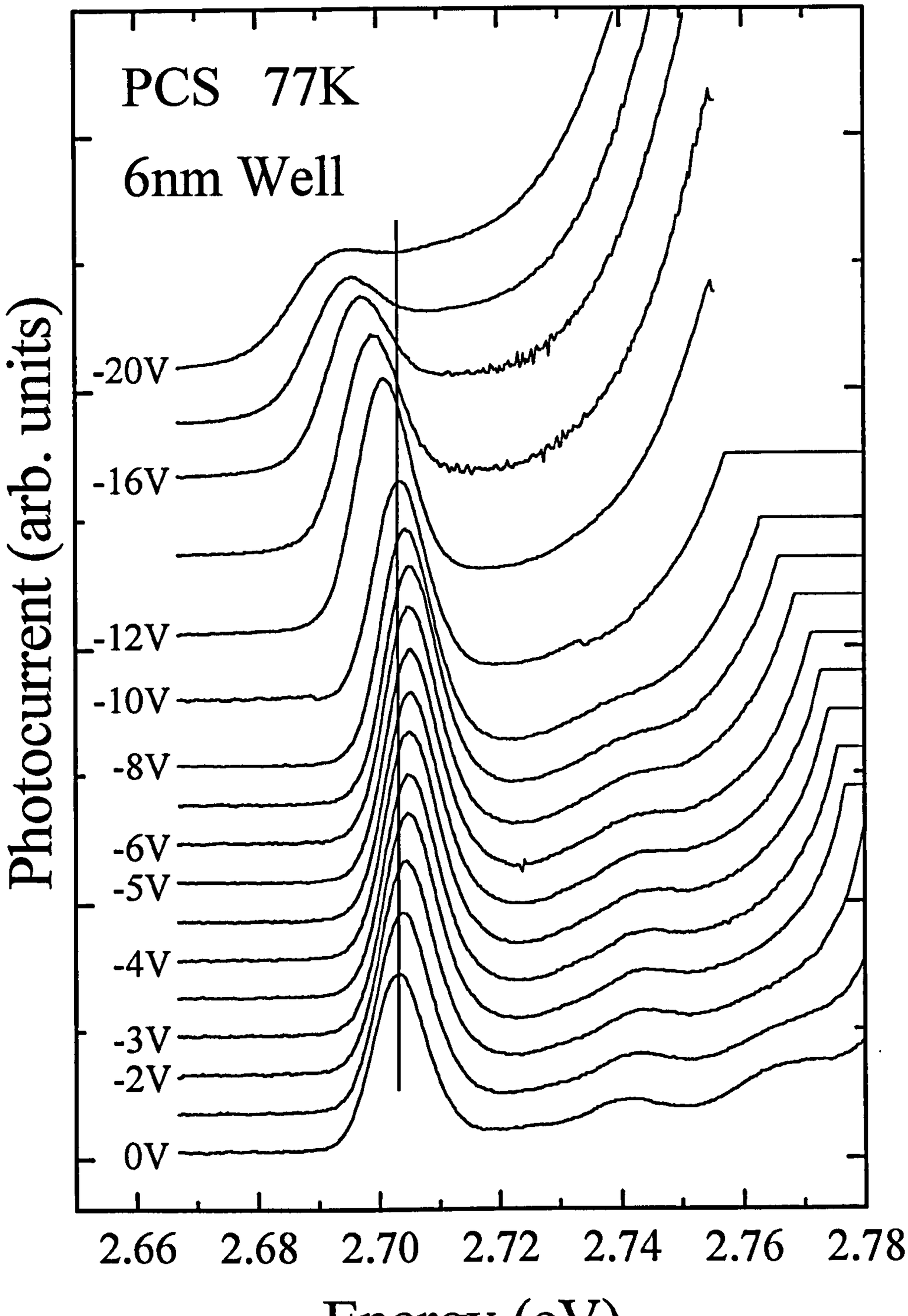

Figure 4-6. *Photocurrent spectra taken at 77K for a 6nm single quantum well piezo structure for a range of external bias values using unpolarised light.*

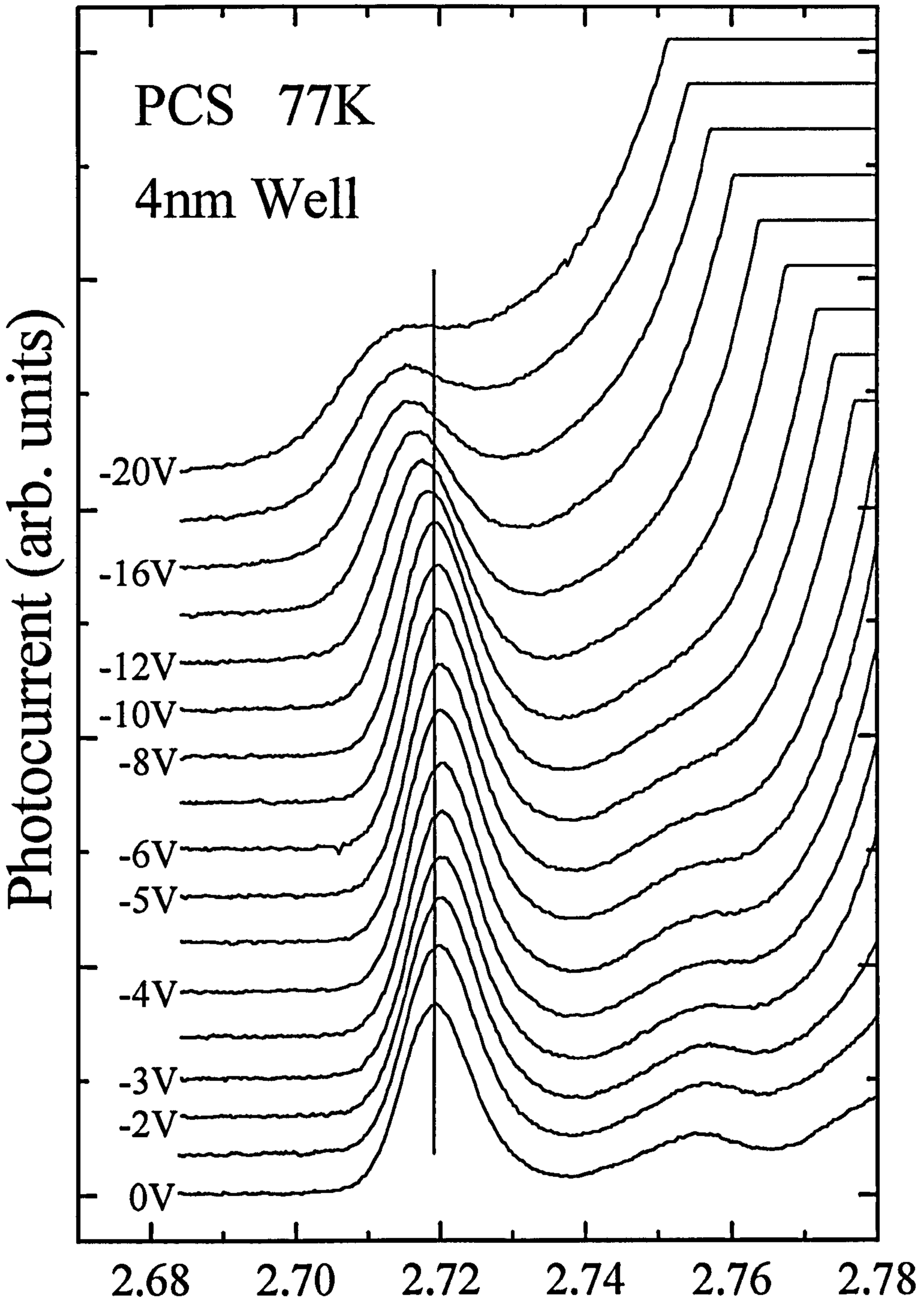

Figure 4-7. *Photocurrent spectra taken at 77K for a 4nm single quantum well piezo structure for a range of external bias values using unpolarised light.*

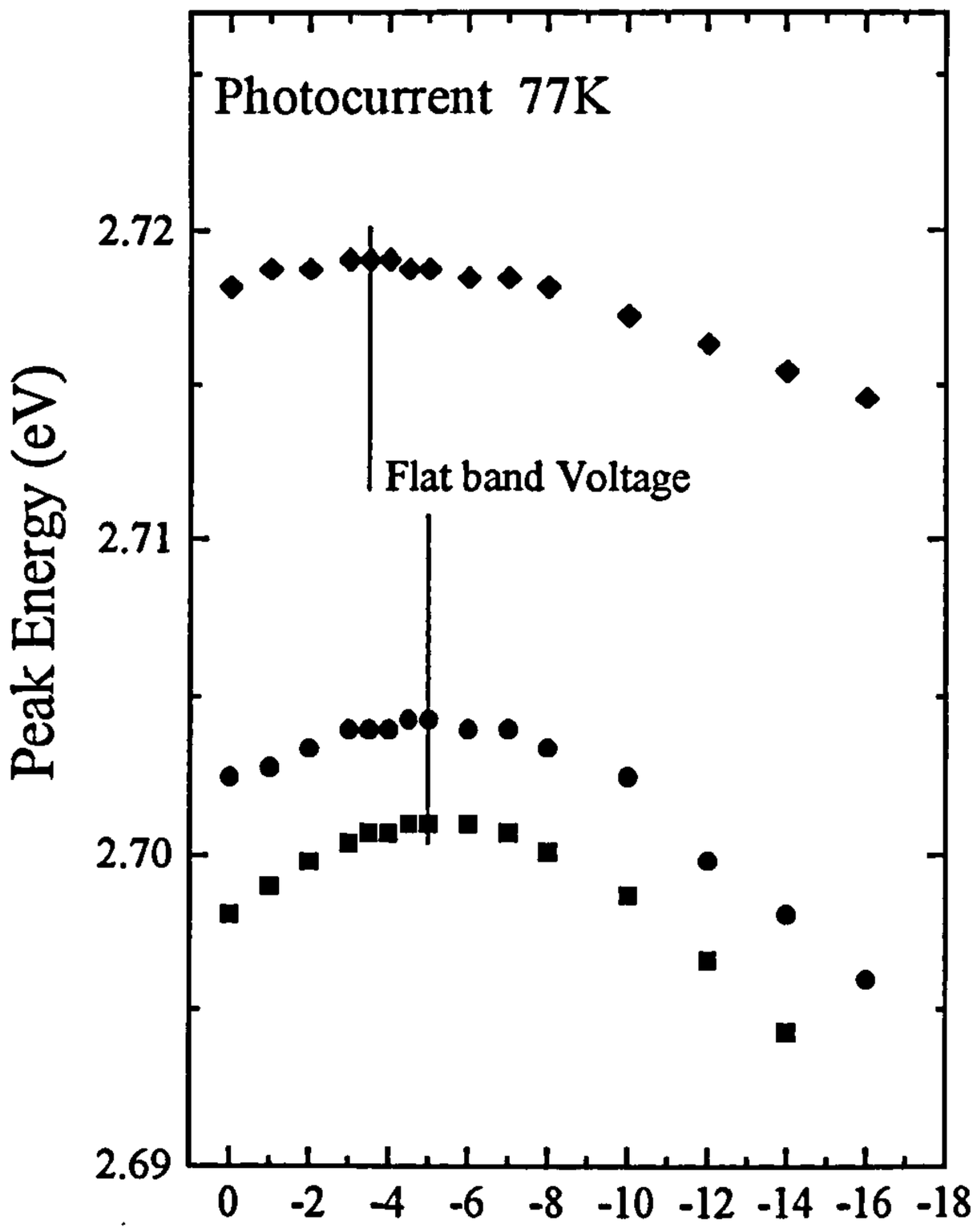

Figure 4-8. *Shift of the e1hh1 transition as a function of external bias for the 4nm (◆), 6nm (●) and 8nm (■) single quantum well piezo structures as measured by photocurrent spectra.*

If we examine the photocurrent results in figure 4-8 we see that for the 6nm and 8nm quantum well samples the flat band voltages are the same while the 4nm quantum well gives a somewhat smaller value which can be accounted for by a slightly lower cadmium content. Any decrease in the Cd percentage will result in a smaller lattice mismatch with the ZnSe buffer layer and so the strain will be reduced giving a decrease of the internal field, as observed. The values for the cadmium percentage in

the well layer were estimated from the Zn / Cd flux ratio during growth and an approximation of their accuracy is given in table 4-1.

Table 4-1. *Sample details and photocurrent experimental data of the single quantum well piezo structures.*

Well width (nm)	4	6	8
Cadmium % (±1)	11.8	13.1	12.4
Piezoelectric shift (meV)	0.9	1.8	2.9
Flat band voltage in quantum well (V)	-4.9	-6.4	-6.4

The flat band voltage for the 6nm and 8nm quantum well is obtained at an applied voltage of -5V. If the epilayer in the Schottky junction is completely depleted, the external field strength can be calculated from equation (4-2).

$$F_{ext} = (V_b + V_i) / d \qquad (4\text{-}2)$$

V_b is the external bias voltage, V_i is the built-in voltage of the gold / ZnSe contact measured at about -1.4V [7], and d is the total thickness of the epilayer. Therefore the real flat band voltage is -6.4V. At the flat band condition for the quantum well, the piezoelectric field is equal and opposite to the external field, i.e. $F_{piezo} = -F_{ext}$. Consequently the piezoelectric field is easily determined from the flat band voltage and the values for each well are given in table 4-2. As a comparison, values calculated from

the theoretical predictions of equation (3-35) are shown, and they show good agreement. Given the uncertainties of the values involved, a value of 0.42V/μm (±0.03) per percent of cadmium in the well is proposed. Equation (3-35) predicts a value of 0.39V/μm.

Table 4-2. *Data calculated from the experimental data of the single quantum well piezo structures.*

Well width (nm)	4	6	8
Piezoelectric field (V/μm) (±0.5)	4.4	5.8	5.8
Theoretical field (V/μm)	4.15	4.55	4.33
Piezo field per Cd% (V/μm/Cd%) (±0.08)	0.37	0.44	0.47

Although the well width does not affect the magnitude of the flat band voltage, it does influence the size of the piezoelectric shift of the excitonic transitions. As the results indicate, the blue shift of the excitonic transitions increases with the well width because, while the tilt of the quantum well band edge is the same regardless of well width, a larger well allows a greater energy displacement of the sub-bands within the well and so allows the electron and hole sub-bands to move closer together, as seen in figure 4-9. This is also illustrated in the dependence of the shift on L_w, the well width, shown by equation (3-37).

It was expected that the shift in the larger wells would have been smaller than predicted due to a reduction in the exciton binding energy in the well at zero bias. This is due to the lower wavefunction overlap that would occur in a wide well under a net electric field compared to a narrower well, see figure 4-9. This would increase the energy of the transition at zero bias, thereby reducing the observable shift, as the binding energy would be restored to normal at the flat band condition. However, the results in table 4-1 indicate that this relationship is quasi-linear, therefore this effect is too small to be detected.

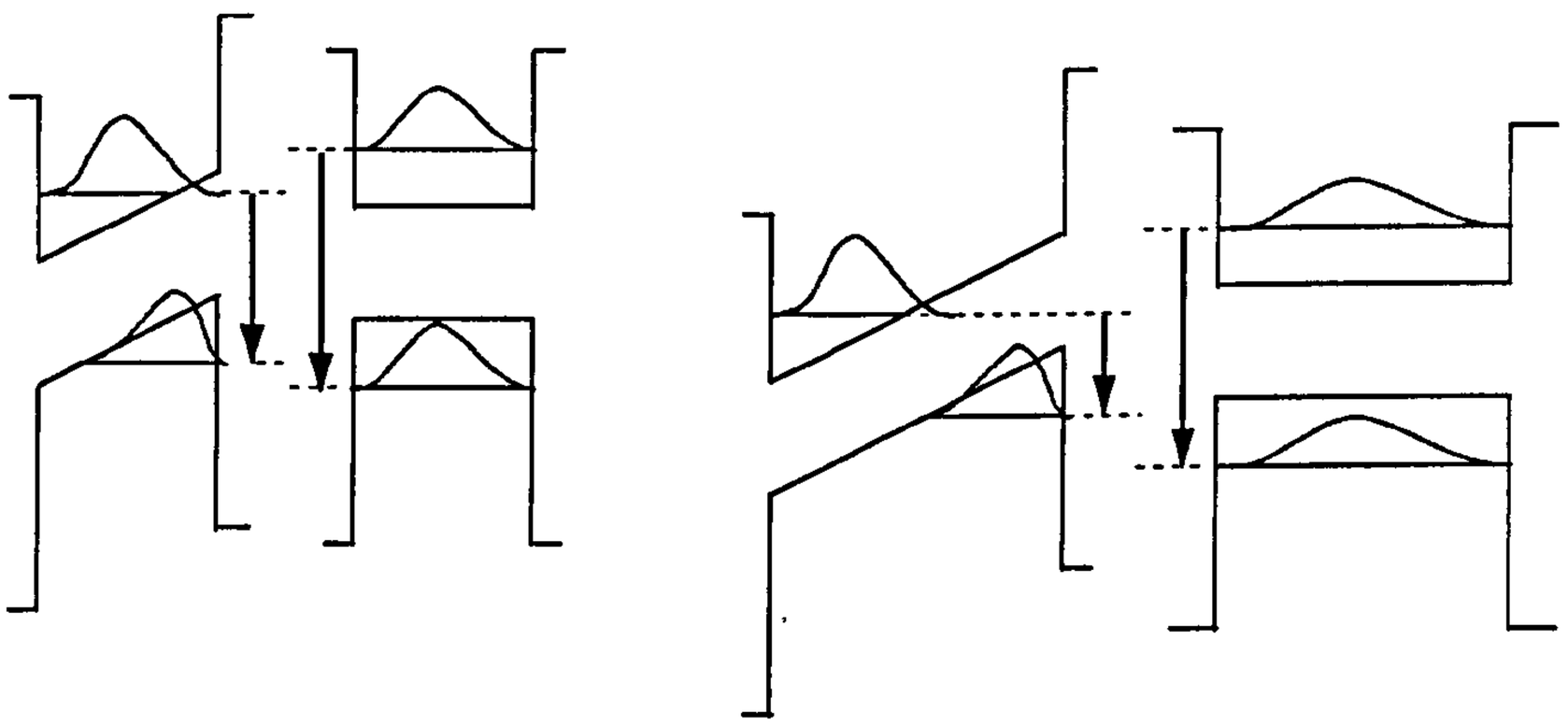

Figure 4-9. *The effect of the well width on the size of the piezoelectric shift and also on the wavefunction overlap in the energy levels.*

2.2.5. Transition identity.

At zero bias the spectrum for the 8nm well shows four transitions. A model using an 8×8 **k·p** method to calculate the band structure of $Zn_{1-x}Cd_xSe$ / ZnSe quantum wells grown on the (001) plane gives the band structure transition for an 8nm well with x=0.124 as shown on figure 4-10 [8]. Therefore it is possible to calculate the difference in energy of each transition from e1hh1 and the values are given in table 4-3. Every transition observed in figure 4-5 has an energy split close to one of these theoretical values, therefore table 4-3 also shows the experimental results proposed for each transition identity.

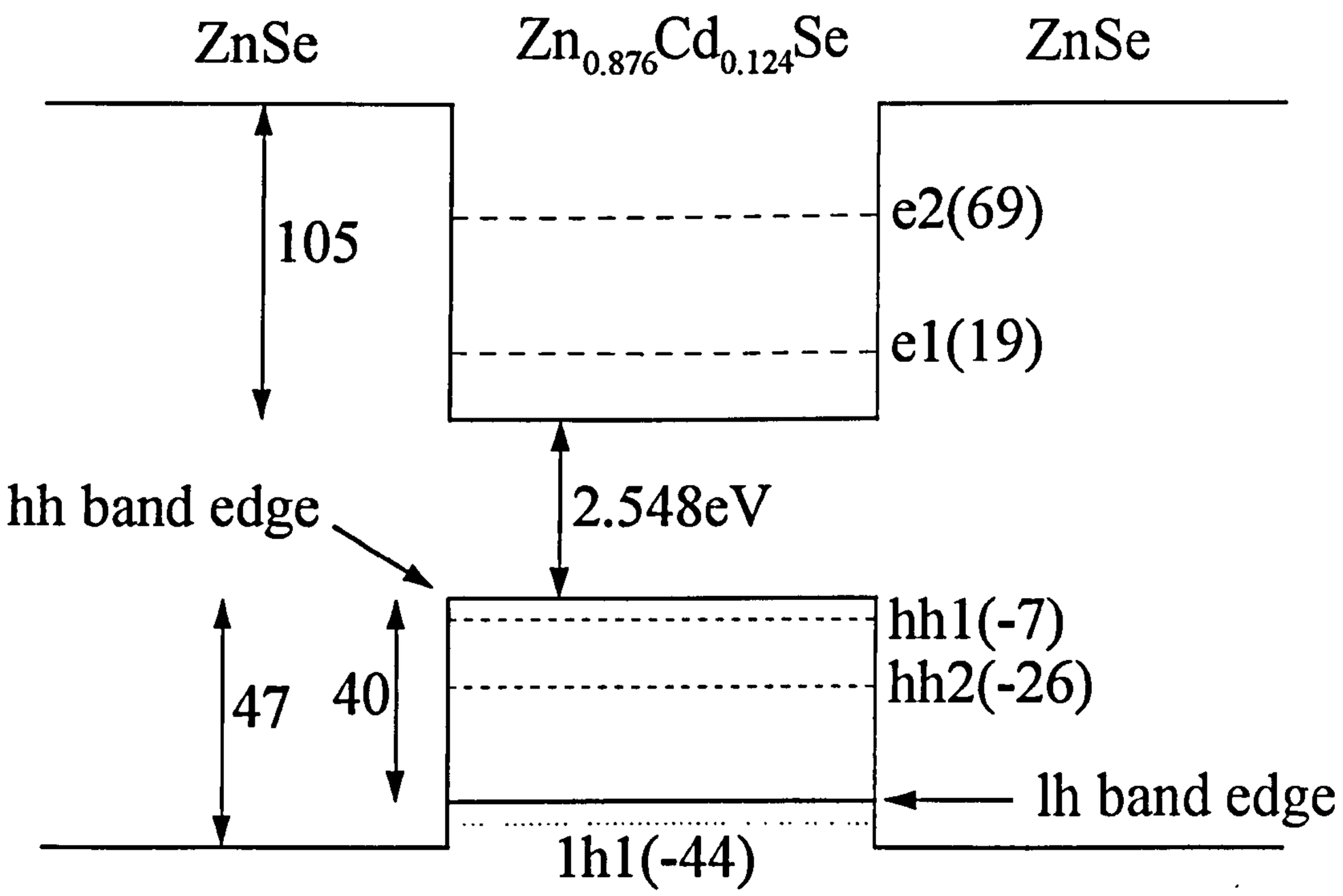

Figure 4-10. *Band structure for an 8nm $Zn_{1-x}Cd_xSe$ / ZnSe with x=0.124 grown on the (001) plane calculated from an 8×8 **k·p** model. All values are in meV, unless denoted otherwise.*

Table 4-3. ***k·p** model theoretical energy differences from the e1hh1 transition for an 8nm $Zn_{1-x}Cd_xSe$ / ZnSe quantum well with x=0.124 grown on the (001) plane, and suggested experimental values for each transition from the (211) 8nm sample.*

Transition	Energy difference from e1hh1(meV)	Suggested experimental differences (meV)
e1hh2	19	15
e1lh1	37	36
e2hh1	50	52
e2hh2	69	-
e2lh1	87	-

Hensel *et al.* [9] found that the band energy splitting of the heavy and light hole states was nearly independent with respect to the growth direction. This can be confirmed as the same **k·p** model has been adapted for the calculations on quantum well layers grown on the (111) plane [8]. Table 4-4 gives theoretical values for the energy differences between e1hh1 and four other transitions for 8nm wells of various cadmium contents for growth on the (001) and (111) planes.

Table 4-4. *k·p model theoretical energy differences from the e1hh1 transition for an 8nm $Zn_{1-x}Cd_xSe$ / ZnSe quantum well for various cadmium contents for layers grown on the (001) and the (111) plane.*

(001) Growth	Energy difference from e1hh1 (meV)			
Cadmium %	e1hh2	e1lh1	e2hh1	e2hh2
10	17	30	45	-
15	20	47	54	74
20	21	61	60	81

(111) Growth	Energy difference from e1hh1 (meV)			
Cadmium %	e1hh2	e1lh1	e2hh1	e2hh2
10	-	-	-	-
15	-	-	56	-
20	30	-	65	95

This establishes that the alignment of the growth plane has only a small effect on the energy differences. The gaps in the table are where the transition involves an energy state that is not confined, due to the strong field in (111) strained layers. It is assumed that all the required energy states are confined for the layers on the (211) plane as it has a lower electric field. Since the (211) plane lies between the (001) and

(111) planes we consider the values in table 4-3 to be valid for the wells grown on (211). These figures show good agreement with the spectrum leading to the labelling of the transitions suggested in table 4-3 and shown on figure 4-11.

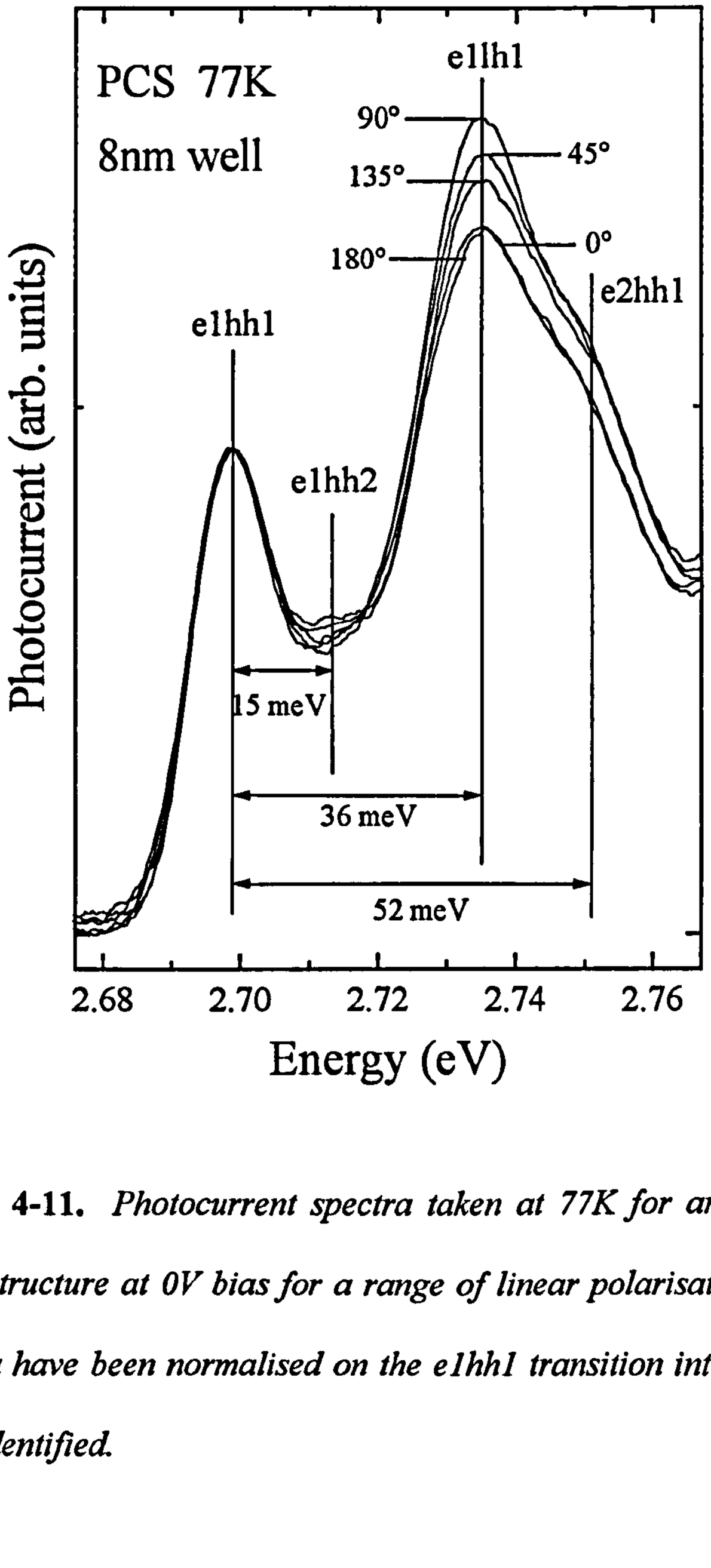

Figure 4-11. *Photocurrent spectra taken at 77K for an 8nm single quantum well piezo structure at 0V bias for a range of linear polarisations of the input light. The spectra have been normalised on the e1hh1 transition intensity. The transitions have been identified.*

It has previously been shown that forbidden transitions ($\Delta n \neq 0$) are observed in asymmetric well profiles while the allowed transitions ($\Delta n = 0$) are weakened [10]. Therefore the identifications on figure 4-11 are consistent with figure 4-5 : the oscillator strengths of the two allowed transitions (e1hh1 and e1lh1) increase as the flat band is reached while the e1hh2 transition becomes strictly forbidden but then reappears at a bias of -14V. The e2hh1 transition is masked by the shift of the bulk ZnSe band edge at any bias of -2V or more, so no conclusion can be drawn from its oscillator strength variation, other than that it exists when the well is under a net electric field.

Finally, a further confirmation of the light hole nature of the e1lh1 transition is shown in figure 4-11 by the linear polarisation dependence of this transition when normalised against a heavy hole transition, due to the specific symmetry character of the heavy and light hole states, as observed in InAs / GaAs quantum wells by Brandt *et al.* [11]. They used linear polarisation in PLE experiments to selectively excite light and heavy hole states. The anisotropy shown in figure 4-11 is weak which is due to the excitation geometry being off-axis from the growth plane. However, the cyclic nature of the results (i.e. the oscillator strength is increased as the polarisation angle is increased from 0° to 90° and then returns to the same level at 180°) indicates that this effect is unlikely to be random.

4.3. Photoluminescence excitation.

4.3.1. Introduction.

Photoluminescence excitation (PLE) also provides an absorption curve but differs from photocurrent in that it has a higher resolution because the light source is a laser and not a broad white light passed through a monochromator. It also relies on the process of photoluminescence (PL) (see chapter 5) to provide the output. Again, the piezoelectric effect will be demonstrated by applying an external bias. PLE has previously been performed on piezoelectric structures [12,13,14], but never with an applied bias.

Briefly, photoluminescence occurs when a semiconductor is illuminated with light which has photons with a higher energy than the band gap. To maximise the PL, the incident radiation should provide photons with an energy at around the absorption maximum, e.g. for ZnSe, the 351nm (about 3.53eV) line on an Ar^+ laser is used. When the photons are absorbed an electron is excited to the conduction band leaving a hole in the valence band. The electron then decays to the lowest possible level in the conduction band through non-radiative processes. Radiative recombination then takes place and a photon is emitted and detected by the experiment. Aspects of PL will be explored in more detail in chapter 5.

PLE provides an absorption curve by varying the energy of the excitation photons while monitoring the PL output. As shown in chapter 3, the absorption curve

for a quantum well has a step-like feature, so when the excitation photon energy is the same as that of an allowed absorption transition, a peak will occur in the PL output.

4.3.2 Experiment.

The experimental set-up is a minor variation on the PL set-up and is shown on figure 4-12.

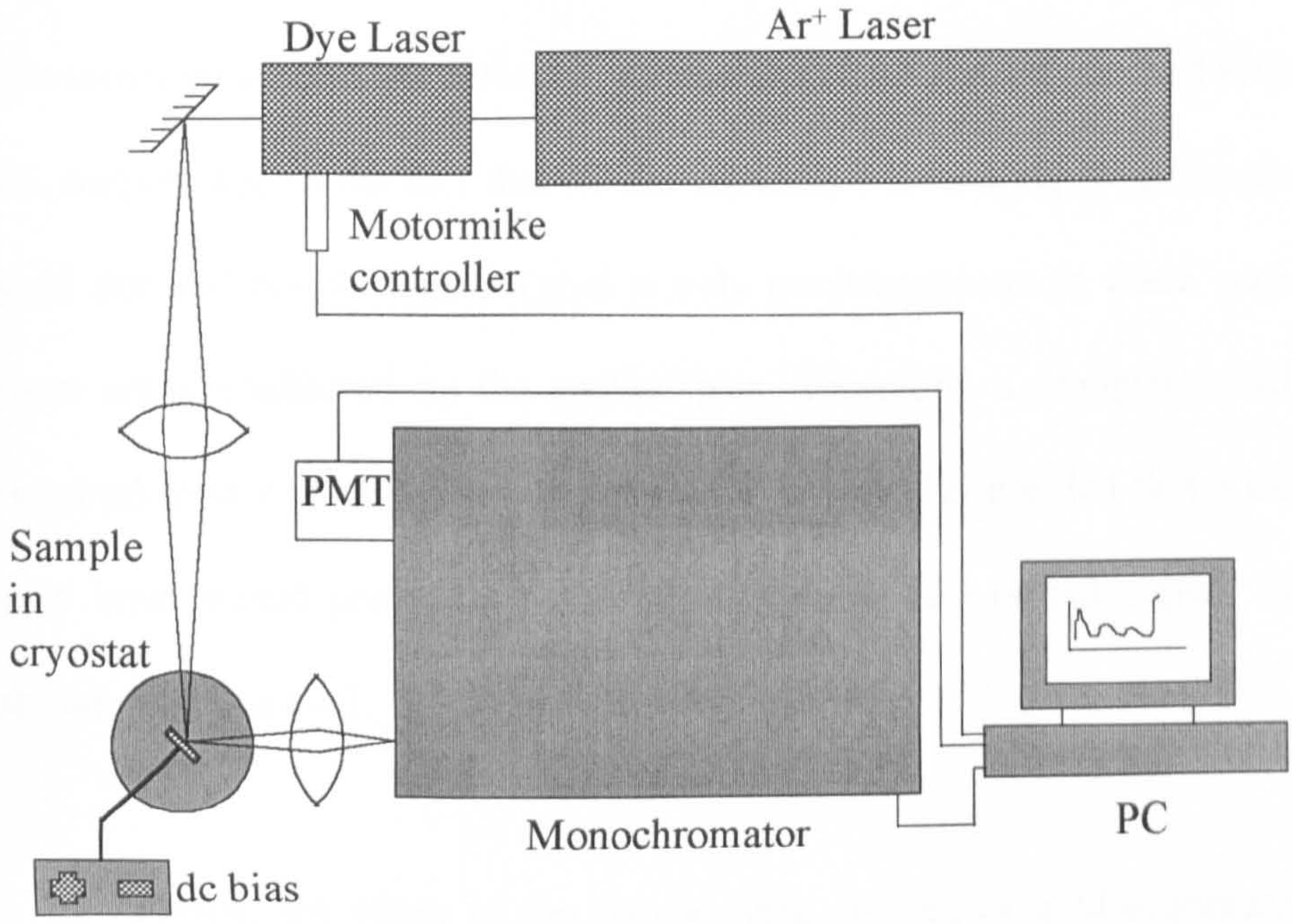

Figure 4-12. *PLE experimental set-up.*

The PC controls data acquisition from the detector, a photomultiplier tube (PMT), the position of the monochromator through a stepping motor and the wavelength emitted by the dye laser. The variation of the wavelength of the excitation source requires a tuneable laser over the desired range. This experiment needs to scan

from the quantum well PL emission (in this case, about 460nm) to the ZnSe band edge (about 440nm) to cover all the confined states in the well. The source used was an optically pumped dye laser, and the dye used was Stilbene 3, which has an wavelength output between 420nm and 470nm. Fortunately, this dye is pumped by the 351nm line of the Ar^+ laser, the same as for normal PL experiments. The output wavelength of the dye laser is controlled by rotating a birefringent filter within the laser cavity which uses polarisation and phase to set a wavelength condition.

Early experiments attempted to use the same gold contacts that were used in the photocurrent section. However, it was found that an applied bias had little effect on the PL output, due to the fact that all the emission was coming from the area around the gold dot and not through it (gold is only semitransparent at these wavelengths), *i.e.* from areas unaffected by the applied bias. Therefore, a complete gold contact was required to provide a uniform external bias. It was also decided that a thin track in the gold layer would provide a much stronger input and output signal. The details are shown in figure 4-13.

Finally, the edges of the sample were cleaved as gold evaporated around the edge would short circuit any applied bias through to the substrate. The sample used in this experiment was the same 8nm single quantum well used in the photocurrent section.

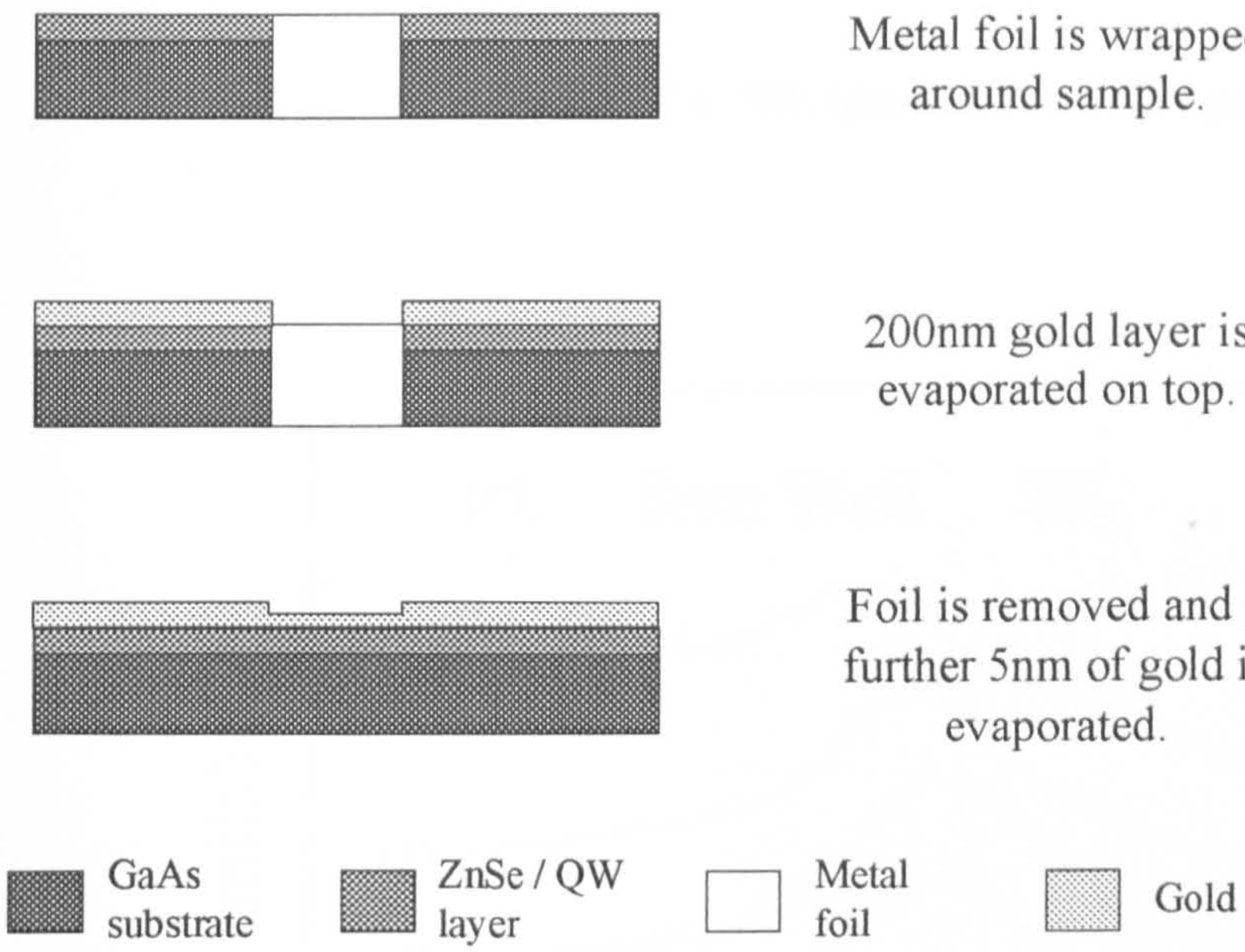

Figure 4-13. *Gold contact process for applying a bias in PL and PLE experiments.*

4.3.3. Results.

In the PLE experiments, the first procedure was to take a PL scan of the quantum well to ensure that the detection during the PLE is maximised. When an external bias was applied, the energy of the PL emission was shifted (as expected) so a new PL scan was taken for each PLE scan, and these are shown on figure 4-14.

It is convenient to start the PLE scan at the low energy end, as this is where the monochromator will be positioned. It is common practice to place a strong neutral density filter before the monochromator (in this case, a 10^4 and a 10^2 filter were both used) until the excitation source has passed the PL emission energy of the quantum

well. This protects the PMT detector (which would not survive having a direct laser on its surface) and also provides a useful calibration for the scan. This explains the sharp peak at the beginning of each of the PLE spectra shown on figure 4-15.

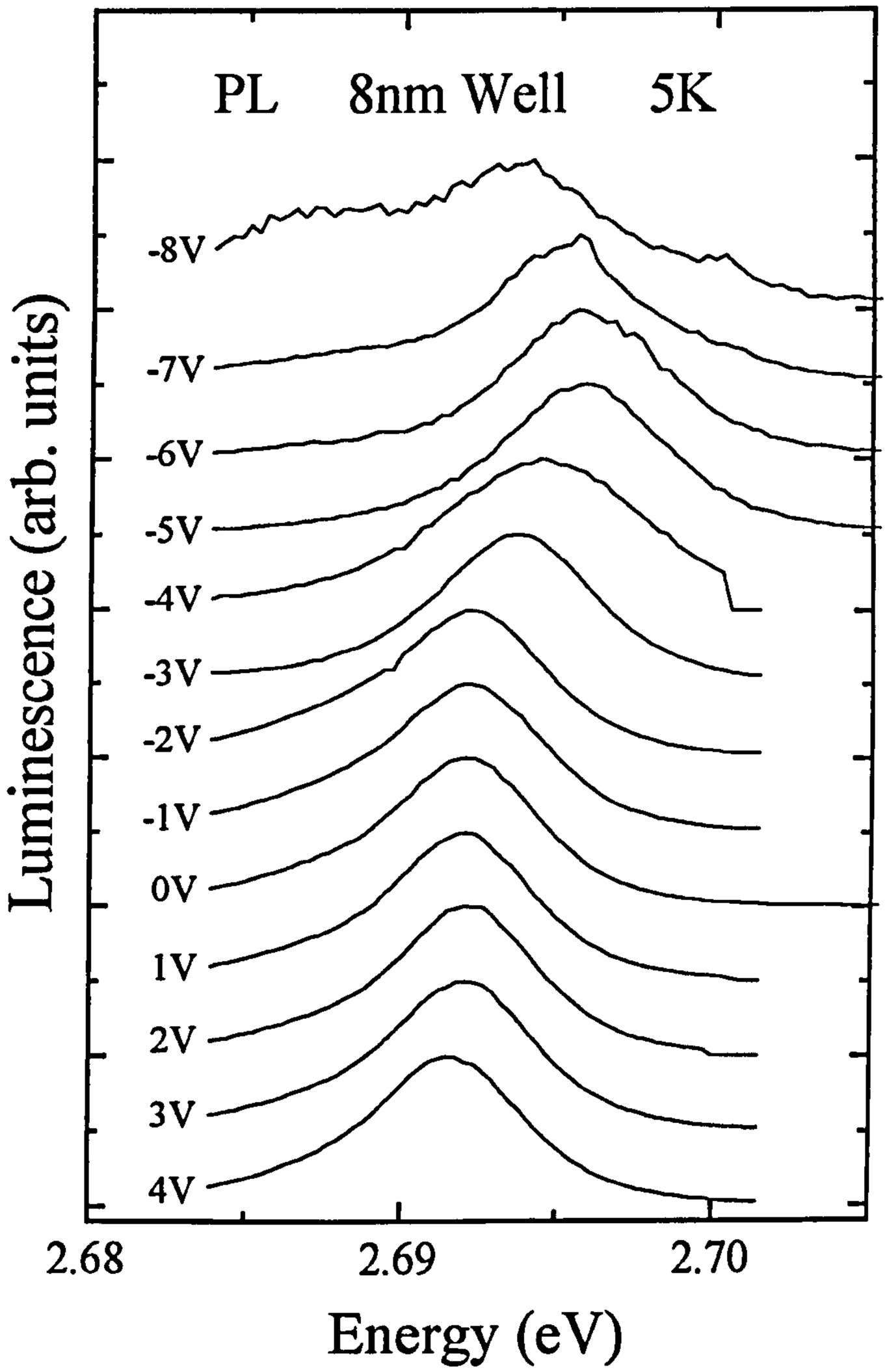

Figure 4-14. *PL spectra taken at 5K for an 8nm single quantum well piezo structure for a range of external bias values. The spectra have been normalised. The excitation wavelength was ≅438nm.*

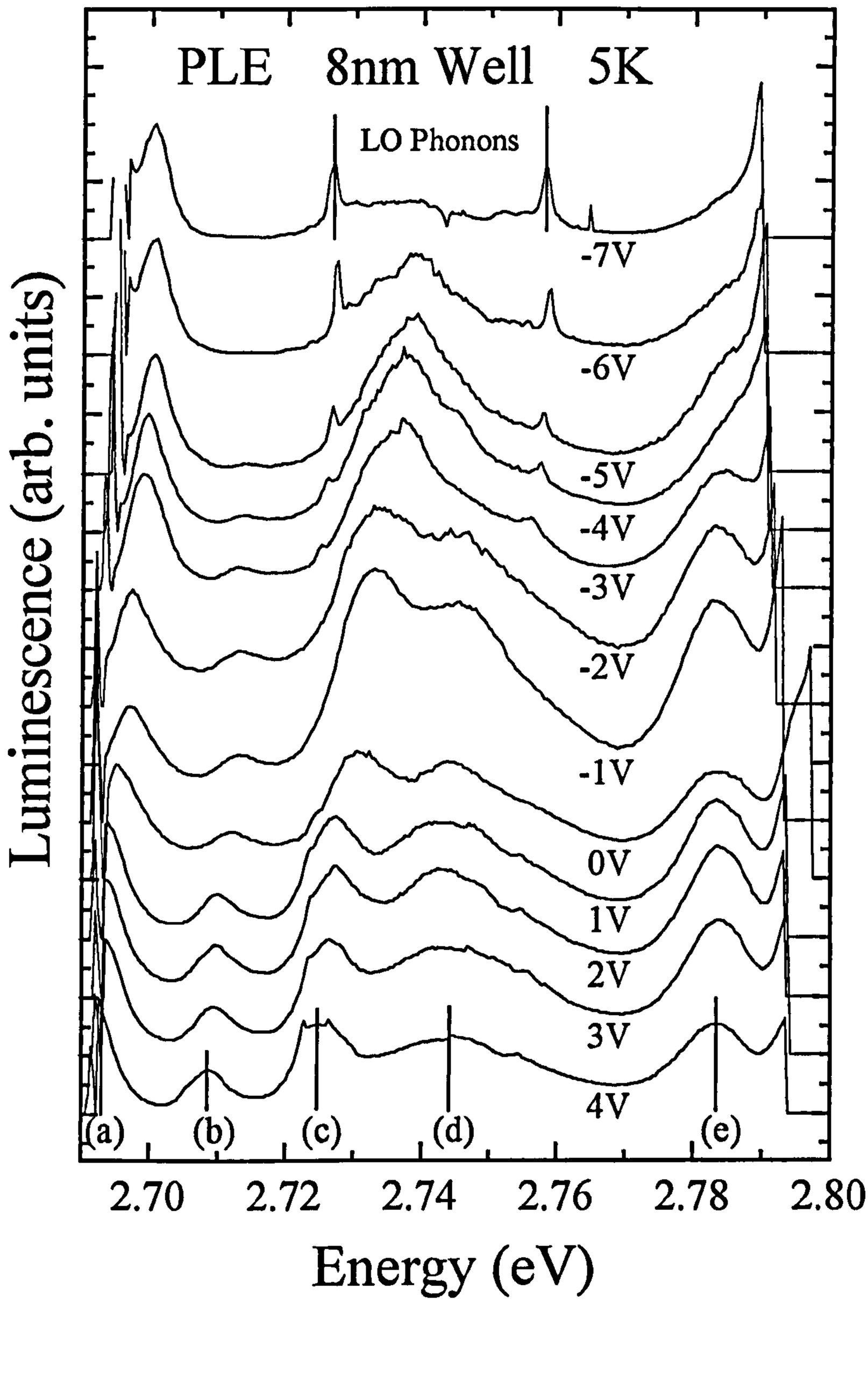

Figure 4-15. *PLE spectra taken at 5K for an 8nm single quantum well piezo structure for a range of external bias values. The spectra have been normalised to the height of the e1hh1 peak* (a).

As with the photocurrent, the characteristic blue shift and then red shift is seen in the e1hh1 transition (a). The maximum blue shift is found at an external bias of -5V, virtually the same as found with the photocurrent. The shift of the PL emission and the e1hh1 PLE peaks with applied bias are shown on figure 4-16.

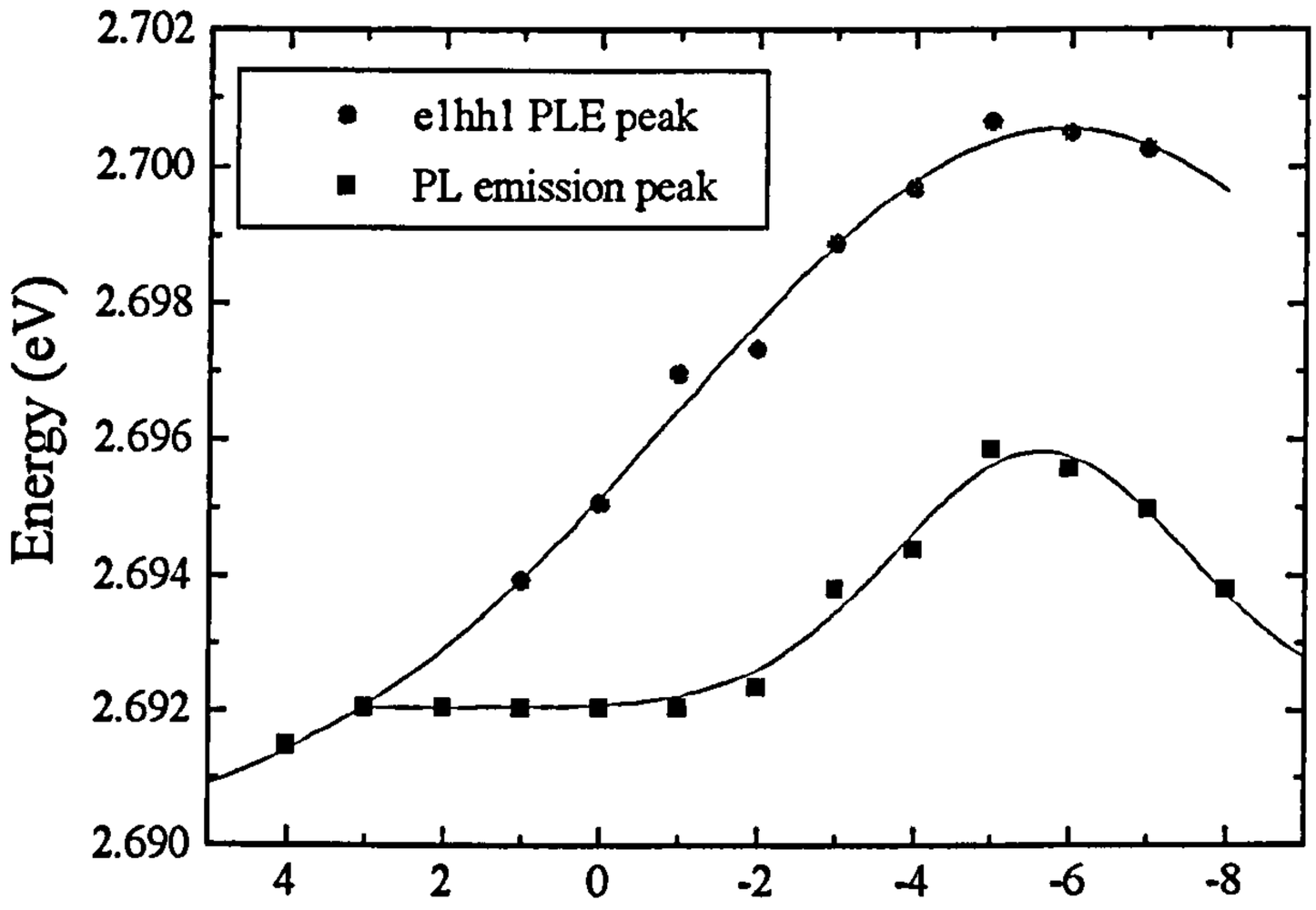

Figure 4-16. *Shift of the PL emission peak and the e1hh1 PLE peak with applied bias for an 8nm single quantum well piezo structure. This figure is discussed further in chapter 5.*

4.3.4. Discussion.

Due to the greater detail allowed by PLE there are now five distinguishable transitions in the spectra, labelled (a) to (e) on figure 4-15. The average difference

between each transition and e1hh1 were calculated (when possible) and are shown in table 4-5, along with the theoretical results from table 4-3, all of which show good agreement. One strange feature of the PLE spectra is the non-appearance of the e2hh2 transition. This may be due to the transition being dominated on either side by forbidden transitions (e2hh1 and e2lh1) when the well is tilted, and when the flat band is reached (at -5V bias) the transition is lost in the shift of the bulk ZnSe.

Table 4-5. ***k·p** model theoretical energy differences from the e1hh1 transition for an 8nm $Zn_{1-x}Cd_xSe$ / ZnSe quantum well with x=0.124 grown on the (001) plane, and mean experimental differences for each transition from the PLE results.*

Transition	**k·p** model theoretical energy difference from e1hh1(meV)	PLE experimental differences from e1hh1(meV)
e1hh2 (b)	19	15.2
e1lh1 (c)	37	36.8
e2hh1 (d)	50	48.5
e2hh2	69	-
e2lh1 (e)	87	87.2

The PLE spectra give a better indication of the relative oscillator strengths of the transitions at each bias value. These results confirm what was suggested in the

photocurrent section : the forbidden transitions (b) and (d) are reduced in strength as the flat band condition is approached while the allowed transitions (a) and (c) are increased. The nature of transition (e) is difficult to describe due to the shift in the ZnSe absorption at high reverse bias.

As with the photocurrent studies, it is possible to provide a confirmation of the transition identity through a polarisation study. In this case the circular polarisation effect was studied. It has been shown that the dipole nature of the electron orbitals in the valence band (a p-orbital) and the conduction band (an s-orbital) and the difference in the angular momentum states between the heavy hole and light hole states leads to selection rules for the nature of the light associated with interband transitions, be it absorption or emission [15]. As a consequence it is possible to distinguish between light and heavy hole transitions by polarising the excitation source in PLE and then altering the sign, i.e. switching from left- to right-circularly polarised light. Circularly polarised light can be produced by a Fresnel rhomb as shown in figure 4-17.

The importance of the Fresnel rhomb is that it will maintain the circular polarisation of the output light over a range of wavelengths, because the two 45° retardations are due to an internal reflection at a particular angle, which is pre-designed to fit the refractive index of the rhomb. The refractive index of a material only experiences small changes with wavelength, so this condition will be maintained over a reasonable wavelength range. Circularly polarised light produced by linear polarisers and quarter-wave ($\lambda/4$) plates would however be unsuitable for this experiment, as $\lambda/4$

plates are strictly designed for a particular wavelength. They may of course be used to polarise the input in a simple luminescence experiment.

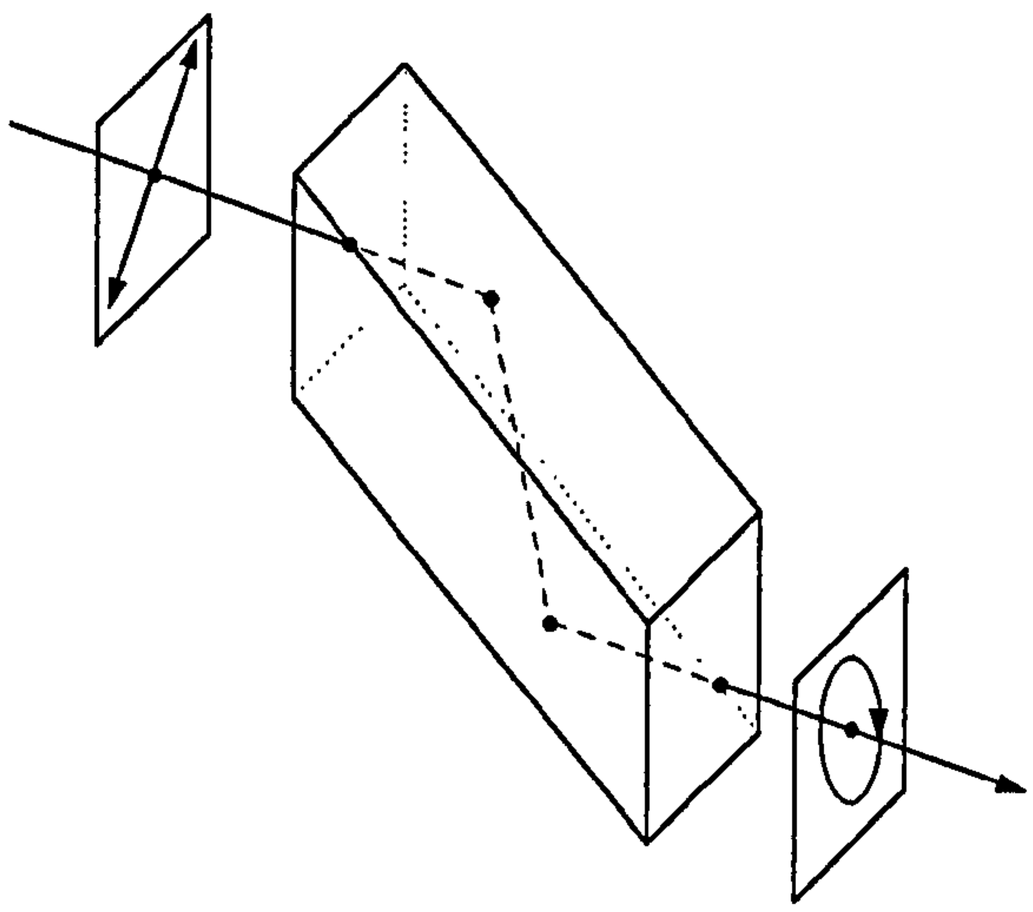

Figure 4-17. *The Fresnel rhomb causes the initial beam (linearly polarised at 45°) to be internally reflected twice, thereby imparting a 90° relative phase shift to its components and generating circularly polarised light. Left- and right-circularly polarised light is selected by rotating the linear polariser by 90°* [16].

A linear polariser and the Fresnel rhomb were positioned in front of the cryostat and the beam was adjusted to compensate for the offset. A PLE scan was performed (with no applied bias) and then repeated after rotating the linear polariser by 90°. The results are shown on figure 4-18. The variation in height of the third transition confirms its light hole nature.

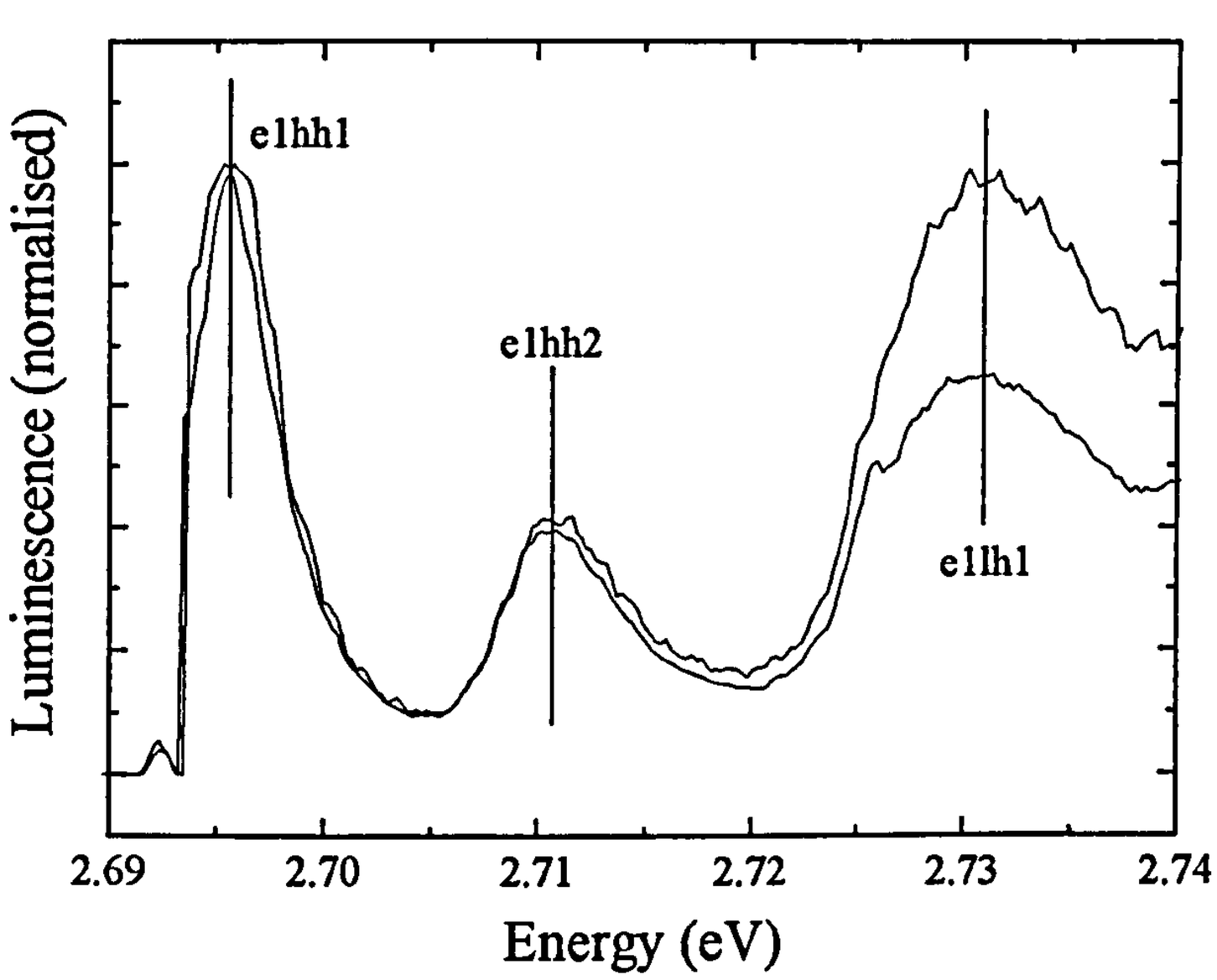

Figure 4-18. *PLE spectra taken at 5K for an 8nm single quantum well piezo structure with no applied bias using left- and right-circularly polarised light. The spectra have been normalised to the height of the e1hh1 peak.*

The identity of transition (e), proposed as e2lh1, can be validated by comparing the direct experimental values for its transition energy and values calculated from the other transition energies (where available) by the equation

$$E_2LH_1 = E_2HH_1 + (E_1LH_1 - E_1HH_1) \qquad (4\text{-}3)$$

The values are given in table 4-6 and show good agreement.

Table 4-6. *Comparison of energy values for the e2lh1 transition from direct measurement and calculated from the values of other transitions.*

Bias voltage (V)	Transition energy (eV) (direct measurement)	Transition energy (eV) (calculated measurement)	Difference between direct and calculated values (meV)
1	2.7835	2.7770	6.5
0	2.7836	2.7799	3.7
-1	2.7832	2.7811	2.1
-2	2.7836	2.7815	2.1

There is one final feature of the PLE scans not yet discussed and that is the sharp pair of transitions that first appear at -3V bias and then increase in intensity as the reverse bias is increased until they dominate the spectra at -7V. These may be due to resonant Raman scattering, but may also be transitions known as LO (longitudinal - optic) phonon replicas and are indicated as such on figure 4-15. Phonons are lattice vibrations that travel through a crystal lattice in either transverse (the molecules oscillate at right-angles to the direction of the vibration wave) or longitudinal (the molecules oscillate in the direction of the vibration wave) modes. In the model of a chain of alternately large and small atoms, it was found that the lattice vibrations formed two branches, optic and acoustic [17]. The optic branch is given this name because of its ability to interact with light.

As will be explained in chapter 5, electrons that are excited across the band gap lose energy through non-radiative interactions until they reach the bottom of the conduction band. These interactions may well be phonon related, and LO phonon replicas are commonly observed in PLE experiments because of the variation in the excitation source. If the difference between the energy of the excitation photons and the detection wavelength (set near the band gap) is an integral number of LO phonon energies, then a resonance will occur and there will be a increase in the output intensity. This is illustrated on figure 4-19.

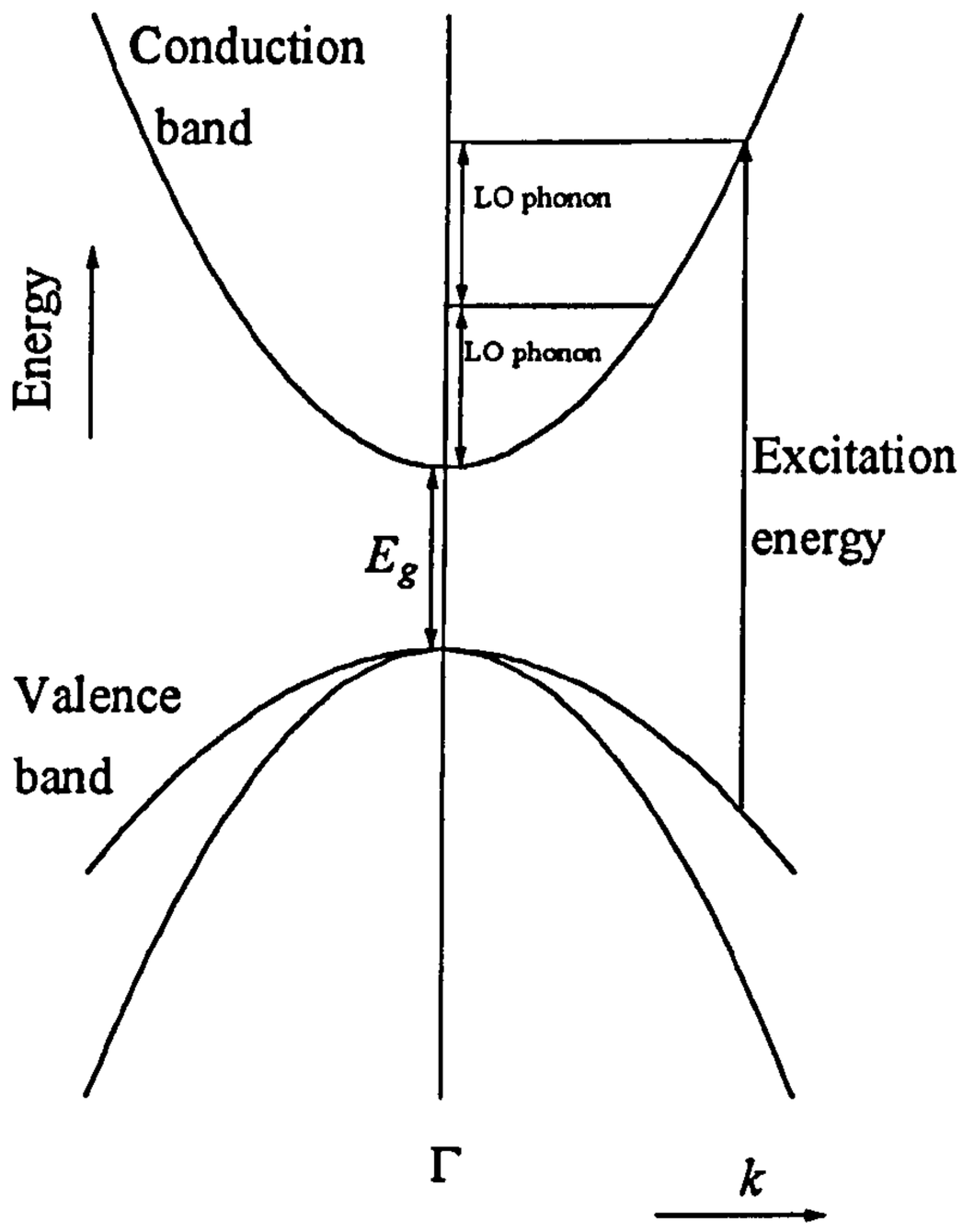

Figure 4-19. *Band structure of ZnSe showing the mechanism of the LO phonon replica in a PLE experiment.*

The LO phonons observed on figure 4-15 occur at intervals of about 31.3meV which is very close to the documented value of 31meV for the LO phonon in ZnSe

[18]. The phonon transitions become more prominent because the intensity of the PLE spectra dropped off rapidly as the reverse bias was increased, and so it is difficult to determine the nature of the PLE transitions in the -7V scan.

4.4. Conclusion.

The piezoelectric effect has been investigated in ZnCdSe / ZnSe single quantum wells by photocurrent spectroscopy and PLE spectroscopy. The internal field was calculated from the flat band condition in the quantum wells. From the results a value of 0.42V/μm (±0.03) per percent of cadmium in the well layer is proposed. The well width produces an effect on the piezoelectric shift but has no effect on the flat band voltage. The transitions were unambiguously identified using an 8×8 **k·p** model which was consistent with a polarisation study and the variation in oscillator strengths of the transitions.

4.5. References.

[1] S.Y. Wang, Thesis of Heriot-Watt University, Edinburgh, 1994.

[2] E.A. Caridi, T.Y. Chang, K.W. Goossen and L.F. Eastman, Appl. Phys. Lett. **56**, 659 (1990).

[3] A.S. Pabla, J.L. Sanchez-Rojas, J. Woodhead, R. Grey, J.P.R. David, G.J. Rees, G. Hill, M.A. Pate, P.N. Robson, R.A. Hogg, T.A. Fisher, A.R.K. Willcox, D.M. Whittaker, M.S. Skolnick and D.J. Mowbray, Appl. Phys. Lett. **63**, 752 (1993).

[4] J.L. Sanchez-Rojas, A. Sacedón, F. González-Sanz, E. Calleja and E. Muñoz, Appl. Phys. Lett. **65**, 2042 (1994).

[5] S.Y. Wang, P.J. Thompson, G. Horsburgh, T.A. Steele, G.D. Brownlie, K.A. Prior and B.C. Cavenett, J. Cryst. Growth **159**, 459 (1996).

[6] D.L. Smith and C. Mailhiot, J. Appl. Phys. **63**, 2717 (1988).

[7] B.A. Morgan, K.M. Ring, K.L. Kavanagh, A.A. Talin, R.S. Williams, T. Yasuda, T. Yasui and Y. Segawa, J. Appl. Phys. **79**, 1532 (1996).

[8] M. Livingstone, Thesis of Heriot-Watt University, Edinburgh, 1996.

[9] J.C. Hensel and G. Feher, Phys. Rev. **129**, 1041 (1963).

[10] R.A. Hogg, T.A. Fisher, A.R.K. Willcox, D.M. Whittaker, M.S. Skolnick, D.J. Mowbray, J.P.R. David, A.S. Pabla, G.J. Rees, R. Grey, J. Woodhead, J.L. Sanchez-Rojas, G. Hill, M.A. Pate and P.N. Robson, Phys. Rev. B **48**, 8491 (1993).

[11] O. Brandt, H. Lage and K. Ploog, Phys. Rev. B **45**, 4217 (1992).

[12] G. Duggan, K.J. Moore, A. Raukema, G.T. Jaarsma and K. Woodbridge, Phys. Rev. B **45**, 4494 (1992).

[13] M. Ilg, M.I. Alonso, A. Mazuelas, E. Tournié and K.H. Ploog, J. Cryst. Growth **150**, 482 (1995).

[14] H.Q. Hou and C.W. Tu, J. Appl. Phys. **75**, 4673 (1994).

[15] C. Weisbuch and B. Vinter, *Quantum Semiconductor Stuctures*, Academic Press (1991).

[16] E. Hecht, *Optics*, (2nd edition), Addison-Wesley (1987).

[17] G. Burns, *Solid State Physics*, Academic Press (1985).

[18] S.S. Mitra, Phys. Rev. **132**, 986 (1963).

5. EMISSION SPECTROSCOPY OF PIEZOELECTRIC QUANTUM WELLS.

5.1. Introduction.

In this chapter the influence of the piezoelectric effect on the photoluminescence (PL) emission spectra of single quantum wells grown on (211) substrates and the resulting effect on the localisation of carriers will be studied. The first section will illustrate the effect on the PL by the application of an external bias, as in chapter 4, and the second section will demonstrate the screening of the piezoelectric field by the production of free carriers.

While there are many forms of luminescence (e.g. electroluminescence, cathodoluminescence) this chapter is only concerned with photoluminescence which occurs when the electron-hole pair is created by optical excitation. If the energy band structure of a semiconductor as summarised in chapter 1 is considered, the dynamics of photoluminescence can be explained. If the material is at very low temperature and the electrons are excited by optical stimulation with sufficient energy (*i.e.* greater than the band gap) they will cross the band gap and occupy the conduction band, leaving holes in the valence band. The electrons will then decay through non-radiative processes (they can lose energy through phonon interactions which is dissipated through lattice

vibrations) to the lowest energy level in the conduction band, after which the annihilation of the electron-hole pair results in the emission of a photon.

To consider luminescence it is important to understand the excitonic effect mentioned in chapter 3. If an electron and a hole are in close proximity then there is a Coulombic attraction between them. This bound pair has less energy than an electron and a hole isolated from each other, therefore their energy is less than that of the band gap. Electrons and holes orbit each other as in a hydrogen-like atom, and in semiconductors excitons are free to move through the material. The Bohr model of the Hydrogen atom states that the energy of an electron in a quantised orbit around the proton nucleus is :

$$E_n^H = -A\frac{m_H}{\varepsilon_0^2 n^2} \tag{5-1}$$

where

$$m_H = \frac{m_e m_p}{m_e + m_p} \tag{5-2}$$

m_e and m_p are the electron and proton masses respectively and A is a constant. This model can be adapted for the exciton by substituting the hole mass for the proton mass to give μ, the equivalent of m_H, and to consider the bulk dielectric constant ε_r with ε_0. Given that E_1^H = -13.6eV it is possible to simplify the exciton model as shown :

$$E_n^{ex} = -13.6\frac{\mu}{m_H \varepsilon_r^2}\frac{1}{n^2} \quad eV \tag{5-3}$$

As in the hydrogen atom model, the energy of the electron-hole pair varies as $1/n^2$ where n = 1,2,3... although only the lowest values of n are normally considered. Excitons will exist while the temperature is such that $E_b > kT$, where E_b is the exciton binding energy given by E_n^{ex} in equation (5-3) and is typically of the order of a few meV.

A further aspect to consider is that of impurities and defects in the crystal lattice. Even a low level of impurity in a semiconductor structure can completely dominate the luminescence spectrum. In the simplest case impurities are donors and / or acceptors where donors are atoms in the lattice which supply an extra electron (e.g. iodine replacing selenium atoms in ZnSe), while acceptors are atoms which have an electron missing (e.g. nitrogen replacing selenium atoms in ZnSe). There is also the possibility of isoelectronic impurities (e.g. tellurium replacing selenium atoms in ZnSe). Excitons are attracted to these impurities and become bound to them, thus lowering their energy once more, forming acceptor bound excitons ((A^0X), known as I_1) or donor bound excitons ((D^0X), known as I_2). In addition to the exciton spectra, if both donors and acceptors are present then electrons and holes recombine in the luminescence to produce donor-acceptor pair (DAP) emissions. For example, in the case of ZnSe which is naturally n-type [1], a DAP is observed when the material is p-doped by nitrogen. The DAP emissions often completely dominates any free or bound exciton emission. Structural defects in the crystal lattice also contribute to the luminescence as recombination sites with a reduced energy [2].

There are practical aspects of photoluminescence to be considered. When analysing a photoluminescence spectrum, it should always be remembered that it is a competitive process, with each possible emission process contesting the available electron-hole pairs. They will naturally emit with the lowest possible energy, although that particular mechanism may be limited (e.g. the number of impurities available) and so more than one emission is often observed. Finally, the intensity is greater at lower temperatures, first because excitons will exist and furthermore because excited electrons with very low thermal energy will be brought swiftly back to recombine with the holes. This is why most luminescence experiments are performed at low temperatures, as well as preventing any thermally excited electrons occupying the conduction band.

5.2. Application of external bias.

5.2.1. Introduction.

The application of an external bias in photoluminescence has not been extensively used in demonstrating the piezoelectric effect. Previously, if the presence of an internal field was to be shown in such a manner the most popular method was photocurrent (see chapter 4), although other methods have been tried such as electroreflectance [3], photoreflectance [4] or even photocapacitance [5]. This may be due to the practical difficulties and unusual results that are obtained, as will be demonstrated in this section. While there has been some research on this subject

[6,7,8], the only sustained body of work was by Sánchez-Rojas *et al.* [9] who began by studying the effects of an external bias on a multiple quantum well structure held in the intrinsic region of a p-i-n diode, fabricated with InGaAs / GaAs on a (111) substrate. They discovered the appearance of some unexplained extra transitions at certain bias values which they later attributed to coupling between wells [5], similar to reference 7. However, there has been no previous research on the effect of external bias on a single quantum well in an undoped piezoelectric structure by photoluminescence.

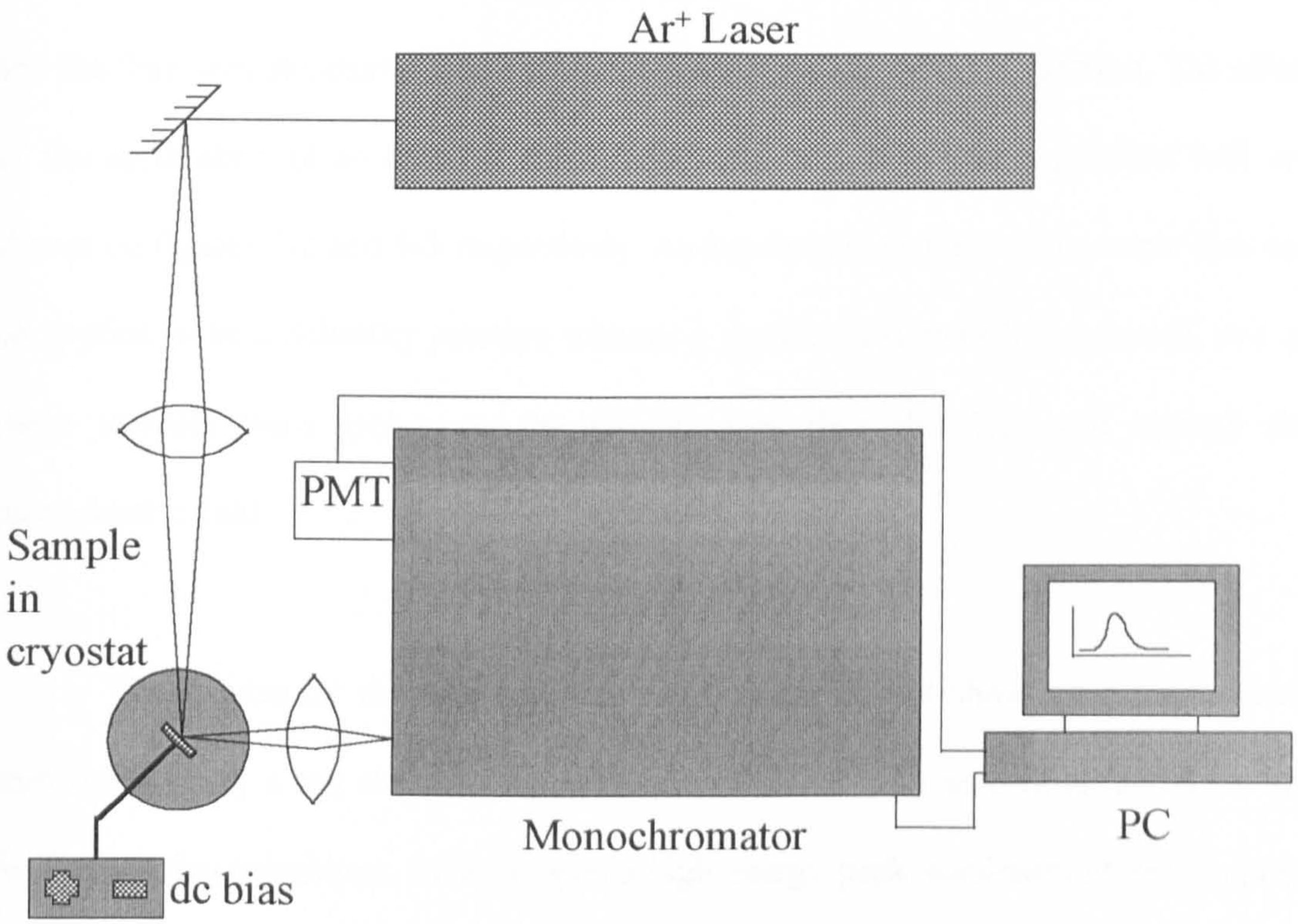

Figure 5-1. *Experimental set-up for the study of photoluminescence with the application of an external bias.*

The PL output was studied using the set-up in figure 5-1. The Ar^+ laser can supply a variety of wavelengths, in this case the 351nm (3.53eV) line was used. The gold contact on the sample surface for each of these experiments consisted of a thick 200nm layer with a thin 5nm thick track running across the surface to allow strong input and output signals, as detailed in chapter 4.

A simple piezoelectric shift in the PL emission peak when an external bias is applied has already been observed in chapter 4, however this section will examine some unusual effects that were observed in other experiments of a similar nature. The 4nm and the 8nm well structures used in chapter 4 were used again in this section. The effect of the application of an external bias on the 8nm and 4nm single quantum well are shown on figures 5-2 and 5-3 respectively. As expained in chapter 4, a reverse bias can be applied to be a Schottky junction without a significant current being passed, and as these samples were grown on the (211)B face then this bias will oppose the piezoelectric field.

The spectra for the 4nm and 8nm wells clearly do not show the expected blue shift followed by a red shift as seen in chapter 4. What both spectra in fact show are two competing transitions. In both cases a high energy peak dominates at zero applied bias, and a lower energy peak which is promoted as a reverse bias is applied. After a certain bias value the application of more voltage results in the return of the high energy transition at the expense of the low energy peak.

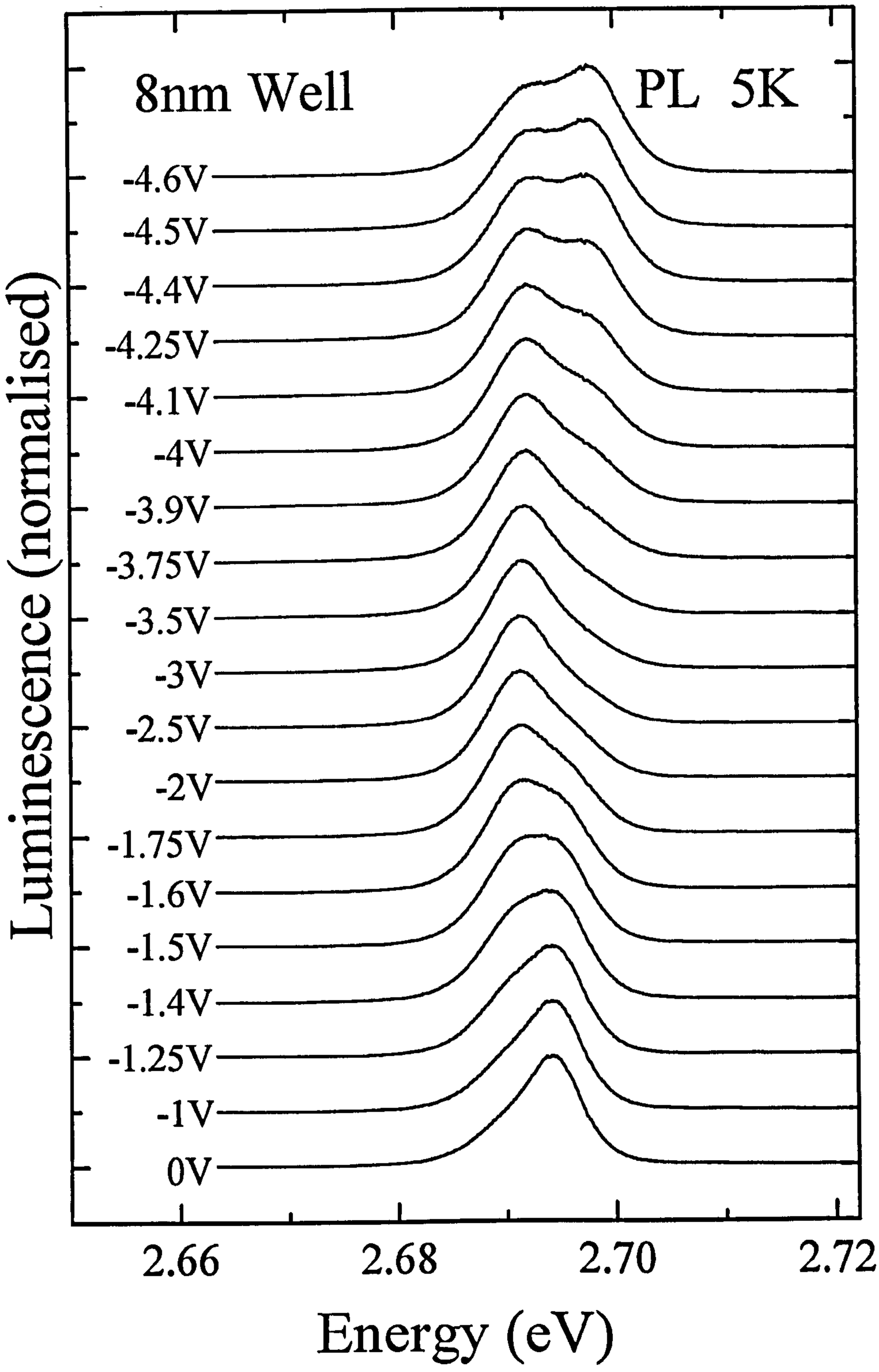

Figure 5-2. *Photoluminescence spectra taken at 5K for an 8nm single quantum well piezo structure for a range of external bias values.*

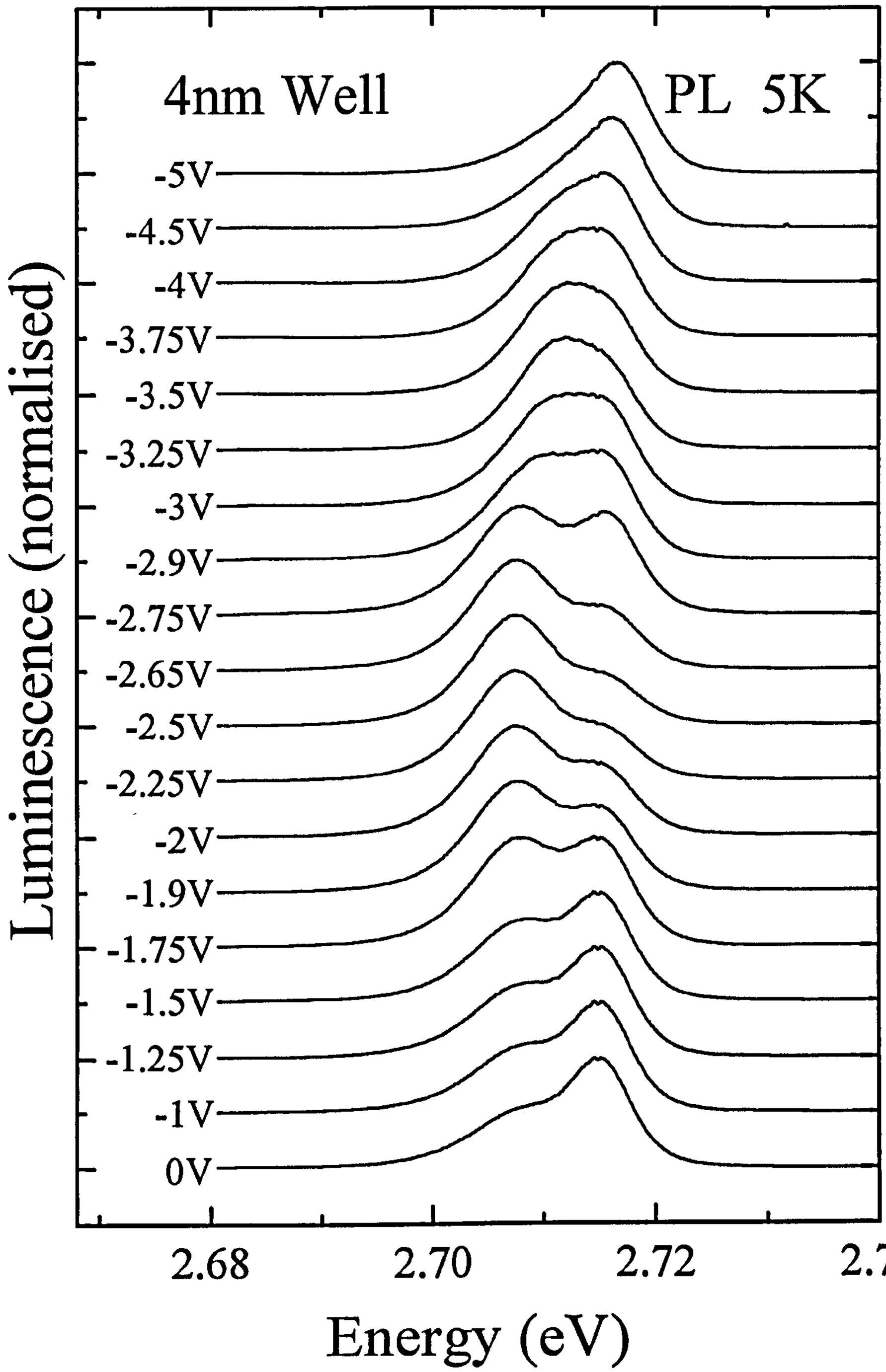

Figure 5-3. *Photoluminescence spectra taken at 5K for an 4nm single quantum well piezo structure for a range of external bias values.*

5.2.2. Discussion.

The absence of the piezoelectric shift will be discussed first. The blue shifts recorded by the photocurrent experiments in chapter 4 were 0.9meV and 2.9meV for the 4nm well and the 8nm well respectively. If such small shifts did occur in the two studies performed, they could easily have been lost in the competition between the two transitions, as the exact peak position of either peak is difficult to determine due to the proximity of the two peaks.

However, there may be an alternative method to determine the flat band voltage and hence the internal piezoelectric field. It is proposed that the high and low energy transitions observed in figures 5-2 and 5-3 are the free exciton (FX) and donor-bound excitons (D^0X) respectively. This can be explained through the effect of an applied bias on the width of the electron and hole wavefunctions (see figures 5-13 and 5-14). When no bias is applied, the wavefunctions are compressed towards one side of the well by the internal piezoelectric field. When the flat band voltage is applied, the wavefunctions are allowed to spread across the whole width of the well, and if further bias is applied then the wavefunctions will be compressed at the other side of the well. Therefore, the active width of the quantum well is widest when the flat band voltage is applied, *i.e.* the when the band edges are flat.

The donor concentration in the well layer will be some finite number per cm^3. Therefore the number of available donors will be greater when the flat band voltage is applied due to the expanded wavefunctions. It can therefore be deduced that the

relative intensity of the donor-bound exciton will reach its maximum when the flat band voltage is applied.

It is therefore possible to make an estimate of the flat band voltage from figures 5-2 and 5-3 by determining when the donor-bound exciton is strongest. Again, it is difficult to be precise because of the proximity of the transitions, but the flat band voltages are estimated at -2.5V for the 4nm well and -3V for the 8nm well, which translate to -3.9V and -4.4V respectively when the 1.4V of the gold / semiconductor Schottky contact is taken into account. These are roughly 25% less than the values obtained in chapter 4, although the value for the 4nm well is within the quoted error margins. The energy difference observed between (D^0X) and (FX) is approximately 6meV, close to the value of 8meV observed previously by Neukirch *et al.* [10] in a 5nm $Zn_{1-x}Cd_xSe$ / ZnSe well with $x = 0.18$.

The recognised method of identifying free and donor-bound excitons is to increase the excitation density. The available donor species would become saturated and above a certain excitation density only the free exciton would increase in intensity [10]. A problem was anticipated in piezoelectric quantum wells, however, due to the screening effect. As explained in chapter 3, a high injection of free carriers screens the piezoelectric field and therefore reduces the tilt in the band edge, which would also affect the competition between the FX and D^0X transitions. To avoid this problem, the experiment is performed at or around the flat band voltage so that a variation in the excitation power will only influence the FX and D^0X transitions directly and have no

effect on the tilt of the band edge. The results for the 8nm well are shown on figure 5-4 and clearly show the promotion of the FX transition with increased excitation intensity.

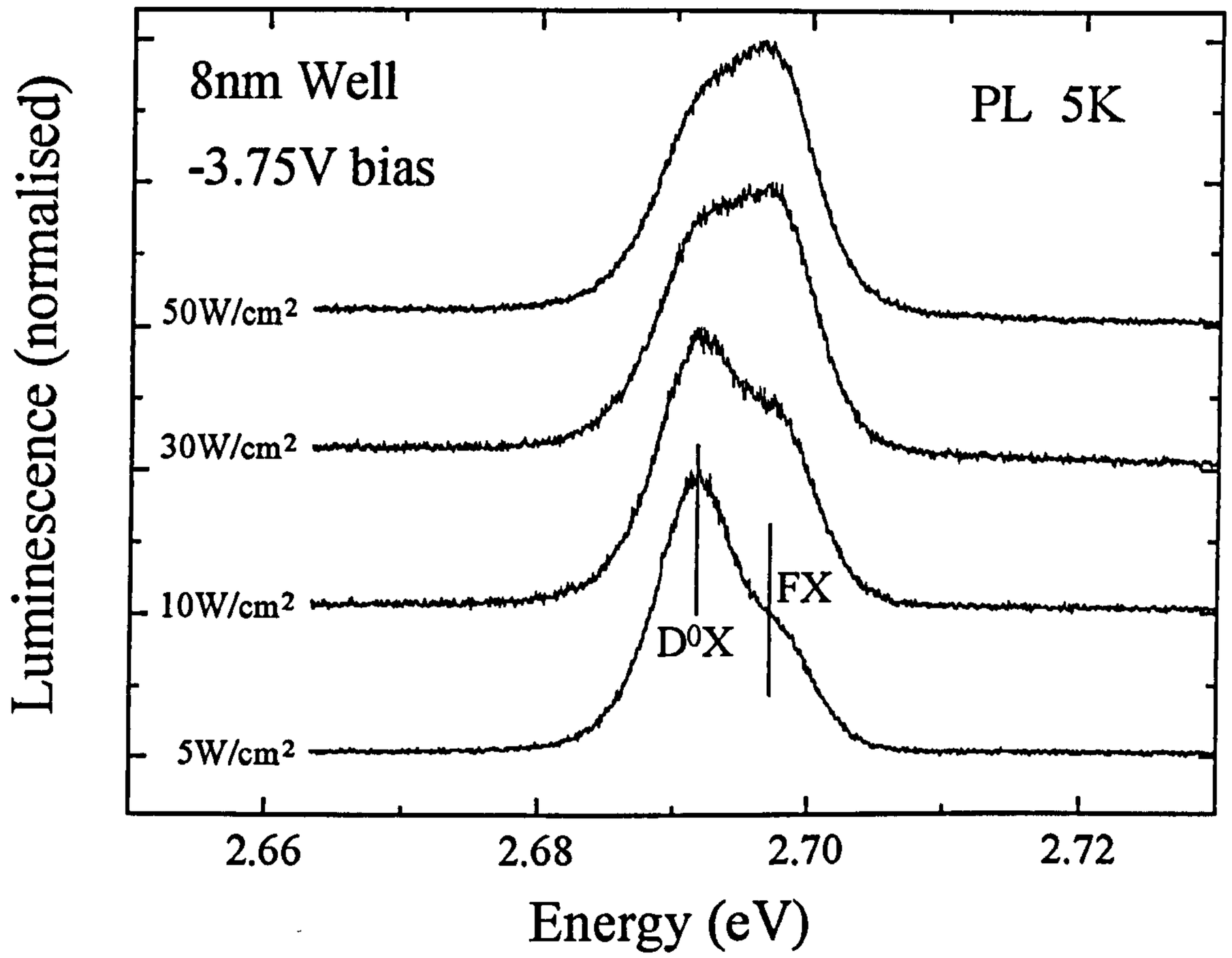

Figure 5-4. *Photoluminescence spectra taken at 5K for an 8nm single quantum well piezo structure for a range of excitation power densities, identifying the free and donor-bound excitons. A bias of -3.75V was applied to ensure that the band edge was flat and did not affect the FX and D^0X intensities.*

In order to observe the effect of a very large field in a quantum well region, a 10nm quantum well structure was grown to the same specifications as those in chapter 4, in this case with a cadmium content of approximately 15% [11]. However, in this

case it was grown on the (211)A face as opposed to (211)B. The only consequence of this is that the field will be of the same magnitude but in the opposite direction. Therefore any reverse bias applied will add to the internal field rather than oppose it. The results are shown on figure 5-5.

A high energy shoulder emerges when a reverse bias is applied and its relative intensity is increased at the expense of the other transition. At first this may appear similar to the previous result where a high energy transition is promoted as the tilt in the band edge is increased, indicating a free and bound exciton combination. However, in this case the energy difference is considerably larger (approximately 15meV). Furthermore a study by Godlewski *et al.* [12] on CdMnTe / CdTe quantum wells indicates that the FX to D^0X energy seperation is reduced when the well width is increased.

This transition is therefore identified as PL emission from the e1hh2 transition. As mentioned in chapter 4, transitions previously forbidden in a square well profile will become allowed when an electric field tilts the band edge, and at the large reverse bias voltages reached on figure 5-5 this tilt will be very large, allowing the e1hh2 transition to take over as the main emission transition. It is unlikely that this new transition is e1lh1 because it is an allowed transition in a square well.

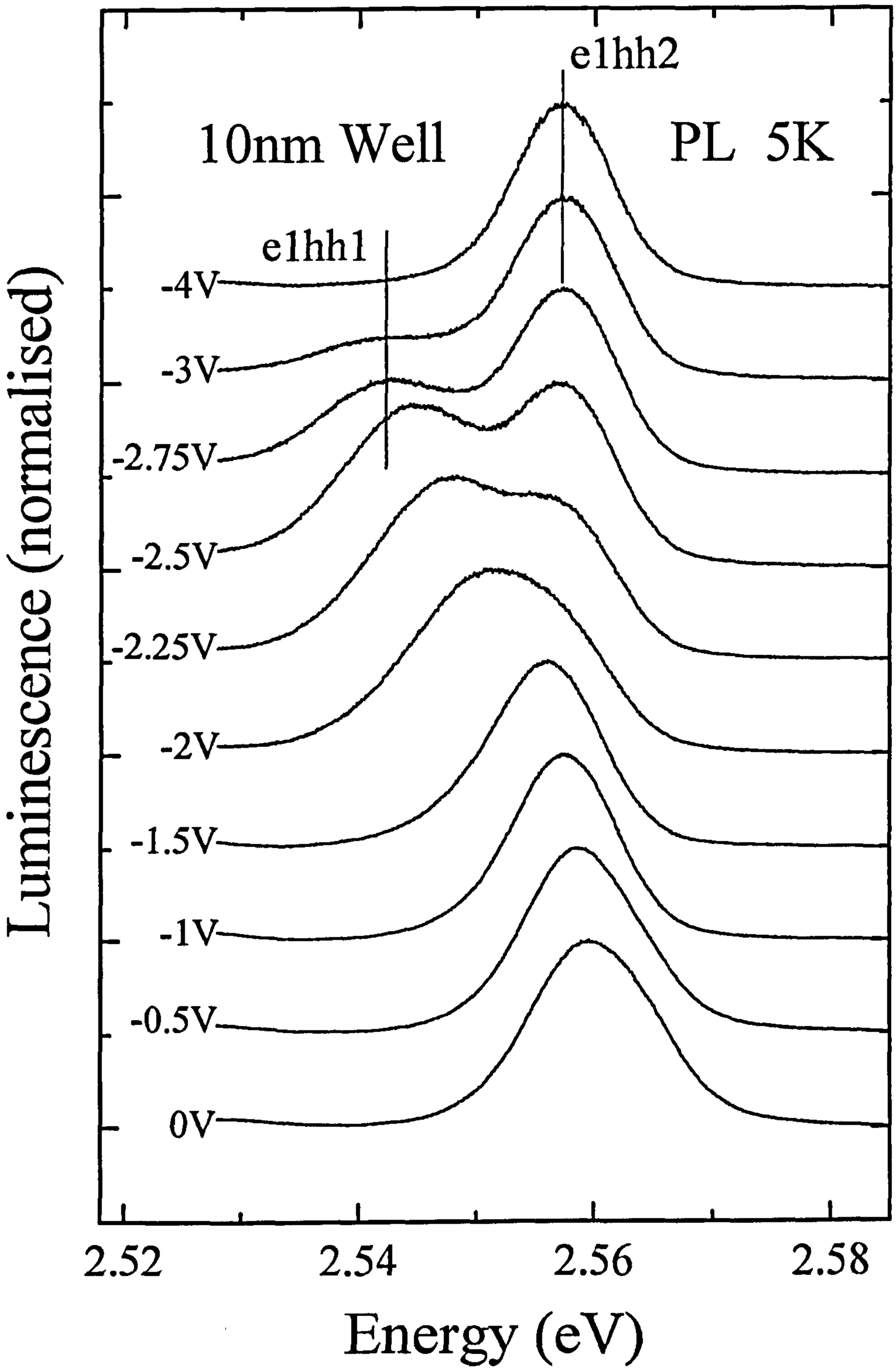

Figure 5-5. *Photoluminescence spectra taken at 5K for an 10nm single quantum well piezo structure grown on (211)A for a range of external bias values.*

5.3. Carrier Screening.

5.3.1. Introduction.

The screening effect was described in chapter 3 and involves the blue shift of a quantum well emission with increasing pump power. The sample used to demonstrate this effect was the 10nm ZnCdSe / ZnSe single quantum well on (211)A used in the previous section (the direction of the field is irrelevant in this experiment). The experimental set-up for the experiments was similar to that of the first section, but with the minor changes as shown in figure 5-6. The power of the excitation source was controlled by the Ar^+ laser power supply and also by using neutral density filters.

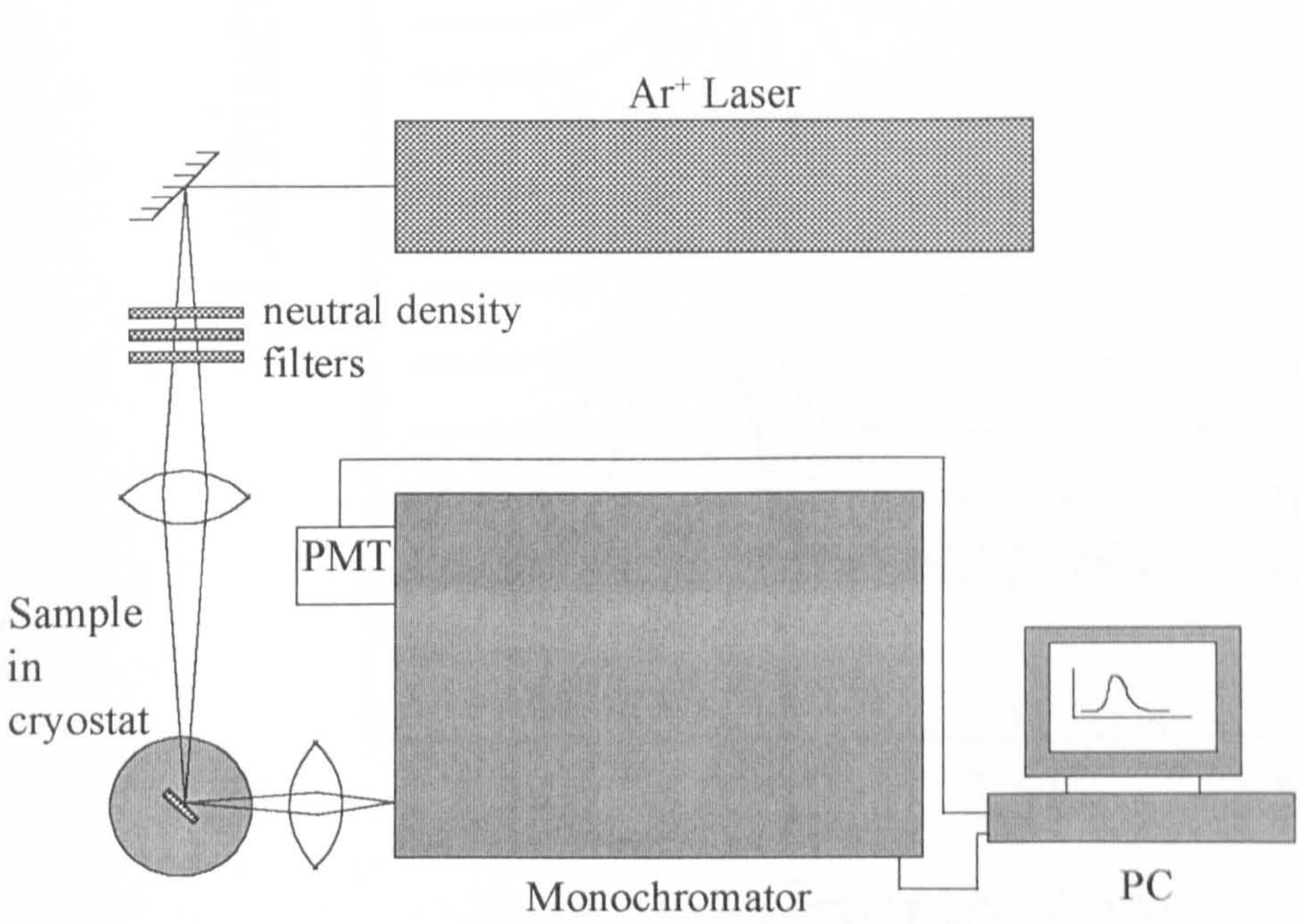

Figure 5-6. *Photoluminescence experimental set-up for demonstration of the screening effect.*

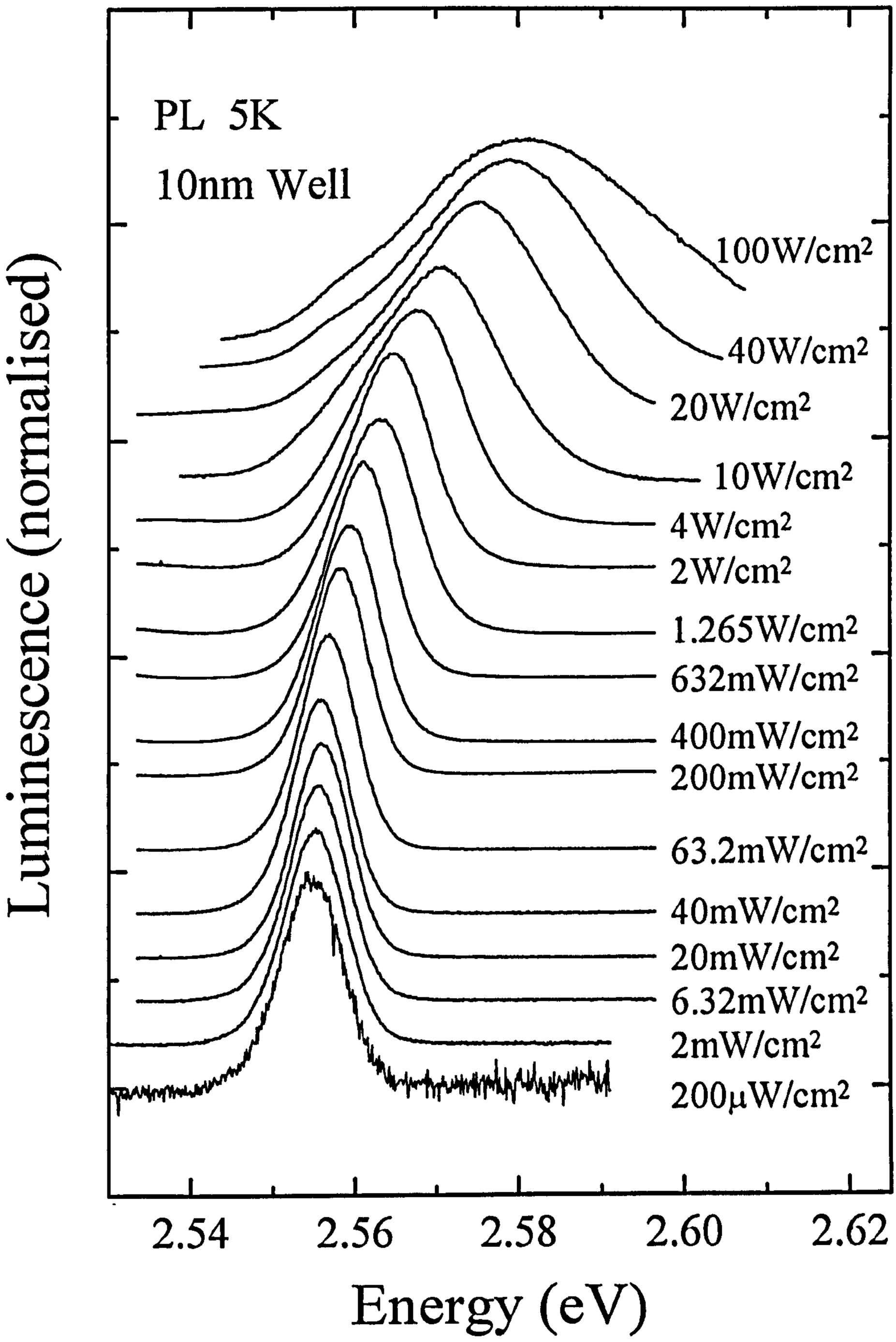

Figure 5-7. *Photoluminescence spectra taken at 5K for a 10nm single quantum well piezo structure for a range of excitation power density values.*

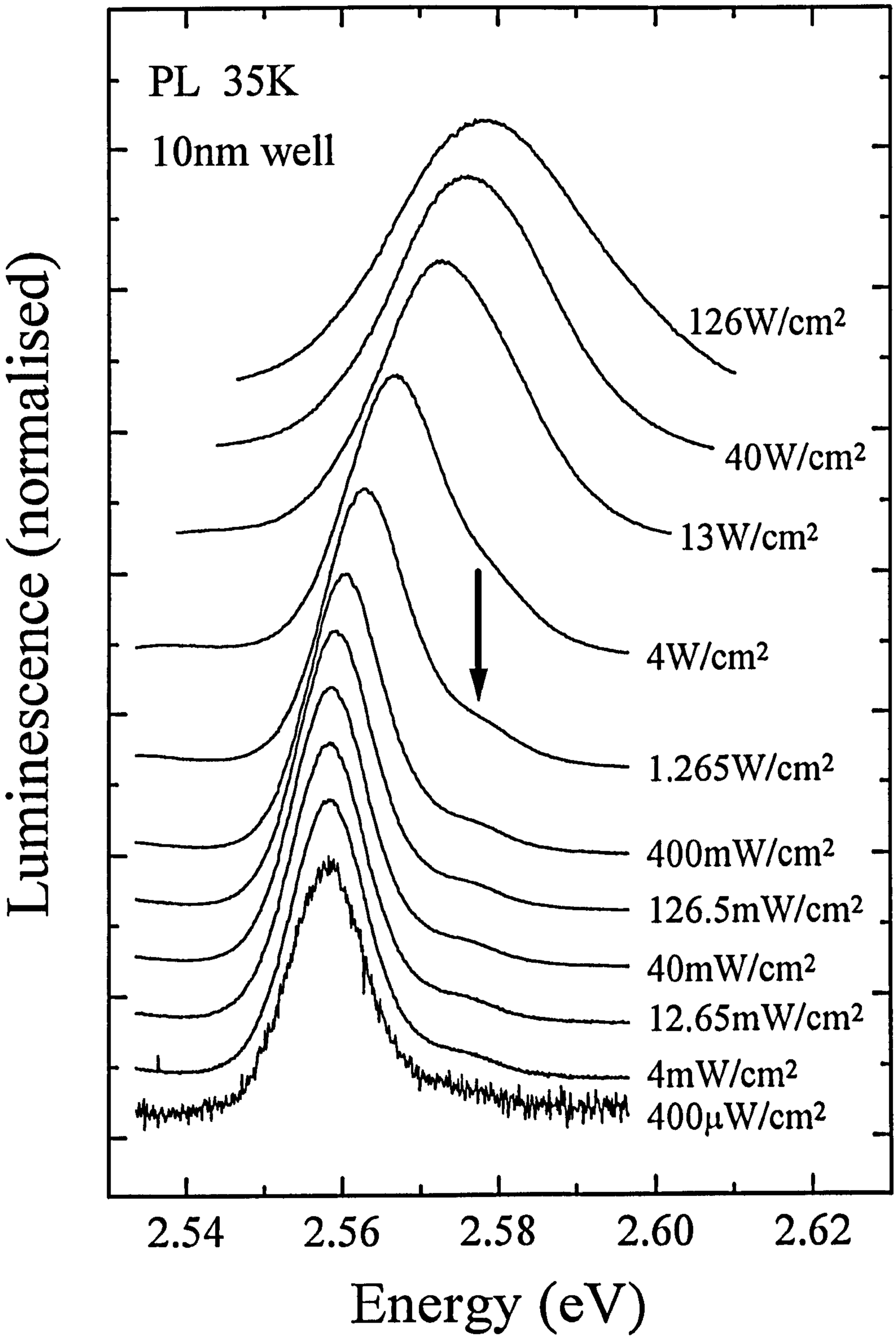

Figure 5-8. *Photoluminescence spectra taken at 35K for a 10nm single quantum well piezo structure for a range of excitation power density values.*

A large range of neutral density filters (from $10^{0.5}$ to 10^{4}) made it possible to vary the excitation power density over several decades. The results for the 10nm SQW are shown on figure 5-7, in this case the sample was held at 5K in the helium flow cryostat.

Figure 5-7 clearly shows the blue shift expected with an increasing excitation power as the generation of free carriers at opposite ends of the well screens the piezoelectric field. This experiment was then repeated at a temperature of 35K and the results are shown in figure 5-8. Again, the expected blue shift is evident. The two results are combined in a semi-logarithmic plot shown on figure 5-9.

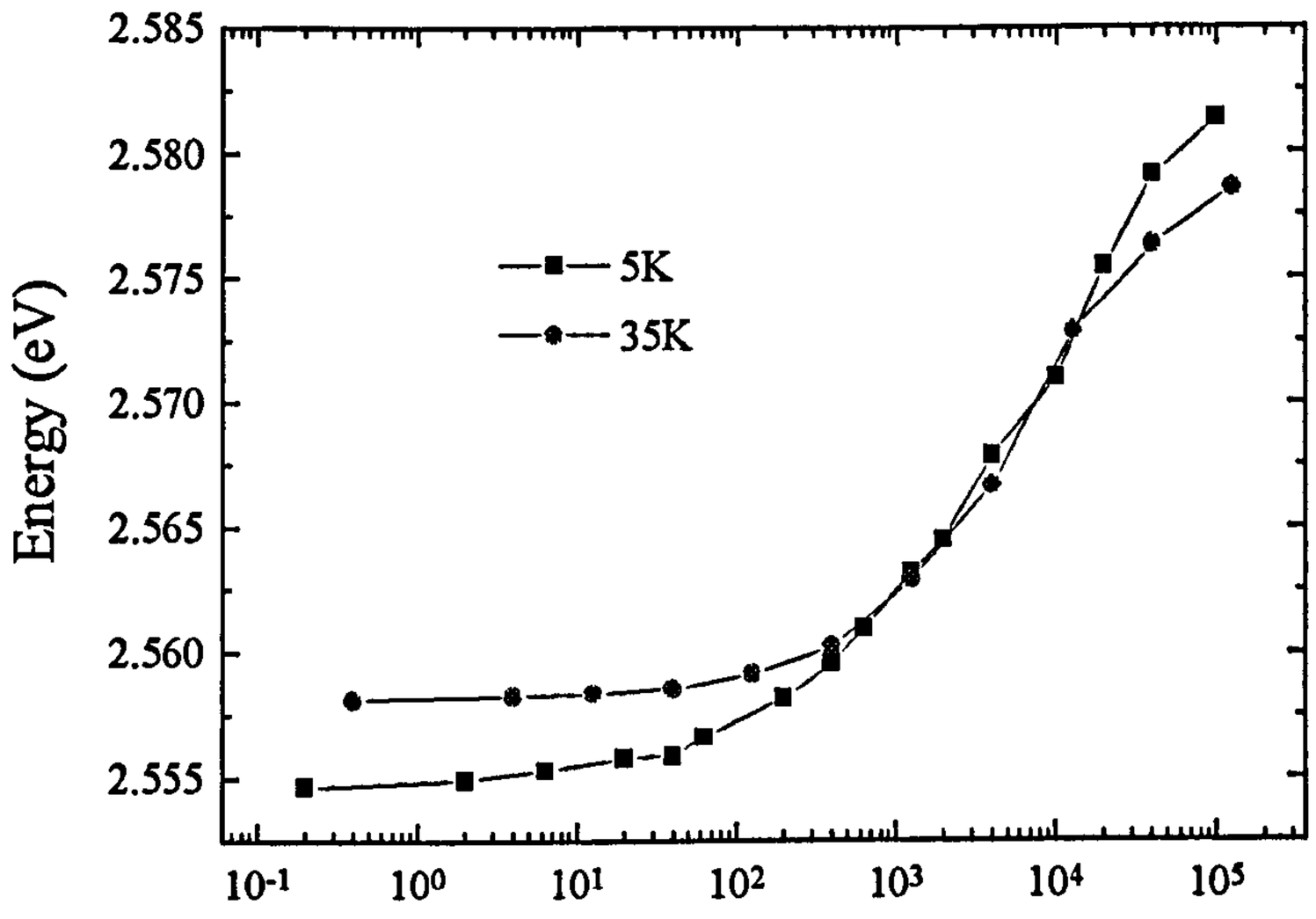

Figure 5-9. *Variation in PL emission energy with excitation power density for a 10nm single quantum well piezo structure at temperatures of 5K and 35K.*

5.3.2. Discussion.

The first point to be considered is the emergence of a high energy shoulder on the quantum well emission spectra performed at 35K, indicated by the black arrow on figure 5-8. This is very similar to a result obtained by Moore *et al.* [13] on GaInAs / GaAs quantum wells grown on a (111) orientation. They attribute a high energy shoulder observed during the screening process to photoluminescence from the e1hh2 transition made possible when the hole Fermi energy crosses the second heavy-hole band, *i.e.* heavy holes in the hh1 sub-band are given enough energy to significantly populate the hh2 sub-band and then recombine with electrons in the e1 sub-band producing luminescence.

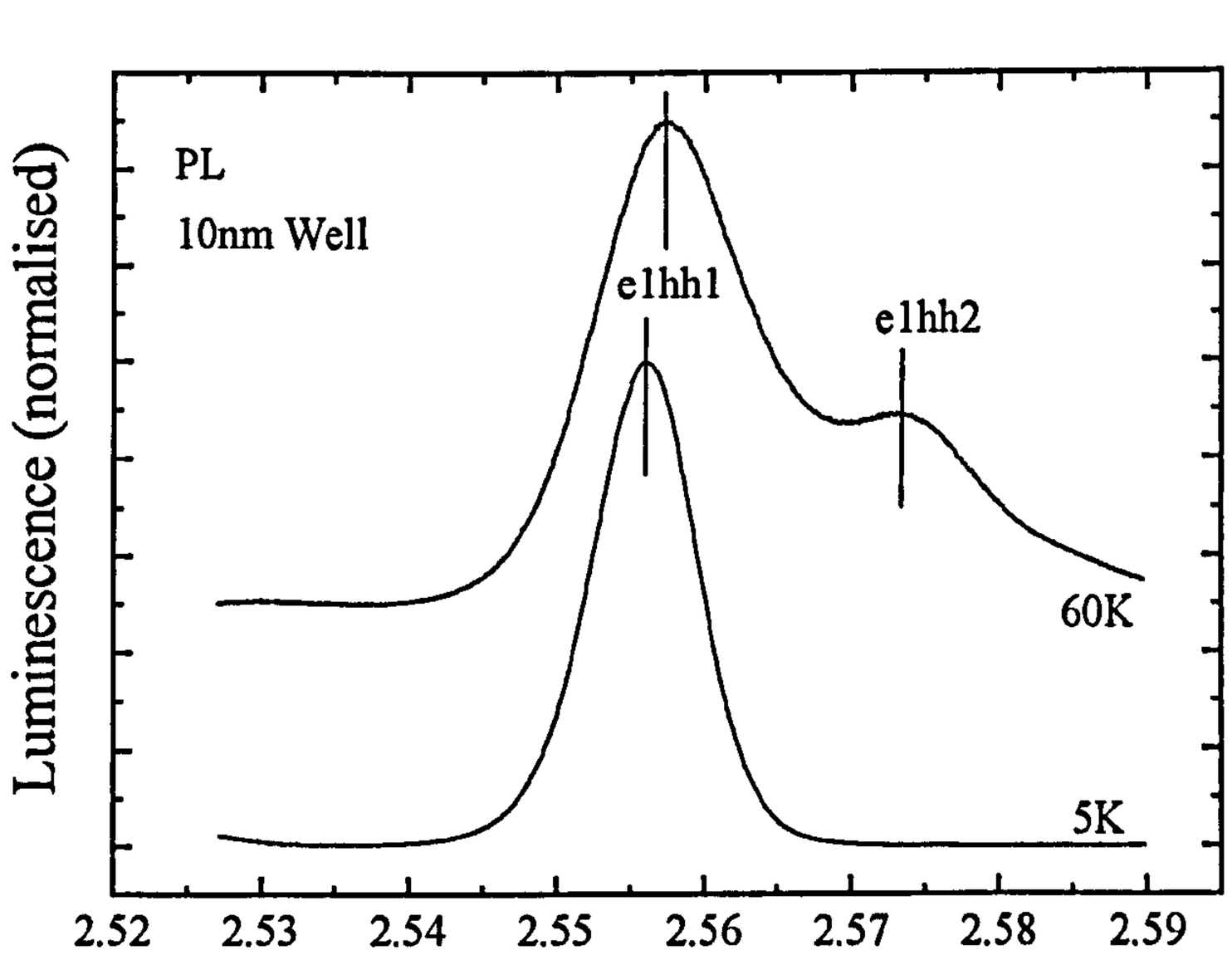

Figure 5-10. *PL at 5K and 60K for a 10nm ZnCdSe / ZnSe single quantum well piezo structure at an excitation of ≈ 5mW, showing thermal population of the hh2 sub-band.*

It has already been shown in chapter 4 that the e1hh2 transition is the lowest energy transition after e1hh1 in ZnCdSe / ZnSe quantum wells, and a PL / temperature study of the same 10nm quantum well has shown that it is possible to thermally populate the hh2 sub-band, as shown in figure 5-10. This explains why the high energy shoulder was evident in the screening study at 35K but was not observed when the same experiment was conducted at 5K.

The next point of interest to be considered is the different screening behaviour at 5K and 35K shown on figure 5-9. The result is unusual because at low pump power the 5K emission is at a lower energy than the 35K emission, while at high pump power the opposite is true. Theoretically, the energy of a PL emission should follow the temperature dependence of the band gap which increases as the temperature is lowered due to the thermal contraction of the crystal lattice. However, at very low temperatures the energy of the PL emission can be shifted to a lower energy. This is due to a previously documented effect where a difference in energy is observed between the PL emission and corresponding e1hh1 absorption peak [14,15], where the energy difference is known as the Stokes shift and is atributed to exciton localisation, *i.e.* the excitons are physically trapped into a limited area because it allows an emission of lower energy. Electron-hole recombination will always occur with the process which releases the lowest possible photon energy. It has been shown by Zu *et al.* [16] that the magnitude of the localisation effect can be observed by varying the temperature and observing the *deviation* of the PL emission from the expected temperature dependence at low temperatures. The temperature dependence of the PL from the 10nm single quantum well piezo structure is shown on figure 5-11.

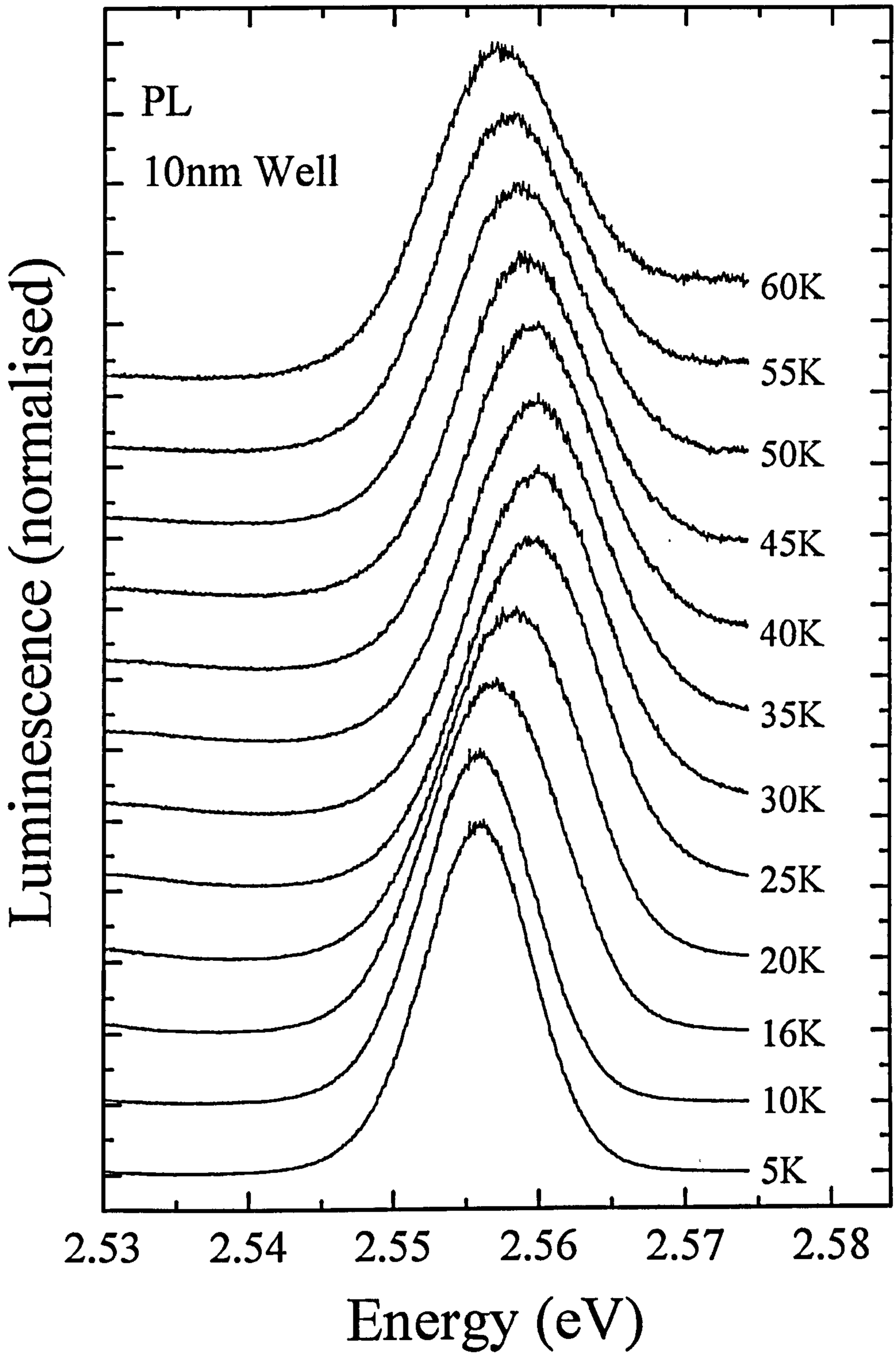

Figure 5-11. *Temperature variation of the PL emission of a ZnCdSe / ZnSe 10nm single quantum well piezo structure.*

The variation of the PL emission energy with temperature is shown on figure 5-12. The theoretical temperature dependence of the band gap of ZnSe was part of an extensive review by Skromme [17], who compared the two parameter functions of O'Donnell *et al.* [18] with the established semi-empirical formula of Varshni [19]. Skromme explains that neither formula provides an accurate fit from very low temperature up to room temperature, and proceeds to offer a three parameter function that gives good agreement with the experimental results, given as equation (5-4). The Varshni relation (given as equation (5-5)) was found to be inaccurate at very low temperatures where the actual band gap is nearly temperature independant.

$$E_g(T) = E_0 - \frac{\alpha T^3}{T^2 + \beta T + \gamma} \tag{5-4}$$

$$E_g(T) = E_0 - \frac{\alpha T^2}{T + \beta} \tag{5-5}$$

The theoretical line of the Varshni relation shown on figure 5-12 uses the values for α and β found by Shirakawa *et al.* [20] for ZnSe ; $\alpha = 8.59\times10^{-4}$eV/K and $\beta =$ 405K. The value of E_0 was adjusted to give the best fit (at high temperature) to account for the exciton binding energy and the piezoelectric shift. The line for the Skromme model was found using a least-square fit to the experimental values for temperatures on and above 40K, below which localisation occurs. The parameters provided by this fit were $\alpha = 6.23$meV/K, $\beta = 514.5$K and $\gamma = 361817\text{K}^2$. The Skromme model shall be considered here due to its better fit at low temperature in reference 17.

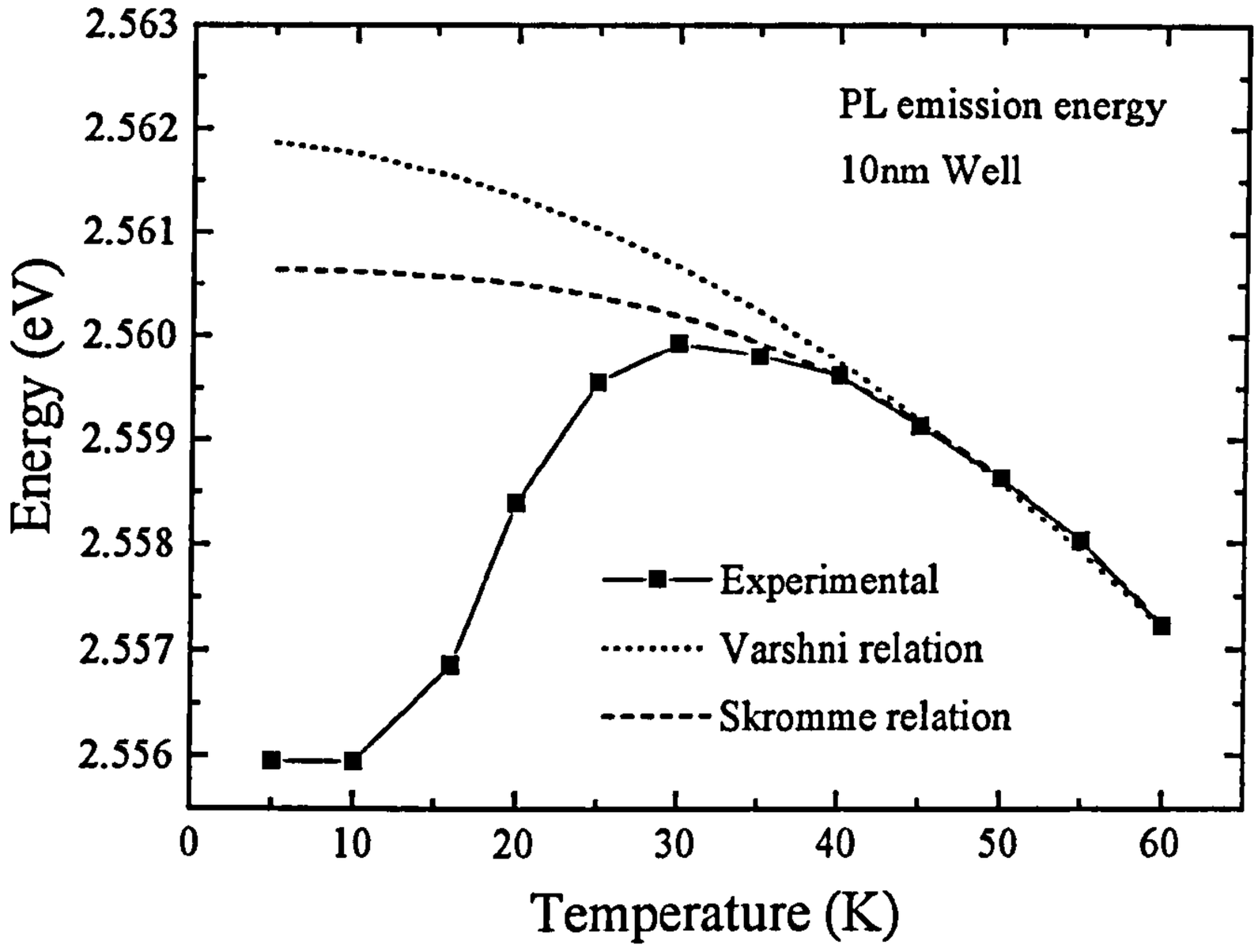

Figure 5-12. *Temperature variation of the PL emission energy of a 10nm ZnCdSe / ZnSe single quantum well piezo structure shown with the theoretical Varshni and Skromme relations.*

The deviation of the experimental points from the theoretical curve at low temperatures shows that exciton localisation is occurring with a difference of 4.6meV between the experimental and the expected PL emission at 5K. This is a stronger effect than in reference 16 which observed a corresponding difference of 2meV in an InGaAs / GaAs single quantum well.

It was stated by Bastard *et al.* that the Stokes shift between the luminescence line and the corresponding absorption peak is caused by exciton localisation on interface defects [14]. Therefore it would be expected that the magnitude of the

localisation will be greater in a quantum well that is subject to an electric field because the wavefunctions of the electron and hole are concentrated on or around the interfaces with the barrier layers. This is shown in figures 5-13 and 5-14 which display the e1 and hh1 wavefunctions for a 10nm $Zn_{0.85}Cd_{0.15}Se$ / ZnSe single quantum well as derived by the solutions given in chapter 3, for wells with and without an internal field respectively.

All wavefunctions were normalised such that

$$\int_{-\infty}^{\infty} \varphi^* \varphi \, dz = 1 \tag{5-6}$$

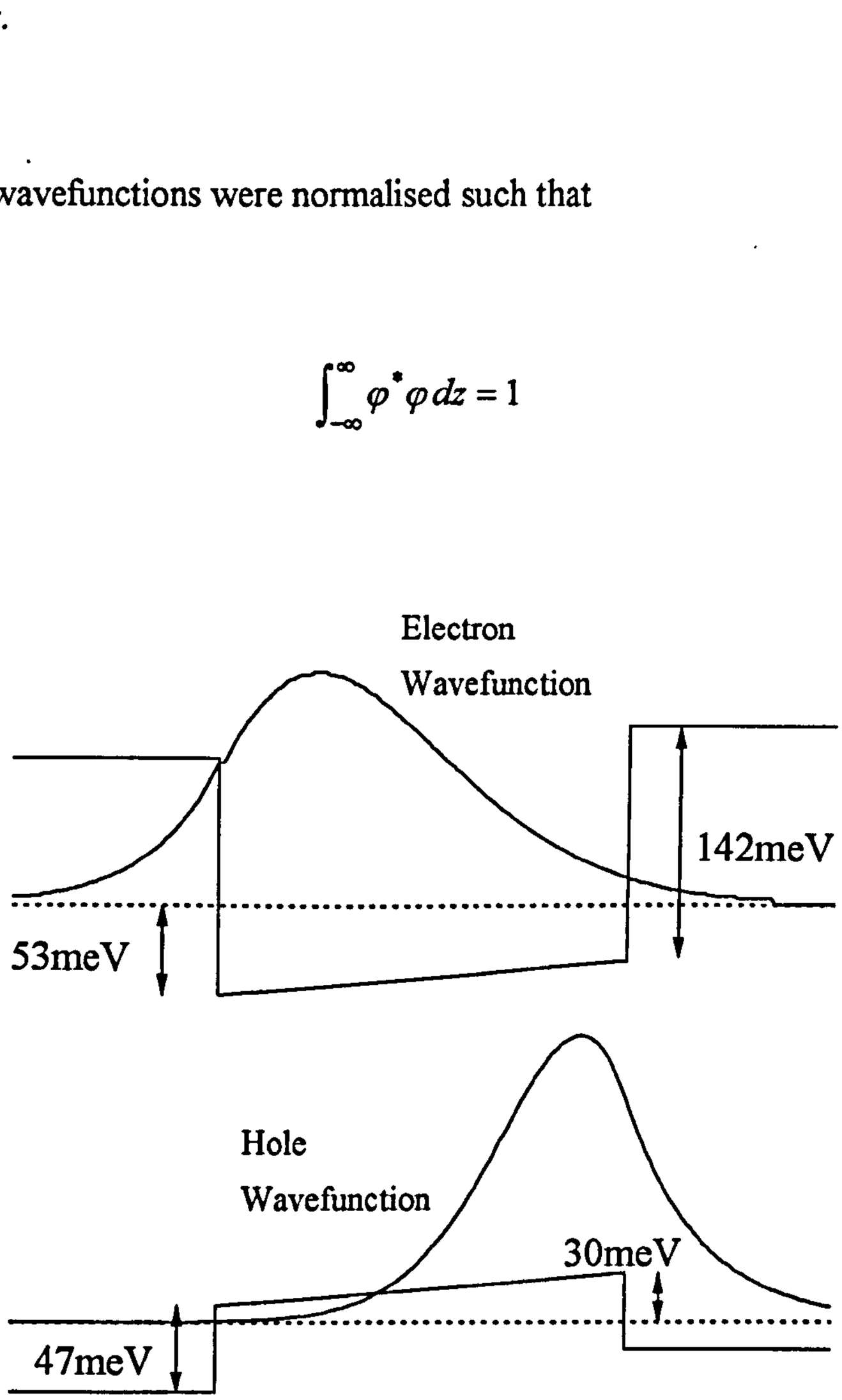

Figure 5-13. *Calculated e1 and hh1 wavefunctions for a 10nm $Zn_{0.85}Cd_{0.15}Se$ / ZnSe single quantum well with an internal field.*

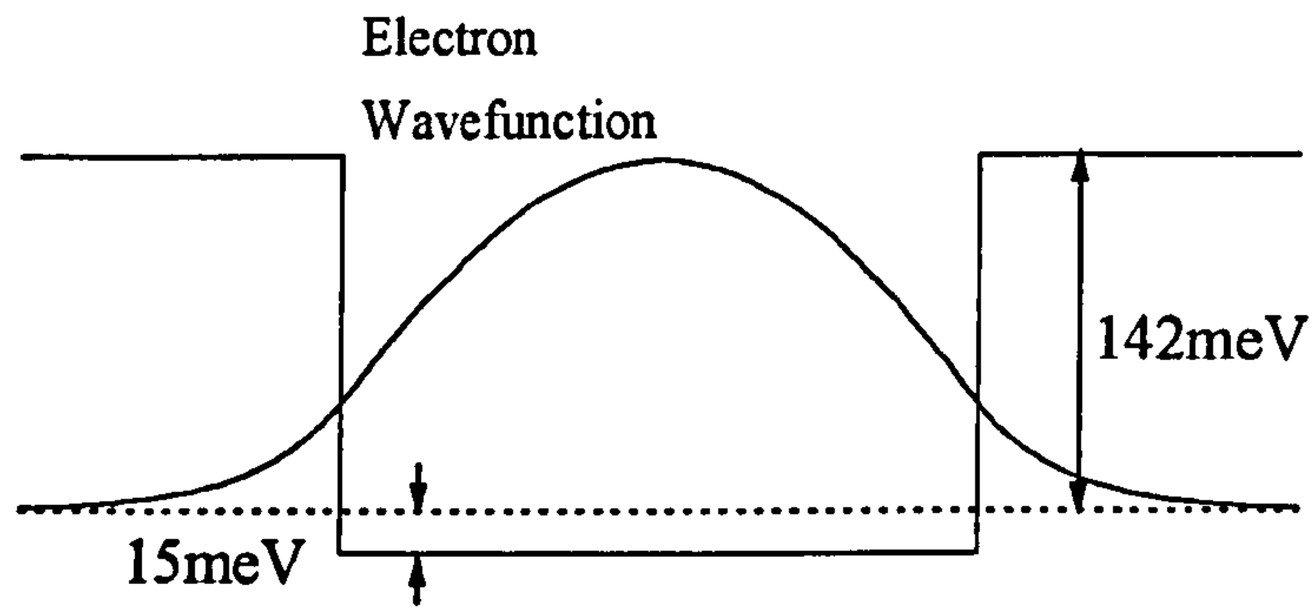

Figure 5-14. *Calculated e1 and hh1 wavefunctions for a 10nm $Zn_{0.85}Cd_{0.15}Se$ / ZnSe single quantum well without an internal field.*

This proposal is consistent with the screening results shown on figure 5-9. At low injection, the band edges are tilted and the localisation is identified by the relative positions of the low temperature and higher temperature emissions. This situation is reversed at high injection when the presence of free carriers screens the internal field and flattens the band edge, allowing the carrier wavefunctions to occupy the middle of the well and therefore reducing the localisation.

Bastard *et al.* defined the Stokes shift as being the difference between the PL emission peak and the e1hh1 PLE peak [14], and the Stokes shift has been shown to decrease with increasing temperature [15] as would be expected considering the effect

of temperature on the localisation. However, this means that the proposal that the localisation is reduced in the flat band condition is in disagreement with the results from the PLE section of chapter 4, given as figure 4-16.

In this case the difference between the PL emission peak and the e1hh1 PLE peak (*i.e.* the Stokes shift) is greater at the flat band state (-5V bias) than when an internal field is present. Given the evidence suggesting that the localisation is reduced at the flat band condition, along with the unusual behaviour of the PL emission peak position at bias values between 4V and -1V, it has to be assumed that these values have been shifted to higher energies. In this case it is attributed to the screening effect, as it was necessary to excite the samples with a significant energy density to obtain a reasonable output signal through the gold contact layer.

5.4. Conclusion.

The piezoelectric effect has been demonstrated in ZnCdSe / ZnSe single quantum wells by photoluminescence spectroscopy, through the screening of the field by the generation of free carriers and by an application of an external bias. The presence of the internal field has been shown to have a direct effect on the relative intensity of the free and donor-bound exciton emissions. The screening results showed that the presence of an internal field increases the magnitude of exciton localisation by concentrating the carrier wavefunctions close to interface defects.

5.5. References.

[1] K.A. Prior, W. Meredith, G.D. Brownlie, Z. Zhu, P.J. Thompson, J.S. Milnes, I.S. Hauksson, G. Horsburgh, T.A. Steele, S.Y. Wang and B.C. Cavenett, Mater. Sci. Engin. **B43**, 9 (1997).

[2] Y.G. Shreter, Y.T. Rebane, O.V. Klyavin, P.S. Aplin, C.J. Axon, W.T. Young and J.W.Steeds, J. Cryst. Growth **159**, 883 (1996).

[3] R.L. Tober and T.B. Bahder, Appl. Phys. Lett. **63**, 2369 (1993).

[4] H. Qiang, F.H. Pollak, C. Mailhiot, G.D. Pettit and J.M. Woodall, Phys. Rev. B **44**, 9126 (1991).

[5] J.L. Sánchez-Rojas, A. Sacedón, E. Calleja, E. Muñoz, A. Sanz-Hervás, G. De Benito and M López, Phys. Rev. B **53**, 15469 (1996).

[6] T.S. Moise, L.J. Guido and R.C. Barker, J. Appl. Phys. **74**, 4681 (1993).

[7] O. Brandt, K. Kanamoto, Y. Tokuda, Y. Abe, Y. Wada and N. Tsukada, J. Appl. Phys. **75**, 2105 (1994).

[8] P.O. Vaccaro, K. Tominaga, M. Hosoda, K. Fujita and T. Watanabe, Jpn. J. Appl. Phys. **34**, 1362 (1995).

[9] J.L. Sánchez-Rojas, A. Sacedón, F. Calle, E. Calleja and E. Muñoz, Appl. Phys. Lett. **65**, 2214 (1994).

[10] U. Neukirch, D. Weckendrup, J. Gutowski, D. Hommel and G. Landwehr, J. Cryst. Growth **138**, 861 (1994).

[11] S.A. Telfer, G. Horsburgh, J.S. Milnes, C. Morhain, P.J. Thompson, K.A. Prior and B.C. Cavenett, J. Cryst. Growth **184/185**, 51 (1998).

[12] M. Godlewski, Z. Wilamowski, T. Wojtowicz, G. Karczewski, J. Kossut, P.O. Holtz, J.P. Bergman and B. Monemar, J. Cryst. Growth **184/185**, 957 (1998).

[13] K.J. Moore, P. Boring, B. Gil and K. Woodbridge, Phys. Rev. B **48**, 18010 (1993).

[14] G. Bastard, C. Delalande, M.H. Meynadier, P.M. Frijlink and M. Voos, Phys. Rev. B **29**, 7042 (1984).

[15] C. Delalande, M.H. Meynadier and M. Voos, Phys. Rev. B **31**, 2497 (1985).

[16] Z.Y. Zu and M. Gal, J. Lumin. **50**, 153 (1991).

[17] B.J. Skromme, Annu. Rev. Mater. Sci. **25**, 601 (1995).

[18] K.P. O'Donnell and X. Chen, Appl. Phys. Lett. **58**, 2924 (1991).

[19] Y.P. Varshni, Physica **34**, 149 (1967).

[20] Y. Shirakawa and H. Kukimoto, J. Appl. Phys. **51**, 2014 (1980).

6. CRITICAL THICKNESS OF PIEZOELECTRIC QUANTUM WELLS.

6.1. Introduction.

A heterojunction is created at the interface of two different semiconductors. The difference may only be in the introduction of a percentage of a third element (e.g. a $Zn_{1-x}Cd_xSe$ quantum well between ZnSe barrier layers) or the layers may be from entirely different groups of compounds (e.g. ZnSe layers grown on GaAs substrates). Nevertheless, the consequences are the same : any lattice mismatch between the layers (i.e. any difference between the lattice constants) will produce strain in the layer. When a heterojunction is formed the layer being grown on top will maintain a constant level of strain, known as pseudomorphic growth, until it reaches a *critical thickness.* Traditional theory would claim that at this point dislocations are created and any further growth will see a reduction in the strain as the layer relaxes and an increase in the population of dislocations. However, studies in this subject suggest that the reality is more complicated.

GaAs/InGaAs strained layers have shown evidence of two critical thicknesses, one at the occurrence of the first dislocations and a larger one at the commencement of relaxation [1]. The smaller critical thickness is denoted h_{cd} and is defined by Matthews and Blakeslee [2] to correspond to the formation of the first misfit

dislocation. Experimentally, this process can be observed using X-ray topography and values have been recently obtained for both InGaAs [3] and ZnSe [4] on (001) GaAs substrates. The second value, h_{cr}, is defined as the threshold thickness above which long-range lattice relaxation is observed [5] which only occurs once the strain fields of individual dislocations begin to overlap. For a typical semiconductor layer about 1μm thick, this gives a lower detection limit of about 10^4 cm^{-2} dislocations. This lattice relaxation can be estimated *in-situ* from the reflection high-energy-electron diffraction (RHEED) streak spacing [6,7,8,9]. However, it is more usually determined post-growth by observing either the change in interplanar spacings by high resolution X-ray diffraction [10,11] or the changes in the photoluminescence (PL) emission spectra where the decrease in strain produces a slight energy shift possibly followed either by a broadening of the PL line or a decrease of the intensity with a broadening of the line [8,12]. Other methods have been used such as reverse leakage current in p-i-n structures [13]. All the methods are often used in conjunction with transmission electron microscopy (TEM) which is able to directly observe evidence of strain relaxation [14].

In layers with small strains, there may be a considerable difference between h_{cd} and h_{cr}. A good example can be seen in the case of ZnSe grown directly on to (001) GaAs substrates where the strain is 0.27% and it has been shown that h_{cd} is 97.5(±2.5)nm [4] as illustrated in figures 6-1 (a) and (b). They show X-ray topographs of ZnSe epilayers on GaAs which reveal that the first dislocations are formed between 95nm and 100nm [15].

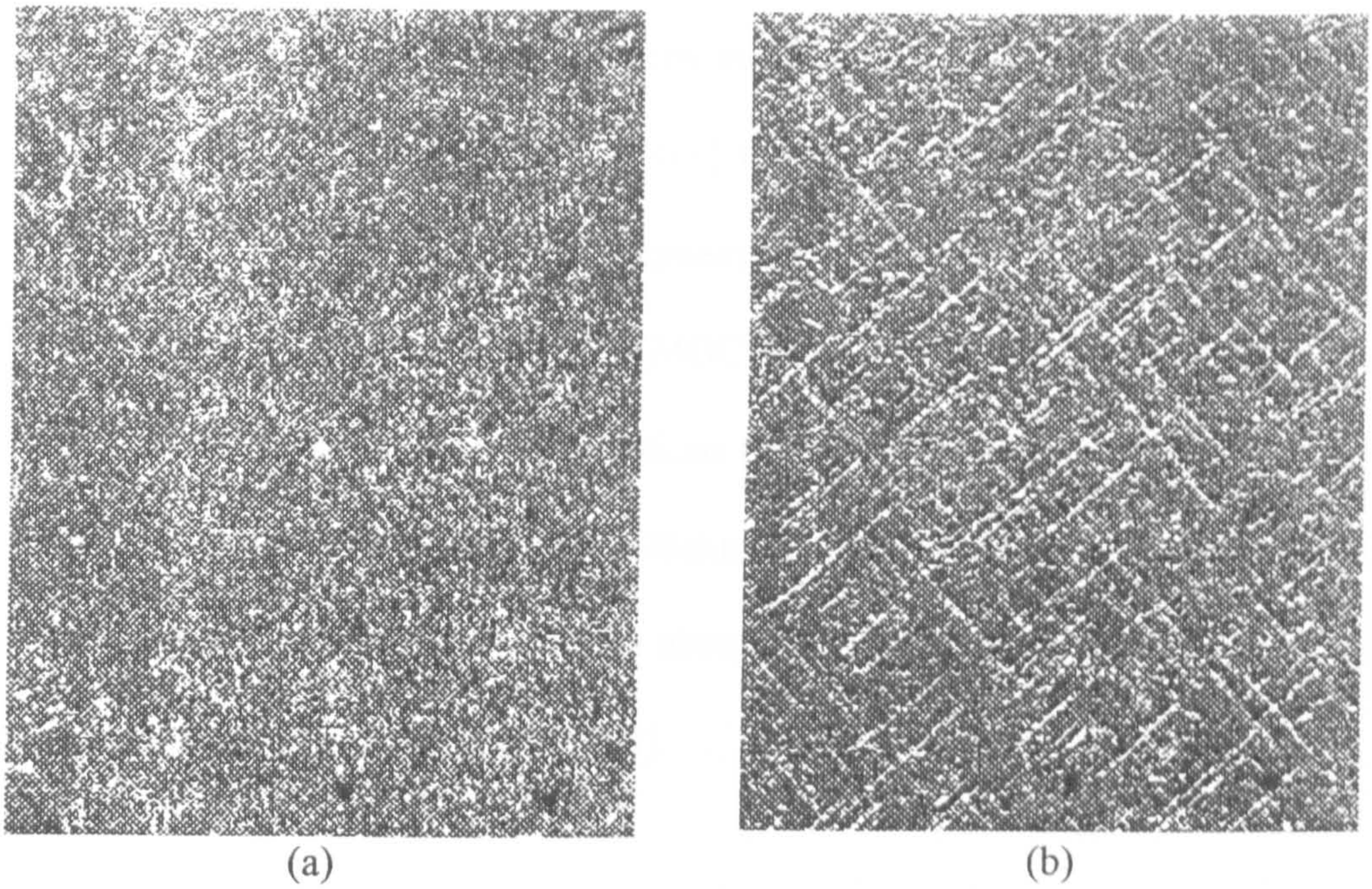

(a) (b)

Figure 6-1. *X-ray topographs of ZnSe epilayers on GaAs,* (a) *95nm and* (b) *100nm thick.*

However, samples grown under similar conditions give a value for h_{cr} of 150nm as measured by both X-ray double crystal rocking curves [16,17] and PL [18], which shows the variation of the free and bound exciton emission with ZnSe epilayer thickness. The emissions (and therefore the band gap) begin to drop in energy at a thickness of about 150nm which indicates the commencement of relaxation, as the strained band gap has a higher energy than the unstrained.

For a given strain the formation of the first dislocation, giving h_{cd}, will primarily be a function of the elastic constants of the material and the nature of the pre-existing defects, whereas h_{cr} will depend principally on the rate of dislocation formation in the growing semiconductor, which is a function of the growth method.

Thus, for ZnSe grown on (001) GaAs by migration enhanced epitaxy a value of 250nm was obtained for h_{cr} by Gaines *et al.* [19] while Wolf *et al.* [20] have obtained values of 220(±20)nm for molecular beam epitaxy (MBE) ZnSe and 100(±20)nm for metal-organic chemical vapour deposition (MOCVD) ZnSe. In addition, it should be noted that both critical thicknesses are functions of the substrate orientation, as will be seen in section 6.2.1. on the Matthews / Blakeslee model. Anan *et al.* found that h_{cr} for InGaAs grown on (111)B GaAs was about twice that of a (001) structure produced under the same growth conditions [21].

This chapter will examine $Zn_{1-x}Cd_xSe$ / ZnSe quantum well heterostructures which have been under intense investigations in recent years due to the research into producing laser diodes in the blue-green region with practical lifetimes, of which they would be the active region. Studies have shown that the lifetime is limited by the development of dark line defects [22] formed by dislocations and stacking faults [23] propagating into the active layer. This study is only sensitive to the relaxation of strain and not the formation of the first dislocations. An indication of the importance of the previously undiscovered h_{cd} is shown on figure 6-2, which displays the variation of quantum well emission energy with the well width. The lines labelled (1) and (2) correspond to the critical thickness for each value of cadmium percentage in the quantum well calculated by extrapolating the values of h_{cr} and h_{cd} respectively from ZnSe on (001) GaAs to ZnCdSe on ZnSe.

Previously the quantum wells would be designed to be before line (1), assuming that they would be free of defects. However, the discovery of h_{cd} would

indicate that any structures that appear in the shaded region of figure 6-2 would contain dislocations and indeed some of the reported laser structures in the published data are within this region [24], so they are not formed by true pseudomorphic growth. Furthermore, as later devices used ZnSSe cladding layers instead of ZnSe [25] and given that the relative lattice parameters are such that CdSe > ZnSe > ZnS, then the restrictions on the active ZnCdSe layer are tightened further.

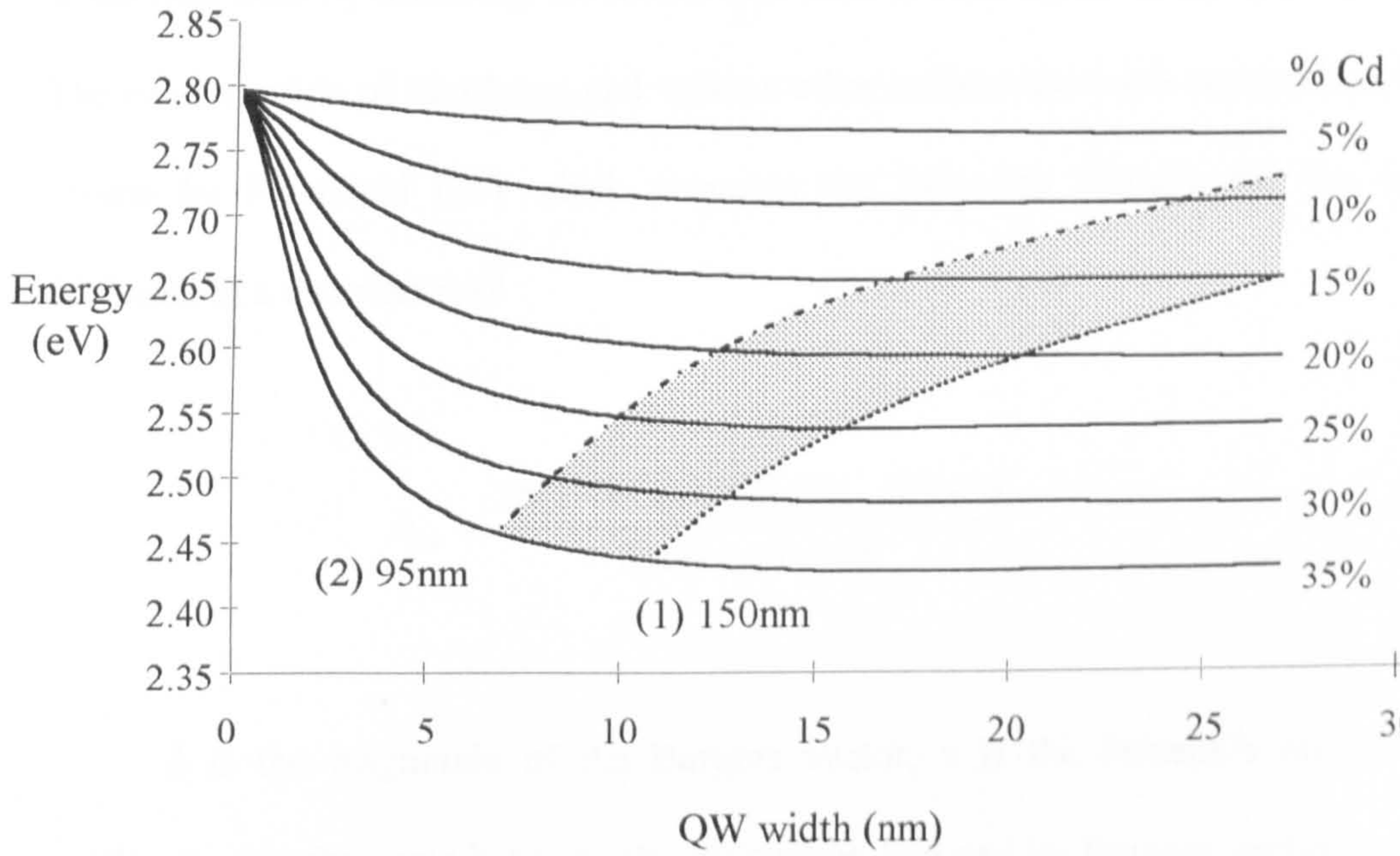

Figure 6-2. *Variation of ZnCdSe quantum well emission energy with well width plotted for different cadmium mole fractions in the well. Curves marked* (1) *and* (2) *represent the maximum thickness which can be grown for a given cadmium content given a critical thickness for ZnSe of 150nm* (1) *or 95nm* (2) [15].

6.2. Models.

6.2.1. Matthews / Blakeslee model.

Most of the work to date makes reference to the model of Matthews and Blakeslee [2] which is an iterative formula that derives the first critical thickness for the formation of the first dislocations, h_{cd}, from certain lattice parameters and the strain mismatch by balancing the forces that exist in both layers of the heterojunction. The other models of Matthews and various other collaborators are summarised in the review by Fitzgerald [26] which proposes the following formula for the critical thickness of a quantum well :

$$h_{cd} = \frac{2b(1-\nu\cos^2\alpha)[\ln(h_{cd}/b)+1]}{8\pi\varepsilon(1+\nu)\cos\lambda} \qquad (6\text{-}1)$$

b is the magnitude of the Burgers vector, ν is the Poisson's ratio of the overlayer, α is the angle between the dislocation line and its Burgers vector, ε is the lattice mismatch and finally λ is defined as the angle between the Burgers vector and that direction in the film plane which is perpendicular to the line of intersection of the slip plane and the interface. For a single layer growth, the factor of 2 on the numerator is removed.

To produce a model for the ZnCdSe / ZnSe system, the following definitions are required :

The lattice mismatch is defined by the lattice parameter, a, by

$$\varepsilon = \frac{a_{ZnCdSe} - a_{ZnSe}}{a_{ZnSe}} \tag{6-2}$$

Poisson's ratio is calculated from the elastic moduli c_{11} and c_{12} by

$$\nu = \frac{c_{12}}{c_{11} + c_{12}} \tag{6-3}$$

The Burgers vector describes the shift of material that produces a dislocation. The most likely Burgers vector for zincblende material is shown on figure 6-3 and has a magnitude, b, defined by :

$$b = \frac{a_{ZnCdSe}}{\sqrt{2}} \tag{6-4}$$

c_{11}, c_{12} and a_{ZnCdSe} are calculated from linear interpolations between known values for ZnSe and CdSe.

In zincblende structures, the most common slip plane is the (111) plane or a 90° rotation of that plane, i.e. one of (111), $(\bar{1}\,11)$, $(1\,\bar{1}\,1)$ and $(11\,\bar{1})$. By symmetry, the planes $(\bar{1}\,\bar{1}\,1)$ and $(11\,\bar{1})$ are the same. The most dominant type of misfit dislocation observed is the so-called 60° dislocation [26] as shown in figure 6-3 where the angle α between $\underline{c}$ and $\underline{b}$ is 60°.

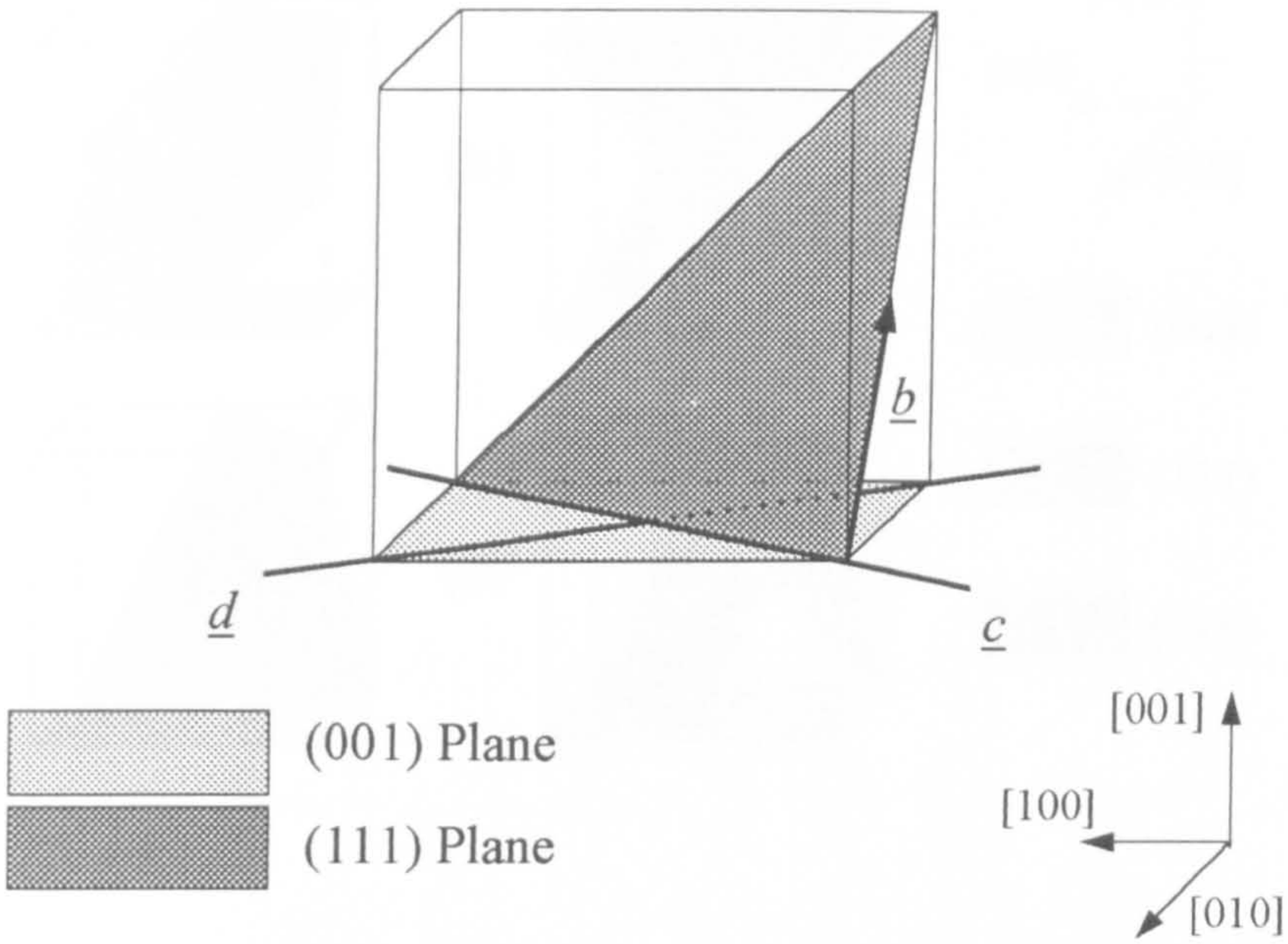

Figure 6-3. *The dislocation line (c), slip plane* (111) *and Burgers vector (b) in a zincblende crystal. d is a line in the film plane which is perpendicular to the intersection of the slip plane (in this case,* (111)*) and film plane (in this case,* (001)*).*

To determine the angle λ one has to determine the line $\underline{d}$ as defined in the caption of figure 6-3. In the case of layers grown on (001) substrates, λ is either 60° or 90°, whatever slip plane is considered. Since cos(90°) is zero and would give a zero denominator in equation (6-1), this option is not considered.

For growth on the (211) plane, the only parameter to change is λ. However, one has to consider the results when each of the four possible slip planes intersect with the (211) growth plane, as shown on figure 6-4.

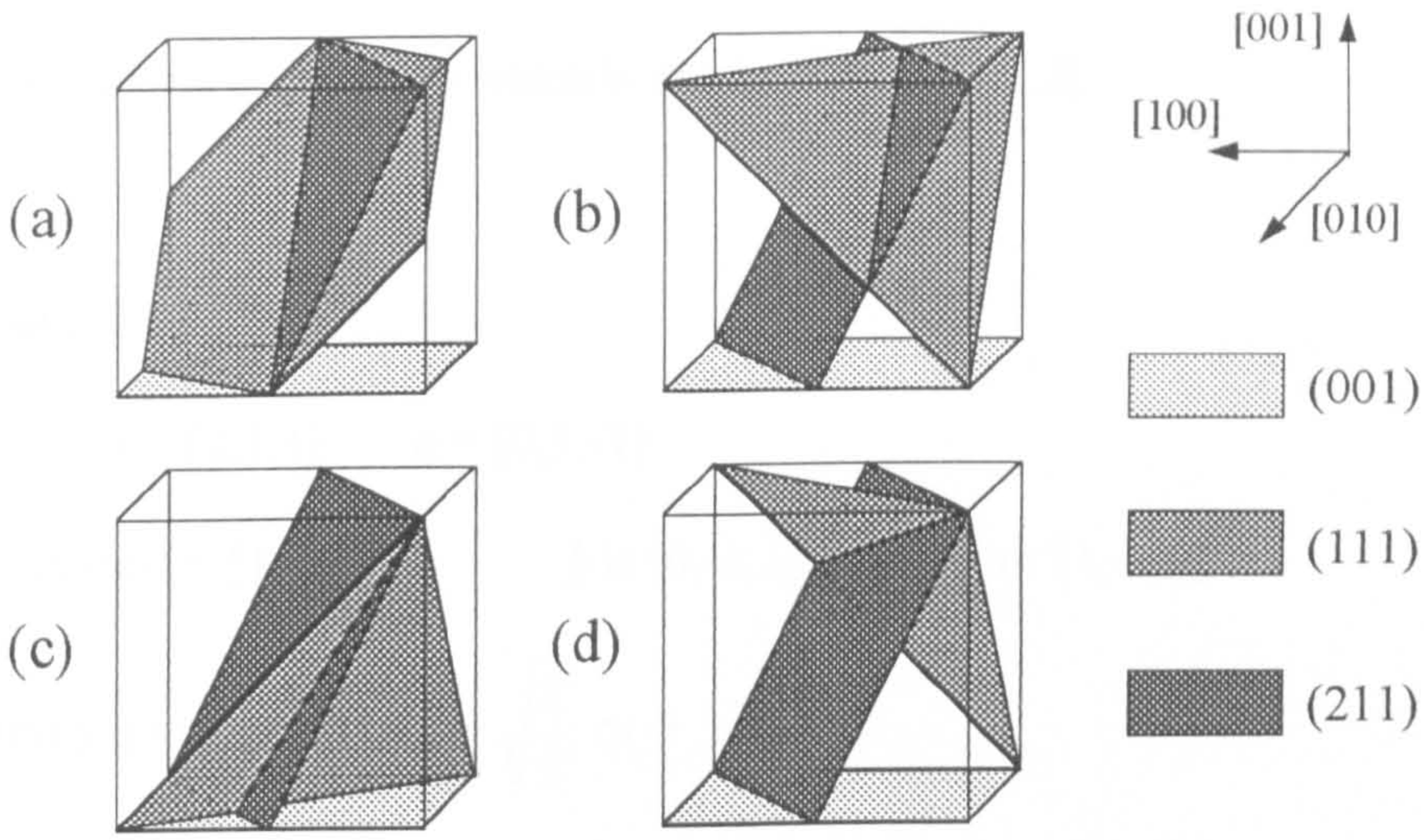

Figure 6-4. *Intersections of the* (211) *plane with* (a) *the* (111) *plane,* (b) *the* $(\bar{1}\,11)$ *plane,* (c) *the* $(1\,\bar{1}\,1)$ *plane and* (d) *the* $(11\,\bar{1})$ *plane.*

We can calculate λ from the scalar product of the Burgers vector and the line $\underline{d}$ as defined in the caption of figure 6-3. The scalar product of two vectors is defined by

$$(a_1,a_2,a_3).(b_1,b_2,b_3) = |a||b|\cos\lambda = a_1b_1 + a_2b_2 + a_3b_3 \qquad (6\text{-}5)$$

To simplify the calculations, a vector $\underline{n}$ is defined as the normal to the film plane and a vector $\underline{a}$ is defined as the line of intersection of the slip plane and the (211) growth plane. Therefore, in general, $\underline{d}$ will be a vector that is perpendicular to both $\underline{a}$ and $\underline{n}$. In each case $\underline{b}$ can be one of the three Burgers vector directions contained in the slip plane, e.g. for a (111) slip plane, $\underline{b}$ can be [0,-1,1], [-1,0,1] or [1,-1,0]. Only the absolute values of cos λ were considered, as negative values would produce

obtuse angles. When the smallest angle between the two lines is considered, one produces the acute angle which is obtained from $|\cos\lambda|$.

Case (a).

$\underline{n} = [2,1,1]$ $\underline{a} = [0,1,-1]$

therefore $\underline{d} = [1,-1,-1]$ $\underline{b}$ is [0,-1,1], [-1,0,1] or [1,-1,0]

From $\underline{b}.\underline{d}$ one gets $\cos\lambda = \sqrt{\frac{2}{3}}$ or 0

Giving $\lambda = 35.26°$ or 90° respectively.

Case (b).

$\underline{n} = [2,1,1]$ $\underline{a} = [0,1,-1]$

therefore $\underline{d} = [1,-1,-1]$ $\underline{b}$ is [0,-1,1], [1,0,1] or [1,1,0]

From $\underline{b}.\underline{d}$ one gets $\cos\lambda = \sqrt{\frac{2}{3}}$ or 0

Giving $\lambda = 35.26°$ or 90° respectively.

Case (c).

$\underline{n} = [2,1,1]$ $\underline{a} = [-2,1,3]$

therefore $\underline{d} = [1,-4,2]$ $\underline{b}$ is [0,1,1], [1,0,-1] or [1,1,0]

From $\underline{b}.\underline{d}$ one gets $\cos\lambda = \frac{m}{\sqrt{42}}$ $m = 1,2$ or 3

Giving $\lambda = 81.12°$, 72.02° and 62.42° respectively.

Case (d).

$\underline{n} = [2,1,1]$ $\underline{a} = [-2,3,1]$

therefore $\underline{d} = [1,2,-4]$ $\underline{b}$ is [0,1,1], [1,0,1] or [-1,1,0]

From $\underline{b}.\underline{d}$ one gets $\cos\lambda = \frac{m}{\sqrt{42}}$ $m = 1,2$ or 3

Giving $\lambda = 81.12°$, 72.02° and 62.42° respectively.

Therefore five possible values for λ are obtained, however $\lambda = 90°$ is again ignored. The remaining four values for λ were used in equation (6-1) and the results are shown in figure 6-5.

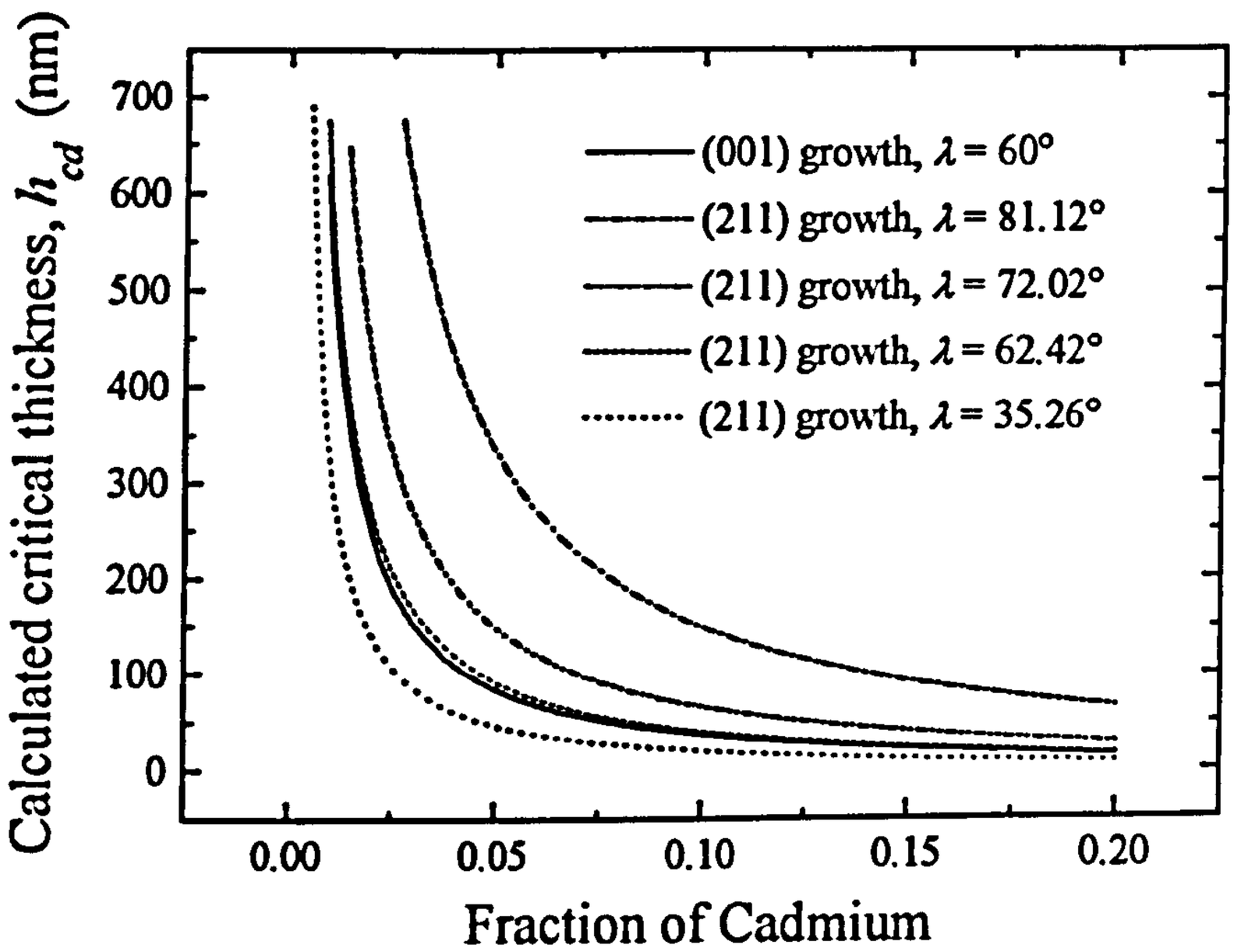

Figure 6-5. *Matthews / Blakeslee calculations for the critical thickness of $Zn_{1-x}Cd_xSe$ / ZnSe quantum wells grown on various substrate orientations.*

The critical thickness calculation that is to be considered for (211) growth is that which gives the lowest value (*i.e.* $\lambda = 35.26°$), lower than that for (001) growth. If one considers the growth process, when the first possible value for h_{cd} is reached then this dislocation mechanism becomes active and dislocations will be formed. The rate of dislocation formation may increase when the other values of h_{cd} are reached, depending on the amount of dislocations formed at the first h_{cd}. It is interesting to note that in the previously mentioned work by Anan *et al.* [21] for (111) growth, they calculated a value for $\cos\lambda$ of $1/\left(2\sqrt{3}\right)$, giving $\lambda = 73.22°$, and therefore a value of h_{cd} greater than (001) growth, but they do not specify which slip plane was considered in the calculations, as clearly the (111) plane will not relieve any strain in (111) growth. However, their calculations appear to be in agreement with their experimental observations.

6.2.2 Dunstan model.

Another model has been developed that uses a simple geometrical argument to predict the second critical thickness for lattice relaxation, h_{cr}, that is in good agreement with previous models and also predicts the strain relaxation after the critical thickness has been reached [27]. It predicts a critical thickness h_{cr} given by

$$h_{cr} = k_1 \frac{b}{\varepsilon_0} \tag{6-6}$$

where ε_0 is the unrelaxed misfit strain and b is the magnitude of the Burgers vector of the misfit dislocation. Furthermore, it predicts that after the critical thickness has been passed, the strain in the layer can be calculated by

$$\varepsilon(h) = k_2 \frac{b}{h} \tag{6-7}$$

k_1 and k_2 are constants of proportionality and are expected to be of the order of unity. If k_1 and k_2 are the same then there is no discontinuous relaxation at the critical thickness [28]. If they are different, then the strain in layers below the critical thickness is given by equation (6-6) and the relaxation in layers above the critical thickness is given by a reduced value of k_2 in equation (6-7). This is shown in figure 6-6 which relates the strain in the layer to the thickness of the layer. For layers below the critical thickness, the strain is always at a given magnitude. For layers above the critical thickness, the strain is given by curve (a) for $k_1 = k_2$ or (b) for $k_1 \neq k_2$ which shows the discontinuous drop in the strain at the critical thickness. Curve (a) decays as $k_1 b/h$ while curve (b) decays as $k_2 b/h$.

This relationship was compared with experimental analysis of GaInAs / GaAs layers and showed good agreement except for those samples with thicknesses considerably greater than h_{cr} [28]. At these values the samples were shown to have less strain than predicted by the theory, a phenomenon for which the authors could only speculate. It will be shown in this chapter that this short-coming is repeated in our results for which an amendement to the Dunstan model is proposed.

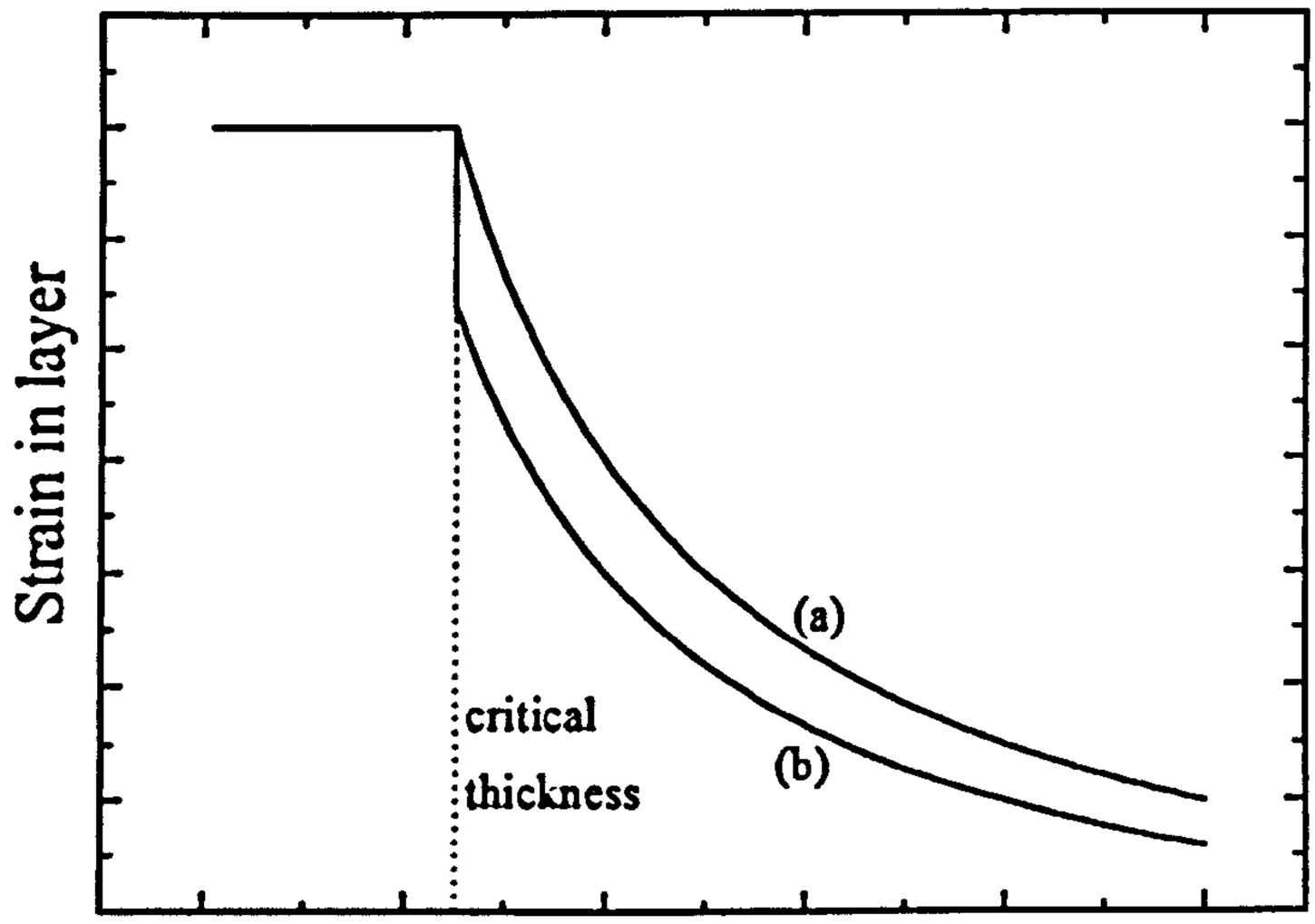

Figure 6-6. *Strain in a semiconductor layer against the layer thickness for* (a) $k_1 = k_2$ *and* (b) $k_1 \neq k_2$.

6.3. Application of the piezoelectric effect.

This chapter presents a new method for measurement of h_{cr} taking advantage of the built-in piezoelectric effect in strained quantum wells, which occurs in any (h11)-orientated zincblende structure and any wurtzite structures grown with the typical (0001) orientation. This approach is very convenient as it does not require the knowledge of any parameters of the investigated material. Furthermore, it can be extremely sensitive to the degree of relaxation of the layer.

As explained in chapter 3, strained quantum well layers in piezoelectric semiconductors have their transitions shifted to lower energies by the quantum confined Stark effect. For the built-in field due to the piezoelectric effect, F^{st}_{piezo}, the magnitude of this shift depends on the magnitude of the internal strain in the layer and the layer thickness. This is shown in equation (6-8) which gives the energy of the ground state transition in a compressively-strained quantum well.

$$E_1HH_1 = E_g^{st} + E_1 + HH_1 - |e|F^{st}_{piezo}L_w - E_b \tag{6-8}$$

E_g^{st} is the band gap of the strained layer, E_1 and HH_1 are the confinement energies of the first quantum well states for the electrons and holes respectively, and E_b is the exciton binding energy. The term $|e|F^{st}_{piezo}L_w$ is the shift in energy due to the internal electric field where L_w is the width of the quantum well. F^{st}_{piezo} is linearly dependent on the strain in the layer [29].

As explained in the model of the triangular well detailed in chapter 3, the wavefunction overlap in piezoelectric structures will decrease with increasing well width and therefore E_b can be ignored for wide wells [30]. Furthermore, the confinement energies E_1 and HH_1 in wide wells will no longer depend on the well thickness but only on the piezoelectric field which defines the well shape and so E_1 and HH_1 can be found by solving the finite triangular well model. Therefore, for a given lattice mismatch the piezoelectric field is fixed as long as the layer has not relaxed and so E_1 and HH_1 will remain constant for wide wells provided that equation (6-9) is true.

$$L_w \geq \frac{2E}{e\left|F_{piezo}^{st}\right|} \tag{6-9}$$

where E is either E_1 or HH_1.

Therefore, above this thickness, the excitonic transition energy E_1HH_1 decreases linearly with the thickness of the layer since F_{piezo}^{st} is fixed by the strain and will remain constant for a given lattice mismatch (i.e. percentage of Cadmium) until the onset of relaxation of the layer at h_{cr}. Hence its value is simply given by

$$E_1HH_1 = E_g^{st} + E_1 + HH_1 - |e|F_{piezo}^{st} L_w \tag{6-10}$$

This relationship no longer applies above the threshold thickness h_{cr} where two effects have to be considered. Firstly, a change of the band gap energy occurs when going from the fully-strained to the fully-relaxed regime. This effect is usually quite small especially when heavy holes are involved and, in fact, for $Zn_{0.85}Cd_{0.15}Se$, the band gap variation is as small as 9meV which is of the same order as a change in the Cd content of less than 1%. Therefore optical spectroscopy is of little use to determine h_{cr} for (001)-oriented samples. The second effect, which is usually much more important, is the reduction in F_{piezo}^{st} due to the strain relaxation. In the case of (211)-$Zn_{1-x}Cd_xSe$ / ZnSe quantum wells, F_{piezo}^{st} has been estimated to be 0.42V/μm per percent of cadmium in a fully strained well layer (see chapter 4), which gives a shift of 120meV between a fully-relaxed and a fully-strained 20nm $Zn_{0.85}Cd_{0.15}Se$ / ZnSe quantum well,

and a piezoelectric field of 6.3V/μm. Our calculations show that (E_1+HH_1) will reduce from 85meV to nearly zero as the strain is decreased and the QW shape changes from triangular to square. This is a significantly smaller change than that in $e\left|F_{piezo}^{st}\right|L_w$ showing that the most important effect at relaxation is the decrease of the piezoelectric field.

A new equation has been developed to describe E_1HH_1 in a piezoelectric quantum well that considers the degree of strain S. Ignoring E_b, the energy E_1HH_1 is

$$E_1HH_1 = S\left(E_g^{st} - e\left|F_{piezo}^{st}\right|L_w\right) + (1-S)E_g^{unstrained} + S^{2/3}(E_1 + HH_1) \qquad (6\text{-}11)$$

where S is expected to vary as $(1/L_w)$ for $L_w > h_{cr}$ from the model of Dunstan *et al.* [27]. The 2/3-power dependence for the E_1 and HH_1 energies is exact in the case of an infinite barrier height and is still a good approximation for relatively small barrier potentials ; using 142meV and 47meV respectively for the conduction and valence band offsets between $Zn_{0.85}Cd_{0.15}Se$ and ZnSe, the error induced by such an approximation is always smaller than 5meV.

The striking feature of this model will be the clear change in behaviour of the E_1HH_1 transition energy at the threshold thickness. For $L_w < h_{cr}$, $S = 1$, however after h_{cr}, there is a sharp change in the value of S as shown in figure 6-6. Hence the value of h_{cr} is precisely determined by the abrupt transition from one regime to the other.

6.4. Experiment.

To illustrate this approach a set of $Zn_{0.85}Cd_{0.15}Se$ quantum wells with thicknesses ranging from 10nm to 40nm were grown by MBE. They consisted of a fully relaxed 1μm layer of ZnSe on the (211)B GaAs substrate, the well layer and then a 0.1μm capping layer of ZnSe. Growth details can be found elsewhere [31]. The composition and thickness of the ZnCdSe quantum wells were calculated from a thick relaxed epilayer by PL and reflectivity respectively. The full set of samples has been grown in the same run in order to minimise any composition variations after the growth of the calibration layer.

The PL spectra are shown in figure 6-7 for different well widths and it can be seen that as the well width increases the E_1HH_1 transition energy moves to a lower value up to a well thickness of 20nm, when the exciton peak begins to move back to higher energy. This indicates that relaxation occurs between widths of 20nm and 30nm. We note that each PL spectrum was obtained with the minimum possible excitation power to avoid any blue shift due to the screening effect of carriers on the electric field [32]. This will be explained in section 6.5.

The results are displayed in figure 6-8 which shows, in addition to the experimental points, the exciton energies for the fully relaxed case corresponding to the internal field strength being zero (curve *a*), the energies for the fully strained (211) oriented samples as determined from equation (6-10) for $L_w < h_{cr}$ (curve *d*) and the

energies for the partially relaxed regime for $L_w > h_{cr}$ defined by equation (6-11) (curve *c*).

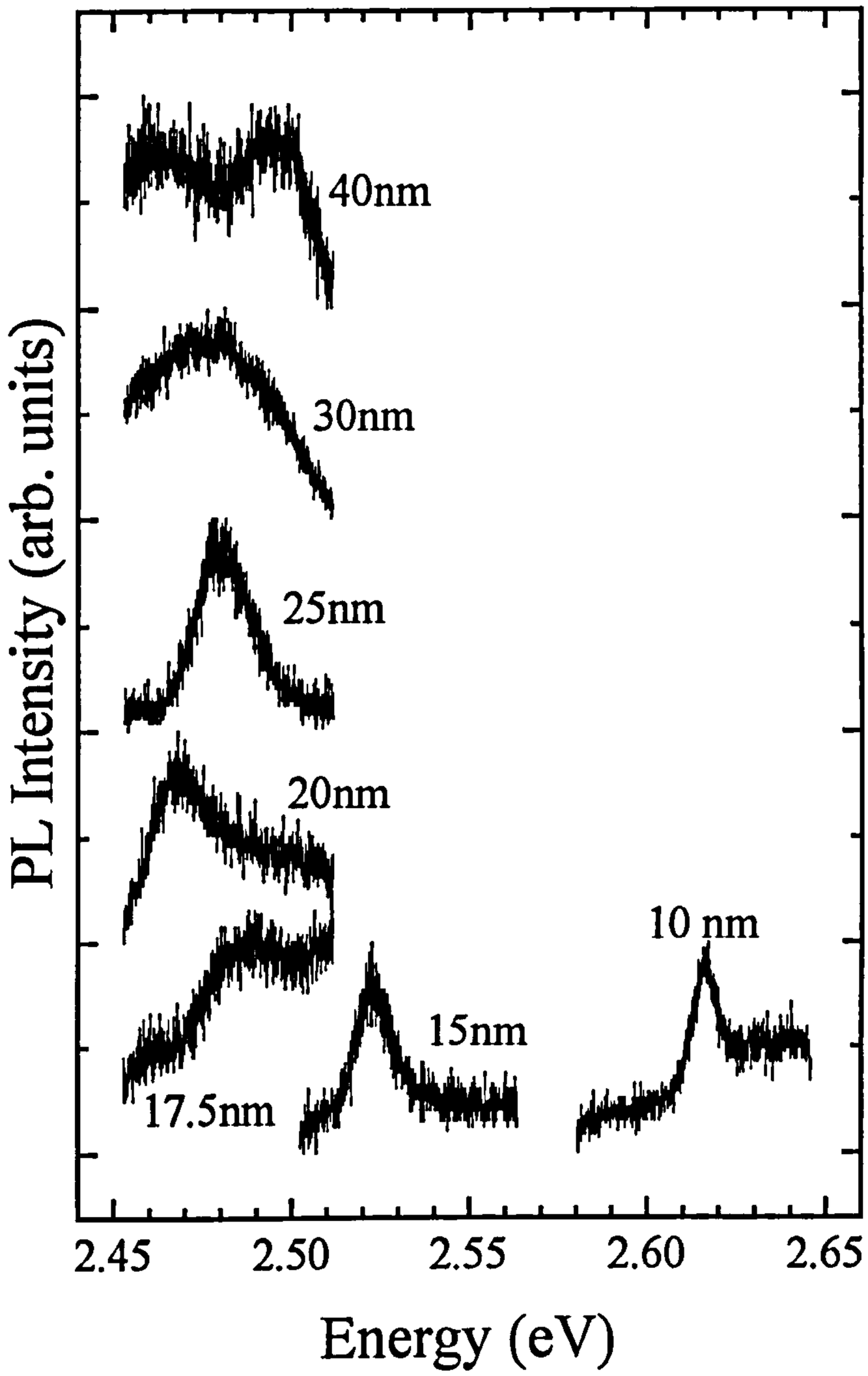

Figure 6-7. *PL spectra of $Zn_{0.85}Cd_{0.15}Se$ / ZnSe single quantum wells of various widths grown on (211)B substrate recorded at 5K and at an excitation density of between $10\mu Wcm^{-2}$ and $10^5\mu Wcm^{-2}$. The surrounding luminescence is the deep band from the ZnSe barrier layers.*

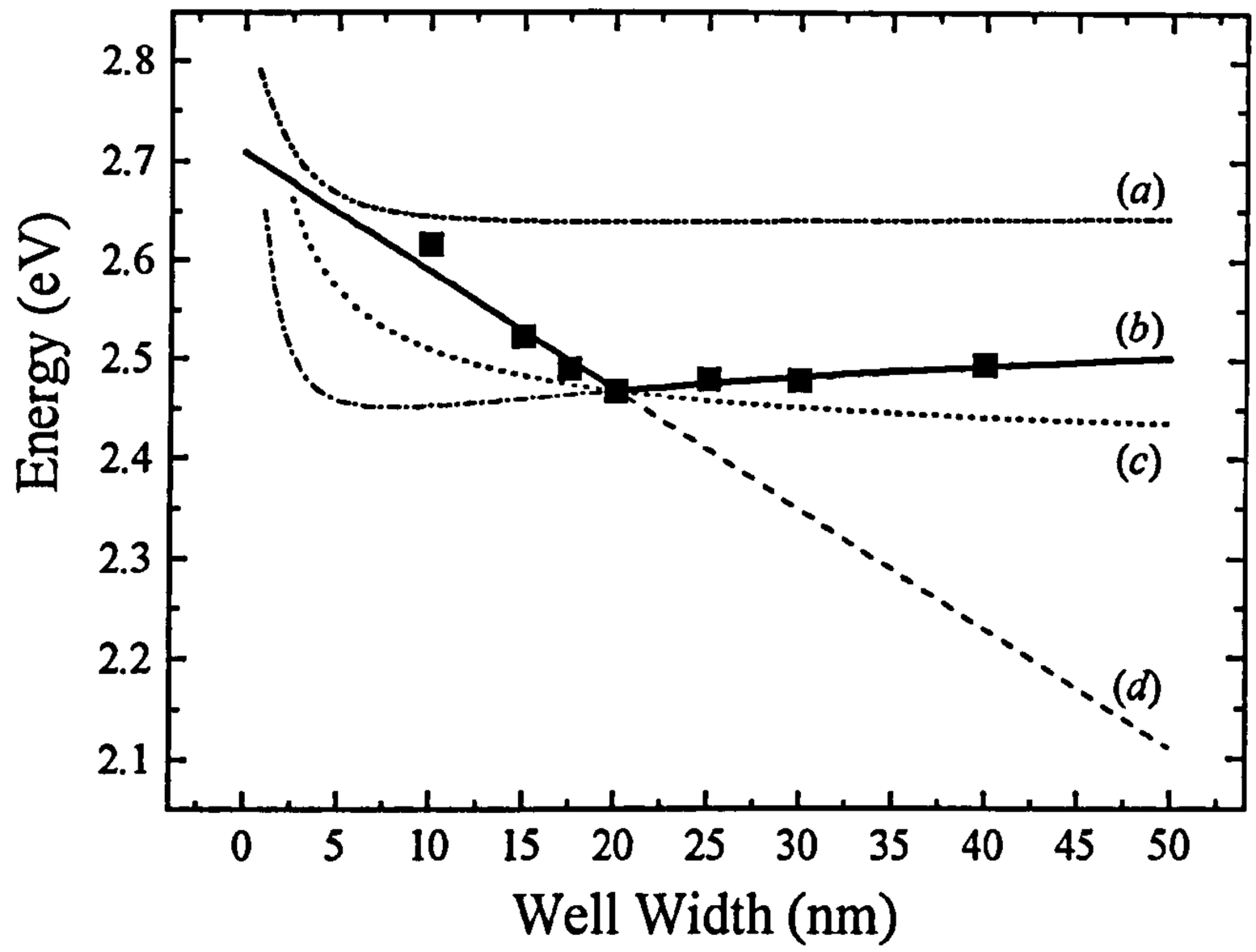

Figure 6-8. *The variation of the PL emission with well width for* $Zn_{0.85}Cd_{0.15}Se$ / *ZnSe single quantum wells on a (211)B substrate showing the on-set of strain relaxation* (■). *Calculated variations considering no piezoelectric field, (curve a), Eq.* (6-10) *(curve d), Eq.* (6-11) *combined with the model of Dunstan et al* [27] *(curve c) and Eq.* (6-11) *combined with our alteration as given in Eq.* (6-12) *(curve b) are also displayed. Note that for the calculation without a piezoelectric field, the excitonic binding energy has a strong contribution for large quantum wells which disappears when a field is present.*

It is worth noting that within Dunstan's description [27] the dependence of the energy on the well width is almost completely removed (see curve *c*) as the variation in energy is only due to the effect of strain on the band gap. As a result this model never allows for complete relaxation.

To produce a more accurate simulation of the relaxation, we propose an empirical amendment to the model of Dunstan *et al.* [27] and the use of a more general form of S:

$$S \propto \frac{1}{(L_w)^n} \tag{6-12}$$

Using $n \approx 1.4$ in this expression for S, as obtained from a least-square fit, we now have a much more realistic prediction, shown as curve b, where E_1HH_1 tends to $E_g^{unstrained}$ as L_w becomes very large and the slope of relaxation has the correct curvature for $L_w > h_{cr}$. As it can be seen from figure 6-8, an excellent agreement is found between the data with equation (6-10) and equation (6-11) over the whole range of values of L_w. The intersection of the two line fits describing the fully-strained and the partially relaxed regimes is well established at 20nm, thus we can say that h_{cr} is 20nm.

A model suggested by Lovergine *et al.* [33] stated that the residual strain in an epilayer greater than the critical thickness can be expressed as

$$\varepsilon = \varepsilon_1 \left[1 - A b_{eff}\right]^{2h/a} \tag{6-13}$$

a is the lattice parameter, b_{eff} is the effective burgers vector, h is the layer thickness, ε_1 is the strain before relaxation and A is a constant. This reduces to equation (6-14).

$$S = \frac{\varepsilon}{\varepsilon_1} = \exp(kh) \tag{6-14}$$

k is a constant that combines A, b_{eff}, and a. However, when this was fitted to the data points it was found to have an opposite curvature to that experimentally observed, as shown in figure 6-9.

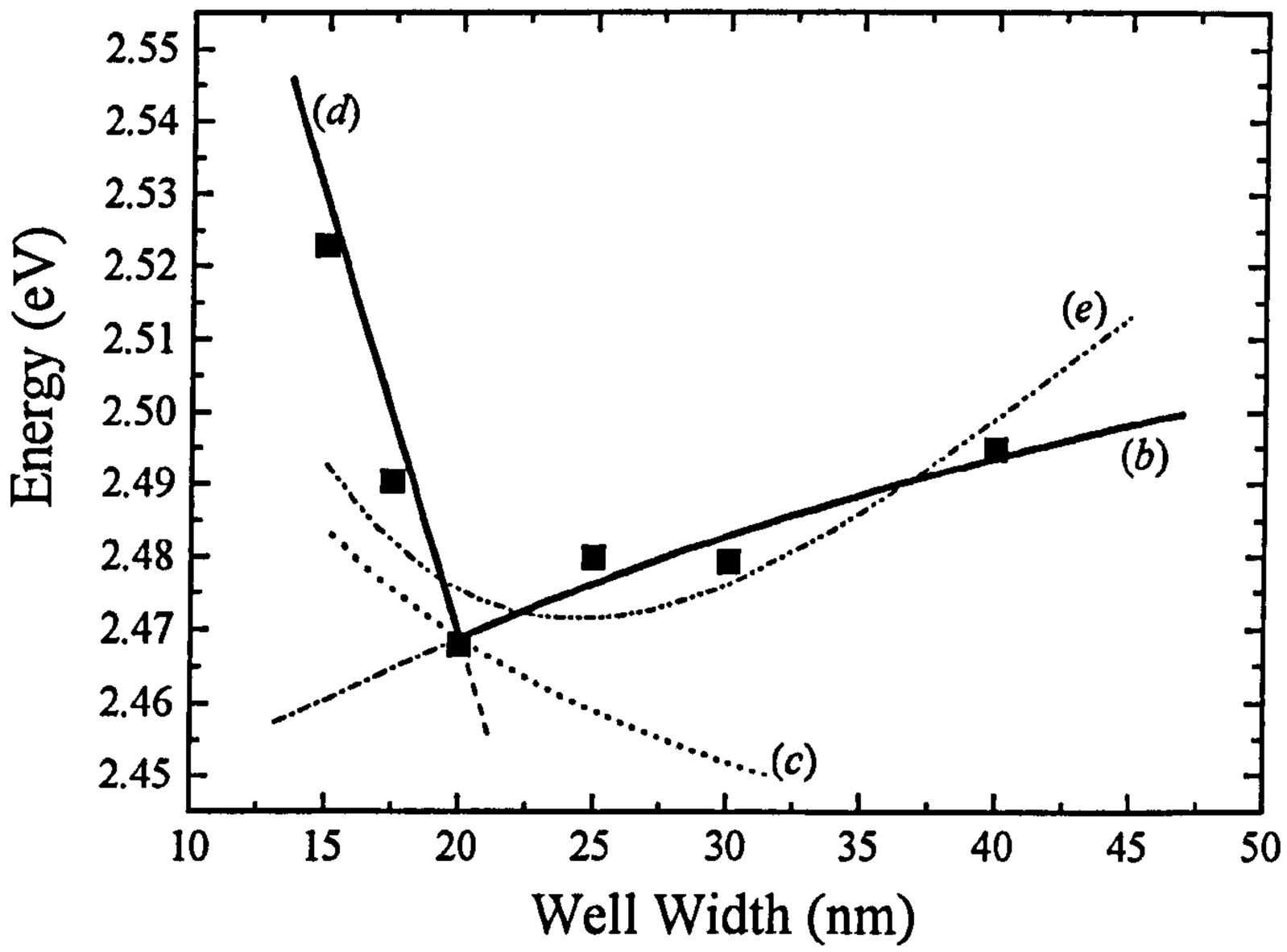

Figure 6-9. *An expanded portion of figure* 6-8, *with the additional line fit of curve* (e) *from the model proposed by Lovergine et al.* [33].

Recall that S is defined as the degree of strain such that

$$S = \frac{\varepsilon(h)}{\varepsilon_0} \tag{6-15}$$

However, if this is combined with equations (6-6) and (6-7) of the Dunstan model, and providing $k_1 = k_2$, it is found that

$$S = \frac{h_{cr}}{h} \tag{6-16}$$

Therefore the least square fit mentioned above would independently produce a value of h_{cr}, which was 20nm, which is in good agreement with the previously found figure. However, it would be unwise to take this figure independently, because the least square fit was only modelled on half the data points and it also produced a value of 12V/μm for the piezoelectric field, a factor of 2 larger than the expected figure of 6.3V/μm. This value was also used in curves (*c*) and (*d*) in figure 6-8. Fitting the Lovergine model produced an even more inaccurate value for the field of 25V/μm.

A list of the results provided by the Matthews / Blakeslee calculations of h_{cd} in section 6.2.1 is shown in table 6-1 for ZnCdSe quantum wells with a cadmium percentage of 15%.

As mentioned before, the lowest calculated value for h_{cd} is that considered for the first dislocations. The value of h_{cd} for (211) growth of $Zn_{0.85}Cd_{0.15}Se$ on ZnSe is therefore considered to be 12.07nm, giving a value of 0.61 for the fraction h_{cd}/h_{cr}. This is very close to $h_{cd}/h_{cr} = 0.63$ given by references 4 and 16 for ZnSe grown on (001) GaAs substrates. This indicates that the rate of dislocation formation from the first at h_{cd} up to the point that the strain fields overlap at h_{cr} is similar in both cases. However,

this rate does depend on the growth method, hence the difference in values for h_{cr} for ZnSe on (001) GaAs given by references 16, 19 and 20 in the introduction.

Table 6-1. *Calculated values of h_{cd} for $Zn_{0.85}Cd_{0.15}Se$ / ZnSe quantum wells for various substrate orientations by the Matthews / Blakeslee formula.*

Plane orientation	λ	h_{cd} (nm)
(001)	60°	22.50
(211)	35.26°	12.07
(211)	62.42°	24.77
(211)	72.02°	40.77
(211)	81.10°	93.61

From these results the advantages of using the piezoelectric effect for determining the critical thickness is clearly demonstrated and can be summarised as follows :

(i) The QCSE induced shift arising from the internal field is very large resulting in high sensitivity. For instance, a blue shift of 170meV is observed for the 40nm quantum well.

(ii) Comparing the observed exciton peak positions with those calculated for the fully strained and unstrained cases allows a measurement of the internal field

strength to be made and hence an evaluation of the degree of relaxation. This is illustrated for this study in figure 6-10.

(iii) There is no requirement for previous knowledge of the material parameters, such as lattice parameters of the compounds, elastic stiffness tensor elements, deformation potential of the bands, dielectric constants, carrier effective mass and band offsets. Although we have made a detailed calculation of the confinement energy (E_1+HH_1) for the triangular well, in general, an estimate of this energy can be obtained by extrapolating a linear fit of the data points up to h_{cr} (similar to curve *d*) back to $L_w = 0$ and then subtracting the band gap of the strained quantum well material. This value can then be used to fit the relaxed data with equation (6-11).

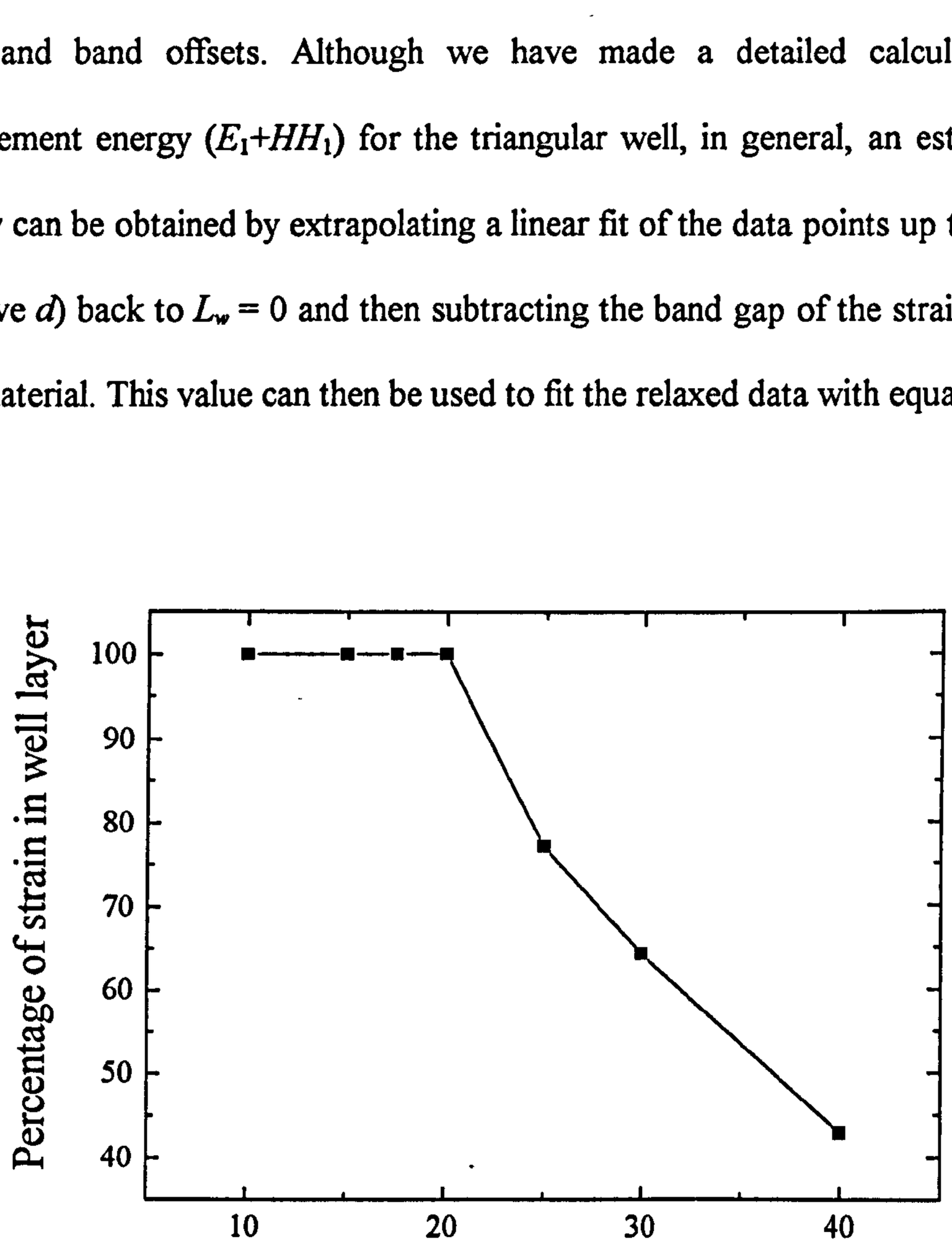

Figure 6-10. *Residual strain calculated for ZnCdSe / ZnSe quantum wells on (211)B GaAs.*

6.5. Carrier screening of the piezoelectric field.

As mentioned in chapter 3, the piezoelectric field can be screened by photoexcited carriers. Therefore the measurements of the band gap in the quantum well samples for the critical thickness study had to be taken with as low an excitation power as possible as any screening would give an artificially high value for the band gap energy. To check that screening was minimised, the effect of varying the pump excitation was studied on some of the quantum wells used in this study, and the results are shown in figure 6-11.

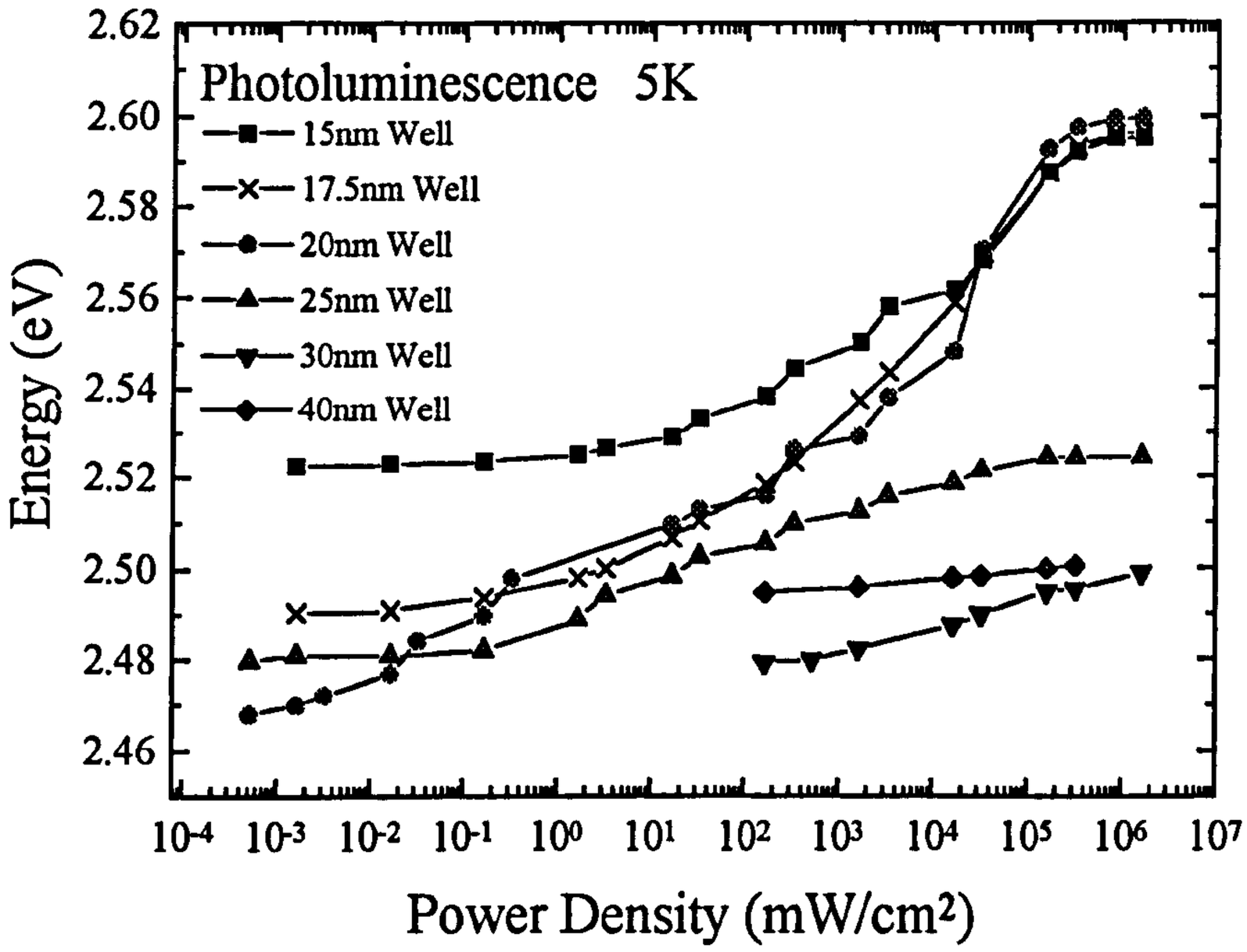

Figure 6-11. *The variation in PL emission energy with the power density of the excitation for $Zn_{0.85}Cd_{0.15}Se$ / ZnSe single quantum wells on (211)B GaAs.*

The emission energy from the 15nm, 17.5nm and 20nm wells were able to screen to an energy just below the equivalent (001) quantum well emission (≈2.62eV), as predicted. However, the three larger wells seem unable to reach this level and table 6-2 shows that the screening ability is reduced as the well width increases (the shifts in the 15nm and 17.5nm wells are lower than the 20nm well because they had a smaller piezoelectric field to screen out).

Table 6-2. *Shift in PL emission peak caused by free carrier screening in $Zn_{0.85}Cd_{0.15}Se$ / ZnSe single quantum wells of various widths.*

Well Width (nm)	Screening Shift (meV)
15	72.5
17.5	106.0
20	131.6
25	44.8
30	19.6
40	5.9

Screening in larger wells requires a greater input of free charge. To produce an electric field of a given magnitude (which screening requires) over a larger distance requires a larger potential difference, as E-field = Voltage / Distance, and therefore a larger charge input. Clearly for wells greater than 20nm in width, our maximum power density was insufficient to screen the entire piezoelectric field.

The ability of the larger wells to screen out the piezoelectric field is also limited by a reduced carrier confinement. Figure 6-12 shows broad photoluminescence scans for five of the samples used above.

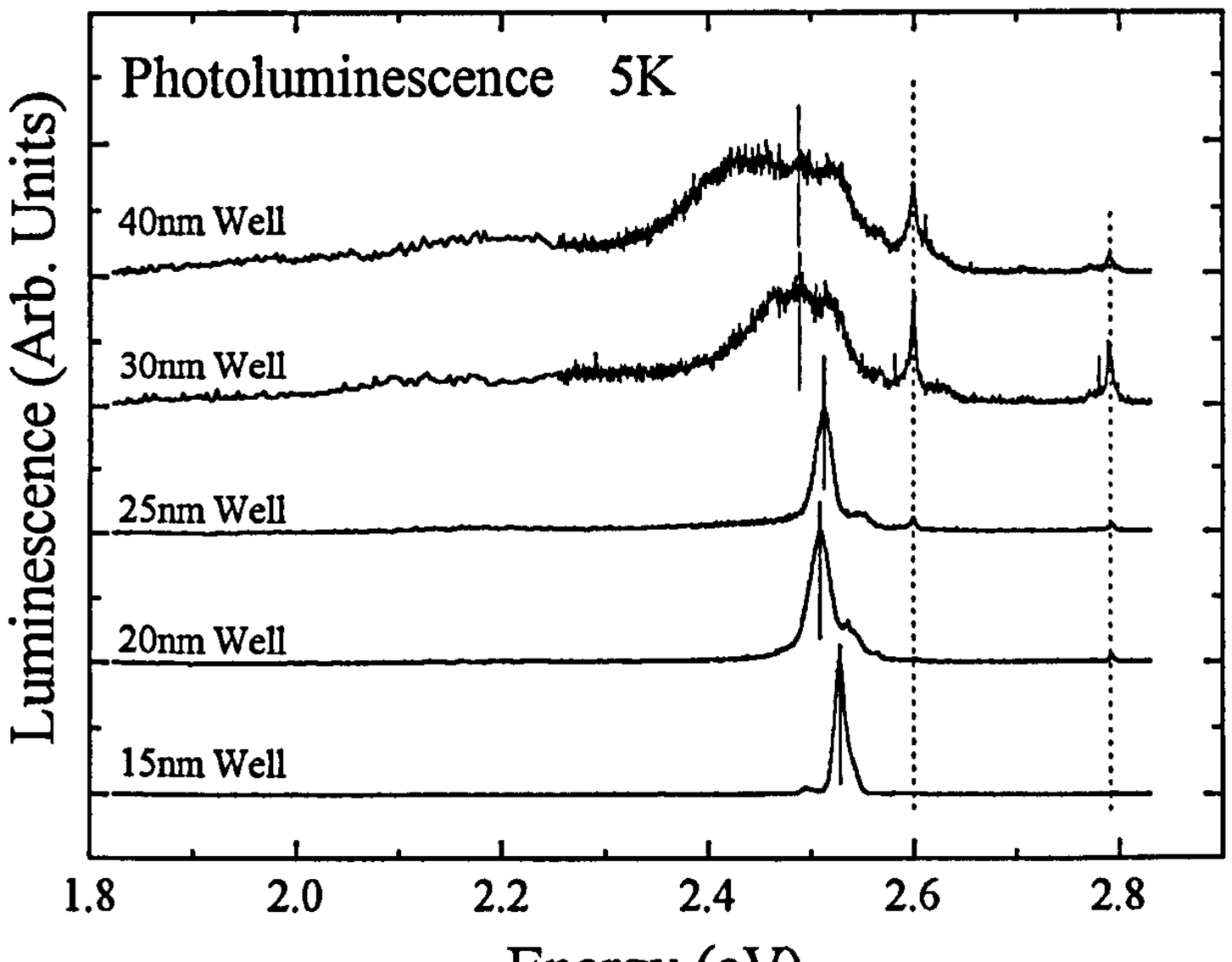

Figure 6-12. *Broad PL scans for $Zn_{0.85}Cd_{0.15}Se$ / ZnSe single quantum wells of various widths, showing the Y_0 defect related emission at 2.6eV and the ZnSe exciton emission at 2.8eV. The quantum well emissions are identified by the solid vertical lines.*

Clearly the carriers created in the larger well samples are not easily confined within the wells for the 30nm and 40nm wells. This lack of confinement will limit the ability to build up charge under strong excitation and therefore make it more difficult to screen the piezoelectric field. The quantum well emissions in these two cases were

clearly difficult to identify, and this could be only be confirmed by their observed blue shift under increased excitation as shown in figure 6-11.

6.6. Conclusion.

A novel method of determining the critical thickness for strain relaxation in piezoelectric semiconductor heterostructures has been demonstrated. The critical thickness of $Zn_{0.85}Cd_{0.15}Se$ on ZnSe grown on a (211)B GaAs substrate was 20nm. This technique for measuring the critical thickness relies only on the presence of an internal piezoelectric field and as such is not limited to any one particular materials system or plane. In compound semiconductors with the zincblende structure, all planes with Miller indices (h11) are suitable. In the case of semiconductors with the wurtzite structure, the (0001) basal plane is the most commonly used and this can show a strong piezoelectric field under biaxial strain. This method can therefore be used to determine h_{cr} for nitride alloy systems as long as the strain is sufficiently small that relaxation does not occur where quantum confinement effects dominate.

6.7. References.

[1] R.H. Dixon and P.J. Goodhew, J. Appl. Phys. **68**, 3163 (1990).

[2] J.W. Matthews and A.E. Blakeslee, J. Cryst. Growth **27**, 118 (1974).

[3] C.R. Whitehouse, A.G. Cullis, S.J. Barnett, B.F. Usher, G.F. Clark, A.M. Keir, B.K. Tanner, B. Lunn, J.C.H. Hogg, A.D. Johnson, G. Lacey, W. Spirkl, W.E. Hagston and J.H. Jefferson, J. Cryst. Growth **150**, 85 (1995).

[4] G. Horsburgh, K.A. Prior, W. Meredith, I. Galbraith, B.C. Cavenett, C.R. Whitehouse, G. Lacey, A.G. Cullis, P.J. Parbrook, P. Möck and K. Mizuno, Appl. Phys. Lett. **72**, 3148 (1998).

[5] P. Kidd, P.F. Fewster, N.L. Andrew and D.J. Dunstan, Inst. Phys. Conf. Ser. **134**, 585 (1994).

[6] M. Hopkinson, J.P.R. David, P.A. Claxton and P. Kightley, Appl. Phys. Lett. **60**, 841 (1992).

[7] N. Grandjean, J. Massies, C. Delamarre, L.P. Wang, A. Dubon, and J.Y. Laval, Appl. Phys. Lett. **63**, 66 (1993).

[8] J. Cibert, Y. Gobil, Le Si Dang, S. Tatarenko, G. Feuillet, P.H. Jouneau and K. Saminadayar, Appl. Phys. Lett. **56** 292 (1990).

[9] T. Reisinger, A. Rosenauer, F. Franzen and W. Gebhardt, *Semiconductor Heteroepitaxy*, edited by B. Gil and R.-L. Aulombard (World Scientific, Montpelier, 1995), p. 118.

[10] E. Tournié, C. Ongaretto, M. Laügt and J.-P. Faurie, Appl. Phys. Lett. **72**, 217 (1998).

[11] E. Tournié, H.-P. Schönherr, K. Ploog, C. Giannini and L. Tapfer, Appl. Phys. Lett. **61**, 846 (1992).

[12] N.G. Anderson, W.D. Laidig, R.M. Kolbas and Y.C. Lo, J. Appl. Phys. **60**, 2361 (1986).

[13] H. Temkin, D.G. Gershoni, S.N.G. Chu, J.M. Vandenberg, R.A. Hamm and M.B. Panish, Appl. Phys. Lett. **55**, 1668 (1989).

[14] J.-P. Reithmaier, H. Cerva and R. Lösch, Appl. Phys. Lett. **54**, 48 (1989).

[15] C.B. O'Donnell, G. Lacey, G. Horsburgh, A.G. Cullis, C.R. Whitehouse, P.J. Parbrook, W. Meredith, I. Galbraith, P. Möck, K.A. Prior and B.C. Cavenett, J. Cryst. Growth **184/185**, 95 (1998).

[16] H. Mitsuhashi, I. Mitsuishi, M. Mizuta and H. Kukimoto, Jpn. J. Appl. Phys. **24**, L578 (1985).

[17] J. Petruzzello, B.L. Greenberg, D.A. Cammack and R. Dalby, J. Appl. Phys. **63**, 2299 (1988).

[18] G.D. Brownlie, Z. Zhu, G. Horsburgh, T.A. Steele, P.J. Thompson, J.M. Wallace, K.A. Prior and B.C. Cavenett, J. Cryst. Growth **159**, 321 (1996).

[19] J. M. Gaines, J. Petruzzello and B. Greenberg, J. Appl. Phys. **73**, 2835 (1993).

[20] K. Wolf, S. Jilka, A. Rosenauer, G. Schütz, H. Stanzl, T. Reisinger and W. Gebhardt, J. Phys. D : Appl. Phys. **28**, A120 (1995).

[21] T. Anan, K. Nishi and S. Sugou, Appl. Phys. Lett. **60**, 3159 (1992).

[22] S. Guha, H. Cheng, M.A. Haase, J.M. DePuydt, J. Qiu, B.J. Wu and G.E. Hofler, Appl. Phys. Lett. **65**, 801 (1994).

[23] S. Guha, J.M. DePuydt, J. Qiu, G.E. Hofler, M.A. Haase, B.J. Wu and H. Cheng, Appl. Phys. Lett. **63**, 3023 (1993).

[24] S. Hayashi, A. Tsujimura, S. Yoshii, K. Ohkawa and T. Mitsuyu, Jpn. J. Appl. Phys. **31**, L1478 (1992).

[25] J. Petruzzello, R. Drenten and J.M. Gaines, J. Cryst. Growth **138**, 686 (1994).

[26] E.A. Fitzgerald, Mater. Sci. Rep. **7**, 87 (1991).

[27] D.J. Dunstan, S. Young and R.H. Dixon, J. Appl. Phys. **70**, 3038 (1991).

[28] D.J. Dunstan, P. Kidd, L.K. Howard and R.H. Dixon, Appl. Phys. Lett. **59**, 3390 (1991).

[29] D.L. Smith and C. Mailhiot, J. Appl. Phys. **63**, 2717 (1988).

[30] Le Si Dang, R. André and J. Cibert, Ann. Phys. **20**, C2-101 (1995).

[31] S.A. Telfer, G. Horsburgh, J.S. Milnes, C. Morhain, P.J. Thompson, K.A. Prior and B.C. Cavenett, J. Cryst. Growth **184/185**, 51 (1998).

[32] I. Sela, D.E. Watkins, B.K. Laurich, D.L. Smith, S. Subbanna and H. Kroemer, Appl. Phys. Lett. **58**, 684 (1991).

[33] N. Lovergine, L. Liaci, J.-D. Ganière, G. Leo, A.V. Drigo, F. Romanato, A.M. Mancini and L. Vasanelli, J. Appl. Phys. **78**, 229 (1995).